UNIVERSITY OF CALIFORNIA SAN DIEGO

Addressing the Scalable Manufacturing Considerations of All-Solid-State Batteries

A dissertation submitted in partial satisfaction of the
requirements for the degree Doctor of Philosophy

in

Materials Science and Engineering

by

Yu-Ting Chen

Committee in charge:

Professor Zheng Chen, Chair
Professor Ying Shirley Meng, Co-Chair
Professor Eric Fullerton
Professor Ping Liu
Professor Michael Sailor

2023

The dissertation of Yu-Ting Chen is approved, and it is acceptable in quality and form for publication on microfilm and electronically.

University of California San Diego

2023

DEDICATION

To my family, for their unwavering support and encouragement.

TABLE OF CONTENTS

LIST OF ABBREVIATIONS

ASSB: All-Solid-State Battery

SSE: Solid-State Electrolyte

ML: Machine Learning

ASSPC: All-Solid-State Pouch Cell

UPCH: Uniaxial Pouch Cell Holder

IPCH: Isostatic Pouch Cell Holder

Li: Lithium

LIB: Lithium-Ion Battery

EV: Electric Vehicle

SEI: Solid Electrolyte Interphase

cathode electrolyte interphase

Li_6PS_5Cl

$LiNi_{0.5}Mn_{1.5}O_4$

PTFE: Polytetrafluoroethylene

Li-S: Lithium-Sulfur

Li-O_2: Lithium-Oxygen

P%: Polymer content

L:S: Liquid to solid ratio

X:B: Cosolvent ratio

ρ: Density

Ω: Ohmic resistance

σ_i^N: Normalized conductivity

DoT: Deviation of thickness

RD: Relative thickness deviation

PCA: Principal Component Analysis

SVM: Support Vector Machine

NCM811: $LiNi_{0.8}Co_{0.1}Mn_{0.1}O_2$

PBMA: Poly(butyl methacrylate)

XRD: X-ray diffraction

SEM: Scanning Electron Microscopy

EIS: Electronic Impedance Spectroscopy

DC: Direct Current

PEEK: Polyether ether ketone

AC: Alternating Current

SEBS: Polystyrene-block-polyethylene-ran-butylene-block-polystyrene

SVD: Singular Values Decomposition

FIB: Focused-Ion-Beam

Anova: Analysis of Variance

CE: Coulombic Efficiency

ss-NMR: Solid-State Nuclear Magnetic Resonance

FTIR: Fourier-Transform Infrared Spectroscopy

TGA: Thermal Gravimetric Analysis

DSC: Differential Scanning Calorimetry

VGCF: Vapor-Grown Carbon Fibers

CV: Cyclic Voltammetry

ICSD: Inorganic Crystal Structure Database

ATR: Attenuated Total Reflection

XPS: X-ray Photoelectron Spectroscopy

STA: Simultaneous Thermal Analyzer

QMS: Quadrupole Mass Spectrometer

MS: Mass Spectrometry

MAS NMR: Magic Angle Spinning Nuclear Magnetic Resonance

HETCOR: Heteronuclear Correlation

TMS: Tetramethylsilane

T1: Spin-Lattice Relaxation Time

LYC: Li_3YCl_6

LZC: Li_2ZrCl_6

LIC: Li_3InCl_6

LSV: Linear scan voltammetry

OCV: Open circuit voltage

AB: Acetylene black

EDS: Energy dispersive X-ray spectroscopy

$\chi_{Pauling}$: Pauling electronegativity

PVDF: Polyvinylidene fluoride

NMP: N-Methyl-2-Pyrrolidone

LIST OF FIGURES

LIST OF TABLES

ACKNOWLEDGEMENTS

I would like to thank my advisors Professor Ying Shirley Meng and Professor Zheng Chen for all the opportunities and guidance in my research training and professional development, as well as building upon our common goals toward commercializing our discoveries. I would also like to recognize my committee Chair, Professor Ping Liu for his support, committee members Professor Eric Fullerton and Professor Michael Sailor for their valuable feedback.

I am extremely grateful toward my past and present team members in the solid-state team, Dr. Darren Tan, Dr. Erik A. Wu, Dr. Jean-Marie Doux, Dr. Jihyun Jang, Dr. Jin An Sam Oh, Dr. Jeongbeom Lee, Dr Long Hoang Bao Nguyen, Dr. Yuju Jeon, Dr. Wei Tang, Dr. Ke Zhou, So-Yeon Ham, Dong-Ju Lee, Grayson Deysher, Phillip Ridley, Ashley Cronk, Marta Vicencio, Jerry Yang, Junlin Wu, and Dapeng Xu for the years of enjoyable and highly productive work culture. Their intellectual and passionate contributions were essential toward the discoveries made, and I feel extremely fortunate to have worked with such wonderful colleagues.

Special thank to Yijie Yin for helping me design isostatic pouch cell holders.

I would also like to thank my collaborators: Dr. Alejandro A. Franco (LRCS, RS2E), Dr. Maxwell Marple (LLNL), Dr. Hoe Jin Hah (LG Energy Solution) and Yeeun Kim (LG Energy Solution) for their hard work and invaluable inputs toward the solid-state battery research. Specifically, Dr. Alejandro A. Franco and his team for their machine learning expertise, Dr. Maxwell Marple for NMR support, Dr. Hoe Jin Hah and Yeeun Kin for their help to conduct experiments for SSE exposure in dry rooms.

I would like to thank my family and friends for giving me their support during my time at UCSD. My peers, Chih-Chung Shu, Yu-Jeng Ku and Ya-Wen Cheng for their unwavering advice and encouragement during challenging periods, as well as motivating me to remain healthy physically and mentally.

I acknowledge the financial support from LG Energy Solution through the Battery Innovation Contest (BIC) program and Future Research Laboratory (FRL) program. I would like

to also acknowledge the UCSD Crystallography Facility, as well as the San Diego Nanotechnology Infrastructure (SDNI) of UCSD, a member of the National Nanotechnology Coordinated Infrastructure, which is supported by the National Science Foundation (GrantECCS-1542148). Characterization work was performed in part at the UC Irvine Materials Research Institute (IMRI) using instrumentation funded in part by the National Science Foundation Major Research Instrumentation Program under Grant No. CHE-1338173, as well as Lawrence Livermore National Laboratory under Contract DE-AC52-07NA27344, release number LLNL-JRNL-786041.

I acknowledge the assistance from the UCSD Crystallography Department, Dr. Milan Gembicky, and Baharak Sayahpour, for their assistance on air-sensitive capillary XRD measurements and their willingness to discuss data and experiments at all times.

Chapter 2, in full, is a reprint of the material “Fabrication of High-Quality Thin Solid-State Electrolyte Films Assisted by Machine Learning.” as it appears in ACS Energy Letters. Chen, Y.-T.; Duquesnoy, M.; Tan, D. H. S.; Doux, J.-M.; Yang, H.; Deysher, G.; Ridley, P.; Franco, A. A.; Meng, Y. S.; Chen, Z. 2021, *6*, 1639−1648. The dissertation author was the first author of this paper, all authors contributed to this work.

Chapter 3, in full, is a reprint of the material “Investigating dry room compatibility of sulfide solid-state electrolytes for scalable manufacturing.” as it appears in Journal of Materials Chemistry A. Chen, Y.-T.; Marple, M. A.; Tan, D. H. S.; Ham, S. Y.; Sayahpour, B.; Li, W. K.; Yang, H.; Lee, J. B.; Hah, H. J.; Wu, E. A.; Doux, J.-M.; Jang, J.; Ridley, P.; Cronk, A.; Deysher, G.; Chen, Z.; Meng, Y. S. 2022, *10*, 7155−7164. The dissertation author was the first author of this paper, all authors contributed to this work.

Chapter 4, in full, has been submitted for publication as “Investigating dry room compatibility of Chloride solid-state electrolytes for scalable manufacturing” as a research article in Journal of Electrochemical Society. Chen, Y.-T.; Tan, D. H. S.; Ham, S. Y.; Sayahpour, B.; Lee, J. B.; Kim, Y.; Song, M. S.; Nguyen, L. H. B.; Oh, J. A. S.; Ridley, P.; Cronk, A.; Deysher, G.; Jang,

J.; Chen, Z.; Meng, Y. S. 2023, *170*, 080521. The dissertation author was the first author of this paper, all authors contributed to this work.

Chapter 5, in full, is a reprint of the material in preparation “Enabling uniform and accurate control of cycling pressure for all-solid-state batteries”. Chen, Y.-T.; Ham, S. Y.; Yang, J.; Lee, D. J.; Vicencio, M.; Lee, J. B.; Tan, D. H. S.; Chouchane, M.; Cronk, A.; Song, M. S.; Yin, Y. J.; Qian, J. T.; Oh, J. A. S.; Jang, J.; Chen, Z.; Meng, Y. S. The dissertation author was the first author of this papers, all authors contributed to this work.

VITA

2014 Bachelor of Science, Chemistry, National Taiwan University

2016 Master of Science, Chemistry, National Taiwan University

2023 Doctor of Philosophy, Materials Science and Engineering, University of California San Diego

PUBLICATIONS

(* = authors contributed equally to the work)

1. (In preparation) “Enabling uniform and accurate control of cycling pressure for all-solid-state batteries” Chen, Y.-T. Ham, S. Y., Yang, J., Lee, D. J., Vicencio, M., Lee, J. B., Tan, D. H. S., Chouchane, M., Cronk, A., Song, M. S., Yin, Y. J., Qian, J. T., Oh, J. A. S., Jang, J., Chen, Z., Meng, Y. S.

2. “High-Performing All-Solid-State Sodium-Ion Batteries Enabled by the Presodiation of Hard Carbon” Oh, J. A. S., Deysher, G., Ridley P., Chen, Y.-T., Cheng, D., Cronk, A., Ham, S.-Y., Tan, D. S. H, Jang, J., Nguyen, J. H. B., Meng, Y. S., *Adv. Energy Mater.*, **2023**, 2300776.

3. “Physio-Electrochemically Durable Dry-Processed Solid-State Electrolyte Films for All-Solid-State Batteries” Lee, D. J., Jang J., Lee, J.-P., Wu, J., Chen, Y.-T., Holoubek, J., Yu, K., Ham, S.-Y., Jeon, Y., Kim T.-H., Lee, J. B., Song, M.-S., Meng, Y. S., Chen, Z. *Adv. Func. Mater.* **2023**, 2301341.

4. “Overcoming the Interfacial Challenges of $LiFePO_4$ in Inorganic All-Solid-State Batteries” Cronk, A., Chen, Y.-T., Deysher, G., Ham, S.-Y., Yang, H., Ridley, P., Sayahpour, B., Nguyen, L. H. B., Oh, J. A. S., Jang, J., Tan, D. H. S., Meng, Y. S. *ACS Energy Lett.* **2023**, 8, 827-835.

5. “Assessing the critical current density of all-solid-state Li metal symmetric and full cells” Ham, S.-Y., Yang, H., Nunez-cuacuas, O., Tan, D. H. S., Chen, Y.-T., Deysher, G., Cronk, A., Ridley, P., Doux J.-M., Wu, E. A., Jang, J., Meng, Y. S. *Energy Stor. Mater.* **2023**, 55, 455-462.

6. “Glass-Ceramic Sodium-Deficient Chlorides with High Sodium-ion Conductivity” Ridley, P., Nguyen, L. H. B., Sebti, E., Duong, G., Chen, Y.-T., Sayahpour, B., Cronk, A., Deysher, G., Ham, S.-Y., Oh, J. A. S., Wu, E. A., Tan, D. H. S., Doux, J.-M., Clément, R., Jang, J., Meng, Y. S. Archive.org

7. “Evaluating Electrolyte–Anode Interface Stability in Sodium All-Solid-State Batteries” Deysher, G., Chen, Y.-T., Sayahpour, B., Lin, S. W.-H., Ham, S.-Y., Ridley, P., Cronk, A., Wu, E. A., Tan, D. H. S., Doux, J.-M., Ho, J. A. S., Jang, J., Nguyen, L. H. B., Meng, Y. S. *ACS Appl. Mater. Interfaces* **2022**, 14, 47706-47715.

8. “Enabling a Co-Free, High-Voltage $LiNi_{0.5}Mn_{1.5}O_4$ Cathode in All-Solid-State Batteries with a Halide Electrolyte” Jang, J., Chen, Y.-T., Deysher, G., Cheng, D., Ham, S.-H., Cronk, A., Ridley, P., Yang, H., Sayahpour, B., Han, B., Li, W., Yao, W., Wu, E. A., Doux, J.-M., Nguyen, L. H. B., Oh, J. A. S., Tan, D. H. S., Meng, Y. S. *ACS Energy Lett*. **2022**, 7, 2531-2539.

9. “Transport and Mechanical Aspects of All-Solid-State Lithium Batteries” Deysher, G., Ridley, P., Ham, S.-Y., Doux, J.-M., Chen, Y.-T., Wu, E. A., Tan, D. H. S., Cronk, A., Jang, J., Meng, S. *M. Mater. Today Phys.* **2022**, 100679.

10. “Investigating dry room compatibility of sulfide solid-state electrolytes for scalable manufacturing” Chen, Y.-T., Marple, M. A., Tan, D. H. S., Ham, S. Y., Sayahpour, B., Li, W. K., Yang, H., Lee, J. B., Hah, H. J., Wu, E. A., Doux, J.-M., Jang, J., Ridley, P., Cronk, A., Deysher, G., Chen, Z., Meng, Y. S. *J. of Mater. Chem. A* **2022**, 10, 13, 7155-7164.

11. “Carbon-free high-loading silicon anodes enabled by sulfide solid electrolytes” Tan, D. H. S., Chen, Y.-T., Yang, H., Bao, W., Sreenarayanan, B., Doux, J.-M., Li, W.-K., Lu, B., Ham, S.-Y., Sayahpour, B., Scharf, J., Wu, E. A., Deysher, G., Han, H. E., Hah, H. J., Jeong, H., Lee, J. B., Chen, Z., Meng. Y. S. *Science* **2021**, 373, 6562, 1494-1499.

12. “Fabrication of High-Quality Thin Solid-State Electrolyte Films Assisted by Machine Learning” Chen, Y.-T., Duquesnoy, M., Tan, D. H. S., Doux, J.-M., Yang, H., Deysher, G., Ridley, P., Franco, A. A., Meng, Y. S, Chen, Z. *ACS Energy Lett.* **2021**, 6, 4, 1639–1648.

13. “New insights into Li distribution in the superionic argyrodite Li_6PS_5Cl” Zhao, E., He, L., Zhang, Z., Doux, J.-M., Tan, D. H. S., Wu, E. A., Deysher, G., Chen, Y.-T., Zhao, J., Wang, F., Meng, Y. S. *Chem. Comm.* **2021**, 57, 82, 10787-10790.

14. “A Facile, Dry-Processed Lithium Borate-Based Cathode Coating for Improved All-Solid-State Battery Performance” Wu, E. A., Jo, C., Tan, D. H. S., Zhang, M., Doux, J.-M., Chen, Y.-T., Deysher, G., Meng, Y.-S. *J. Electrochem. Soc.* **2020**, 167, 130516.

ABSTRACT OF THE DISSERTATION

Addressing the Scalable Manufacturing Considerations of All-Solid-State Batteries

by

Yu-Ting Chen

Doctor of Philosophy in Materials Science and Engineering

University of California San Diego, 2023

Professor Zheng Chen, Chair
Professor Ying Shirley Meng, Co-Chair

All-solid-state batteries (ASSBs) are viewed as promising next-generation energy storage devices due to their enhanced safety, which results from replacing organic liquid electrolytes with non-flammable solid-state electrolytes (SSEs). However, ASSBs are still in the development

stage, and further efforts are required before they can be commercialized. While energy density, power density, and cycle life are frequently mentioned challenges for real-world applications, the progress on scalable manufacturing of ASSBs is often overlooked. Recognizing this, the thesis aims to address practical manufacturing considerations for ASSBs, including layer fabrication, material selection, and cell integration.

In the field of layer fabrication, most studies have emphasized only electrochemical performance, neglecting the uniformity of the films. The relationship between manufacturing parameters and the physical properties of SSE films was analyzed using machine learning (ML), revealing that both ionic conductivity and film uniformity are crucial for quality evaluation. To underscore the importance of material selection for scalable manufacturing, the stability of sulfide and chloride SSEs in ambient air and dry rooms was assessed, as dry rooms are often utilized in the scalable manufacturing of Li batteries. The degradation mechanisms of different SSEs were investigated, and their recoverability after degradation was evaluated. Lastly, all materials were integrated into all-solid-state pouch cells (ASSPCs) and operated using newly designed isostatic pouch cell holders (IPCHs), which provide cycling pressure with improved uniformity and accuracy compared to conventional uniaxial pouch cell holders (UPCHs). IPCHs significantly increased the utilization and capacity retention of ASSPCs and are lighter than UPCHs. The research potential of IPCHs was demonstrated by establishing an accurate relationship between electrochemical performance and cycling pressure. Collectively, these findings contribute significantly to the advancement and understanding of the complexities involved in the development and scalability of ASSBs.

Chapter 1. Introduction

1.1 All-Solid-State Batteries

Since the introduction of lithium (Li)-ion batteries (LIBs) in the 1990s,[1] their distinguished attributes, notably high energy density (approximately 250 $Whkg^{-1}$), outstanding cycle life, low self-discharge, and lightweight nature, have revolutionized the landscape of portable electronic devices and electric vehicles (EVs).[2] Nevertheless, a significant safety concern arises when LIBs are subjected to overheating, triggering a cascade of events, such as thermal runaway, separator melting, reaction of the organic solvent with the anode, decomposition of the solid electrolyte interphase (SEI) and cathode, and the release of flammable gases and oxygen. These events amplify the risks of fires, explosions, and other related hazards.[3-4] Central to these safety challenges is the employment of combustible liquid electrolytes, especially as the issues intensify in next-generation, high energy-density lithium-based batteries like Li-metal, Li-sulfur (Li-S), and Li-oxygen/air (Li-O_2/air) batteries.[2, 5]

In response to these challenges and to align with the surging market demands, there is an urgent call for innovations to enhance both safety and energy density. A pivotal step in this direction is to replace liquid electrolytes with solid-state electrolytes (SSEs), a transition considered promising to augment the safety and energy density of LIBs. In fact, all-solid-state batteries (ASSBs) are expected to increase the energy density by over 20% compared to conventional LIBs, especially when paired with high-capacity anodes that are incompatible with liquid electrolytes.[6] Despite these advancements, the inherent boundaries set by the cathode/anode chemistry of LIBs underscore that there's restricted room for elevating their energy densities further. Consequently, Li-metal and Si anode, distinguished by their impressive theoretical specific capacity (3860 mAh g^{-1} for Li and practically 3590 mAh g^{-1} for $Li_{15}Si_4$) and a favorable electrochemical potential,[7] has garnered significant attention. This culminated in the emergence of ASSBs utilizing Li or Si anodes as a potential successor to LIBs, drawing

widespread recognition for their enhanced safety and formidable energy density, exceeding 500 Wh kg^{-1} .[8-9]

In contemporary battery research, the spotlight is intensely cast on safety, energy density, cost-effectiveness, and environmental sustainability. The paradigm shifts towards SSEs and high-capacity anodes, moving away from traditional liquid electrolytes and graphite, epitomizes a transformative approach in battery technology. This transition addresses the pressing safety concerns while concurrently catering to the ever-expanding energy density requirements. While the prospects of ASSBs radiate promise, the journey to their practical implementation is riddled with obstacles, notably poor interface contact, diminished ionic conductivity, and subpar electrode design. Current research strategies primarily target these impediments, albeit within strictly defined conditions such as specific temperatures and pressures. As a result, a disparity exists between laboratory prototypes and their scaled-up counterparts, despite the validation of certain innovative techniques at the laboratory scale. The thesis will delve deep into the nuances of ASSB technology, illuminating the path from recent advancements to design intricacies, and addressing the challenges of scale-up.

1.2 Fabrication of All-Solid-State Batteries

Similar to conventional LIBs, ASSBs also consist of cathode, electrolyte and anode layers. However, SSEs cannot flow like liquid electrolytes, cathodes often appear in the form of composites. Most cathode composites consist of uniform mixtures of active cathode materials, SSEs to transport Li ions, and carbon additives to conduct electrons. Most studies utilize alloy anodes in ASSBs, as they often exhibit high electronic conductivity and sufficient ionic conductivity, and thus SSEs and carbon additives are not mandatory. There are a wide variety of SSEs with different properties, such as ionic conductivity, mechanical properties, chemical and electrochemical stability windows, that are suitable for pairing with different anode or cathode

materials.[10-11] All ingredients are solid and typically assembled into cells by pelletizing the powders layer by layer or staking the preformed free-standing films followed by calendering. Slurry and dry process are the two most used methods to fabricate free-standing films.

1.2.1 Selecting Inorganic Solid-State Electrolyte

The history of alkaline metal ionic conductor can be dated back to 1960s, when Na^+-β-Al_2O_3 was synthesized.[12] Afterwards, polyethylene oxide was reported as ionic conductor in 1973, and thus SSEs were no longer limited to inorganic materials. SSEs need to exhibit high ionic conductivity to reduce the polarization during cell operation to enable high power density of ASSBs, while possess low electronic conductivity to prevent short circuit or current leakage between cathodes and anodes. As SSEs are in direct contact with cathodes and anodes, forming stable and intimate interfaces is requisite during cell operation.[9, 13] While the electrochemical windows of SSEs may not cover the electrochemical potential of cathodes and anodes, most interfaces will eventually stabilize if cathode electrolyte interphases (CEI) on cathode interfaces and solid electrolyte interphases (SEI) on anode interfaces are ionically conductive and electronically insulative.[14-16] In some cases, additional coating layers are required to mitigate anion exchange between cathodes and SSEs. The mechanical properties, specifically Young's modulus, of SSEs determine whether they form intimate contact with electrode materials easily.[17] Simple cold press or warm press can be applied to calender the cell when SSEs with lower Young's modulus are employed, while SSEs with high Young's modulus may demand high temperature sintering.[18-19] The chemical stability in air largely influences the processability in scalable manufacturing, as they need to be processed in dry rooms.[20] Unlike Ar-filled gloveboxes used in research labs, dry rooms are employed in battery industry, since they are cheaper to maintain and provide large space for manufacturing equipment.[21-22] However, H_2O (regulated depending on the dew point rating of dry rooms), O_2, and CO_2 exist in dry room atmosphere, and they are considered to be chemically incompatible with some SSEs. Hence, selecting SSEs that

are compatible with dry room environments is crucial for scalable manufacturing. Several categories of SSEs have been reported: Oxides, sulfides, halides, borohydrides and polymers.[23-24] SSEs from each category have different properties. Here, only oxides, sulfides and halides are discussed (Figure 1.1), as borohydrides are expensive to prepare, and polymers often exhibit worse chemical and electrochemical properties than inorganic SSEs.

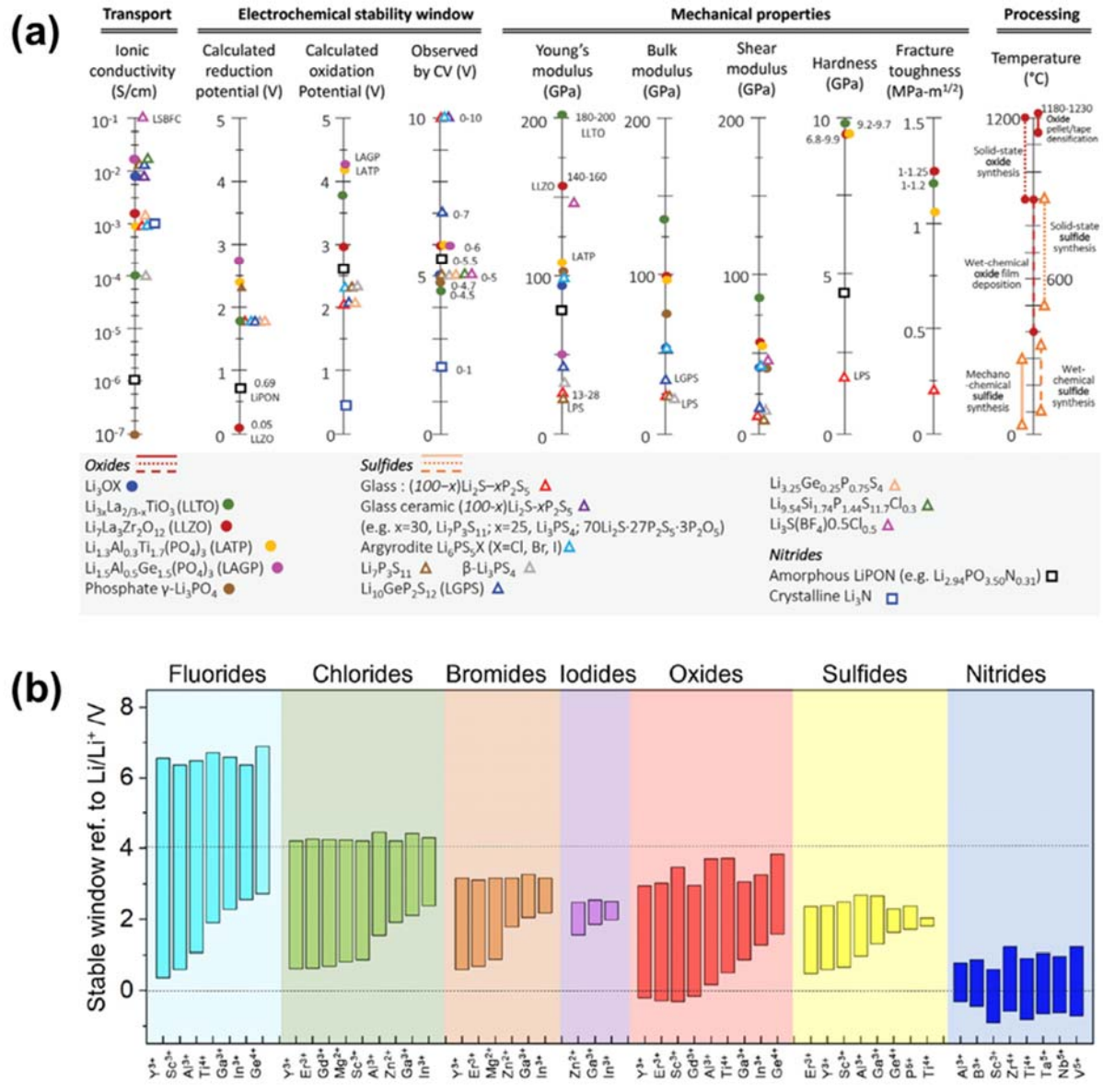

Figure 1.1. (a) A list of physical and electrochemical properties of oxide and sulfide SSEs.[2] (b) the calculated electrochemical windows of halide, oxide and sulfide electrolytes.[25]

1.2.1.1 Oxide Electrolytes

The most reported oxide SSEs can be grouped into four major categories: garnet (e.g., $Li_7La_3Zr_2O_{12}$), perovskite (e.g., $Li_{3.3}La_{0.56}TiO_3$), NASICON (e.g., $LiTi_2(PO_4)_3$), and LISICON-type (e.g., $Li_{14}Zn(GeO_4)_4$).[26-27] Garnet SSEs are the frequently used SSEs because of their high conductivity. Garnet-like SSEs were first synthesized in 2003 with a low ionic conductivity of 10^{-6} S cm^{-1}. It was after the emergence of the doping techniques that stabilized their cubic structure to room temperature that garnets started to draw attention due to their superior ionic conductivity of 10^{-3} S cm^{-1}.[28] Although perovskite SSEs also possess high bulk conductivity of 10^{-3} S cm^{-1}, their grain boundary resistance is large, resulting in low overall ionic conductivity of 10^{-5} S cm^{-1}. Hence, their application is rather limited.[29-30] NASICON type SSEs are another category that capture much interest. They are relatively resistant to air exposure and exhibit decent ionic conductivity, especially after melting, quenching and annealing technique was developed.[31-33] Despite the thermal and water stability of LISICON SSEs, their low ionic conductivity restricts further development.

Oxide SSEs exhibit decent ionic conductivity and outstanding oxidation stability, as a high potential is required to oxidize O^{2-} ions.[34] However, they are not stable against anode materials. Transition metals tend to reduce during Li insertion (e.g. $Ti^{4+} + e^- \rightarrow Ti^{3+}$), and Li dendrites can grow along the grain boundary, or even inside a single crystal $Li_7L_3Zr_2O_{12}$. Moreover, the sintering temperature of oxide SSEs is usually close to or exceed 1000°C, making their fabrication process energy consuming. Furthermore, their high Young's modulus prevents them from forming intimate contact with electrode materials after cold or warm press. High temperature sintering, and adulteration of polymer electrolytes, or even liquid electrolytes, are often the measures to improve interfacial contact.[26-27] Hence, the application of oxide SSEs in ASSBs is considered limited.

1.2.1.2 Sulfide Electrolytes

Sulfide SSEs can be categorized into two groups: binary and ternary systems. The binary systems are made up of Li_2S and P_2S_5, examples being Li_3PS_4 and $Li_7P_3S_{11}$.[35-36] On the other hand, ternary systems are composed of Li_2S, P_2S_5, and MS_2 (with M representing Si, Ge, or Sn), like $Li_{10}GeP_2S_{12}$ and Li_6PS_5X (where X can be Cl, Br, or I).[37]

Sulfide SSEs exhibit excellent ionic conductivity, with many exceeding 10^{-3} S cm^{-1}. However, since S^{2-} and P^{5+} are easily oxidized at 2.3 V or reduced at 1.3 V vs Li^+/Li, sulfide SSEs generally show narrow electrochemical windows. Tan et al. found that Li_6PS_5Cl (LPSCl) forms S and P_2S_5 upon oxidation, and Li_2S and Li_3P after reduction.[38] When contacting layered oxide cathodes, S^{2-} often undergoes ion exchange reaction with O^{2-} in cathode materials and forms transition metal sulfides, PO_4^{3-} and SO_4^{2-}. Moreover, S^{2-} tends to react with moisture in ambient air to form toxic H_2S.[39] Some research doped heavy metals, such as Sn and Sb, to reduce the reactivity, but the effect is limited.[17, 40] Despite these drawbacks, sulfide SSEs still catch much attention, as the electrochemical window is not the only metric that dictate the stability of SEI and CEI. For example, LPSCl was demonstrated to be stable for 500 cycles in Li_3BO_3-coated $LiNi_{0.8}Co_{0.1}Mn_{0.1}O_2$ | Si, whose operating electrochemical potentials on both cathode and anode are well beyond the stability window of LPSCl.[41-42] While LPSCl forms SEI (consists of Li_2S, Li_3P and LiCl) and CEI (consists of S, P_2S_5 and LiCl) with the electrode materials in the beginning, its CEI and SEI are electronically insulative to prevent further side reactions, and thus passivate quickly. Ion-exchange reaction of S^{2-} and O^{2-} was also alleviated with LBO coating. Nevertheless, such a strategy does not apply to the cathodes with large surface area (e.g., $LiFePO_4$). On the other hand, when heavy metal ions, such as Ge^{4+} in $Li_{10}GeP_2S_{12}$, are contained in sulfide SSEs, they reduce to metal form when exposed to reduction environment, making the SEI electronic conductive and thus the SEI is not passivated.[43-44] On another hand, despite their reactivity with ambient air, the root cause of degradation is moisture.[45] Hence, sulfide SSEs were found to be

dry room compatible. Regarding the processibility, sulfide SSEs require much lower synthesizing temperature than oxide SSEs, resulting in lower energy consumption, and their low Young's modulus make them adaptable to simple cold or warm press during calendering. Combining the above results, sulfide SSEs are considered promising for scalable manufacturing for ASSBs.

1.2.1.3 Halide Electrolytes

Halide SSEs, such as $LiAlCl_4$, Li_2MnCl_4 and Li_3InBr_6 were studied several decades ago but did not gain much attention, due to their low ionic conductivity of less than 10^{-7} S cm^{-1}.[46] It was until 2018, when Tetsuya Asano et al. obtained Li_3YCl_6 and Li_3YBr_6 with high ionic conductivity of approximately 10^{-3} S cm^{-1} through high energy ball mill, that halide SSEs regained research interest.[47] Most halide SSEs have a chemical formula of Li_aMX_b, where M is metallic cation and X is halide anion. Halide SSEs with several metal centers have been studied, including rare-earth elements (e.g., Sc, Y, La-Lu), group 13 elements (e.g., Al, Ga, In), and transition metal elements (e.g., Fe, Zr, Hf). Halides with mixed metal centers (e.g., $Li_{3-x}In_{1-x}Zr_xCl_6$) were also synthesized to improve either ionic conductivity or moisture stability.[48-49] Depending on the ionic radius ratio between metal center and halide anion, halide SSEs exhibit three major structures: Trigonal (P - 3 m 1), orthorhombic (P n m a), and monoclinic (C 2 / m).

Most halide SSEs are hygroscopic, originating from their metal halide precursors. As such, they are also considered sensitive to air exposure since they undergo hydration or hydrolysis reaction when reacting with moisture. Some halide SSEs can be recovered by simple heating (e.g., Li_3InCl_6. This SSE can even be synthesized through water mediated process), others experience irreversible degradation.[50-51] Some halide SSEs rely on low crystallinity or disordered structures to increase ionic conductivity, and thus they can be sensitive to temperature, as heating and cooling the SSEs results in higher crystallinity and their ionic conductivity drop significantly. The oxidation stability of halide SSEs originates from their anions, and the stability decreases

from F^- to I^-. Chloride SSEs are the most studied halides, due to their better ionic conductivity (10^{-4} – 10^{-3} S cm^{-1}) than fluorides and superior oxidation stability (4.0 – 4.3 V vs Li^+ / Li) compared to sulfide electrolytes. For example, Jang et al. utilized Li_3YCl_6 as catholyte and enabled high voltage $LiNi_{0.5}Mn_{1.5}O_4$ (LNMO) ASSBs, and Cronk et al. realized $LiFePO_4$ ASSBs with Li_2ZrCl_6 catholyte.[52-53] Nevertheless, most halide SSEs are not reductive stable, as most of their metal centers would reduce to metallic form and result in electronically conductive SEI. Halide SSEs possess low Young's modulus, and are suitable for calendering with simple cold / warm press. Due to their oxidation stability and low Young's modulus, chloride SSEs still gain much attention, and efforts are continuously made to mitigate the moisture and temperature sensitivity problems.

1.2.2 Fabricating Electrodes and Electrolyte Layers

Aiming to commercialize ASSBs, not only pouch type format must be developed to address energy density advantages, but the manufacturing process must also mimic the existing techniques used by conventional LIBs to avoid the efforts and costs required to redesign new fabrication equipment.[27, 54] There are already multiple established cell configurations used for conventional LIBs: cylindrical, prismatic, single sheet stacking and Z-stacking (Figure 1.2). Unlike conventional LIBs, ASSBs require fabrication press, typically from 100 to 500 MPa, after assembly to densify the cell and facilitate interfacial contact. The inner layers of cylindrical or prismatic configuration may suffer from ununiform pressure and increase the chance of cell failure. As such, only single sheet stacking and Z-stacking are suitable for ASSBs. To conduct sheet stacking, each layer should either be coated on a substrate (such as metal current collectors) or free standing. As the inorganic SSEs are brittle, high thickness is required to mechanically support ASSBs.[55-56] As such, it is imperative to add polymer binders to form thin and flexible layers. Slurry process and dry process are the two methods frequently used to produce films.

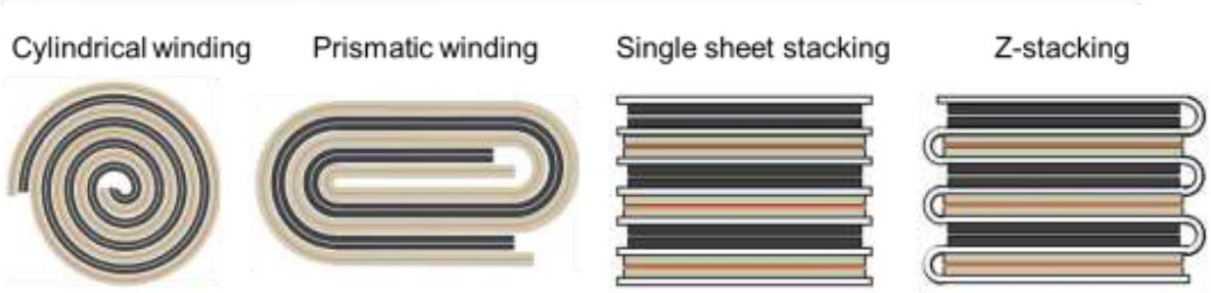

Figure 1.2. A list of cell configurations used for conventional LIBs.

1.2.2.1 Slurry Process

To conduct the slurry process, powders are uniformly mixed with polymer binders and solvents to form slurries, and then cast on smooth and flat substrates using doctor blades. After drying the solvents, polymer binders are coated on SSE particles and glue them together to form films. Most sulfide SSEs are not chemically stable with polar solvents. Hence, solvents with low polarity should be used, and this also limits the polarity of polymer binders since the binders need to be soluble in solvents.[57] As SSE and electrode material particles need to be uniformly dispersed in slurries, a suitable composition is essential to obtain good rheological properties. However, when increasing the coating thickness, particles inevitably precipitate due to density difference, and hence the slurry process is not suitable for fabricating cathode films that requires high loading. Nevertheless, slurry process still has the edge over dry process to fabricate thin layers (less than 50 μm) and can be used to cast high-capacity anodes (such as Si). When casting SSE separator layers, ionic conductivity and mechanical strength of their free-standing films should be considered. As there may be residual solvents after drying, and binders (which are less ionically conductive than SSEs) sitting in between SSE particles, the electrochemical performance, especially ionic conductivity, can be influenced significantly. It is also difficult to produce slurry-processed SSE films, as it is mechanically weak and cannot be adapted to scalable pouch stacking process that requires films with basic mechanical strength to prevent rupture. Although

non-woven cloth supported separator with excellent mechanical strength had been proposed, cloth fibers usually deteriorate the surface uniformity and cause other issues such as short circuit.

1.2.2.2 Dry Process

Polytetrafluoroethylene (PTFE) is almost always used as the binder in dry process due to its low yield strength and malleability. When a uniform powder-PTFE mixture is subjected to a shear force, PTFE particles will deform and fibrillate (Figure 1.3a, b).[58] The powder particles will be bound by PTFE nano fibers and form dry-processed films. Dry process is considered more environmentally, as it does not require extra energy to dry solvents. Nevertheless, scalable production techniques for dry process are not as mature as wet process and further development is mandatory.[59-60] Dry process also has the advantages on fabricating thick cathode composite while maintaining uniform, and better preserve the ionic conductivity since one-dimensional PTFE fibers do not block interfaces between particles as much as two-dimensional binders in slurry-processed films.[56, 61] Nevertheless, it is difficult to fabricate dry-processed film thinner than 50 μm, as the precision of hot rollers will become demanding, and a much higher shear force will be applied to thinner films, resulting in severe particle cracks. As PTFE fibers are mechanically stronger and bind particles more effectively than binders used in slurry process, stronger free-standing films can be obtained with lower PTFE ratio (typically less than 1%), making it suitable for layer stacking process. Nevertheless, PTFE is susceptible to reduction (Figure 1.3c) and extra low ratio (< 0.2%) is requisite when SSE separator layers are in contact with anodes.

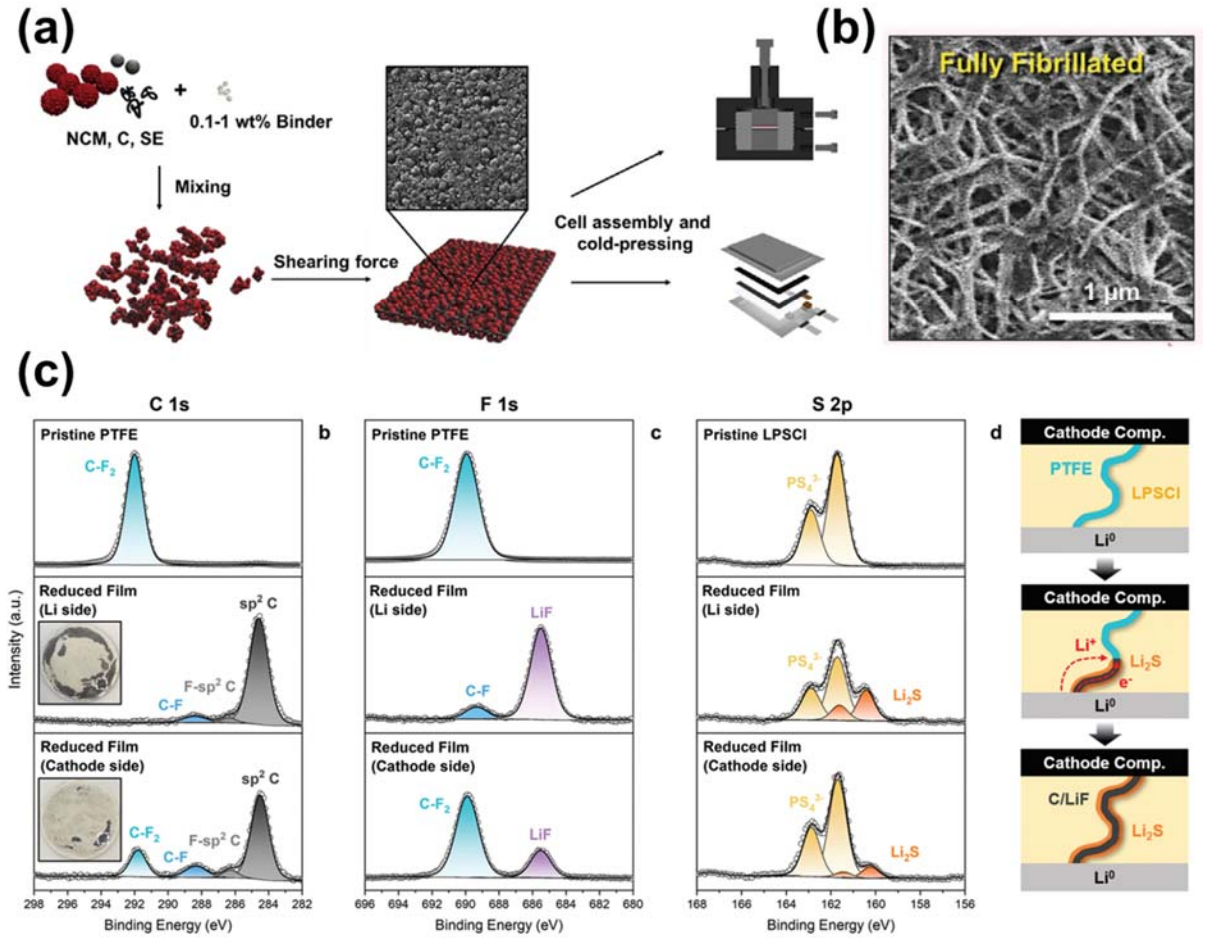

Figure 1.3. When a uniform powder-PTFE mixture is (a) subjected to a shear force, (b) PTFE particles will deform and fibrillate. (c) PTFE is susceptible to reduction and form sp^2 carbon and LiF. Conductive sp^2 carbon often result in excess SSE decomposition and current leakage.

1.3 Pressure for Fabrication and Cycling

Unlike conventional LIBs that utilize liquid electrolytes, SSEs in all ASSBs cannot flow and conform to the shape of electrode materials. As such, pressure is required both in fabrication and cycling of ASSBs.[62] As large voids are omnipresent between particles in as-fabricated films, either slurry-processed or dry-processed, and inter-layer gaps need to be eliminated after layer stacking, a fabrication press must be applied. During cycling, electrode materials undergo volume change and interfaces between SSE and electrode material may partially lose contact over time. Hence, it is imperative to apply cycling pressure to maintain intimate interfacial contact. Intuitively, higher

fabrication and cycling pressures usually result in better interfacial contacts and thus higher electrochemical performance. However, optimum pressures exist in pressure sensitive electrode materials, such as Li metal anode.[63-64] Due to the low creep strength of Li metal, excess fabrication pressure would cause Li to creep across the SSE separators and cause short circuit. Over pressurizing Li metal during cycling also results in electromechanical failure due to synergistic effect of creeping during Li plating, and under pressurizing leads to void formation during Li stripping. As a result, both fabrication and cycling pressure may post significant influence over critical current density of Li metal anode.

Methods of cell pressurizing also affect the electrochemical performance of ASSBs. Uniaxial press is commonly used in both fabrication and cycling press in most lab scale ASSBs due to its simplicity. However, as the pressure is only applied from one direction, any slight defects on dies can easily deteriorate pressure uniformity and the pressure will also concentrate on the edges of layers. Multiple studies have shown that utilizing isostatic press for calendering can effectively improve pressure uniformity, as the pressure is applied through fluids and is uniform in all directions and all points.[64-66] Although isostatic fabrication press vastly improve the performance of ASSBs (e.g. Lee et al. fabricated Ag-C anode all-solid-state pouch cells that operated for 1000 cycles), isostatic cycling press has yet to be discussed.[65] Apart from the methods of pressurizing the ASSBs, designs of cell holders and modules should be addressed. An ideal cell holder will be light weight to increase the module energy density, and able to accommodate volume change of ASSBs during cycling while maintaining a constant cycling pressure to ensure the optimum operation condition of ASSBs.

In this thesis, multiple challenges regarding scalable manufacturing of ASSBs will be discussed. It includes quality control of SSE separator films, guidelines for SSE selection for dry

room manufacturing process, and finally the possibility of large format ASSBs and the design of cell holders.

References

1. Scrosati, B., History of lithium batteries. *J. Solid State Electrochem.* **2011,** *15* (7-8), 1623-1630.

2. Kim, K. J.; Balaish, M.; Wadaguchi, M.; Kong, L.; Rupp, J. L., Solid-state Li–metal batteries: challenges and horizons of oxide and sulfide solid electrolytes and their interfaces. *Adv. Energy Mater.* **2021,** *11* (1), 2002689.

3. Liu, K.; Liu, Y.; Lin, D.; Pei, A.; Cui, Y., Materials for lithium-ion battery safety. *Science advances* **2018,** *4* (6), eaas9820.

4. Duan, J.; Tang, X.; Dai, H.; Yang, Y.; Wu, W.; Wei, X.; Huang, Y., Building safe lithium-ion batteries for electric vehicles: a review. *Electrochemical Energy Reviews* **2020,** *3*, 1-42.

5. Bruce, P. G.; Freunberger, S. A.; Hardwick, L. J.; Tarascon, J.-M., Li–O2 and Li–S batteries with high energy storage. *Nat. Mater.* **2012,** *11* (1), 19-29.

6. Janek, J.; Zeier, W. G., A solid future for battery development. *Nat. Energy* **2016,** *1* (9), 1-4.

7. He, X.; Bresser, D.; Passerini, S.; Baakes, F.; Krewer, U.; Lopez, J.; Mallia, C. T.; Shao-Horn, Y.; Cekic-Laskovic, I.; Wiemers-Meyer, S., The passivity of lithium electrodes in liquid electrolytes for secondary batteries. *Nature Reviews Materials* **2021,** *6* (11), 1036-1052.

8. Judez, X.; Eshetu, G. G.; Li, C.; Rodriguez-Martinez, L. M.; Zhang, H.; Armand, M., Opportunities for rechargeable solid-state batteries based on Li-intercalation cathodes. *Joule* **2018,** *2* (11), 2208-2224.

9. Zhao, Q.; Stalin, S.; Zhao, C.-Z.; Archer, L. A., Designing solid-state electrolytes for safe, energy-dense batteries. *Nature Reviews Materials* **2020,** *5* (3), 229-252.

10. Horowitz, Y.; Schmidt, C.; Yoon, D.-h.; Riegger, L. M.; Katzenmeier, L.; Bosch, G. M.; Noked, M.; Ein-Eli, Y.; Janek, J.; Zeier, W. G.; Diesendruck, C. E.; Golodnitsky, D., Between Liquid and All Solid: A Prospect on Electrolyte Future in Lithium-Ion Batteries for Electric Vehicles. *Energy Technology* **2020,** *8* (11).

11. Lim, H.-D.; Park, J.-H.; Shin, H.-J.; Jeong, J.; Kim, J. T.; Nam, K.-W.; Jung, H.-G.; Chung, K. Y., A review of challenges and issues concerning interfaces for all-solid-state batteries. *Energy Storage Materials* **2020,** *25*, 224-250.

12. Yamaguchi, G.; Suzuki, K., On the structures of alkali polyaluminates. *Bull. Chem. Soc. Jpn.* **1968,** *41* (1), 93-99.

13. Manthiram, A.; Yu, X.; Wang, S., Lithium battery chemistries enabled by solid-state electrolytes. *Nature Reviews Materials* **2017,** *2* (4), 1-16.

14. Han, F.; Westover, A. S.; Yue, J.; Fan, X.; Wang, F.; Chi, M.; Leonard, D. N.; Dudney, N. J.; Wang, H.; Wang, C., High electronic conductivity as the origin of lithium dendrite formation within solid electrolytes. *Nat. Energy* **2019,** *4* (3), 187-196.

15. Ye, L.; Li, X., A dynamic stability design strategy for lithium metal solid state batteries. *Nature* **2021,** *593* (7858), 218-222.

16. Chen, Y.; Wang, Z.; Li, X.; Yao, X.; Wang, C.; Li, Y.; Xue, W.; Yu, D.; Kim, S. Y.; Yang, F., Li metal deposition and stripping in a solid-state battery via Coble creep. *Nature* **2020,** *578* (7794), 251-255.

17. Park, K. H.; Bai, Q.; Kim, D. H.; Oh, D. Y.; Zhu, Y.; Mo, Y.; Jung, Y. S., Design Strategies, Practical Considerations, and New Solution Processes of Sulfide Solid Electrolytes for All-Solid-State Batteries. *Adv. Energy Mater.* **2018,** *8* (18).

18. Lee, S.-E.; Sim, H.-T.; Lee, Y.-J.; Hong, S.-B.; Chung, K. Y.; Jung, H.-G.; Kim, D.-W., Li6PS5Cl-based composite electrolyte reinforced with high-strength polyester fibers for all-solid-state lithium batteries. *J. Power Sources* **2022,** *542*, 231777.

19. Minami, K.; Hayashi, A.; Tatsumisago, M., Crystallization process for superionic Li7P3S11 glass–ceramic electrolytes. *J. Am. Ceram. Soc.* **2011,** *94* (6), 1779-1783.

20. Cao, D.; Zhao, Y.; Sun, X.; Natan, A.; Wang, Y.; Xiang, P.; Wang, W.; Zhu, H., Processing Strategies to Improve Cell-Level Energy Density of Metal Sulfide Electrolyte-Based All-Solid-State Li Metal Batteries and Beyond. *ACS Energy Letters* **2020,** *5* (11), 3468-3489.

21. Degen, F.; Schütte, M., Life cycle assessment of the energy consumption and GHG emissions of state-of-the-art automotive battery cell production. *Journal of Cleaner Production* **2022,** *330*, 129798.

22. Grady, H., Lithium metal for the battery industry. *J. Power Sources* **1980,** *5* (1), 127-135.

23. Kim, K. J.; Balaish, M.; Wadaguchi, M.; Kong, L.; Rupp, J. L. M., Solid-State Li–Metal Batteries: Challenges and Horizons of Oxide and Sulfide Solid Electrolytes and Their Interfaces. *Adv. Energy Mater.* **2020,** *11* (1).

24. Zhang, Q.; Cao, D.; Ma, Y.; Natan, A.; Aurora, P.; Zhu, H., Sulfide-Based Solid-State Electrolytes: Synthesis, Stability, and Potential for All-Solid-State Batteries. *Adv. Mater.* **2019,** *31* (44), e1901131.

25. Kwak, H.; Wang, S.; Park, J.; Liu, Y.; Kim, K. T.; Choi, Y.; Mo, Y.; Jung, Y. S., Emerging Halide Superionic Conductors for All-Solid-State Batteries: Design, Synthesis, and Practical Applications. *ACS Energy Letters* **2022,** *7* (5), 1776-1805.

26. Jiang, P.; Du, G.; Cao, J.; Zhang, X.; Zou, C.; Liu, Y.; Lu, X., Solid-State Li Ion Batteries with Oxide Solid Electrolytes: Progress and Perspective. *Energy Technology* **2023,** *11* (3), 2201288.

27. Schnell, J.; Tietz, F.; Singer, C.; Hofer, A.; Billot, N.; Reinhart, G., Prospects of production technologies and manufacturing costs of oxide-based all-solid-state lithium batteries. *Energy Environ. Sci.* **2019,** *12* (6), 1818-1833.

28. Luo, W.; Gong, Y.; Zhu, Y.; Fu, K. K.; Dai, J.; Lacey, S. D.; Wang, C.; Liu, B.; Han, X.; Mo, Y., Transition from superlithiophobicity to superlithiophilicity of garnet solid-state electrolyte. *J. Am. Chem. Soc.* **2016,** *138* (37), 12258-12262.

29. Deng, Z.; Ni, D.; Chen, D.; Bian, Y.; Li, S.; Wang, Z.; Zhao, Y., Anti-perovskite materials for energy storage batteries. *InfoMat* **2022,** *4* (2), e12252.

30. Yan, S.; Yim, C.-H.; Pankov, V.; Bauer, M.; Baranova, E.; Weck, A.; Merati, A.; Abu-Lebdeh, Y., Perovskite solid-state electrolytes for lithium metal batteries. *Batteries* **2021,** *7* (4), 75.

31. He, L.; Oh, J. A. S.; Watarai, K.; Morita, M.; Zhao, Y.; Sun, Q.; Sakamoto, T.; Lu, L.; Adams, S., Electromechanical failure of NASICON-type solid-state electrolyte-based all-solid-state Li-ion batteries. *Chem. Mater.* **2021,** *33* (17), 6841-6852.

32. Zuo, D.; Yang, L.; Zou, Z.; Li, S.; Feng, Y.; Harris, S. J.; Shi, S.; Wan, J., Ultrafast Synthesis of NASICON Solid Electrolytes for Sodium-Metal Batteries. *Adv. Energy Mater.* **2023,** *13* (37), 2301540.

33. Huang, C.; Li, Z.; Duan, S.; Xie, S.; Yuan, S.; Hou, S.; Cao, G.; Jin, H., Improving the stability of NASICON-type electrolyte with Li metal anode by interfacial modification. *J. Power Sources* **2022,** *536*, 231491.

34. Han, X.; Wang, S.; Xu, Y.; Zhong, G.; Zhou, Y.; Liu, B.; Jiang, X.; Wang, X.; Li, Y.; Zhang, Z., All solid thick oxide cathodes based on low temperature sintering for high energy solid batteries. *Energy Environ. Sci.* **2021,** *14* (9), 5044-5056.

35. Yu, C.; van Eijck, L.; Ganapathy, S.; Wagemaker, M., Synthesis, structure and electrochemical performance of the argyrodite Li 6 PS 5 Cl solid electrolyte for Li-ion solid state batteries. *Electrochim. Acta* **2016,** *215*, 93-99.

36. Wu, J.; Liu, S.; Han, F.; Yao, X.; Wang, C., Lithium/sulfide all-solid-state batteries using sulfide electrolytes. *Adv. Mater.* **2021,** *33* (6), 2000751.

37. Kamaya, N.; Homma, K.; Yamakawa, Y.; Hirayama, M.; Kanno, R.; Yonemura, M.; Kamiyama, T.; Kato, Y.; Hama, S.; Kawamoto, K.; Mitsui, A., A lithium superionic conductor. *Nat Mater* **2011,** *10* (9), 682-6.

38. Tan, D. H.; Wu, E. A.; Nguyen, H.; Chen, Z.; Marple, M. A.; Doux, J.-M.; Wang, X.; Yang, H.; Banerjee, A.; Meng, Y. S., Elucidating reversible electrochemical redox of Li6PS5Cl solid electrolyte. *ACS Energy Letters* **2019,** *4* (10), 2418-2427.

39. Singer, C.; Töpper, H.-C.; Kutsch, T.; Schuster, R.; Koerver, R.; Daub, R. d., Hydrolysis of Argyrodite Sulfide-Based Separator Sheets for Industrial All-Solid-State Battery Production. *ACS Applied Materials & Interfaces* **2022,** *14* (21), 24245-24254.

40. Kang, S.-G.; Kim, D.-H.; Kim, B.-J.; Yoon, C.-B., Sn-Substituted Argyrodite Li6PS5Cl Solid Electrolyte for Improving Interfacial and Atmospheric Stability. *Materials* **2023,** *16* (7), 2751.

41. Zhang, H.; Zhao, H.; Xu, J.; Zhang, J., Optimizing Li2O-2B2O3 coating layer on LiNi0. 8Co0. 1Mn0. 1O2 (NCM811) cathode material for high-performance lithium-ion batteries. *International Journal of Green Energy* **2020,** *17* (7), 447-455.

42. Mo, W.; Wang, Z.; Wang, J.; Li, X.; Guo, H.; Peng, W.; Yan, G., Tuning the surface of LiNi0. 8Co0. 1Mn0. 1O2 primary particle with lithium boron oxide toward stable cycling. *Chem. Eng. J.* **2020,** *400*, 125820.

43. Leube, B. T.; Inglis, K. K.; Carrington, E. J.; Sharp, P. M.; Shin, J. F.; Neale, A. R.; Manning, T. D.; Pitcher, M. J.; Hardwick, L. J.; Dyer, M. S., Lithium Transport in Li4. 4 M 0.4 M′ 0.6 S4 (M= Al3+, Ga3+, and M′= Ge4+, Sn4+): Combined Crystallographic, Conductivity, Solid State NMR, and Computational Studies. *Chem. Mater.* **2018,** *30* (20), 7183-7200.

44. Ong, S. P.; Mo, Y.; Richards, W. D.; Miara, L.; Leeb, H. S.; Ceder, G., Phase stability, electrochemical stability and ionic conductivity of the Li10Æ1 MP2X12 (M ¼ Ge, Si, Sn, Al or P, and X ¼ O, S or Se) family of superionic conductors.

45. Chen, Y.-T.; Marple, M. A.; Tan, D. H.; Ham, S.-Y.; Sayahpour, B.; Li, W.-K.; Yang, H.; Lee, J. B.; Hah, H. J.; Wu, E. A., Investigating dry room compatibility of sulfide solid-state electrolytes for scalable manufacturing. *J. Mater. Chem. A* **2022,** *10* (13), 7155-7164.

46. Li, X.; Liang, J.; Yang, X.; Adair, K. R.; Wang, C.; Zhao, F.; Sun, X., Progress and Perspectives for Halide Solid-State Electrolyte for All-Solid-State Lithium Batteries. *Energy* **2018,** *11* (4), 719-1000.

47. Asano, T.; Sakai, A.; Ouchi, S.; Sakaida, M.; Miyazaki, A.; Hasegawa, S., Solid halide electrolytes with high lithium-ion conductivity for application in 4 V class bulk-type all-solid-state batteries. *Adv. Mater.* **2018,** *30* (44), 1803075.

48. Fu, J.; Yang, S.; Hou, J.; Azhari, L.; Yao, Z.; Ma, X.; Liu, Y.; Vanaphuti, P.; Meng, Z.; Yang, Z., Modeling assisted synthesis of Zr-doped Li3-xIn1-xZrxCl6 with ultrahigh ionic conductivity for lithium-ion batteries. *J. Power Sources* **2023,** *556*, 232465.

49. Liu, Y.; Wang, S.; Nolan, A. M.; Ling, C.; Mo, Y., Tailoring the cation lattice for chloride lithium-ion conductors. *Adv. Energy Mater.* **2020,** *10* (40), 2002356.

50. Jia, G.; Deng, Z.; Ni, D.; Ji, Z.; Chen, D.; Zhang, X.; Wang, T.; Li, S.; Zhao, Y., Temperature-dependent compatibility study on halide solid-state electrolytes in solid-state batteries. *Frontiers in Chemistry* **2022,** *10*, 952875.

51. Wang, S.; Xu, X.; Cui, C.; Zeng, C.; Liang, J.; Fu, J.; Zhang, R.; Zhai, T.; Li, H., Air sensitivity and degradation evolution of halide solid state electrolytes upon exposure. *Adv. Funct. Mater.* **2022,** *32* (7), 2108805.

52. Jang, J.; Chen, Y.-T.; Deysher, G.; Cheng, D.; Ham, S.-Y.; Cronk, A.; Ridley, P.; Yang, H.; Sayahpour, B.; Han, B., Enabling a co-free, high-voltage LiNi0. 5Mn1. 5O4 cathode in all-solid-state batteries with a halide electrolyte. *ACS Energy Letters* **2022,** *7* (8), 2531-2539.

53. Cronk, A.; Chen, Y.-T.; Deysher, G.; Ham, S.-Y.; Yang, H.; Ridley, P.; Sayahpour, B.; Nguyen, L. H. B.; Oh, J. A. S.; Jang, J., Overcoming the Interfacial Challenges of LiFePO4 in Inorganic All-Solid-State Batteries. *ACS Energy Letters* **2023,** *8* (1), 827-835.

54. Zhang, Z.; Wu, L.; Zhou, D.; Weng, W.; Yao, X., Flexible Sulfide Electrolyte Thin Membrane with Ultrahigh Ionic Conductivity for All-Solid-State Lithium Batteries. *Nano Lett.* **2021,** *21* (12), 5233-5239.

55. Hong, S.-B.; Lee, Y.-J.; Kim, U.-H.; Bak, C.; Lee, Y. M.; Cho, W.; Hah, H. J.; Sun, Y.-K.; Kim, D.-W., All-Solid-State Lithium Batteries: Li+-Conducting Ionomer Binder for Dry-Processed Composite Cathodes. *ACS Energy Letters* **2022,** *7* (3), 1092-1100.

56. Gyulai, A.; Bauer, W.; Ehrenberg, H., Dry Electrode Manufacturing in a Calender: The Role of Powder Premixing for Electrode Quality and Electrochemical Performance. *ACS Appl. Energy Mater.* **2023,** *6* (10), 5122-5134.

57. Tan, D. H.; Banerjee, A.; Deng, Z.; Wu, E. A.; Nguyen, H.; Doux, J.-M.; Wang, X.; Cheng, J.-h.; Ong, S. P.; Meng, Y. S., Enabling thin and flexible solid-state composite electrolytes by the scalable solution process. *ACS Appl. Energy Mater.* **2019,** *2* (9), 6542-6550.

58. Lee, D. J.; Jang, J.; Lee, J. P.; Wu, J.; Chen, Y. T.; Holoubek, J.; Yu, K.; Ham, S. Y.; Jeon, Y.; Kim, T. H., Physio-Electrochemically Durable Dry-Processed Solid-State Electrolyte Films for All-Solid-State Batteries. *Adv. Funct. Mater.* **2023**, 2301341.

59. Ryu, M.; Hong, Y. K.; Lee, S. Y.; Park, J. H., Ultrahigh loading dry-process for solvent-free lithium-ion battery electrode fabrication. *Nat Commun* **2023,** *14* (1), 1316.

60. Borchers, A.; Pieler, T., Programming pluripotent precursor cells derived from Xenopus embryos to generate specific tissues and organs. *Genes (Basel)* **2010,** *1* (3), 413-26.

61. Wang, C.; Yu, R.; Duan, H.; Lu, Q.; Li, Q.; Adair, K. R.; Bao, D.; Liu, Y.; Yang, R.; Wang, J.; Zhao, S.; Huang, H.; Sun, X., Solvent-Free Approach for Interweaving Freestanding and Ultrathin Inorganic Solid Electrolyte Membranes. *ACS Energy Letters* **2021,** *7* (1), 410-416.

62. Gao, X.; Liu, B.; Hu, B.; Ning, Z.; Jolly, D. S.; Zhang, S.; Perera, J.; Bu, J.; Liu, J.; Doerrer, C.; Darnbrough, E.; Armstrong, D.; Grant, P. S.; Bruce, P. G., Solid-state lithium battery cathodes operating at low pressures. *Joule* **2022,** *6* (3), 636-646.

63. Gu, J.; Liang, Z.; Shi, J.; Yang, Y., Electrochemo-Mechanical Stresses and Their Measurements in Sulfide-Based All-Solid-State Batteries: A Review. *Adv. Energy Mater.* **2022,** *13* (2).

64. Dixit, M.; Beamer, C.; Amin, R.; Shipley, J.; Eklund, R.; Muralidharan, N.; Lindqvist, L.; Fritz, A.; Essehli, R.; Balasubramanian, M.; Belharouak, I., The Role of Isostatic Pressing in Large-Scale Production of Solid-State Batteries. *ACS Energy Letters* **2022,** *7* (11), 3936-3946.

65. Lee, Y.-G.; Fujiki, S.; Jung, C.; Suzuki, N.; Yashiro, N.; Omoda, R.; Ko, D.-S.; Shiratsuchi, T.; Sugimoto, T.; Ryu, S., High-energy long-cycling all-solid-state lithium metal batteries enabled by silver–carbon composite anodes. *Nat. Energy* **2020,** *5* (4), 299-308.

66. Dixit, M.; Beamer, C.; Amin, R.; Shipley, J.; Eklund, R.; Muralidharan, N.; Lindqvist, L.; Fritz, A.; Essehli, R.; Balasubramanian, M., The Role of Isostatic Pressing in Large-Scale Production of Solid-State Batteries. *ACS Energy Letters* **2022,** *7* (11), 3936-3946.

Chapter 2. Fabrication of High-Quality Thin Solid-State Electrolyte Films Assisted by Machine Learning

2.1 Introduction

Li-ion batteries (LIBs) are currently the predominant energy storage technology widely used in portable electronic devices, electric vehicles, and grid energy storage.[1] Conventional LIBs employ liquid electrolytes containing flammable organic solvents, making them susceptible to leakage and potential flammability concerns.[2-5] One of the solutions to circumvent this is to replace liquid electrolytes with inorganic solid-state electrolytes (SSEs) in order to produce all-solid-state batteries (ASSBs) with improved safety and wider operating temperature ranges.[2, 6] As a result, significant efforts have been devoted to developing various SSEs, some of which have exhibited ionic conductivities reaching 10^{-2} S cm^{-1} at room temperature, close to those of liquid electrolytes.[7-9] However, due to mechanical property limitations and under-developed manufacturing processes for inorganic SSEs, cells with pellet-type SSE layers thicker than 200 μm are still predominantly employed in ASSB research.[10] Unlike cathode and anode materials, electrolytes do not store energy and thus using thick SSE layer limits energy density.[2, 11] To compete with conventional LIBs, it is therefore crucial to develop new fabrication processes that enable the manufacturing of cells using film-type SSE layers with reduced thicknesses, ideally 25 – 50 μm, to reach high energy density, while still maintaining ideal mechanical properties.[11] These fabrication techniques must also be compatible with existing manufacturing methods, such as conventional doctor-blade or roll-to-roll coating processes.

The most common way to address these aforementioned issues is to include polymer binders in the SSE composite, as they provide an added flexibility to the fabricated SSE films to compensate for mechanical weakness of pellet-type SSEs. Indeed, mechanical failures of SSEs in ASSBs is detrimental to battery performance.[2] This approach also enables a scalable doctor-blade or roll-to-roll solution process.[12] Film-type SSEs, combining sulfide inorganic SSEs with

polymer binders and fabricated with doctor-blade have been reported in the literature (Table 2.1) with ionic conductivities ranging between 10^{-5} to 10^{-3} S cm^{-1}. This wide conductivity variation can be attributed in part to the usage of different polymer binders and SSEs. However, even when similar polymer binders and electrolytes were used, large variations in ionic conductivity can still be observed, indicating a high sensitivity to processing parameters (e.g., solvents, binder ratio, or liquid to solid ratio of the slurries) over the resulting ionic conductivity. Moreover, most reports limited evaluation of SSE films to mainly ionic conductivity, often ignoring the thickness uniformity of the produced film. Uniform and pinhole-free SSE layers are essential to electronically separate cathodes from anodes and to guide a uniform current and stress distribution, thus preventing short-circuit of ASSBs, which is one of the most important safety requirements for batteries. They are also crucial for maintaining consistent quality in mass production. Thus, a systematic study of the relationship between manufacturing conditions and the performance of SSE films is required.

Table 2.1. Summary of ionic conductivity and thickness of recently reported SSE films processed with different manufacturing conditions.

Electrolyte	Binder	Solvent	Binder content	Liquid : solid ratio	Ionic Conductivity (S cm^{-1})	Thickness (μm)	Ref
Li_6PS_5Cl	Acrylate type	Xylene : Isobutyl isobutyrate (50 : 50)	1 wt%	-	1.3 x 10^{-3}	30	[13]
Li_3PS_4	SBS	Anisole	3 wt%	-	2 x 10^{-4}	60	[14]
$Li_7P_3S_{11}$	SEBS	Xylene	2.5 wt%	1	7 x 10^{-4}	55	[15]
Li_3PS_4	PEO	Acetonitrile	5 wt%	4.6	8.4 x 10^{-6}	10	[16]
Li_6PS_5Cl	PEO	Acetonitrile	5 wt%	-	2.0 x 10^{-4}	65	[17]
Li_3PS_4	NBR	Xylene	3 wt%	-	4.2 x 10^{-4}	-	[18]
Li_3PS_4	NBR	THF	5.5 wt%	-	1.0 x 10^{-4}	70	[19]
Li_6PS_5Cl	NBR	Xylene	-	-	-	30	[20]
Li_6PS_5Cl	poly(tert-butyl acrylate)-b-poly(1,4-butadiene)	Isobutyl isobutyrate	2.5 wt%	-	1.7 x 10^{-3}	150	[21]
Li_6PS_5Cl	PBMA	Xylene : Isobutyl isobutyrate (0 : 100 - 100 : 0)	3% – 10%	0.6 – 1.4	1.5 x 10^{-4} - 8.6 x 10^{-4}	40	This work

SBS, Polystyrene-*block*-polybutadiene-*block*-polystyrene; SEBS, polystyrene-*block*-poly(ethylene-*ran*-butylene)-*block*-polystyrene); PEO, poly(ethylene oxide); NBR, nitrile butadiene rubber; PBMA, poly(butadiene methacrylate); THF, tetrahydrofuran;

Unfortunately, analyzing the correlations between multiple manufacturing parameters and performance metrics is challenging and requires intensive trial and error with conventional experimental methods.[22] Moreover, there may be non-linear trends resulting from the synergistic effects of different manufacturing parameters, making the multi-variable puzzle even more complicated. Mesoscale physical simulations of the actual manufacturing process can offer deep

insights on the mechanism of how manufacturing parameters impact the properties of SSE films,[23-26] but they are considered computationally expensive for high throughput use with current hardware capabilities.[27] Machine learning (ML), with its proficiency in analyzing complex datasets with a large number of variables,[22, 28-32] provides a new pathway to limit time-consuming trial and error processes. Moreover, ML, in combination with statistical methods, allows fast interpretation of data. In fact, ML has already been utilized in the battery field, either in estimating the state of charge or cycle life of cells under operation,[31, 33] as well as to assist in the manufacturing process of LIB electrodes.[22, 27] However, the application of ML to manufacturing flexible SSE films remains unexplored, presenting an opportunity to apply such capabilities to improve performance and overall quality of SSE films used in ASSBs.

This work seeks to predict the quality of SSE films by analyzing the multi-variable interdependencies between performance and manufacturing parameters. The methodology used in this work is schematically presented in Figure 2.1. Before casting, Li_6PS_5Cl (LPSCl) powder, a commonly used inorganic Li^+ conductor, is wet-milled to homogenize its particle size and keeps it approximately one order of magnitude smaller than the target thickness of SSE films, preventing it from negatively affecting their uniformity. Of the multiple input parameters that need to be considered for performance evaluation, polymer content (P%), liquid to solid ratio (L:S), and cosolvent ratio (X:B) are chosen as the manufacturing parameters because they have a significant influence over the rheological properties of SSE slurries. After casting the SSE films, several output parameters: density (ρ), ohmic resistance (Ω), normalized conductivity (σ_i^N), deviation of thickness (DoT: the standard deviation of thickness measured over 9 different points on the SSE films), and relative thickness deviation (RD: the relative standard deviation of thickness, DoT / thickness) are obtained. The obtained experimental dataset, consisting of 110 slurry compositions, is used to perform a Principal Component Analysis (PCA) to determine the most representative observables for performance metrics and manufacturing conditions.[34] Following PCA, the

manufacturing conditions are classified according to a *K-Means* clustering in order to define the quality of SSE film in terms of σ_i^N, DoT, and RD. Afterwards, hyperplanes are assigned using Support Vector Machine (SVM) for a graphical visualization of specific effects.[35-36] This common thread aims to both present groups of manufacturing conditions with similar performances and find the effect of each manufacturing parameter on SSE films. Finally, an SSE film, with manufacturing conditions guided by the ML study, is applied to a NCM811 || LPSCl || LiIn cell to demonstrate the viability of this approach.

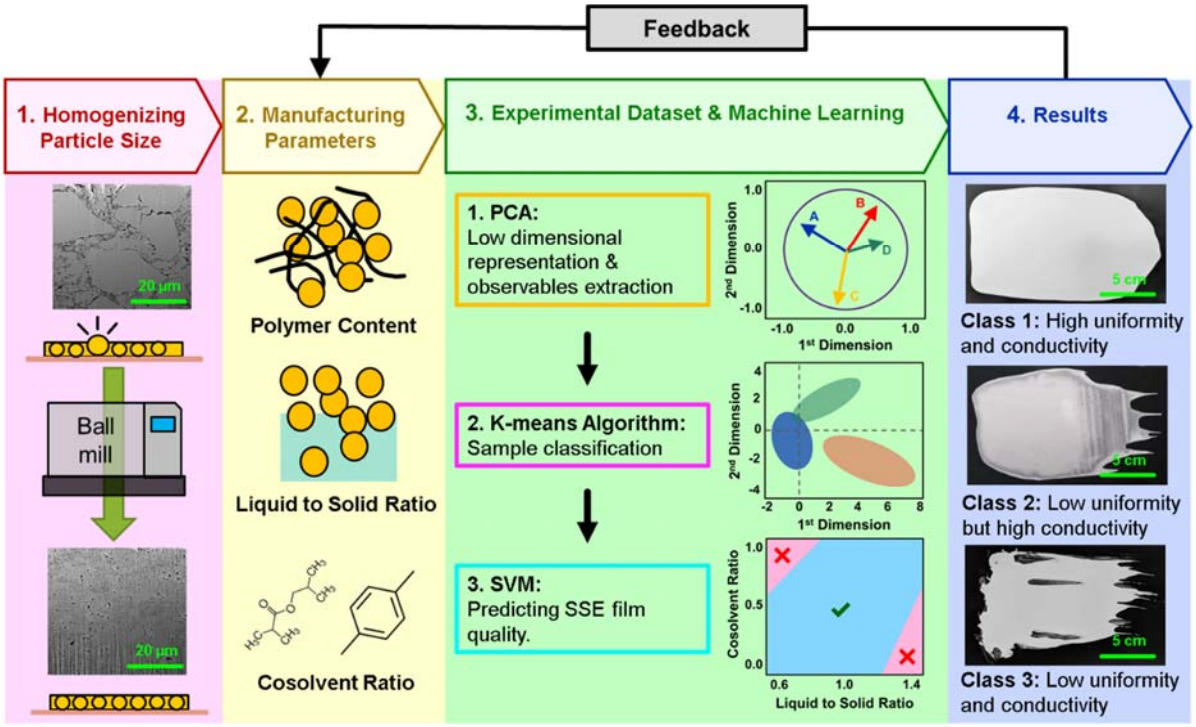

Figure 2.1. A schematic presenting the methodology developed in this work. First, ball-milling is used to reduce the particle size of the LPSCl electrolyte. Then, 110 slurries consisting of different polymer contents, liquid to solid ratios, and cosolvent ratios are fabricated to obtain the dataset. This dataset is fed into the Machine Learning workflow to categorize samples with different properties, as shown in the 4th step.

2.2 Methods and ML Algorithm Details

2.2.1 Electrolyte Powder Preparation – Ball Mill

The Li_6PS_5Cl (LPSCl) electrolyte powder was obtained from NEI and used without further modifications. Both dry ball-milling and wet ball-milling were used to reduce the particle size of

LPSCl. All the ball-milling experiments were conducted using an Emax high energy ball mill machine (Retsch), with 3 mm-diameter zirconia milling media and a zirconia jar, under Ar atmosphere. For dry ball-milling, no solvent was added to the LPSCl and the powder was milled at 400 rpm for 2 hours. For wet ball-milling, 3 g of LPSCl was mixed with 10 mL of xylene to avoid particle aggregation (frequently encountered in dry ball-milling). The mixtures were milled at 300, 400 and 500 rpm for 1 and 2 hours, respectively. After milling, the slurry was vacuum-dried at 80°C for 8 hours to obtain the milled LPSCl powder.

2.2.2 Collection of the Experimental Dataset of SSE Films

In this study, LPSCl (NEI), poly(butyl methacrylate) (PBMA. Mw 211000, Sigma-Aldrich), p-xylene (≥ 99%, Sigma-Aldrich) and isobutyl isobutyrate (≥ 98%, Sigma-Aldrich) were employed to fabricate SSE films. The full process was conducted in an Ar-filled glovebox with oxygen and moisture level below 0.1 ppm. Polymer contents (3%, 5%, 7% and 10%), liquid to solid ratios (μL solvent / mg LPSCl, 0.6, 0.8, 1.0, 1.2 and 1.4) and cosolvent ratios (in volumetric percentage of xylene, 0, 0.25, 0.5, 0.75, 1.0) were selected as manufacturing parameters. A total combination of 100 samples, plus 10 randomly selected samples, were fabricated. The SSE slurries were fabricated by mixing target amount of LPSCl, binder and solvents with an ARM 310 Thinky mixer for 5 min at 2000 rpm. The slurries were then cast on carbon-coated Al foil with a 300 μm doctor blade and dried in ambient pressure for 1 hour. Afterwards, the films were vacuum-dried at 80°C for 8 hours. SSE films were calendered by placing them in between the titanium plungers (described in previous works[37-38]) and applying a uniaxial pressure of 370 MPa. The thickness, deviations of thickness and relative deviation of the SSE films (without calendering) were obtained by measuring at 9 different points on each film using a micrometer. After calendering, both thickness, ionic conductivity (the procedure is described in EIS section) and weight were measured to obtain the Ohmic resistance, normalized conductivity and density values. The observables are defined as following:

- Thickness (μm) is obtained by averaging the 9 measured thickness values.
- Deviation of thickness (μm) is the standard deviation of the same 9 measured values.
- Relative deviation is obtained by dividing deviation of thickness by the thickness.
- Resistance (Ω) is obtained by fitting the Nyquist plot obtained by EIS.
- Normalized conductivity (S cm^{-1}) is obtained with the formula:

$$\frac{Thickness\ (cm)}{Resistance \times surface\ area \times Ionic\ conductivity\ of\ pristine\ LPSCl} \quad (1)$$

Density (mg / μm) is obtained by dividing the weight of the SSE film (mg) with the thickness after pressing (μm).

2.2.3 Characterization

X-ray diffraction (XRD) patterns of LPSCl were obtained by sealing the powders in boron-rich glass capillaries in an Ar-filled glovebox. Measurements were taken using Cu Kα radiation over a 2θ range of 10° to 60°, with a step size of 0.01°, using a Bruker/Nonius Microstar 592 diffractometer. SEM images of the SSE films were obtained with a FEI Scios DualBeam Focused ion beam. All samples were prepared in an Ar-filled glovebox and transferred with an air-tight loader to avoid any atmosphere exposure.

2.2.4 Electronic Impedance Spectroscopy (EIS) and DC Polarization

200 mg of LPSCl solid-state electrolyte powder was placed in a 13 mm PEEK pellet die and pressed at 370 MPa using titanium plungers to obtain a pellet with a thickness of about 1 mm (measured with a Vernier caliper). After assembly, the cell was tightened in a cell holder. The measurement of the SSE film was done by pressing the film inside at the same setup at 370 MPa and tightened in a cell holder. EIS measurements were performed from 1 MHz to 10 Hz, with an applied AC potential of 30 mV, using a Solartron 1260 Impedance Analyzer, at room temperature.

The results were fitted with the Z-View software. DC polarizations were obtained by applying a 0.5 V bias potential for 300 s using the same experimental setup.

2.2.5 Assembling NCM811 | LPSCl | LiIn Cells

To avoid exposure to air, all procedures were conducted in an Ar-filled glove box. NCM811, LPSCl (NEI), vapor grown carbon fiber (>98%, Sigma-Aldrich) and polystyrene-*block*-polyethylene-*ran*-butylene-*block*-polystyrene (SEBS, Sigma-Aldrich), with a weight ratio of 66:33:3:5, were mixed with a mortar and a pestle to form a cathode slurry. The slurry was then cast on an Al foil with a 150 µm doctor blade. After drying for 30 min under ambient pressure, an SSE slurry from class 1 and class 2 were cast on top of the cathode electrode with a 400 µm doctor blade. The SSE-coated cathode electrode was dried for 30 min under ambient pressure and then vacuum-dried at 80°C for 8 h. LiIn anodes were fabricated by pressing Li and In foils together. Before assembling the cell, the SSE-coated cathode electrode was pressed at 370 MPa. Afterwards, LiIn anode was pressed onto the SSE-coated cathode electrode (with the In side facing the cathode) and the pressure was increased to 5 MPa. The cell was then cycled under a stack pressure of 5 MPa and a current density of 100 µA cm^{-1} between 1.875 to 3.625 V vs. LiIn using a setup already described in previous works.[37-38]

2.2.6 Principal Component Analysis

2.2.6.1 Principle and Definition

Principal Component Analysis (PCA) represents a data compression technique for high dimensional dataset studies by features extraction. The idea lies on the projection of the dataset onto a low dimensional subspace built by components, where the latter results from a linear combination of *p* initial features. The components are orthogonal with each other and represent new axes of maximum variance with the purpose to keep as much initial information as possible. The resulting components are called principal components and give the possibility to reflect the

initial dataset in the space where the axes are such components. As an example, a 2D plot, formed by the two principal components, denotes the distribution of the data from the initial dataset. Therefore, the number of principal components (called *k*) is considerably smaller than *p*. As a consequence, taking into account that each raw data is defined with such *p* initial features in the vector space $\mathbb{R}^p$ like $x_i = [x_1, x_2, x_3, \ldots, x_p]$, the problem of the projection through the linear combination is to find *k* vectors namely *z* to build a $p \times k$ matrix Z for projection. Such problem is matrix-wise speaking written as Eq. 1:

$$x_i^T z = c \Leftrightarrow X\,Z = C \qquad (c, i, C) \in \mathbb{R}^k \times \mathbb{N} \times \mathbb{R}^{N \times k} \tag{Eq. 1}$$

where *c* represents the vector of new coordinates, and *C* is the matrix that contains all vectors *c*. In the following, x_i refers to the original raw data.

2.2.6.2 Maximization of Inertia

To obtain the linear combination, it is necessary to search for principal factors that form *Z* under the constraint of maximum variance (*i.e.,* inertia *I*). Indeed, the projection in a vector space reduces the variance of the data while the PCA tries to keep as much variance as possible. *I* can be defined as the distance between raw data from the centroids *g* of the distribution as follows:

$$\begin{aligned} & I = \sum_{i \leq p} \frac{1}{p} * d^2(x_i, g) \\ & \Leftrightarrow I = \sum_{i \leq p} \sigma_{i,i} \\ & \Leftrightarrow \ \sigma_{i,j} = \textstyle\sum_{i \leq N} \frac{1}{p} * (x_{i,l} - g_l)(x_{j,l} - g_l) \\ & \Leftrightarrow \mathrm{V} \coloneqq [\sigma_{ij}] \end{aligned} \tag{Eq. 2}$$

$d(.,.)$ is the Euclidean distance in the vector space, V is initially defined as the variance-covariance matrix resulting from Eq. 2 and stores the pairwise covariances between initial features.

Such matrix admits a singular values decomposition (SVD) and can be deconvoluted by *k eigenvalues* associated to *k eigenvectors*.[39] Indeed, the matrix *V* satisfies the relationship below:

$$Vz_i = \lambda_i z_i \quad \lambda_i \in Spec(V) \quad i \leq k \qquad \text{(Eq. 3)}$$

where *Spec*(*V*) is the spectrum of *V* (*i.e.* the vector of eigenvalues).

As a consequence, from Eq. 2 and Eq. 3, *I* can be summarized by the linear sum of the *p* eigenvalues,[40] where the most of the information is equivalent to get the k highest eigenvalues associated to *k eigenvectors*. The latter are considered as the principal factors to take into account to form the Z matrix.

Similar to Eq. 1, each value inside the *C* matrix is calculated from (z_i, $i \leq k$) and (x_i, $i \leq N$) through the scalar product:

$$< x, z >= X\ Z = C \Leftrightarrow [x_1, x_2, x_3, \dots, x_n]^T * [z_1, z_2, \dots, z_k] = [C_1, C_2, \dots, C_k] \qquad \text{(Eq. 4)}$$

2.2.7 *K-Means* Clustering

2.2.7.1 Purpose of the Clustering and Definition

The study developed focuses on the characterization of the quality of SSE films, based on manufacturing parameters. Therefore, the idea is to differentiate high-quality films from low-quality ones. In combination with the PCA methodology detailed above, the application of a segmentation method on the new low dimensional subspace is to obtain groups (*i.e.*, clusters) with similarities between data inside them. That aims to separate the electrolyte films with the same characteristics in terms of manufacturing parameters and films properties. Indeed, the distinction of clusters according to RD and σ_i^N are the key factors to gather good or bad electrolyte films.

To be more precise, the algorithm is iterative, suggesting that the data within groups are optimized at each loop in order to characterize clusters by centroids μ_j with the best separation of

data. As a consequence, the search of best clusters is summarized by a simple optimization problem that minimizes the within-cluster sum of square written as J below:

$$J \coloneqq \sum_{i \leq N} \sum_{J \leq k} \omega_i^j \left\| x_i - \mu_j \right\|^2 \quad (N, k) \in \mathbb{N}^2 \qquad \text{(Eq. 5)}$$

Where ω_i^j is equal to 1 when the x_i is in the *j*st cluster, else 0. *k* represents the number of clusters, and *N is* the number of training data points.

The algorithm converges when the J is not moving upon a certain threshold. The algorithm is then assigned as follows:

- Randomly initialize *k* centroids for the *k* clusters;
- Put data in the nearest centroids μ_j to complete the clusters;
- Afresh the centroids with the corresponding data;
- Calculate the J metric;
- Repeat step 2 from step 4 until convergence.

2.2.7.2 Empirical Number of Clusters

Data distribution within clusters can be unbalanced due to the feature projection in the low dimensional subspace. Figure 2.2d shows the SSE films far away from the rest of the distribution due to significant differences in terms of SSE films properties. In that sense, the number of clusters was empirically chosen based on such distribution.

Indeed, the number of clusters *k* is basically *a priori* chosen. An inappropriate choice of *k* can result in very poor clustering performances and provide clusters with a very few numbers of data inside. According to the initial problem, the number of clusters was put at *k* = 3 to both, to obtain relevant clustering performances, and to compare clusters in terms of electrolyte properties.

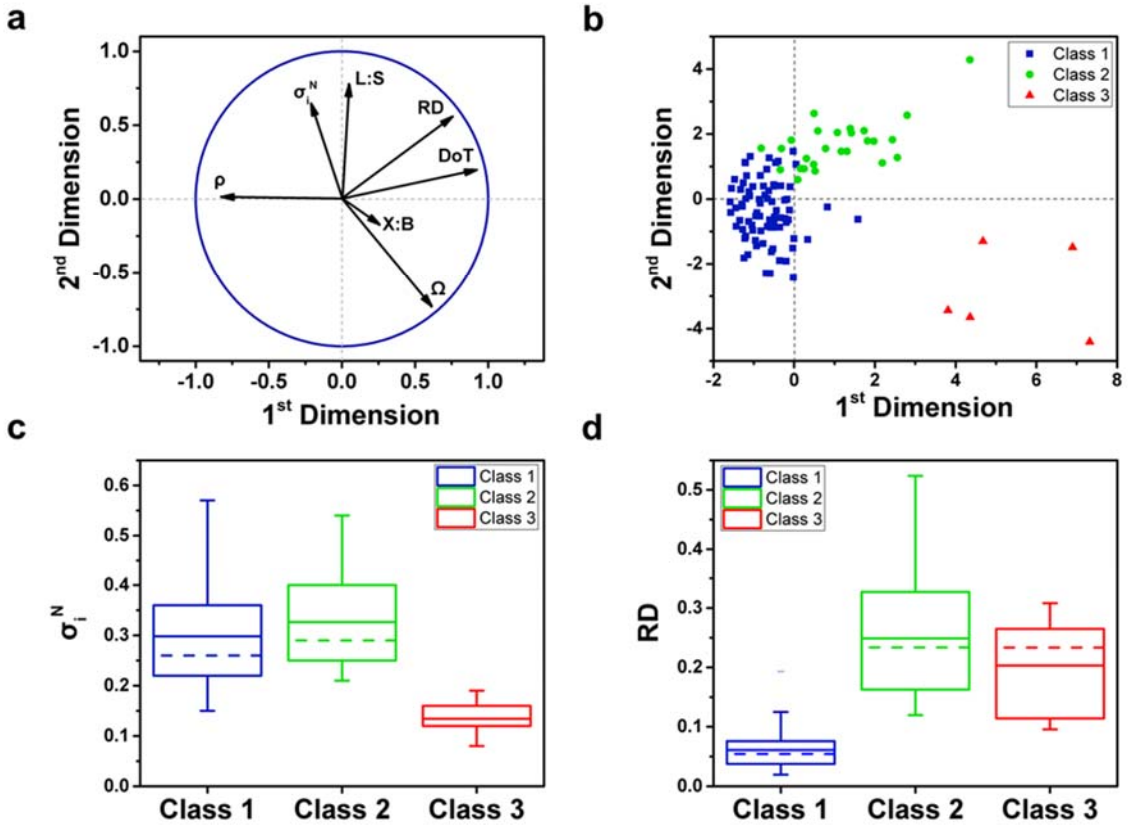

Figure 2.2. The data analysis results coming from the implementation of the PCA and the *K-Means* algorithm which show the linear dependences between initial variables and the grouping of the samples in terms of performance respectively. a) Projection of the initial variables (symbolized by black arrows) onto the 2D plan formed by the first two principal components resulting from the PCA implementation, with the purpose to visualize and analyze the correlation between each pair of variables. For the PCA implementation, P% is not taken into account due to a short number of different modalities. It is considered as a qualitative variable and did not appear in the initial PCA features for better results. However, P% is used for the rest of the analysis. b) All samples are grouped into 3 clusters with the *K-Means* algorithm, here represented within the two first principal components. Those clusters are explicitly defined as *classes* in the rest of the study. Box charts for the comparison of distribution of c) normalized conductivity and d) relative thickness deviation for all 3 classes. Abbreviations: L:S, liquid-to-solid ratio; X:B, cosolvent ratio; ρ, density; Ω, ohmic resistance; σ_i^N, normalized conductivity; DoT, deviation of thickness; RD: relative thickness deviation.

2.2.8 Support Vector Machine

SVM algorithm is a powerful and widely used learning method to separate training points by implementing a decision boundary (*i.e.,* hyperplane). Considering the space of the initial features, the decision boundary can clearly appear and it is straightforward to display the evolution

of the latter when features values are changing. Such methodology was found to be very useful for understanding the parameters interdependencies.

2.2.8.1 Definition of Decision Boundary

The definition of the boundary may depend on the type of the separation. For the study, a linear separation was chosen due to good predictions during the validation of the model. In that sense, the following details for the hyperplane will be based on a linear decision boundary.

The SVM lies on the computation of a hyperplane of which the aim is to separate as much as possible the training data to avoid poor classification results. Considering training data x_i with p features, the hyperplane (defined in a dimension p - 1) is expressed below:

$$(H) \coloneqq \omega_0 + \omega^T x_i = 0 \quad x \in \mathbb{R}^p \qquad \text{(Eq. 6)}$$

where ω is a vector of weights, and $\mathbb{R}^p$ the vector space of dimension p.

Considering the training data points, the algorithm used to find the best ω while fitting the training points in the positive and negative side of (H). Indeed, the closest training points to the hyperplane are the most relevant to obtain the best hyperplane.

2.2.8.2 Distance Calculation for Margin Optimization

To get the hyperplane, the objective is to maximize the margin (*i.e.*, the distance between the hyperplane and training data) that is able to decrease the classification error. Higher is the margin, better is the prediction. Regarding the sign of (H) for training points, the algorithm may predict a class rather than another.

Therefore, the decision boundary lies on the definition of a distance metric to properly fit the hyperplane. In $\mathbb{R}_p$, the distance between points and hyperplane is computed as follows:

$$d_x := \frac{|\omega_0 + \omega^T x|}{\|\omega\|} \quad \text{(Eq. 7)}$$

with ||.|| the Euclidean distance in $\mathbb{R}^p$.

The objective of the SVM is under the constraints that the training data will be correctly predicted. In other words, the goal is summarized as maximizing the lower distance between the hyperplane and training points. It can be written as finding the best weights as:

$$\omega^* = argmax_{\omega}\left(min_x(d_x)\right) \quad \text{(Eq. 8)}$$

As a consequence, during the training, the sign of $\omega_0 + \omega^T x$ concludes on which class the training data belongs to, and say if there is a misclassification for adjusting the weights of the SVM. Considering a binary case with *Y* the output variable defined as $Y \in \{-1, 1\}$, the validation of the model with the testing data points goes through the capability of the latter to not misclassify a new point in the “positive group” rather than the “negative group” (or the contrary). The negative and positive side of the hyperplane (Figure 2.3) is determinant to say is the model predicts correctly. It means that the value of the $\omega_0 + \omega^T x$ is not relevant, but it focuses more on the sign, which can be written more concisely as follows:

$$y_i(\omega_0 + \omega^T x_i) \begin{cases} > 0 & if\ x_i\ correctly\ predicted \\ < 0 & if\ x_i\ not\ correctly\ predicted \end{cases} \quad \text{(Eq. 9)}$$

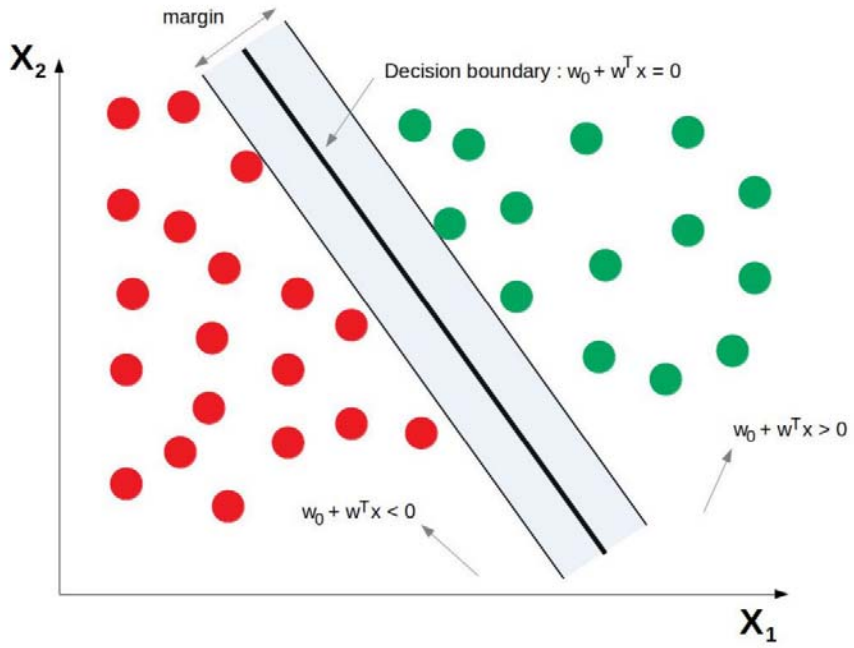

Figure 2.3. Representation of the maximization of the margin in the feature space example of X_1 and X_2 (two-feature example), to separate as much as possible the different classes from the hyperplane. An example of two classes is used with a “positive” and a “negative” group respectively colored in green and red.

2.2.8.3 Multi-Classification SVM

During the training of the algorithm, the hyperplane is fitted by separating the classes on both sides. However, it may be applied for more than two classes, exactly as it has been made for the study since three classes of electrolyte films have been found. Many techniques face the situation like the One-vs-One classifier.[41] According to the latter, it trains $\frac{n(n-1)}{2}$ classifiers when it exists *n* classes on the dataset, meaning that each pair of classes are compared. In this study, two classifiers were used in the SVM model.

2.3 Results and Discussion

As broad particle size distributions of the SSE will adversely affect the uniformity of the SSE films, sizes need to be reduced to around one order of magnitude smaller than the target thickness of the films. This ensures consistency and allows for better film uniformity. As shown in

Figure 2.4a, the pristine LPSCl powder exhibits a non-uniform particle size distribution with particles larger than 20 µm. Hence, reducing the particle size of the pristine powder is necessary. After dry ball-milling, some of the particles remain larger than 15 µm, suggesting that the process is not effective enough (Figure 2.4b). To overcome this, inert solvents are employed in wet ball-milling to prevent the aggregation of the particles and thus allow for reduced particle size. No particles larger than 10 µm are observed after wet ball-milling, as seen in Figure 2.4c-f. When increasing the milling speed to 400 and 500 rpm, the primary particle size can be further reduced, but simultaneously the ionic conductivity of the electrolyte powder decreases significantly. To avoid severe ionic conductivity loss, the milling speed is limited to 300 rpm, with an optimized milling time of 2 hours. Under these milling conditions, the particle size is also further reduced while still preserving the ionic conductivity of the powder. As a result, all the electrolyte powders used for this study are processed using these wet ball-milling conditions.

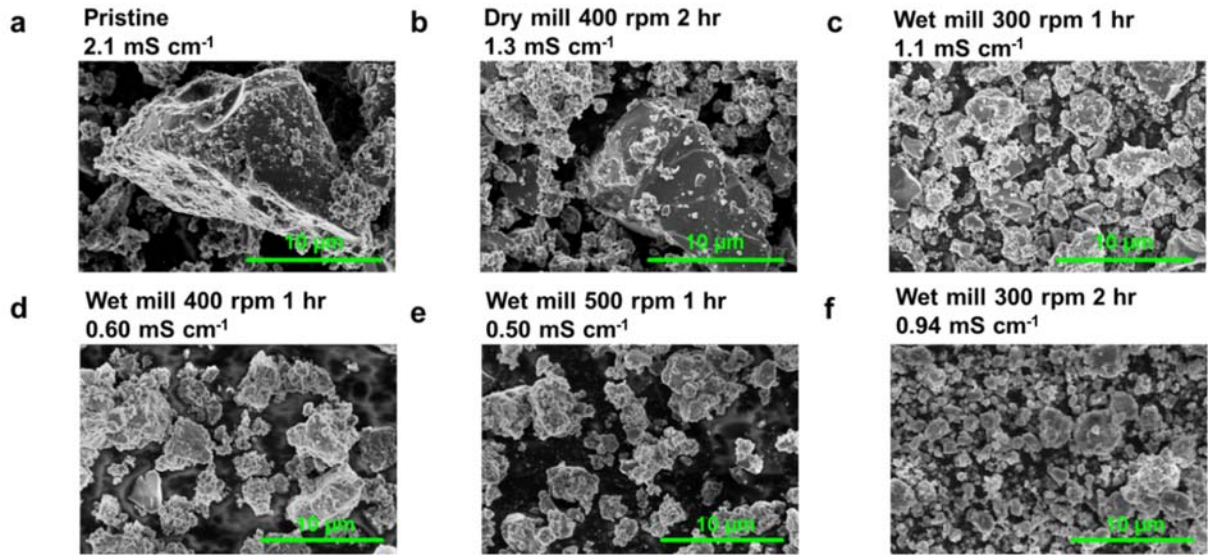

Figure 2.4. SEM images of LPSCl powders. (a) Pristine powder. Powders that underwent (b) dry mill at 400 rpm for 2 hours, wet mill at (c) 300 rpm for 1 hour, (d) 400 rpm for 1 hour, (e) 500 rpm for 1 hour and (f) 300 rpm for 2 hours.

To evaluate the impact of ball-milling on the electrolyte's crystal structure, X-ray diffraction (XRD) patterns of the LPSCl powder are collected before and after various ball-milling procedures

(Figure 2.5a). The positions of all Bragg peaks remain unchanged after ball-milling, indicating that the original LPSCl crystal structure is preserved. However, the samples can be distinguished by different extents of peak broadening (Figure 2.5b), indicating reduction in crystallinity after ball-milling. The peak broadening with increased milling speed is in good agreement with the lower conductivity measured by electrochemical impedance spectroscopy (EIS) presented in Figure 2.5c.

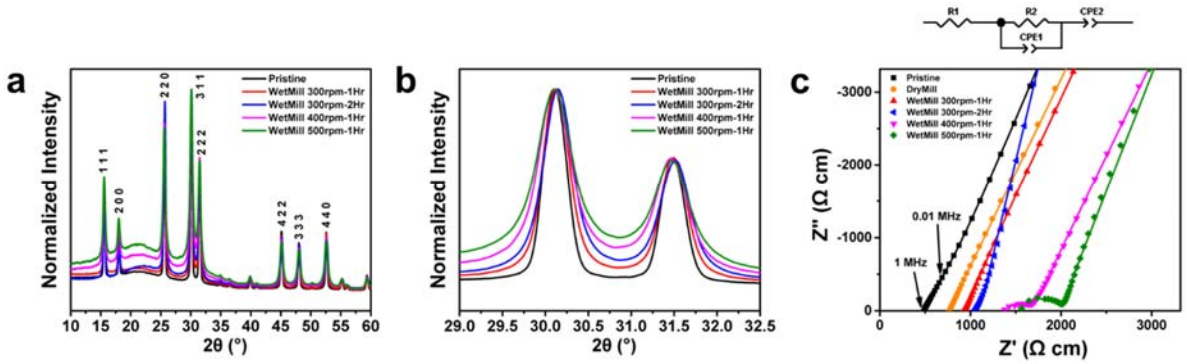

Figure 2.5. The (a) XRD patterns and the (b) magnified view on (3 1 1) and (2 2 2) peaks and the (c) EIS of LPSCl at different ball-mill conditions. The fitted EIS data are presented as solid curves.

To reaffirm the importance of controlling SSE particle size, SSE films are fabricated using pristine and ball-milled LPSCl powder, and their focused-ion-beam (FIB) cross-section images are presented in Figure 2.6. When pristine LPSCl powder is employed, the film exhibits particles larger than 20 μm and is susceptible to crack formation during calendering. This can increase the risk of short circuit when the SSE films are used in ASSBs. On the contrary, a more homogeneous film is obtained when employing ball-milled LPSCl, and no cracks are observed in the cross-sectional image. Thus, the ball-milled electrolyte powder is used for the collection of the dataset necessary for the ML study.

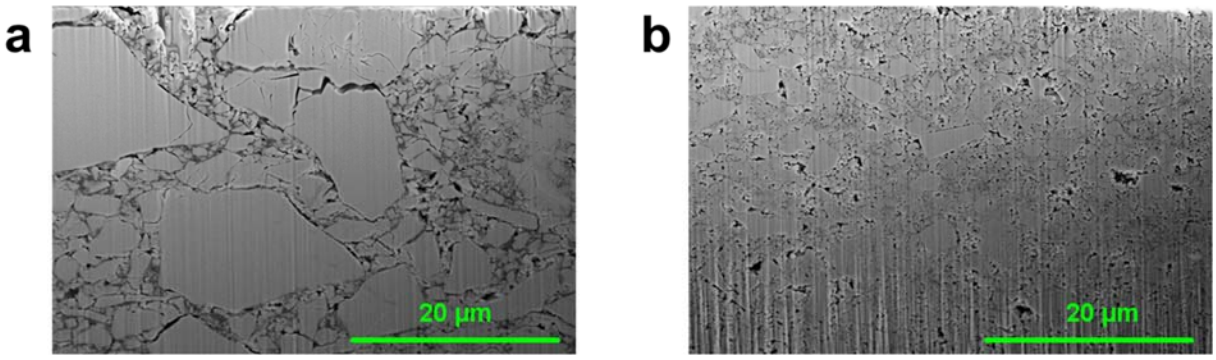

Figure 2.6. The cross-section view of SSE films made of (a) pristine LPSCl powder and (b) LPSCl powder wet-milled at 300 rpm for 2 hours.

To perform the doctor-blade process for LPSCl, solvents with good chemical compatibility with sulfide-based SSEs must be selected, namely, non-polar solvents with high dielectric constant are required.[15] Moreover, suitable vapor pressures (at room temperature, xylene: 10 mmHg; isobutyl isobutyrate: 5 mmHg) and boiling points (xylene: 138°C; isobutyl isobutyrate: 147°C) are also essential for obtaining an optimum drying rate, which significantly influence the quality of SSE films. Thus, *p*-xylene and isobutyl isobutyrate are employed in conjunction for the LPSCl slurry preparation. To evaluate their chemical compatibility with the SSE, LPSCl powder is immersed into each of these solvents and no significant change is observed in both XRD patterns and ionic conductivities after drying (Figure 2.7), indicating that LPSCl does not degrade in either of these two solvents.

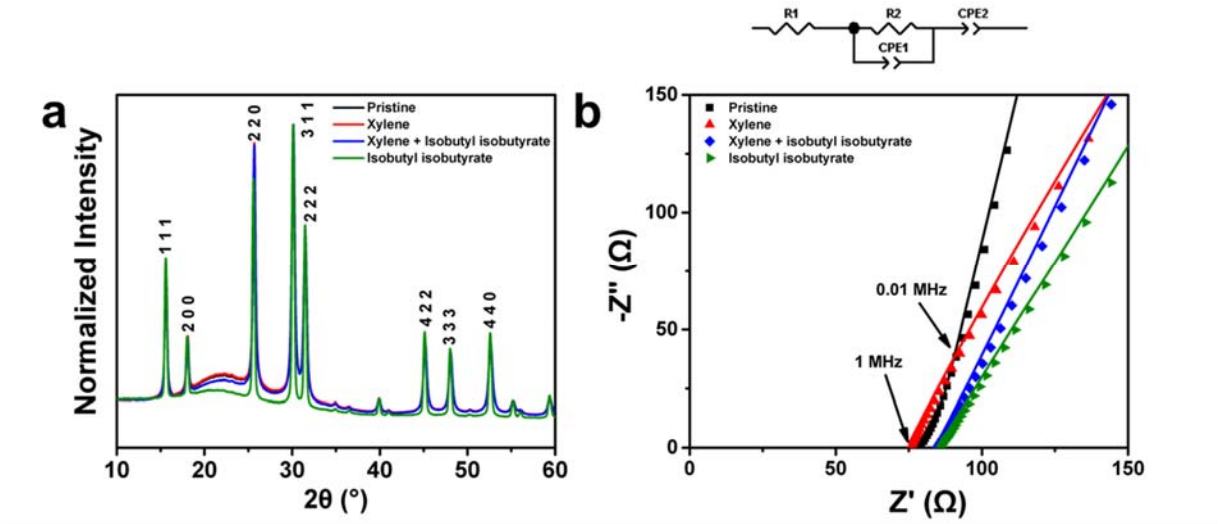

Figure 2.7. The (a) XRD and (b) EIS of LPSCl after exposing to xylene, isobutyl isobutyrate and their cosolvent. The fitted EIS data are presented as solid curves.

After collecting this training dataset, ML algorithms are used to analyze the effect of the polymer content P%, the liquid-to-solid ratio L:S (volume of solvent / weight of LPSCl, in μL / mg), and the cosolvent ratio X:B (xylene to isobutyl isobutyrate ratio, represented by the volumetric percentage of xylene) on the quality of the SSE films. After casting, ρ, Ω, σ_i^N, DoT, and RD are measured. Since eight different variables are experimentally generated, a PCA[34] is conducted to project manufacturing conditions in a reduced dimensional subspace for reflecting (i) interdependencies between variables and (ii) the spread of manufacturing conditions along new principal components. Indeed, such data compression is based on a search for directions of maximum variance to build a new subspace with fewer dimensions, in which the initial raw data are projected. The resulting principal components are a linear combination of initial variables that are orthogonal to each other. This PCA implementation aims at selecting a subset of principal components that can reflect the variance of the experimental dataset to define the relationship between manufacturing conditions and film quality.

The correlations between the initial variables can be visualized by projecting them onto two-dimensional subspace and the result is presented in Figure 2.2a. As expected, the PCA

shows that σ_i^N is inversely correlated with resistance (Equation 1 in SI). However, it appears that while DoT and RD are strongly correlated together, they are not linearly correlated with σ_i^N. As a result, σ_i^N (corresponding to the ionic conductivity of the film) and RD (representing the film uniformity) are employed to evaluate performances of the SSE films. The independence between σ_i^N and RD highlights the shortcomings of evaluating SSE films solely based on ionic conductivities alone, as commonly done in the literature.[13-21] Based on the PCA analysis, it is conceivable that highly conductive films might be perceived as of high quality, while they exhibit large RDs that result in poor cell performance during electrochemical testing.

To visualize the interdependencies among manufacturing conditions and performance, thickness, DoT, and σ_i^N are plotted as a function of L:S and X:B for different P%. As P% increases, the overall thickness also increases, while σ_i^N decreases. This may be a result of higher slurry viscosities that limit the flow along the surface of the substrate. Higher P% also increases the tortuosity of Li^+ diffusion, resulting in poorer bulk σ_i^N compared to bare LPSCl.[12] The thickness increases drastically when high X:B, low L:S, and P% larger than 5% are used. With these manufacturing conditions, slurries become too viscous, causing the LPSCl powder to aggregate. While trends in ionic conductivity are relatively intuitive, the plots for DoT exhibit a complex nonlinear behavior. The region with low deviation shifts dramatically as the P% changes. To obtain a better overview, DoT values are averaged over the four P% and plotted in Figure 2.8. The region with low deviation is found to be distributed in a counterintuitive way. This implies that it is challenging to deconvolute the interdependencies among manufacturing conditions and performance using simple statistical methods. Hence, clustering analysis is employed in the next step.

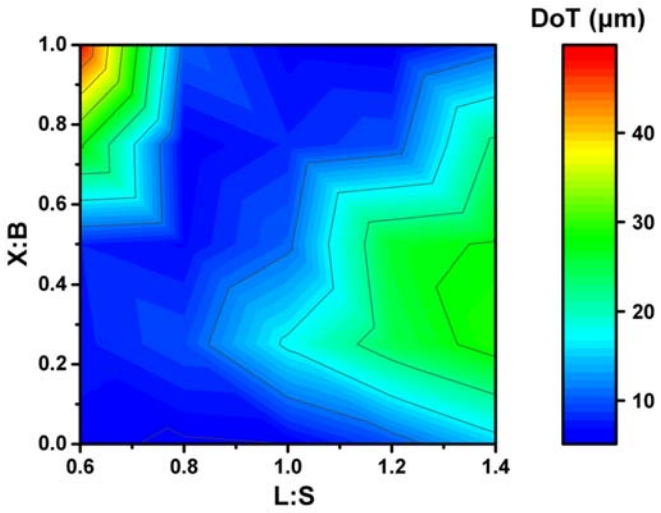

Figure 2.8. The DoT vs L:S and X:B contour plot averaging through P% of 3%, 5%, 7% and 10%.

Before explicitly looking at the effect of manufacturing conditions, it is useful to create groups with similar characteristics in terms of performance, namely, σ_i^N and RD from the PCA results. *K-Means* algorithm is directly applied on principal components and the results are presented in Figure 2.2.[35] The purpose of the algorithm is to obtain clusters of manufacturing conditions represented by centroids in the low dimensional subspace with the same characteristics in terms of performances, without any prior information (patterns of manufacturing values) on the obtained labels. In order to separate the data, *K-Means* algorithm finds patterns where manufacturing conditions inside clusters are similar. The algorithm finds in total 3 different clusters. For the rest of the study, a cluster of manufacturing conditions is called a *class* in order to characterize properly a type of SSE films. The apparent interception of the boundaries from class 1 and class 2 is due to the projection onto a 2D space, whereas the clustering algorithm is applied to more than two principal components. These classes are well separated from each other by other dimensions before projecting on the 2D space. The statistics of σ_i^N and RD in all classes are presented in Figure 2.2c and d, where a non-parametric Kruskal-Wallis test is applied to statistically compare the distributions of σ_i^N and RD between classes.[42] This test is relevant to

compare more than two samples and assume that residuals of the tests are not following a normal distribution, and conclude on possible significant differences between medians of distributions. In that sense, it will validate the *K-Means* clustering in order to discriminate SSE films based on their properties. For the test itself, the *p*-value, generally written as "*p*", represents the probability to reject the hypothesis of the differences in distributions. As a consequence, the test presents significant differences ($p \leq 0.05$) of distribution among the classes in this study.[42] It appears that both class 1 and class 2 exhibit a high ionic conductivity σ_i^N compared to class 3. Class 1 can be further separated from class 2 as it exhibits the lowest RD (i.e., higher film uniformity). To conclude, class 1 exhibits good σ_i^N and low RD; class 2 maintains the good σ_i^N from class 1 while exhibiting an increased RD; class 3 shows the worst performance both in terms of σ_i^N and RD. As a consequence, the classification of the overall performance of SSE films can be defined by common characteristics of observables within each class.

It is also worth looking at the manufacturing condition's relationships with different classes. As the polymer is insulative compared to LPSCl, the ionic conductivity decreases as the P% increases. As expected, the average P% in class 3 is higher than that of class 1 and 2. Nevertheless, no statistical effect is found for P% on RD. When looking at L:S, one may conclude that employing higher L:S facilitates higher σ_i^N according to the PCA result. Indeed, the classes with higher conductivity contain higher ranges of L:S. However, to minimize the RD, the ratio must be kept in an intermediate range, namely, 0.92 ± 0.23, which is the average value within class 1. Class 3 appears to have the highest X:B, implying a possible adverse effect of X:B over performance. However, an Anova calculation (with a logarithmic correction on the dependent variable)[43] indicates that X:B and L:S have synergistic effects on RD. Although qualitative conclusions can be drawn after conducting *K-Means* algorithm, the link between manufacturing conditions and performance remains obscure due to the synergistic effect among different

variables. Thus, numeric relationships between manufacturing conditions and performance need to be deciphered before the ML model can gain the ability to predict the results.

While the manufacturing conditions – performance relationship appears clearer after *K-Means* clustering, it needs to be further deconvoluted through SVM.[36] Such powerful and widely used classification learning technique optimizes the separation of classes from each other by constructing a linear hyperplane in the low dimensional subspace defined above, to maximize the margin between different classes. Therefore, the margin is defined as the distance between the separating hyperplane (also called decision boundary) and training raw data. Larger is the margin, better is the classification prediction. Consequently, the separation of classes and the decision boundaries are interesting as a visualization tool of the results. Indeed, it is possible to fix one manufacturing parameter and display the classification results as well as the decision boundary in a 2D plot formed by ranges of the two other parameters. In that sense, it is possible to analyze the evolution of the boundary when manufacturing conditions change, which reflects their impact on the performance.[22]

This process allows the prediction of film performance associated with a specific set of manufacturing conditions. To train the SVM model, 80% of the total number of raw data are randomly selected as the training dataset, and the remaining data are used as the testing dataset to validate the model. To overcome the unbalanced class distribution, a resampling method is applied on the training dataset to fix the class imbalance (Figure 2.9) by adjusting class distribution over the minority classes (i.e. class 2 and 3).[44] Such random oversampling approach allows the SVM algorithm to learn data distribution in equal proportions of samples per class, whereas unbalanced numbers of samples would cause SVM to yield inaccurate results by prioritizing the class with the largest number of samples. In another word, the metric used to validate the model considers the weighted training of the SVM algorithm by providing a better value, when predicting manufacturing conditions as a minor class.

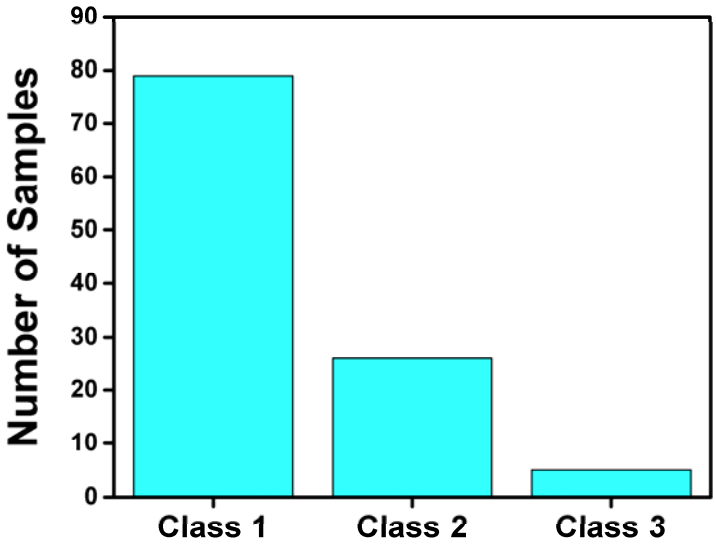

Figure 2.9. The number of samples in each class. Oversampling is required before applying the SVM algorithm due to unbalanced numbers of samples.

The best linear hyperplane is assigned by SVM to divide the space of manufacturing conditions into three regions. The results based on σ_i^N and RD are presented in Figure 2.10. When accounting only for σ_i^N as the performance metric, most of the manufacturing conditions are considered to result in good film quality. However, when considering the RD as well, a large portion of manufacturing conditions, with mid-to-high L:S are no longer qualified so. Therefore, the three regions, from low L:S to high L:S, can be related to class 3, class 1, and class 2, respectively. Besides the data points obtained through experiment, SVM is also able to predict using new manufacturing conditions, interpolating the results with P% of 4%, 6%, 8%, and 9%. When projected on the L:S – X:B plane, the hyperplane appears to be sloped and will shift as P% changes, showing the counterintuitive trend caused by the high interdependency of each manufacturing parameter. When comparing the trends found in Figure 2.10 with the interpretations of *K-Means* clustering and the statistical tests, they match in terms of the effects

of manufacturing parameters, indicating that the ML classifier is suitable for analyzing interdependencies between manufacturing parameters and quality of SSE films.

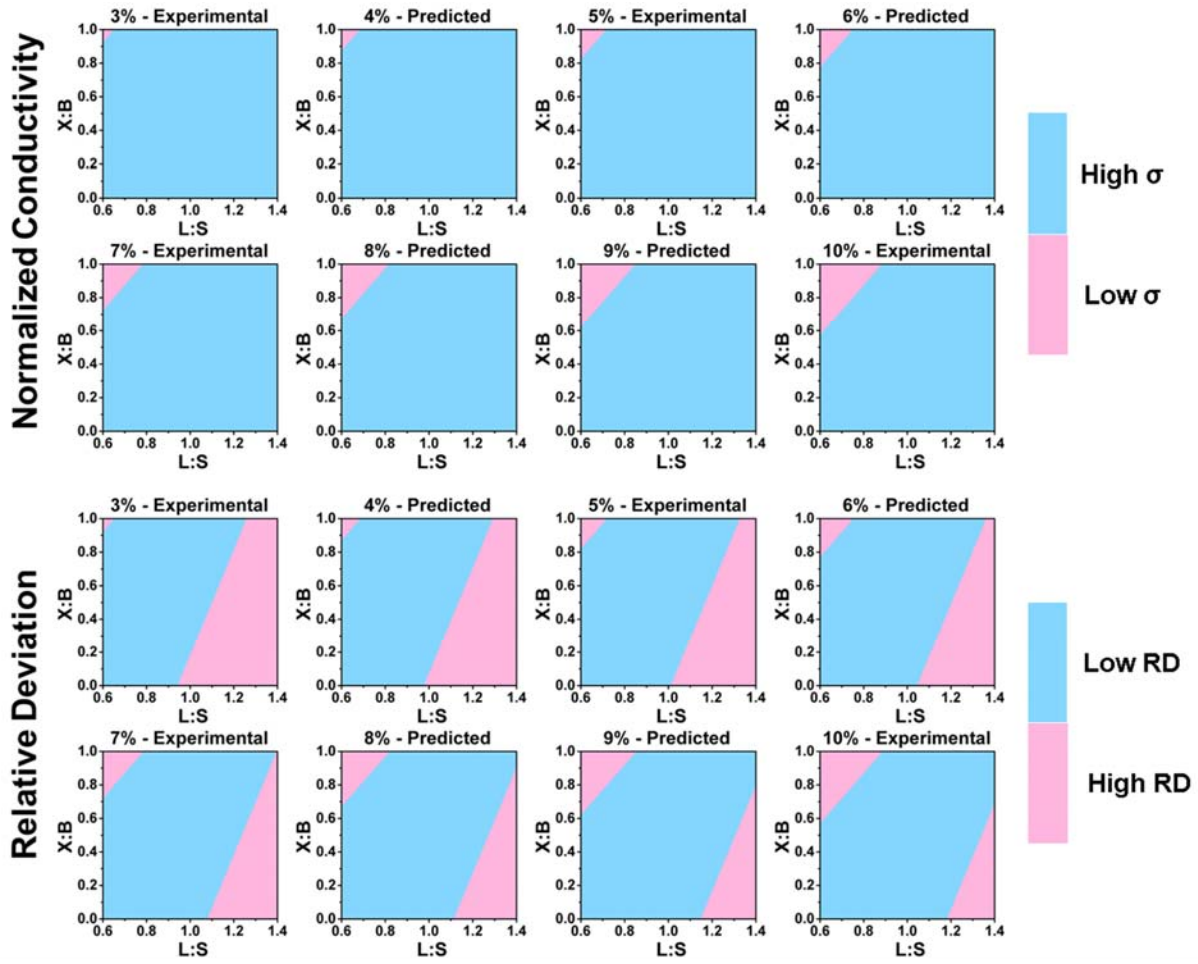

Figure 2.10. SVM classification in terms of the ionic conductivity σ_i^N and the relative thickness deviation RD of SSE films as a function of L:S and X:B ratios. The manufacturing conditions with P% of 3%, 5%, 7% and 10% are obtained through experiment, while 4%, 6%, 8% and 9% are interpolated using the ML model.

The model is validated with the testing dataset through the F1-score metric[45] that reaches a value of 94%. Such a metric is relevant for multi-label classification learning since it helps to balance the metric across the sensitivity and the specificity of the model. The F1-score is an average definition of precision and recall, and an example of a binary classification task is shown below:

$$F1 = 2 \times \frac{precision \times recall}{precision + recall} \quad (1)$$

$$precision = \frac{RP}{RP+FP} \quad (2)$$

$$recall = \frac{RP}{RP+FN} \quad (3)$$

where RP, FP and FN are respectively the true predicted values, the mis-predicted false values, and the mis-predicted true values. The true/false prediction is defined as a manufacturing condition correctly/wrongly classified by the algorithm over the positive/negative value of the output. In the case of the multi-label classification developed in this study, the F1-score is averaged over the values between each pairs of labels for the output of the classification task. Due to the definition of three classes of film quality, it is possible to distinguish good and bad SSE films with respect to each performance variable.

To probe the connection between performance and morphologies of the SSE films, one sample is selected from each class and their morphology observed using digital and scanning electron microscopy (SEM) images, as presented on Figure 2.11. From the digital images, class 1 appears to be the most uniform and exhibits a clear-cut boundary with its substrate. Compared to class 1, class 2 exhibits inferior uniformity with a fading boundary to the substrate, likely due to the higher L:S in its manufacturing conditions. Severe aggregations can be observed in class 3 where the solvents fail to properly disperse the LPSCl powder due to insufficient L:S. When looking at the SEM top-down view images (Figure 2.11d-f), both class 1 and class 2 show uniform surface morphology, with class 1 appearing to be slightly superior. On the other hand, aggregated particles and cracks can be observed on the surface of the class 3 sample. FIB cross sections (Figure 2.11g-i) are collected to probe the interior morphology of the films. The particle distributions of class 1 and class 3 are similar, with class 3 being more porous. Class 2 exhibits smaller overall particle size, especially on the top part of the image, likely due to phase separation between the smaller and larger particles resulting from excessive L:S.

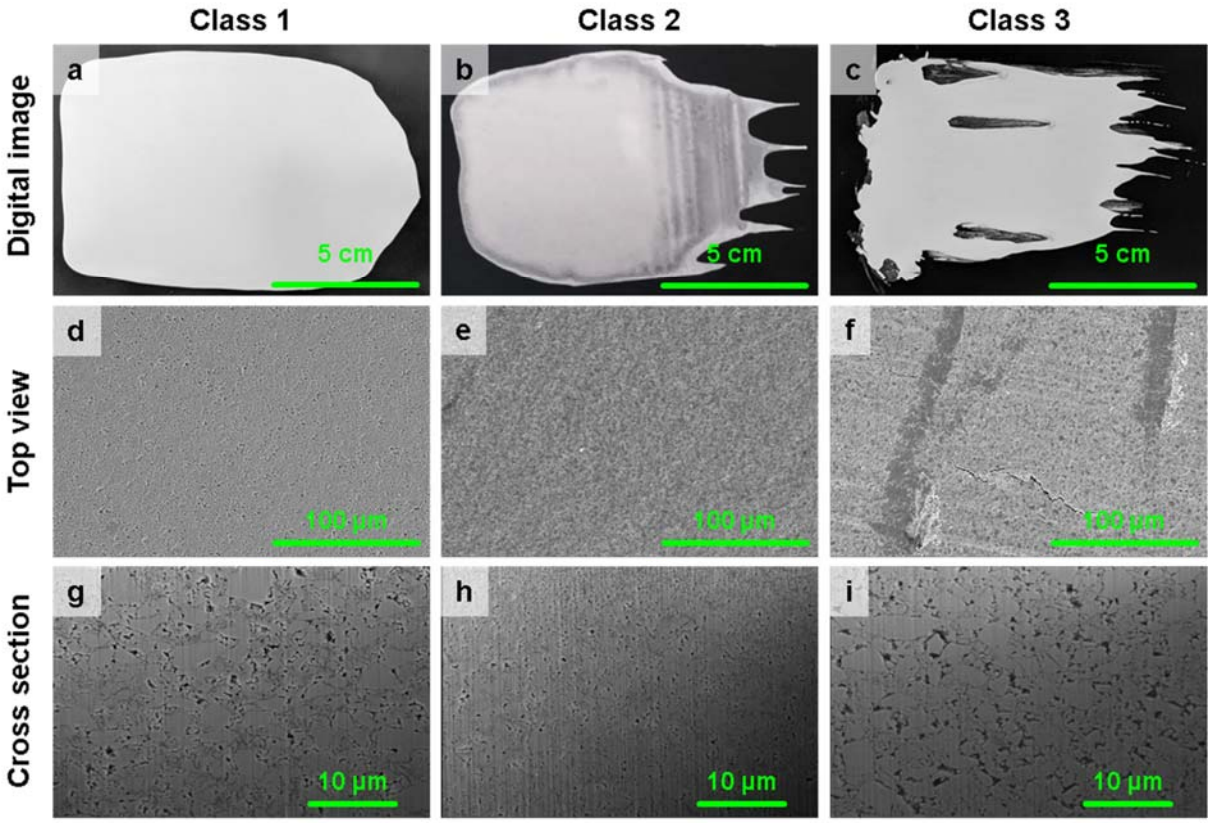

Figure 2.11. Images of representative SSE films from each class. a-c) Digital images, d-f) SEM top view and g-i) FIB cross-section views of the SSE films from a,d,g) class 1, b,e,h) class 2 and c,f,i) class 3.

To verify this assumption, another cross section is taken from the bottom side (Figure 2.12) and it appears that the average particle size is comparable to that of class 1 and 3. Nevertheless, the overall porosity of class 2 is lower than that of class 1, probably due to the close packing of LPSCl particles facilitated by higher L:S, explaining slightly higher σ_i^N in class 2 than class 1. Even though class 2 exhibits dense cross-section morphology, its tendency to phase separate is not desirable for maintaining consistent quality in mass production. To prove its superior quality over the other 2 classes, a uniform free-standing SSE film from class 1 is fabricated and tested in Figure 2.13.

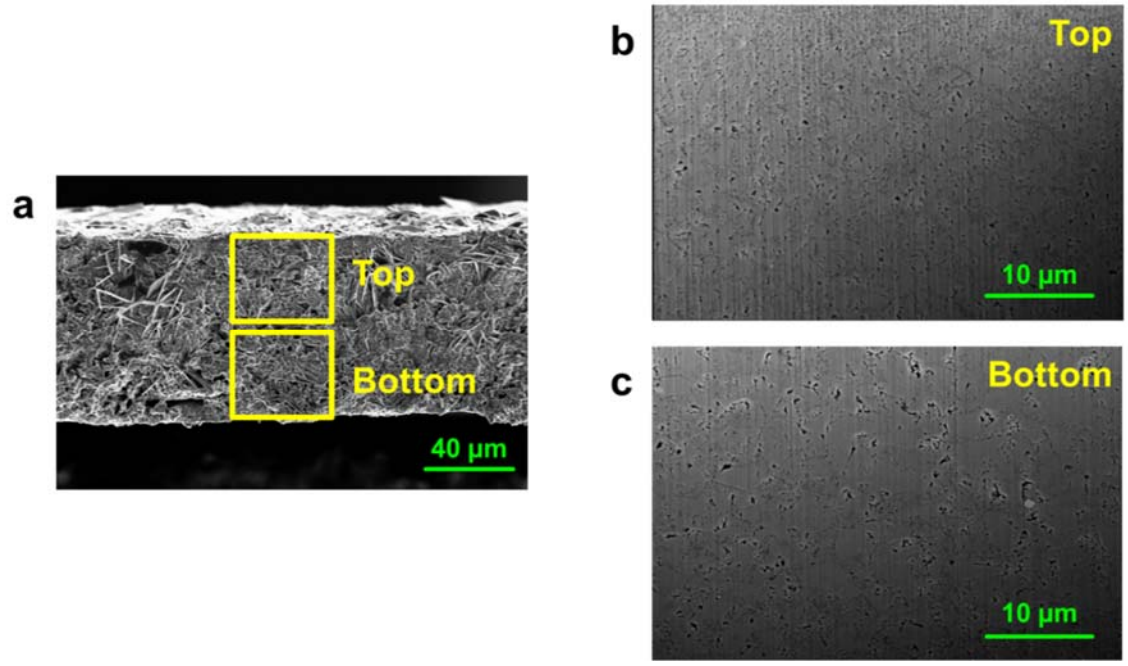

Figure 2.12. The cross-sectional SEM images of an SSE film from class 2. (a) The cross-sectional SEM image of the entire film. The FIB cross-sectional SEM images of (b) top and (c) bottom portion of the SSE film.

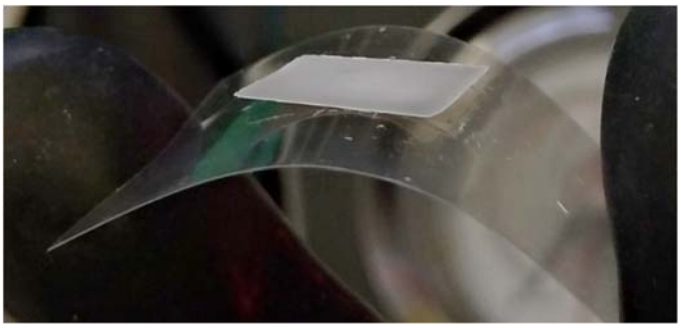

Figure 2.13. To demonstrate the robustness of SSE films selected from class 1, a free-standing SSE film was cast on a PET film and vacuum dried. After calendering, the SSE film can be peeled from the PET film without any damage.

Before the application of SSE films to batteries, it is important to evaluate their electronic conductivity. An SSE with sufficient electronic insulation, preferably below the order of 10^{-9} S cm^{-1}, will prevent charge leakage or even short circuiting of the cells.[46-47] DC polarization and EIS results of the LPSCl powder and film are presented in Figure 2.14. While the pristine LPSCl powder exhibits an ionic conductivity of 2.1 x 10^{-3} S cm^{-1} and an electronic conductivity of 5.1 x 10^{-9} S cm^{-1}, the optimized LPSCl film has an ionic conductivity of 8.6 x 10^{-4} S cm^{-1} and an

electronic conductivity of 1.1 x 10^{-9} S cm^{-1}. For both samples, the electronic conductivities are six orders smaller than their ionic conductivity. It is worth noting that although the LPSCl film exhibits a lower ionic conductivity than its powder form, the ability to be fabricated with reduced thicknesses leads to a lower total impedance as can be seen on Figure 2.14b. The fabrication of SSE films is therefore not only beneficial to energy density of the battery, but also reduces ohmic losses during cycling.

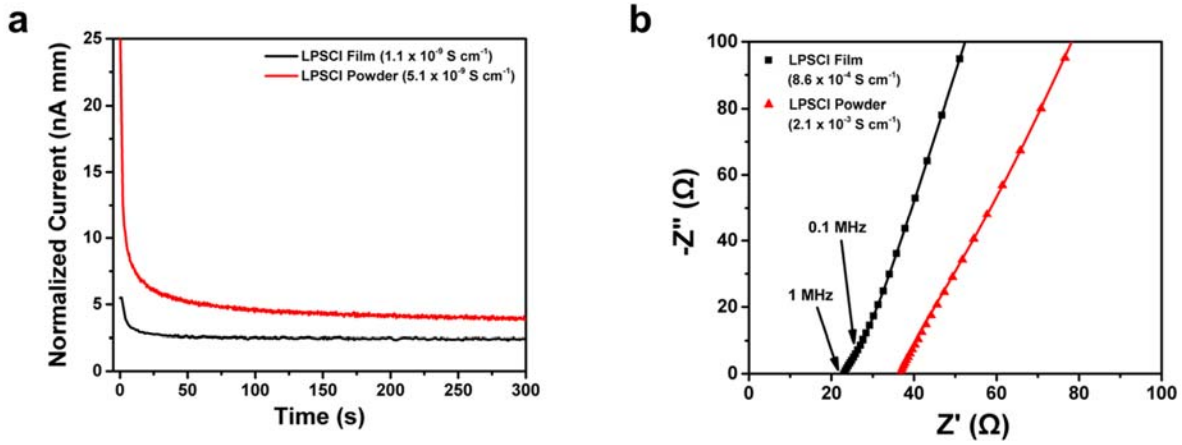

Figure 2.14. (a) DC polarization curves of the LPSCl film and pellet samples. Normalized current is obtained by multiplying the response currents with the thickness of SSE layers. (b) Nyquist plots of the LPSCl film and pellet samples. The fitted EIS data are presented as solid curves.

SSE films from class 1 and 2 are used to prepare NCM811 || LPSCl || LiIn cells. A FIB cross-section image showing the SSE and the cathode layers after calendering is presented in Figure 2.15a. The whole cross-section is observed to be uniform and dense. The cathode composite – SSE layer contact is also observed to be compliant, with no delamination, voids, or cracks observed. Their voltage profiles are presented in Figure 2.15b. When the class 1 film is employed, the cell cycles as expected, while a short-circuit is observed during the first charge with the class 2 film. Non-uniform thickness of SSE films can cause uneven stress distribution during calendering and impact negatively on the integrity of the cell structure, leading to short circuit during the first charge. This illustrates the importance of considering both the uniformity and ionic conductivity of the SSE films for performance evaluation. Figure 2.15c shows the

capacity retention and Coulombic efficiency (CE) of the NCM811 || LPSCl || LiIn cell made with the class 1 film. A 1st cycle CE of 74.1% along with a 1st discharge capacity of 149 mAh g^{-1} is obtained. The initial capacity loss in the first 10 cycles can be attributed to kinetic effects of contact losses and initial impedance growth at the cathode, which is commonly observed in the interfaces between sulfide SSEs and layered-oxide cathodes.[48-49] Variation in CE can be observed, and these may be attributed to the ionic conductivity change of SSE resulting from the slight fluctuation of room temperature. A capacity of 94 mAh g^{-1} is retained after 100 cycles.

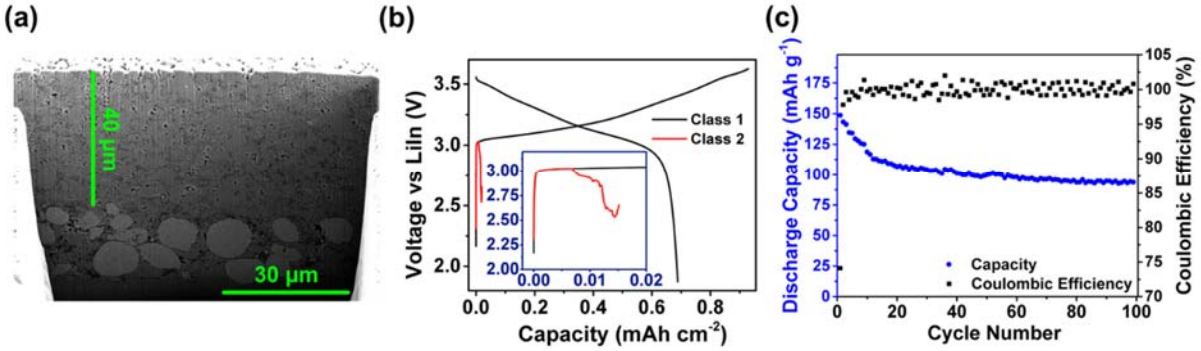

Figure 2.15. SEM cross section image, first cycle voltage profiles capacity retention and Coulombic efficiency of NCM811 || LPSCl || LiIn cells with a cathode loading of 4.75 mg cm^{-2}. a) SEM cross section image indicating that an intimate contact is formed between the electrolyte and the cathode composite. The measured thickness of the SSE film is 40 µm. b) First cycle voltage profiles of NCM811 || LPSCl || LiIn cells prepared using SSE films from class 1 and class 2. Due to lower uniformity, the cell using the class 2 film shorts during the first cycle. c) Capacity retention and Coulombic efficiency of the class 1 cell.

Another NCM811 || LPSCl || graphite cell with an areal capacity of 10 mg cm^{-2} was fabricated and its voltage profiles and EIS are presented in Figure 2.16. The cell has a 1st discharge capacity of 1.61 mAh cm^{-2} and a 1st CE of 76.2%. This demonstrates the possibility of utilizing the ML approach in practical applications. Nevertheless, similar to the NCM811 || LPSCl || LiIn cell, NCM811 || LPSCl || graphite cell also suffers from contact losses at the cathode and its EIS increases from 142 Ω to 178 Ω after the 1st cycle. Future works will be focused on optimizing the cycling pressure of film-type ASSBs to mitigate the capacity loss caused by volume change of layered-oxide cathode materials,[48-50] and to increase the energy density by enabling Li-metal anodes.[37-38,51-52]

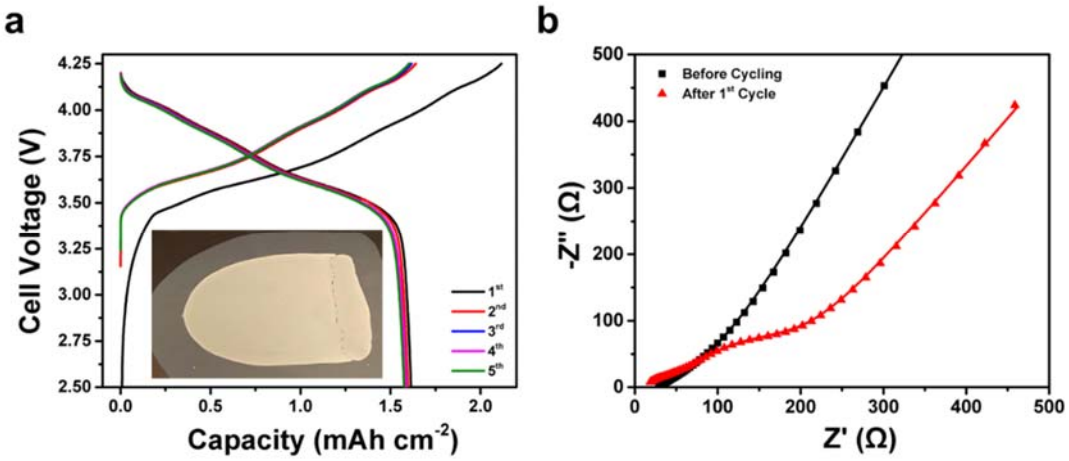

Figure 2.16. The (a) voltage profiles from the 1st to 5th cycle of a graphite || SSE || NCM811 film cell. The inset shows the SSE layer casted over the anode composite layer. (b) EIS of the same cell before cycling, and after the first cycle.

2.4 Conclusion

In summary, this study demonstrates how ML algorithms can be used to predict the performance of the sulfide-based SSE films by deconvoluting the interdependencies between the manufacturing parameters and performance metrics. After collection of the experimental dataset, three algorithms (PCA, *K-Means* algorithm and SVM) in combination with statistical tests are employed to analyze the data. PCA determines the most significant observables for performance evaluation and allows to represent the manufacturing conditions in a low dimensional subspace. A clustering method, the *K-Means* algorithm, is then applied in this subspace to properly define classes of films quality based on the similarity of performance within groups. These 3 classes are defined as class 1 (high σ_i^N and low RD), class 2 (high σ_i^N and high RD) and class 3 (low σ_i^N and high RD). Finally, the SVM model reveals the trends of the effect of the manufacturing parameters on the quality of SSE films according to classes, and supports the results found in the *K-Means* clustering and statistical analysis. Finally, guided by ML, a NCM811 || LPSCl || LiIn cell, utilizing an SSE film with a thickness of 40 µm from class 1, is shown to be able to cycle successfully for 100 cycles. Our results highlight the necessity to account for both uniformity and ionic conductivity when fabricating SSE films and demonstrate how ML can be a powerful tool to guide experiments

towards the optimal fabrication parameters. The methodology provided in this study may benefit the development of future scalable manufacturing process for flexible and uniform SSE films for ASSB applications.

Chapter 2, in full, is a reprint of the material “Fabrication of High-Quality Thin Solid-State Electrolyte Films Assisted by Machine Learning.” as it appears in ACS Energy Letters. Chen, Y.-T.; Duquesnoy, M.; Tan, D. H. S.; Doux, J.-M.; Yang, H.; Deysher, G.; Ridley, P.; Franco, A. A.; Meng, Y. S.; Chen, Z. 2021, *6*, 1639−1648. The dissertation author was the first author of this paper, all authors contributed to this work.

References

1. Chen, T.; Jin, Y.; Lv, H.; Yang, A.; Liu, M.; Chen, B.; Xie, Y.; Chen, Q., Applications of lithium-ion batteries in grid-scale energy storage systems. *Trans. Tianjin Univ.* **2020,** *26* (3), 208-217.

2. Horowitz, Y.; Schmidt, C.; Yoon, D.-h.; Riegger, L. M.; Katzenmeier, L.; Bosch, G. M.; Noked, M.; Ein-Eli, Y.; Janek, J.; Zeier, W. G., Between Liquid and All Solid: A Prospect on Electrolyte Future in Lithium-Ion Batteries for Electric Vehicles. *Energy Technology* **2020,** *8* (11), 2000580.

3. Jung, Y. S.; Oh, D. Y.; Nam, Y. J.; Park, K. H., Issues and challenges for bulk-type all-solid-state rechargeable lithium batteries using sulfide solid electrolytes. *Isr. J. Chem.* **2015,** *55* (5), 472-485.

4. Kerman, K.; Luntz, A.; Viswanathan, V.; Chiang, Y.-M.; Chen, Z., practical challenges hindering the development of solid state Li ion batteries. *J. Electrochem. Soc.* **2017,** *164* (7), A1731.

5. Lee, H.; Oh, P.; Kim, J.; Cha, H.; Chae, S.; Lee, S.; Cho, J., Advances and Prospects of Sulfide All-Solid-State Lithium Batteries via One-to-One Comparison with Conventional Liquid Lithium Ion Batteries. *Adv. Mater.* **2019,** *31* (29), 1900376.

6. Zhang, Q.; Cao, D.; Ma, Y.; Natan, A.; Aurora, P.; Zhu, H., Sulfide-based solid-state electrolytes: synthesis, stability, and potential for all-solid-state batteries. *Adv. Mater.* **2019,** *31* (44), 1901131.

7. Seino, Y.; Ota, T.; Takada, K.; Hayashi, A.; Tatsumisago, M., A sulphide lithium super ion conductor is superior to liquid ion conductors for use in rechargeable batteries. *Energy Environ. Sci.* **2014,** *7* (2), 627-631.

8. Kamaya, N.; Homma, K.; Yamakawa, Y.; Hirayama, M.; Kanno, R.; Yonemura, M.; Kamiyama, T.; Kato, Y.; Hama, S.; Kawamoto, K., A lithium superionic conductor. *Nat. Mater.* **2011,** *10* (9), 682.

9. Janek, J.; Zeier, W. G., A solid future for battery development. *Nat. Energy* **2016,** *1* (9), 1-4.

10. Balaish, M.; Gonzalez-Rosillo, J. C.; Kim, K. J.; Zhu, Y.; Hood, Z. D.; Rupp, J. L., Processing thin but robust electrolytes for solid-state batteries. *Nat. Energy* **2021,** *6*, 227-239.

11. Randau, S.; Weber, D. A.; Kötz, O.; Koerver, R.; Braun, P.; Weber, A.; Ivers-Tiffée, E.; Adermann, T.; Kulisch, J.; Zeier, W. G., Benchmarking the performance of all-solid-state lithium batteries. *Nat. Energy* **2020,** *5* (3), 259-270.

12. Tan, D. H.; Banerjee, A.; Chen, Z.; Meng, Y. S., From nanoscale interface characterization to sustainable energy storage using all-solid-state batteries. *Nat. Nanotechnol.* **2020**, 1-11.

13. Lee, Y.-G.; Fujiki, S.; Jung, C.; Suzuki, N.; Yashiro, N.; Omoda, R.; Ko, D.-S.; Shiratsuchi, T.; Sugimoto, T.; Ryu, S., High-energy long-cycling all-solid-state lithium metal batteries enabled by silver–carbon composite anodes. *Nat. Energy* **2020,** *5* (4), 299-308.

14. Sakuda, A.; Kuratani, K.; Yamamoto, M.; Takahashi, M.; Takeuchi, T.; Kobayashi, H., All-solid-state battery electrode sheets prepared by a slurry coating process. *J. Electrochem. Soc.* **2017,** *164* (12), A2474.

15. Tan, D. H.; Banerjee, A.; Deng, Z.; Wu, E. A.; Nguyen, H.; Doux, J.-M.; Wang, X.; Cheng, J.-h.; Ong, S. P.; Meng, Y. S., Enabling thin and flexible solid-state composite electrolytes by the scalable solution process. *ACS Appl. Energy Mater.* **2019,** *2* (9), 6542-6550.

16. Self, E. C.; Hood, Z. D.; Brahmbhatt, T.; Delnick, F. M.; Meyer III, H. M.; Yang, G.; Rupp, J. L.; Nanda, J., Solvent-Mediated Synthesis of Amorphous Li3PS4/Polyethylene Oxide Composite Solid Electrolytes with High Li+ Conductivity. *Chem. Mater.* **2020,** *32* (20), 8789-8797.

17. Luo, S.; Wang, Z.; Fan, A.; Liu, X.; Wang, H.; Ma, W.; Zhu, L.; Zhang, X., A high energy and power all-solid-state lithium battery enabled by modified sulfide electrolyte film. *J. Power Sources 485*, 229325.

18. Lee, K.; Kim, S.; Park, J.; Park, S. H.; Coskun, A.; Jung, D. S.; Cho, W.; Choi, J. W., Selection of binder and solvent for solution-processed all-solid-state battery. *J. Electrochem. Soc.* **2017,** *164* (9), A2075.

19. Oh, D. Y.; Kim, D. H.; Jung, S. H.; Han, J.-G.; Choi, N.-S.; Jung, Y. S., Single-step wet-chemical fabrication of sheet-type electrodes from solid-electrolyte precursors for all-solid-state lithium-ion batteries. *J. Mater. Chem. A* **2017,** *5* (39), 20771-20779.

20. Nam, Y. J.; Oh, D. Y.; Jung, S. H.; Jung, Y. S., Toward practical all-solid-state lithium-ion batteries with high energy density and safety: comparative study for electrodes fabricated by dry-and slurry-mixing processes. *J. Power Sources* **2018,** *375*, 93-101.

21. Lee, J.; Lee, K.; Lee, T.; Kim, H.; Kim, K.; Cho, W.; Coskun, A.; Char, K.; Choi, J. W., In Situ Deprotection of Polymeric Binders for Solution-Processible Sulfide-Based All-Solid-State Batteries. *Adv. Mater.* **2020,** *32* (37), 2001702.

22. Cunha, R. P.; Lombardo, T.; Primo, E. N.; Franco, A. A., Artificial Intelligence Investigation of NMC Cathode Manufacturing Parameters Interdependencies. *Batteries & Supercaps* **2020,** *3*, 60-67.

23. Rucci, A.; Ngandjong, A. C.; Primo, E. N.; Maiza, M.; Franco, A. A., Tracking variabilities in the simulation of Lithium Ion Battery electrode fabrication and its impact on electrochemical performance. *Electrochim. Acta* **2019,** *312*, 168-178.

24. Franco, A. A.; Rucci, A.; Brandell, D.; Frayret, C.; Gaberscek, M.; Jankowski, P.; Johansson, P., Boosting rechargeable batteries R&D by multiscale modeling: myth or reality? *Chem. Rev.* **2019,** *119* (7), 4569-4627.

25. Ngandjong, A. C.; Rucci, A.; Maiza, M.; Shukla, G.; Vazquez-Arenas, J.; Franco, A. A., Multiscale simulation platform linking lithium ion battery electrode fabrication process with performance at the cell level. *J. Phys. Chem. Lett.* **2017,** *8* (23), 5966-5972.

26. Thomitzek, M.; Schmidt, O.; Röder, F.; Krewer, U.; Herrmann, C.; Thiede, S., Simulating process-product interdependencies in battery production systems. *Procedia CIRP* **2018,** *72*, 346-351.

27. Duquesnoy, M.; Lombardo, T.; Chouchane, M.; Primo, E. N.; Franco, A. A., Data-driven assessment of electrode calendering process by combining experimental results, in silico mesostructures generation and machine learning. *J. Power Sources* **2020,** *480*, 229103.

28. Turetskyy, A.; Thiede, S.; Thomitzek, M.; von Drachenfels, N.; Pape, T.; Herrmann, C., Toward Data-Driven Applications in Lithium-Ion Battery Cell Manufacturing. *Energy Technology* **2020,** *8* (2), 1900136.

29. Bao, J.; Murugesan, V.; Kamp, C. J.; Shao, Y.; Yan, L.; Wang, W., Machine Learning Coupled Multi-Scale Modeling for Redox Flow Batteries. *Adv. Theory Simul.* **2020,** *3* (2), 1900167.

30. Chen, C.; Zuo, Y.; Ye, W.; Li, X.; Deng, Z.; Ong, S. P., A critical review of machine learning of energy materials. *Adv. Energy Mater.* **2020,** *10* (8), 1903242.

31. Severson, K. A.; Attia, P. M.; Jin, N.; Perkins, N.; Jiang, B.; Yang, Z.; Chen, M. H.; Aykol, M.; Herring, P. K.; Fraggedakis, D., Data-driven prediction of battery cycle life before capacity degradation. *Nat. Energy* **2019,** *4* (5), 383-391.

32. Petrich, L.; Westhoff, D.; Feinauer, J.; Finegan, D. P.; Daemi, S. R.; Shearing, P. R.; Schmidt, V., Crack detection in lithium-ion cells using machine learning. *Comput. Mater. Sci.* **2017,** *136*, 297-305.

33. Chemali, E.; Kollmeyer, P. J.; Preindl, M.; Emadi, A., State-of-charge estimation of Li-ion batteries using deep neural networks: A machine learning approach. *J. Power Sources* **2018,** *400*, 242-255.

34. Shah, A.; Chauhan, Y.; Chaudhury, B., Principal component analysis based construction and evaluation of cryptocurrency index. *Expert Systems with Applications* **2021,** *163*, 113796.

35. Likas, A.; Vlassis, N.; Verbeek, J. J., The global k-means clustering algorithm. *Pattern recognition* **2003,** *36* (2), 451-461.

36. Hearst, M. A.; Dumais, S. T.; Osuna, E.; Platt, J.; Scholkopf, B., Support vector machines. *IEEE Intelligent Systems and their applications* **1998,** *13* (4), 18-28.

37. Doux, J.-M.; Yang, Y.; Tan, D. H.; Nguyen, H.; Wu, E. A.; Wang, X.; Banerjee, A.; Meng, Y. S., Pressure effects on sulfide electrolytes for all solid-state batteries. *J. Mater. Chem. A* **2020,** *8* (10), 5049-5055.

38. Doux, J. M.; Nguyen, H.; Tan, D. H.; Banerjee, A.; Wang, X.; Wu, E. A.; Jo, C.; Yang, H.; Meng, Y. S., Stack Pressure Considerations for Room-Temperature All-Solid-State Lithium Metal Batteries. *Adv. Energy Mater.* **2019,** *10* (1), 1903253.

39. J. Shlens. A Tutorial on Principal Component Analysis. *International Journal of Advance Research in Computer Science and Management Studies*, 2005.

40. J. M. Lasgouttes. Variables Quantitatives: Analyse en Composantes Principales. *https://who.rocq.inria.fr/JeanMarc.Lasgouttes/ana-donnees/cours-acp.pdf*, 2019.

41. R. Debnath *et al*. A Decision Based One-Against-One Method for Multi-Class Support Vector Machine. *Pattern Analysis and Applications*, **2004**, 7, 164-175.

42. McKight, P. E.; Najab, J., Kruskal-wallis test. *The corsini encyclopedia of psychology* **2010**, 1-1.

43. Churchill, G. A., Using ANOVA to analyze microarray data. *BioTechniques* **2004,** *37* (2), 173-177.

44. Le, T.; Vo, M. T.; Vo, B.; Lee, M. Y.; Baik, S. W., A hybrid approach using oversampling technique and cost-sensitive learning for bankruptcy prediction. *Complexity* **2019,** *2019*.

45. Popović, M. In *chrF: character n-gram F-score for automatic MT evaluation*, Proceedings of the Tenth Workshop on Statistical Machine Translation, 2015; pp 392-395.

46. Banerjee, A.; Wang, X.; Fang, C.; Wu, E. A.; Meng, Y. S., Interfaces and interphases in All-Solid-State batteries with inorganic solid electrolytes. *Chem. Rev.* **2020,** *120* (14), 6878-6933.

47. Han, F.; Westover, A. S.; Yue, J.; Fan, X.; Wang, F.; Chi, M.; Leonard, D. N.; Dudney, N. J.; Wang, H.; Wang, C., High electronic conductivity as the origin of lithium dendrite formation within solid electrolytes. *Nat. Energy* **2019,** *4* (3), 187-196.

48. Jung, S. H.; Kim, U. H.; Kim, J. H.; Jun, S.; Yoon, C. S.; Jung, Y. S.; Sun, Y. K., Ni-rich layered cathode materials with electrochemo-mechanically compliant microstructures for all-solid-state Li batteries. *Adv. Energy Mater.* **2020,** *10* (6), 1903360.

49. Koerver, R.; Aygün, I.; Leichtweiß, T.; Dietrich, C.; Zhang, W.; Binder, J. O.; Hartmann, P.; Zeier, W. G.; Janek, J. r., Capacity fade in solid-state batteries: interphase formation and chemomechanical processes in nickel-rich layered oxide cathodes and lithium thiophosphate solid electrolytes. *Chem. Mater.* **2017,** *29* (13), 5574-5582.

50. Zhang, W.; Schröder, D.; Arlt, T.; Manke, I.; Koerver, R.; Pinedo, R.; Weber, D. A.; Sann, J.; Zeier, W. G.; Janek, J., (Electro) chemical expansion during cycling: monitoring the pressure changes in operating solid-state lithium batteries. *J. Mater. Chem. A* **2017,** *5* (20), 9929-9936.

51. Kasemchainan, J.; Zekoll, S.; Spencer Jolly, D.; Ning, Z.; Hartley, G.; Marrow, T.; Bruce, P., Critical stripping current leads to dendrite formation on plating in 3 lithium anode solid electrolyte cells. *Nat. Mater.* **2019,** *18* (10), 1105-1111.

52. Wang, Y.; Liu, T.; Kumar, J., Effect of Pressure on Lithium Metal Deposition and Stripping against Sulfide-Based Solid Electrolytes. *ACS Applied Materials & Interfaces* **2020,** *12* (31), 34771-34776.

Chapter 3. Investigating Dry Room Compatibility of Sulfide Solid-State Electrolytes for Scalable Manufacturing

3.1 Introduction

All-solid-state batteries (ASSBs) are viewed as promising candidates for next-generation energy storage media.[1] Unlike conventional Li-ion batteries, ASSBs utilize non-flammable solid-state electrolytes (SSEs), which results in improved safety during operation.[2-5] Among SSEs, oxide-based and sulfide-based materials are the two types that draw the most attention.[6] Furthermore, sulfide electrolytes generally exhibit higher ionic conductivity, some of which are comparable to those of liquid electrolytes.[6-9] This property has been one of the main focuses in the literature, as high conductivity is necessary for enabling high power density batteries. Another advantage of sulfide SSEs is their lower Young's modulus, as softer electrolytes are subject to less stress formation and contact loss resulting from volume change during cell operation.[6] However, sulfide SSEs generally exhibit lower chemical stability than oxides, and their ionic conductivities decrease rapidly when exposed to ambient atmosphere.[6] As such, they are generally handled inside inert-gas-filled gloveboxes. Unfortunately, the essential processes of scalable manufacturing of state-of-the-art Li-ion batteries are conducted in dry rooms rather than gloveboxes, mainly for cost and space considerations. Unlike in Ar-filled gloveboxes, O_2, CO_2, and moisture are all present in a dry room atmosphere and are expected to react with sulfides. Therefore, it is important to understand the influence of air exposure of sulfide SSEs and provide solutions to mitigate any negative effects.

Several studies have proposed methods to increase the air stability of sulfide SSEs. For example, Li_2S-P_2S_5 can be partially substituted with P_2O_5 where the inclusion of oxygen significantly enhanced the air stability of the material.[10-12] Another approach is to apply hard and soft acid and base theory by replacing a hard acid, like P, with soft acids, such as Sn and Sb, to form stronger bonds with S, a soft base.[13, 14] Several Sn- or Sb-based sulfide electrolytes, such

as Li_4SnS_4 and Li_3SbS_4, have been developed and exhibit superior air stability compared to other sulfide-based electrolytes. However, these approaches result in reduced ionic conductivity. To mitigate this issue, a solid solution system consisting of Li_4SnS_4 and Li_3SbS_4 was also studied and achieved an improved ionic conductivity of one order of magnitude compared to its individual components.[14] Another approach consists of incorporating a thin 50 nm oxygen substitution layer, which was applied to the surface of Li_6PS_5Cl (LPSCl) to form a core-shell structure, showing both improved air stability and better preservation of the ionic conductivity.[11]

Despite the efforts invested in improving the air stability of sulfide electrolytes, most studies only assess the stability by measuring the ionic conductivity and H_2S evolution. As such, these studies usually fail to investigate the degradation mechanism of sulfide SSEs during air exposure. Secondly, the effects on post-heat treatment SSEs are also not investigated. On the contrary, these types of fundamental insights on electrolyte stability were recently provided in a halide SSE study, where multiple characterization techniques were employed to compare the structural and compositional changes after ambient air exposure, and reported that heat treating the exposed electrolytes at 260 °C under vacuum could recover their pristine ionic conductivity.[15] In this work, the humidity of the dry room atmosphere was controlled to approximately 100 ppm, which is significantly lower than that of ambient air and is commonly used in today's lithium-ion battery fabrication.[16] Interestingly, we observed exhibiting no significant loss of electrochemical performance. This may be the key to prolonging the exposure time for sulfide SSEs without significantly impairing their ionic conductivities, and hence, provide a pathway toward the scalable production of ASSBs.

This work seeks to study the degradation mechanism of LPSCl during exposure to air and investigate the chemical reactions occurring during the recovery process. Figure 3.1 presents a schematic of the exposure and recovery processes. LPSCl was first exposed to air for 24 hours (denoted as "air-Exp"), and then heat treated at 550°C (denoted as "air-HT"), as it is the annealing

temperature for LPSCl, to investigate the effect of heat treatment on ionic conductivity.[17-23] To study a more extreme case, LPSCl was dissolved in water and then vacuum dried at room temperature (denoted as “water-Exp”), followed by a heat treatment at 550°C (denoted as “water-HT”). The chemical composition of the four samples were then analyzed with multiple characterization techniques such as X-ray powder diffraction (XRD), solid-state nuclear magnetic resonance (ss-NMR) spectroscopy, and both Raman and Fourier-transform infrared spectroscopy (FTIR) spectroscopy.[24] After the heat treatment, the conductivity of both air-Exp and water-Exp samples can be recovered by approximately 3 orders of magnitude. To further understand the chemical reactions during heat treatment, thermal gravimetric analysis (TGA) and differential scanning calorimetry (DSC) were employed, and additional samples were heat-treated at lower temperatures based on the results from thermal characterization. We found that hydrolysis (resulting in H_2S evolution, and thus sulfur loss) and hydration reaction both occur from moisture exposure. Finally, LPSCl samples were exposed in a dry room environment and exhibited a relatively minor ionic conductivity drop. The electrochemical performance of the dry room exposed electrolyte in a $LiNi_{0.8}Co_{0.1}Mn_{0.1}O_2$ (NCM811) half-cell was also maintained, implying that LPSCl is indeed compatible with dry room environments.

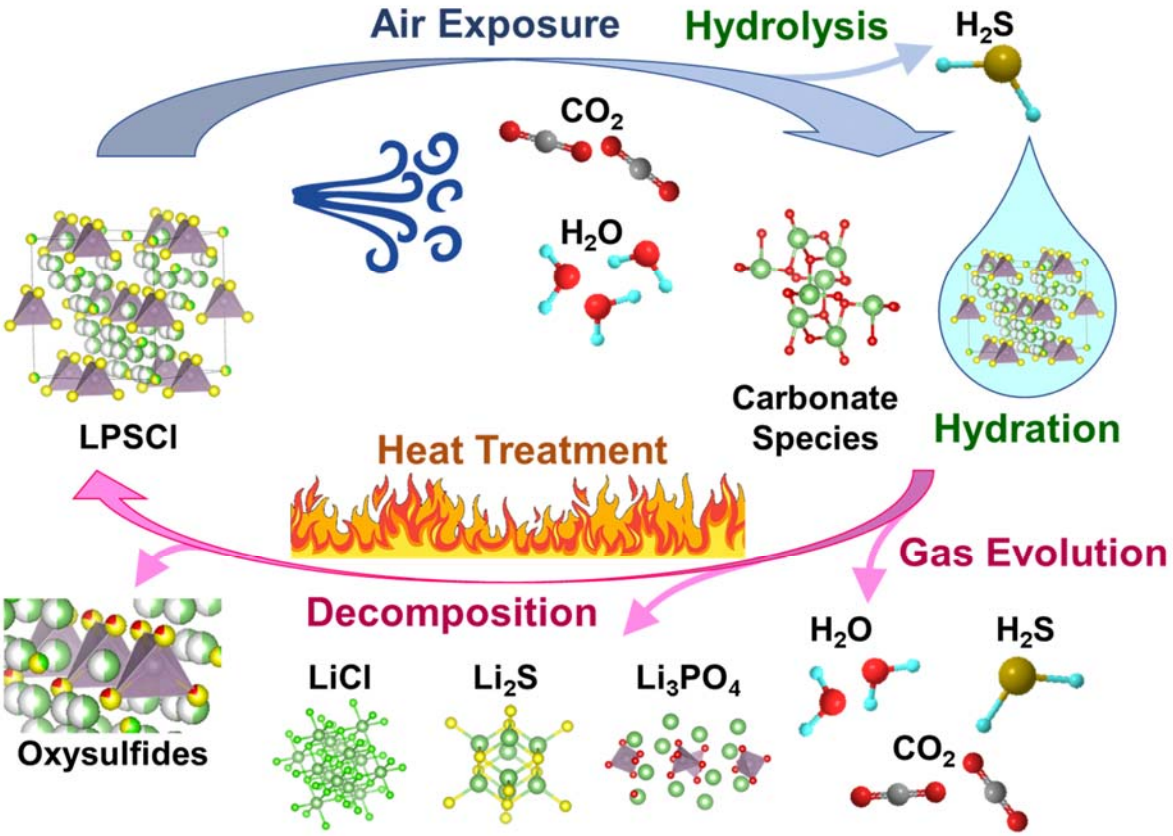

Figure 3.1. Schematic of the chemical reactions that occur when Li_6PS_5Cl is exposed to ambient air and during the subsequent heat treatment process.

3.2 Methods

3.2.1 Exposure and Heat Treatment of LPSCl

To prepare the air-exposed LPSCl sample (air-Exp), 300 mg of LPSCl (NEI) was evenly distributed in a 125 mL wide-mouth glass jar in an Ar-filled glovebox and then transferred to the antechamber with a total volume of 250 L. The chamber door was opened to expose the antechamber to ambient air (relative humidity between 45 to 55%) and closed after 1 minute of exposure. After 24 hours of exposure, the antechamber was vacuumed and purged with Ar, and the air-Exp sample was collected. The water-exposed LPSCl sample (water-Exp) was prepared by completely dissolving 1 g of LPSCl in 5 mL of water. The LPSCl aqueous solution was then vacuum dried at room temperature and the water-Exp sample was collected. 4 batches of 5 g

LPSCl were evenly sprayed on petri dishes and placed in a dry room with a dew point of −45°C for 1, 2, 3 and 24 hours to obtain the dry room exposed samples. The exposed LPSCl samples were heat treated at designated temperatures under vacuum. In summary, 300 mg of LPSCl was placed inside a quartz tube with one end located in a muffle furnace. The other end was connected to a vacuum pump to remove all gases generated during the heat treatment process.

3.2.2. Electrochemical Impedance Spectroscopy (EIS), DC Polarization, Cyclic Voltammetry (CV) and NCM811 Half Cells

To avoid any air exposure, all the electrochemical tests were conducted in an Ar-filled glovebox. 70 mg of LPSCl sample was placed in a 10 mm PEEK die (Figure 3.2) and pressed at 370 MPa using titanium plungers to obtain a pellet with a thickness of about 0.55 mm (measured with a Vernier caliper). Vapor-grown carbon fibers (VGCF) were then added to both sides of the pellet and the cell was pressed again at 370 Mpa. After assembly, the cell was tightened in a cell holder. EIS measurements were performed from 1 MHz to 1 Hz, with an applied AC potential of 30 mV, using a Solartron 1260 Impedance Analyzer, at room temperature. The acquired Nyquist plots were analyzed with Z-View software. DC polarizations were obtained by applying a 1 V bias potential for 300 s using the Solartron SI 1287 Potentiostat.

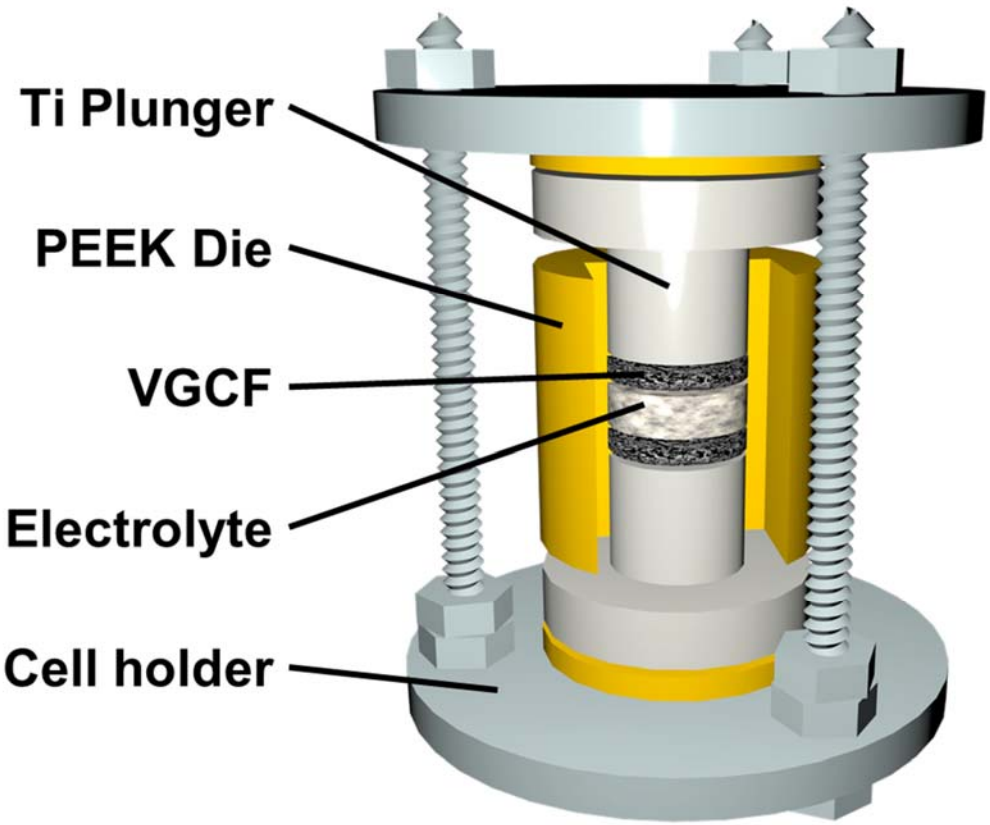

Figure 3.2. The design of an EIS cell used in this work.

To obtain the electrochemical windows for pristine, air-HT, and water-HT LPSCl samples, the powders were mixed with acetylene carbon at a weight ratio of 7:3 (LPSCl:C) using a Retsch Emax ball mill. LiIn alloy was prepared by mixing 30 mg of Li and 990 mg of In powder in a 20 mL sealed glass vial with a vortex mixer. LiIn alloy was used as both counter and reference electrode. Cyclic voltammetry was conducted using LPSCl-C | LPSCl | LiIn cells at a scan rate of 0.1 mV S^{-1} within 0 – 4.3 V voltage range vs Li. Three cycles were collected for each sample.

The $LiNi_{0.8}Co_{0.1}Mn_{0.1}O_2$ (NCM811, LG Chem) all-solid-state half-cell was constructed using 15 mg of NCM811 cathode composite, 70 mg of LPSCl samples, and 30 mg of LiIn alloy anode. NCM811 cathode composite was prepared by mixing NCM811, LPSCl samples, and vapor grown carbon fibers (Sigma-Aldrich) in a weight ratio of 66:31:3 in a mortar and pestle. The

electrolyte and electrolyte powders were pressed at 370 MPa in the experimental setup described above and cycled using Neware Battery cyclers (A211-BTS-1U-ZWJ). Pristine LPSCl was used in the reference cell. Another cell was fabricated using dry room exposed (24 hours) LPSCl (including solid-state electrolyte separator layer and the cathode composite) to evaluate its electrochemical performance. All cells were cycled at C/10 in the 1st cycle and C/3 in the following cycles at 30°C (1 C = 200 mAh g^{-1}).[25]

3.2.3. Characterization

X-ray diffraction (XRD) patterns of LPSCl samples were obtained by sealing the powders in 0.7 mm boron-rich glass capillaries in an Ar-filled glovebox. Measurements were taken using Cu Kα radiation (1.5406 Å) over a 2θ range of 10° to 65°, with a step size of 0.01°, using a Bruker/Nonius Microstar 592 diffractometer. Rietveld refinement was done using GSAS II software. Phase ratios and unit cells of Li_6PS_5Cl (ICSD 259200), Li_2S (ICSD 657596), LiCl (ICSD 26909) and Li_3PO_4 (ICSD 257440) were refined. Fourier transform infrared (FTIR) spectra with an attenuated total reflection (ATR) setup were measured with a Nicolet 6700 Fourier transform infrared spectrometer. Raman spectra were acquired with a Renishaw inVia upright microscope using 532 nm source. X-ray photoelectron spectroscopy was collected using The AXIS Supra XPS by Kratos Analytical. S 2*p* and P 2*p* spectra were collected and analyzed with CasaXPS software. A spin-orbit coupling energy of 1.18 eV was used in S 2*p* fitting and 0.86 eV was used in P 2*p* fitting. The peak area ratio of 2*p* 1/2 and 2*p* 3/2 was fixed to 1:2. A NETZSCH STA 449 F3 Jupiter Simultaneous Thermal Analyzer with Coupled QMS 403 D Aëolos Mass Spectrometer were used to obtain TGA/DSC-MS data (monitoring 18, 34 and 44 molecular weight – corresponding to H_2O, H_2S and CO_2). 15-20 mg of LPSCl samples were placed in an Al_2O_3 pans (6.8 mm in diameter / 85 µL). The samples were prepared within 2 mins to minimize the air exposure. All measurements were conducted in Ar atmosphere, scanning from 30°C to 600°C at a scan rate of 10°C min^{-1}.

Solid-state ^{31}P and ^{7}Li magic angle spinning (MAS) NMR experiments were conducted on a 400 MHz Bruker Neo spectrometer operating at 161.97 and 155.5 MHz for ^{31}P and ^{7}Li, respectively. All samples were handled within an Ar glovebox and subsequently loaded into 4mm pencil-type ZrO_2 rotors with o-ring caps to prevent contamination with ambient air and moisture during the NMR experiments. The samples were spun at 10 kHz and the ^{31}P experiments were collected using a 2.68 μs π/2 pulse (RF field strength ~93 kHz), a recycle delay of 15 s for pristine and dry room LPSCl and 600 s for exposed and heat-treated samples, and with high power proton decoupling using spinal64. $\{^{1}H\}$-^{31}P cross polarization measurement were collected while spinning at 5 and 1.5 kHz, using a ^{1}H π/2 pulse of 2.25 μs (RF field strength ~111 kHz) and contact times of 1 ms or variable contact times from 0.25 ms to 5 ms for generating the CP build-up curves. Hydroxyapatite was used as a standard for setting up the $\{^{1}H\}$-^{31}P cross polarization measurements. ^{31}P spin lattice relaxation was measured with a saturation recovery experiment. 2D ^{1}H-^{31}P HETCOR was acquired while spinning at 5 kHz, using a short contact time (50 μs) and with a 60 s recycle delay. 2D acquisition was acquired using 128 hypercomplex points in t_1 with a 34 μs increment. The indirect ^{1}H dimension was referenced to tetramethylsilane (TMS) by setting the hydroxyl resonance of hydroxylapatite to δ_H = 0.2 ppm.[26] The ^{31}P chemical shift was externally referenced with respect to 85% H_3PO_4 by using the isotropic chemical shift of hydroxylapatite (δ_{iso}= 2.65 ppm). ^{7}Li spectra were collected while spinning at 10 kHz using a hard pulse (10° tip angle of 0.36 μs, RF field strength ~ 77 kHz) to obtain semi-quantitative spectra and with a recycle delay of 2 s. ^{7}Li spin lattice relaxation was measured using an inversion recovery pulse sequence with a π/2 and π pulse length of 2.68 and 5.36 μs, respectively. The ^{7}Li chemical shifts were externally referenced to the isotropic chemical shift of 1M LiCl (aq) (δ_{iso}=0 ppm). Deconvolution of the ^{31}P spectra was carried out using the software dmfit.[27]

3.3 Results and Discussion

To evaluate the influence of air and moisture exposure over the ionic conductivity of LPSCl, electrochemical impedance spectroscopy (EIS) was conducted. The results are summarized in Figure 3.3a and the EIS results are presented in Figure 3.4 and Table 3.1.

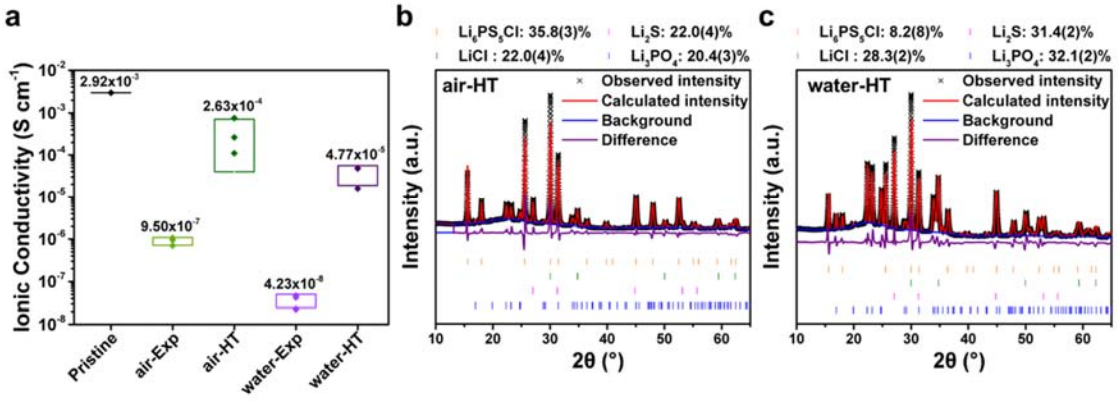

Figure 3.3. a) Ionic conductivity of the pristine, air, and water exposed LPSCl samples before and after heat treatment. All exposure and heat treatment conditions were conducted with three samples and median values are reported. Rietveld refinement results of the XRD patterns of b) the air exposed and heat-treated sample (air-HT) and c) the water exposed and heat-treated sample (water-HT). The molar phase ratios of all phases are labeled on top of the diffraction patterns.

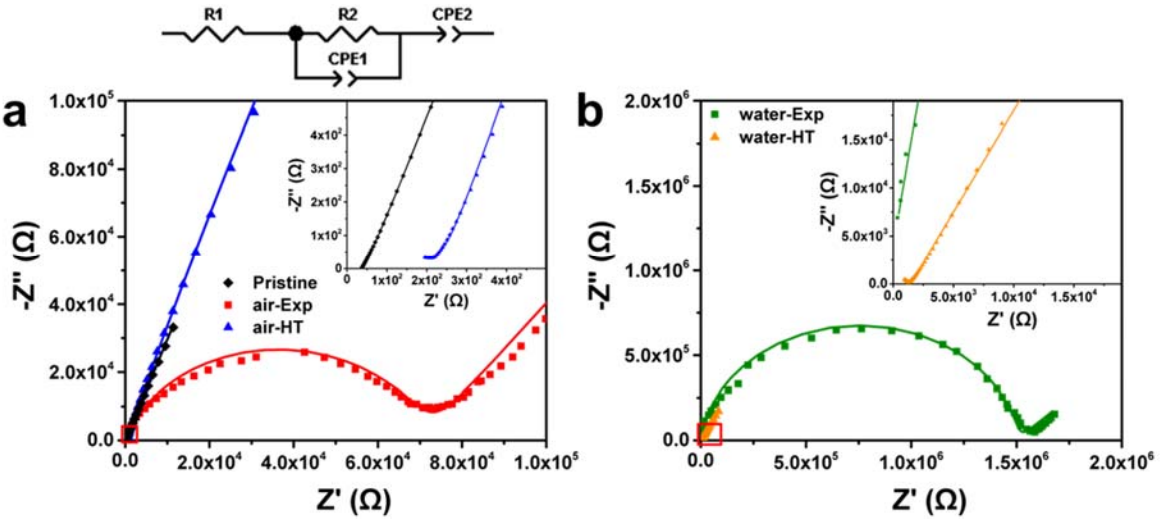

Figure 3.4. The Nyquist plots of a) pristine, air-Exp, air-HT, b) water-Exp and water-HT LPSCl samples.

Table 3.1. The EIS fitting results of pristine, air-EXP, air-HT, water-Exp and water-HT LPSCl samples.

Sample	$R_1 + R_2$	CPE_1-T	CPE_1-P	CPE_2-T	CPE_2-P
Pristine	2.86×10^{1}			6.85×10^{-8}	9.16×10^{-1}
air-Exp	7.10×10^{4}	1.46×10^{-9}	8.05×10^{-1}	1.59×10^{-6}	6.01×10^{-1}
air-HT	2.79×10^{2}	1.83×10^{-6}	1.98×10^{-1}	4.73×10^{-7}	8.25×10^{-1}
water-Exp	1.50×10^{6}	6.74×10^{-11}	9.29×10^{-1}	1.66×10^{-6}	5.04×10^{-1}
water-HT	1.45×10^{3}	5.45×10^{-10}	4.19×10^{-1}	1.43×10^{-6}	7.18×10^{-1}

The ionic conductivity of the air exposed sample dropped from 2.92×10^{-3} to 9.50×10^{-7} S cm^{-1}, suggesting that exposure to ambient air largely degrades LPSCl. When LPSCl is dissolved in water, the ionic conductivity dropped even further to 4.67×10^{-8} S cm^{-1}. Nevertheless, a heat treatment at 550°C was able to partially recover the ionic conductivity of both samples by approximately 3 orders of magnitude. DC polarization was conducted on all the samples and confirmed that the electronic conductivity did not increase following exposure and subsequent heat treatment (Figure 3.5). To investigate the origin of conductivity loss, XRD was conducted to probe the samples' phase compositions. After the exposure, the XRD patterns of both the air-Exp and water-Exp samples changed completely (Figure 3.6).

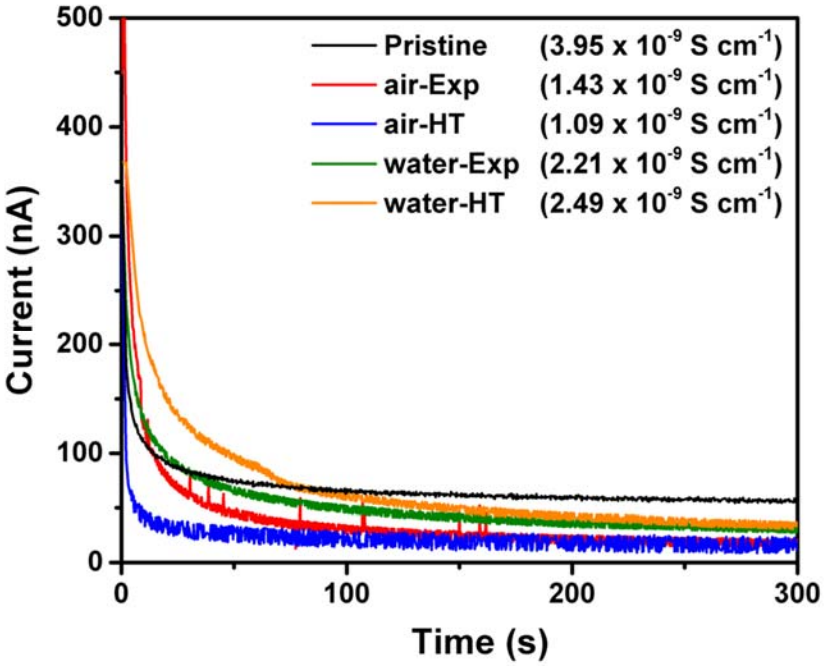

Figure 3.5. The DC polarization plots (applying 1 V bias) of the pristine, air, and water exposed LPSCl samples before and after heat treatment. Their electronic conductivities are of 10^{-9} S cm^{-1} order.

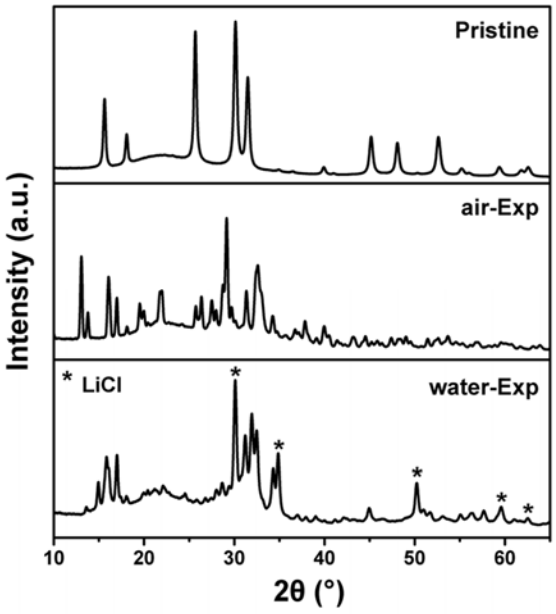

Figure 3.6. The XRD patterns of pristine, air and water exposed LPSCl samples.

LiCl can be observed in water-Exp sample, indicating decomposition of LPSCl when exposed to moisture. After the 550°C heat treatment, all the diffraction peaks in air-HT and water-HT samples can be attributed to four phases: LPSCl, LiCl, Li_2S, and Li_3PO_4.[28-31] Therefore, the diffraction patterns were refined and the results are shown in Figure 3.3b, 3.3c and Table 3.2.

Table 3.2. The Rietveld refinement results of phase ratios and unit cells of air-HT and water-HT.

air-HT		Unit Cell					
Phase	Phase ratio (%)	a (Å)	b (Å)	c (Å)	α (°)	β (°)	γ (°)
Li_6PS_5Cl	35.8(3)	9.8550(7)	9.8550(7)	9.8550(7)	90	90	90
Li_2S	22.0(4)	5.713(1)	5.713(1)	5.713(1)	90	90	90
LiCl	22.0(4)	5.1522(7)	5.1522(7)	5.1522(7)	90	90	90
Li_3PO_4	20.4(3)	6.119(2)	10.487(3)	4.3926(1)	90	90	90

water-HT		Unit Cell					
Phase	Phase ratio (%)	a (Å)	b (Å)	c (Å)	α (°)	β (°)	γ (°)
Li_6PS_5Cl	8.2(8)	9.8924(7)	9.8924(7)	9.8924(7)	90	90	90
Li_2S	31.4(2)	5.7252(4)	5.7252(4)	5.7252(4)	90	90	90
LiCl	28.3(2)	5.1690(3)	5.1690(3)	5.1690(3)	90	90	90
Li_3PO_4	32.1(2)	6.1374(6)	10.513(1)	4.9358(4)	90	90	90

Interestingly, the molar phase ratios of LiCl, Li_2S, and Li_3PO_4 in both samples are close to 1:1:1. Consequently, the net reaction after exposure and heat treatment can be described by the hydrolysis of LPSCl (equation 1):

$$Li_6PS_5Cl + 4\ H_2O \rightarrow LiCl + Li_2S + Li_3PO_4 + 4\ H_2S\uparrow \quad (1)$$

The hydrolysis of LPSCl will generate H_2S gas, resulting in permanent sulfur loss. Thus, LPSCl cannot be fully recovered after heat-treatment. The main difference between the air-HT and the water-HT samples is the amount of remaining LPSCl. Exposing LPSCl to a large excess of water will lead to more severe sulfur loss, and thus lower the LPSCl phase ratio after heat-treatment. As heat treated samples undergo partial decomposition, cyclic voltammetry (CV) was conducted to confirm whether the electrochemical windows changed (Figure 3.7). Both air-HT and water-HT exhibit similar oxidation (2.6 and 3.0 V) and reduction peaks (1.8 and 1.0 V) as pristine LPSCl. Nevertheless, the peak height decreases and can be related with the phase ratio of recovered LPSCl in each sample. Air-HT and water-HT samples also show new reduction (0.8 – 0 V) and oxidation (1.2 V) peaks. These may be attributed to decomposition products, as the peak height is again positively correlated to their phase ratios.

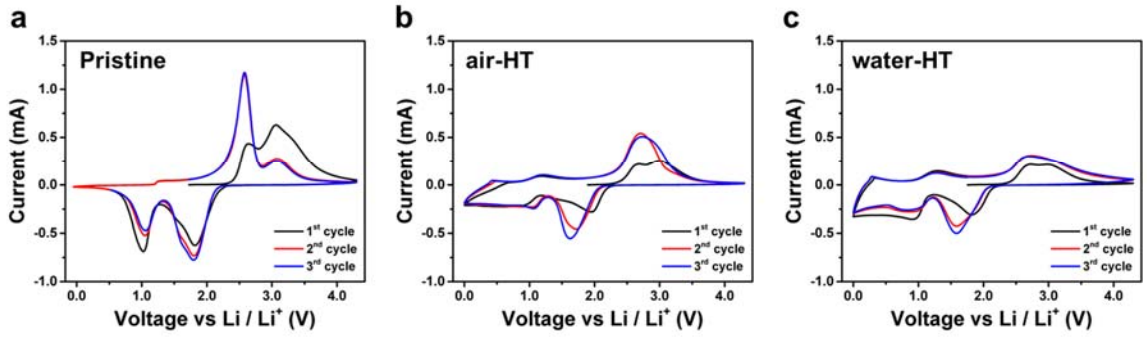

Figure 3.7. The cyclic voltammetry of a) pristine, b) air-HT, and c) water-HT LPSCl samples.

As XRD reflects only the bulk properties of crystalline materials, more characterization methods were subsequently conducted to probe the local chemical environment and nature of chemical bonding. Figure 3.8 presents the S 2*p* and P 2*p* region spectra obtained by X-ray photoelectron spectroscopy (XPS). Pristine LPSCl exhibits an S 2*p* signal at 161.7 eV and a P 2*p* signal at 132.0 eV.[23] Li_2S signal at 160.3 eV was observed in both the air and water exposed samples, confirming that LPSCl decomposes in the presence of moisture. The water-Exp sample also exhibits a minor signal at 163.5 eV, which can be attributed to elemental sulfur or bridging

sulfur atoms of Li_2S_n, resulting from the oxidation of S^{2-} during the exposure to water.[23, 32, 33] After the 550°C heat treatment, the amount of Li_2S increases and the SO_3^{2-} signal at 167.1 eV appears in both the air-HT and water-HT samples. Looking at the P 2*p* spectra, oxysulfides (PO_xS_y) at 133.0 eV form after exposure, and the intensity also increases after the heat treatment in both cases.[11] The P-O signal can be observed at 133.6 eV and 133.8 eV in the air-HT and water-HT samples, indicating the formation of Li_3PO_4.[34] The larger PS_4^{3-} peak area in air-HT than that of water-HT implies a larger degree of LPSCl recovery in air-HT sample. These are consistent with the previous XRD results.

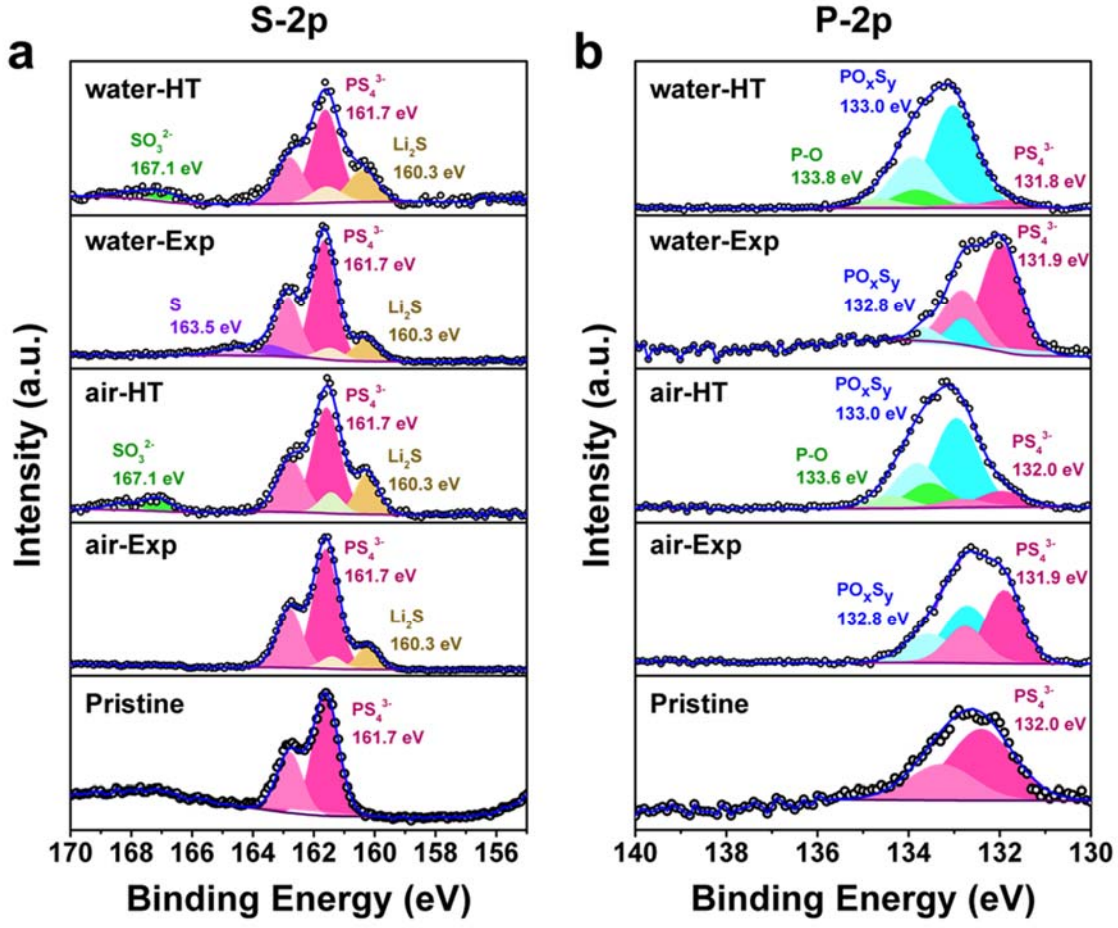

Figure 3.8. The a) S 2*p* and b) P 2*p* XPS of the pristine, air, and water exposed LPSCl samples before and after heat treatment.

The chemical bonds of exposed LPSCl were studied by both FTIR and Raman spectroscopy. The FTIR spectra (Figure 3.9a) show that both the air and water exposed samples exhibit evidence of hydration with a strong O-H stretching peak at 3000 to 3500 cm^{-1}. This indicates that LPSCl does not undergo a complete hydrolysis reaction when exposed to moisture. Asymmetric stretching (1427 cm^{-1}) and out-of-plane bending (864 cm^{-1}) of the carbonate anion were only observed in the air exposed sample, suggesting the formation of carbonate species due to a reaction with CO_2 when exposed to ambient air.[35] The carbonate signals were not observed in the water exposed sample, since LPSCl was not openly exposed to ambient air for a prolonged period of time in this case. As neither Li_2CO_3 nor $LiHCO_3$ is observed in the XRD pattern, the carbonate species may be amorphous or formed only on the surface and in low amounts.[36, 37] After the heat treatment, strong PO_4^{3-} asymmetric stretching peaks appear near 1030 cm^{-1}, in agreement with the Li_3PO_4 formation observed using XRD.[38] The pristine LPSCl shows strong PS_4^{3-} stretching near 425 cm^{-1} in Raman (Figure 3.9b).[39] After exposure to air, a strong peak at 218 cm^{-1} appears and this implies the formation of oxysulfides. The sample exposed to water shows only a minor peak shift, but the peak shape is significantly narrowed compared to that of pristine LPSCl. This indicates the possible formation of different major oxysulfide species from the air-exposed sample. After the heat treatment for both exposed samples, the PS_4^{3-} signal is partially recovered. Oxysulfides can still be observed, as they all exhibit a shoulder sitting around 220 cm^{-1}. However, as the Raman signals of PS_4^{3-} and oxysulfides are close to each other, other characterization methods are required to reveal the specific details on the structure of exposed LPSCl.

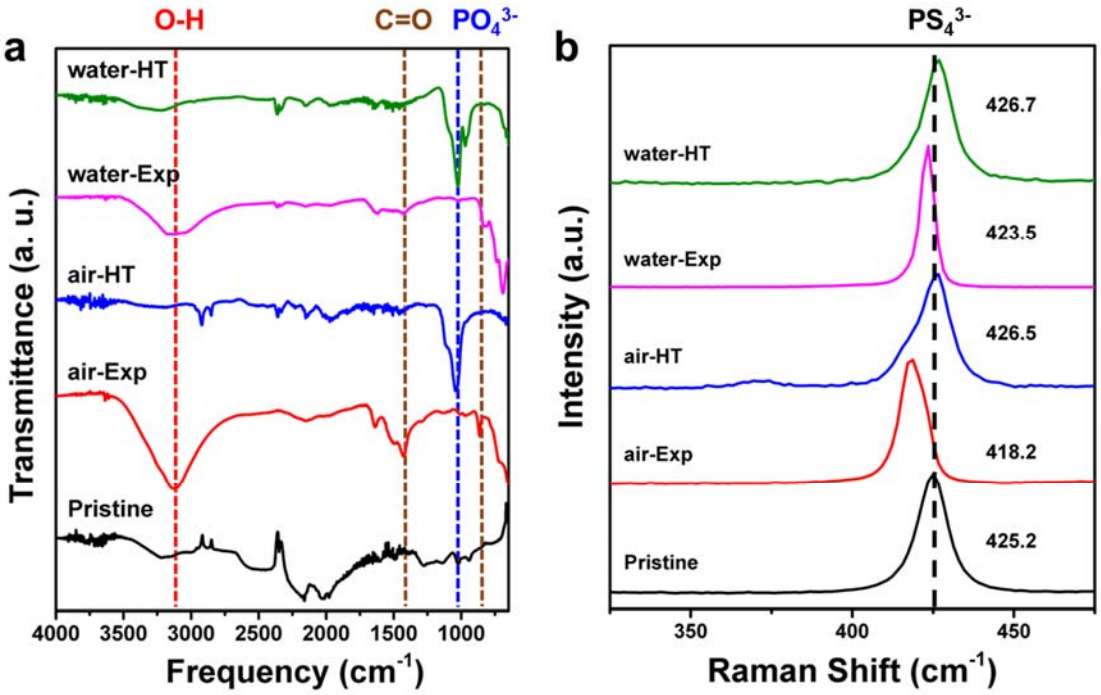

Figure 3.9. a) FTIR and b) Raman spectra of the pristine, exposed and heat-treated LPSCl samples. The main peaks of interested are represented by dashed lines on the FTIR spectra, while the Raman spectra only shows the PS_4^{3-} peak.

To provide more insights on the hydration structure of exposed LPSCl, ^{31}P NMR was conducted (Figure 3.10a). The pristine LPSCl exhibits broad peaks from ~ 85 - 81 ppm, as previously reported in literature [40-42] The peaks are assigned to PS_4^{3-} tetrahedra that are broadened by anion disorder from substitutional mixing of Cl and S atoms.[43] After either air or water exposure, the LPSCl peaks largely disappear and are replaced by two sharper peaks at 83.2 and 76.7 ppm, which are assigned to hydrated POS_3^{3-} and hydrated $PO_2S_2^{3-}$ tetrahedra, respectively. The mixed oxysulfide phosphorous tetrahedra ^{31}P chemical shift values agree with previous reports.[44] Both peaks are present in $\{^1H\}$-^{31}P cross polarization measurements, indicating the phosphorous tetrahedra are spatially close to protons and have moderate dipolar coupling (Figure 3.10b and 3.10c). The air and water exposure appears to create the same hydrated POS_3^{3-} and $PO_2S_2^{3-}$ tetrahedra, evident by the respective peaks having the same chemical shift

anisotropy values (Figure 3.10b and 3.10c) and identical cross-polarization buildup curves (Figure 3.11).

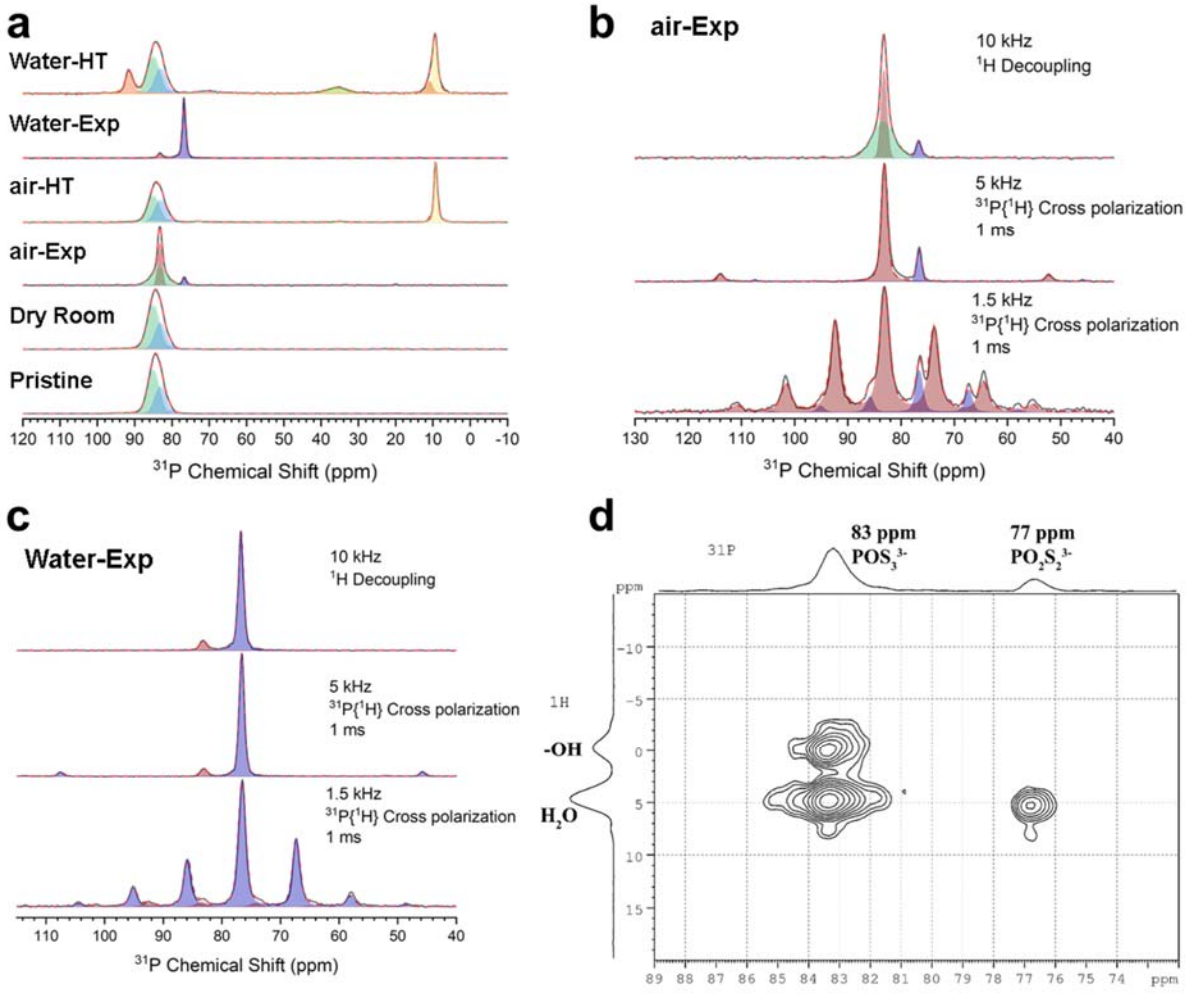

Figure 3.10. a) ^{31}P MAS NMR spectra of the pristine, dry room, exposed and heat-treated LPSCl samples. Comparison of ^{31}P spectra with ^{1}H decoupling (top) to ^{31}P{^{1}H} cross polarization spectra of b) air-Exp and c) water-Exp samples at spinning speeds of 5 (middle) and 1.5 kHz (bottom). Sideband analysis was conducted at both spinning speeds of the CP measurement to determine the chemical shift anisotropy (CSA) of the two hydrated oxysulfide phases, δ_{iso}=76.8 ppm, $\Delta\delta$ = 30.3 ppm, η = 0.63 (δ_{11}=97 ppm, δ_{22}= 73.0 ppm, δ_{33}= 60.3 ppm) and δ_{iso}=83.5 ppm, $\Delta\delta$ = -34.3 ppm, η = 0.94 (δ_{11}=105.7 ppm, δ_{22}= 84.2 ppm, δ_{33}= 60.6 ppm). The CSA is defined with the Haeberlen convention where the principal components are ordered by $|\delta_{zz} - \delta_{iso}| \geq |\delta_{xx} - \delta_{iso}| \geq |\delta_{yy} - \delta_{iso}|$, and where $\delta_{iso} = \frac{1}{3}(\delta_{xx} + \delta_{yy} + \delta_{zz})$; $\Delta\delta = \delta_{zz} - (\delta_{xx} + \delta_{yy})/2$; $\eta = \frac{\delta_{yy} - \delta_{xx}}{\delta_{zz} - \delta_{iso}}$. The CSA is also provided in the standard convention within parenthesis where the principal components are defined by $\delta_{11} \geq \delta_{22} \geq \delta_{33}$. d) ^{1}H-^{31}P HETCOR NMR contour plot showing ^{1}H-^{31}P correlations through dipolar coupling of the air exposed sample. The HETCOR measurement reveals the oxysulfide phosphorous tetrahedra are spatially close to water and hydroxyl groups.

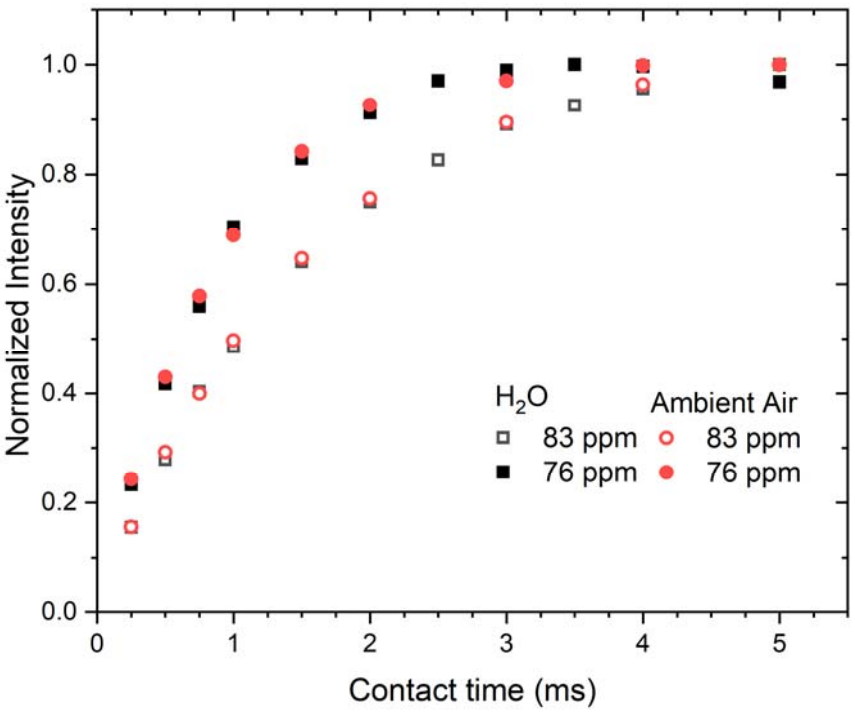

Figure 3.11. $\{^{1}H\}$-^{31}P cross polarization build-up curves from variable contact time measurements. The signal is normalized to highest intensity of each peak. The 83 and 76 ppm peaks have identical CP kinetics across the two samples indicating they are the same phases.

After air exposure, close to 60% of the original LPSCl remains while most degradation produces the hydrated POS_3^{3-} tetrahedra and a minor amount of hydrated $PO_2S_2^{3-}$ tetrahedra (Table 3.3). The LPSCl phase may become disordered after air exposure and thus is not observed in the XRD pattern (Figure 3.6).

Table 3.3. NMR fitting results for pristine and exposed LPSCl.

^{31}P Site	δ_{iso} (ppm)	δ_{width} (ppm)	%	Total Recovered Li_6PS_5Cl (%)	^{31}P SLR T_1 (s)	^{7}Li SLR T_1 (s)
Pristine Li_6PS_5Cl						
Li_6PS_5Cl PS_4^{3-}	85.01	3.66	59			
Li_6PS_5Cl PS_4^{3-}	83.13	3.53	35		4.0	0.16
Li_6PS_5Cl PS_4^{3-}	80.39	1.85	2			
Li_3PS_4	89.08	12	4		-	
Dry Room Li_6PS_5Cl						
Li_6PS_5Cl PS_4^{3-}	85.03	3.88	60			
Li_6PS_5Cl PS_4^{3-}	83.12	3.55	33		3.4	0.19
Li_6PS_5Cl PS_4^{3-}	80.43	1.85	2			
Li_3PS_4	87.94	11.96	5		-	
Ambient Air						
LPSCl PS_4^{3-}	83.42	5.02	57		3.8	0.18
Hydrated POS_3^{3-}	83.27	1.34	36		386	9
Hydrated $PO_2S_2^{3-}$	76.71	1.32	7		534	(LiCl) 11.7
Ambient Air 550°C						
Li_6PS_5Cl PS_4^{3-}	85.03	3.88	37			
Li_6PS_5Cl PS_4^{3-}	83.12	3.55	28.6	67.4	2.9	0.13
Li_6PS_5Cl PS_4^{3-}	80.43	1.85	1.8			
$PO_2S_2^{3-}$	73.11	3.07	1		-	8.7
PO_3S^{3-}	35.06	2.65	0.6		-	6.9
Li_3PO_4	9.3	1.1	31		765.3	(LiCl) 26.5
H_2O						
Hydrated POS_3^{3-}	83.2	1.48	8		742	(LiCl) 25.5
Hydrated $PO_2S_2^{3-}$	76.78	1.06	92		992	
H_2O 550°C						
Li_6PS_5Cl PS_4^{3-}	85.03	3.88	29			
Li_6PS_5Cl PS_4^{3-}	83.12	3.55	17	47	3.1	0.15
Li_6PS_5Cl PS_4^{3-}	80.46	1.9	1			
$P_2S_7^{4-}$	91.47	2.45	13		346.6	
$PO_2S_2^{3-}$	70.67	9.17	4		324.5	
PO_3S^{3-}	35.74	6.53	8		433.4	
PO_4^{3-}	11.03	1.96	6		398.6	
Li_3PO_4	9.47	1.68	22		447.7	(LiCl) 25.7

The hydrated and mixed anion $PO_xS_y^{3-}$ tetrahedra are marked by very long spin-lattice relaxation times (T_1) on the order of 100's of seconds, whereas LPSCl has a T_1 of about ~4 s. This extreme difference of T_1 values can be used as a spectral filter by saturating the signal of the slow relaxing hydrated phases by using a short recycle delay (~15 s) during acquisition. The relaxation filter removes the signal from non-conducting phases and leaves the signal of the fast Li ion conductor LPSCl, demonstrating LPSCl remains after air exposure (Figure 3.12).

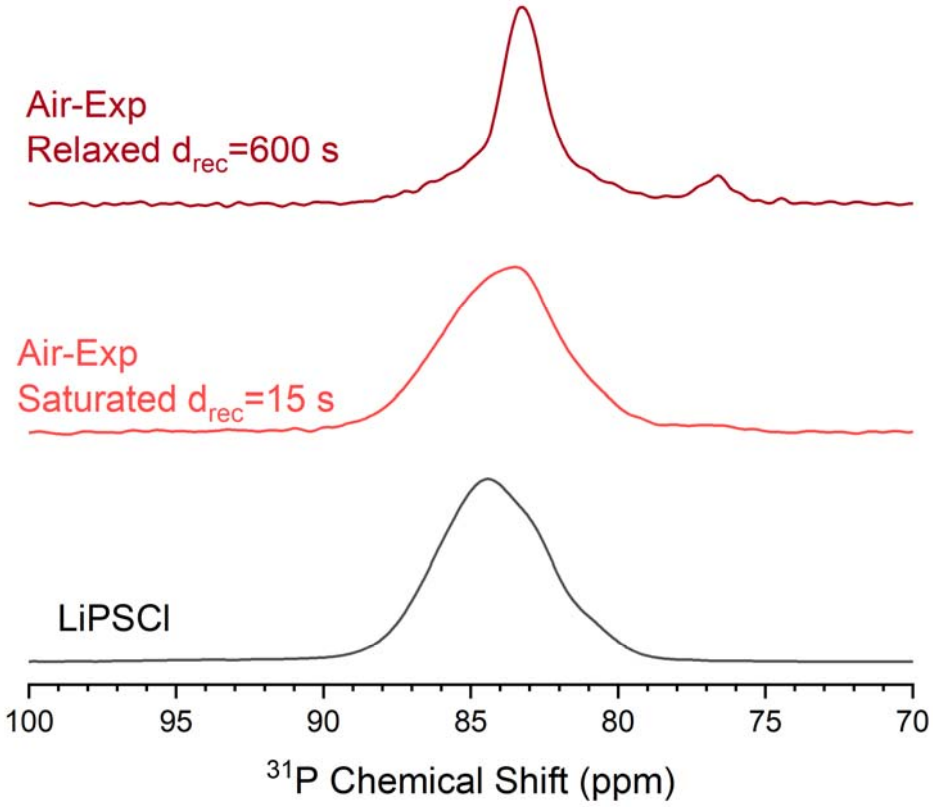

Figure 3.12. ^{31}P spectra of pristine LPSCl (bottom) and air exposed LPSCl collected with a short recycle delay (middle), and long recycle delay (top). Using a short recycle delay saturates the signal of the slowly relaxing phases and makes the signal of the LPSCl clearly observable.

Further information about the state of hydration of the hydrated POS_3^{3-} and $PO_2S_2^{3-}$ phases can be obtained by ^{1}H-^{31}P heteronuclear correlation (HETCOR) measurements (Figure 3.10d). Both phases are spatially close to water molecules (^{1}H δ ~ 4.9 ppm) and the hydrated POS_3^{3-} tetrahedra are also close to -OH groups (^{1}H δ ~ 0 ppm). The difference in neighboring water and

hydroxyl groups between the phases suggests some degree of microstructural heterogeneity caused by regions of more rapid degradation. Contrast to air exposure where some LPSCl remains, exposure to water eliminates the LPSCl signal from the ^{31}P spectra indicating the LPSCl is completely degraded, in agreement with XRD results and the dramatically lowered ionic conductivity. Water exposure converts most of the sample to the hydrated $PO_2S_2^{3-}$ phase with a minor amount of the hydrated POS_3^{3-} phase. After heat treatment, about 67% of LPSCl is reformed in the air exposed sample while only 47% is recovered for the water exposed (Table 3.2). The result is close to the phase ratios of LPSCl : Li_3PO_4 (^{31}P NMR only detects P containing phases) obtained from XRD results (64% for the air exposed sample and 20% for the water exposed sample). The T_1 values for the reformed LPSCl after heat treatment are comparable to the pristine LPSCl, in agreement with the similar recovery observed for the ionic conductivity. The sulfur loss from exposure to moisture/water produces the oxysulfide phosphorous tetrahedra which then largely disassociate into PO_4^{3-} and PS_4^{3-} tetrahedra after heat treatment with only minute amounts of oxysulfide tetrahedra ($PO_2S_2^{3-}$ and PO_3S^{3-}) remaining (Table 3.2). A significant amount of Li_3PO_4 (δ_{iso} = 9.3 ppm[45, 46]) is formed after heat treatment from both air and water exposed samples, in agreement with XRD and FTIR results. Due to the extreme sulfur loss in the water exposed sample, more sulfur deficient phases are formed (Figure 3.13) like $P_2S_7^{4-}$ (δ_{iso} =91.5 ppm), PSO_3^{3-} (δ_{iso} =35 ppm) and another PO_4^{3-} phase (δ_{iso} =11 ppm).[44, 47] This other PO_4^{3-} phase has a slightly higher chemical shift than Li_3PO_4, suggesting it may have a higher coordination to S atoms within its second nearest neighbor shell. As such this resonance could arise from PO_4^{3-} tetrahedra embedded within sulfur rich regions and further speaks to the microstructural heterogeneity. $\{^1H\}$-^{31}P cross polarization was attempted on the heat-treated samples but did not produce appreciable signal, indicating the samples have been completely dehydrated.

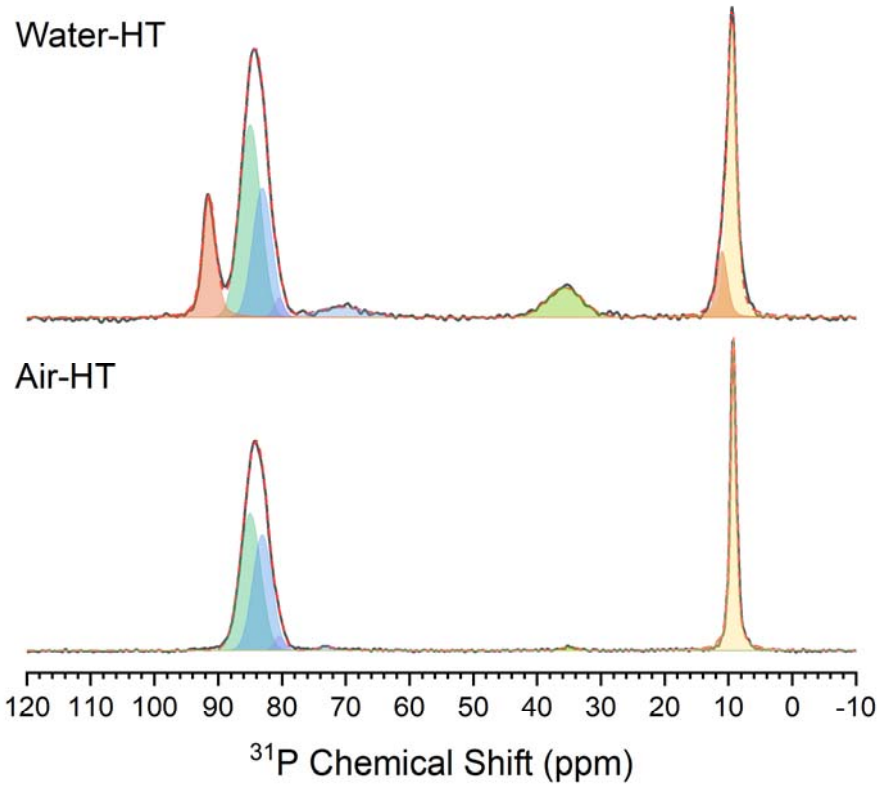

Figure 3.13. Closer view of the ^{31}P spectra of the heat-treated samples to more clearly show the minor oxysulfide phases still present.

^{7}Li NMR was also performed to track the decomposition from the perspective of Li ions. Unfortunately, ^{7}Li spectra are less elucidating chemically relative to ^{31}P NMR because of strong homonuclear dipolar coupling considerably broadens the signal, ^{7}Li has a narrow chemical shift range, and the rapid motion of Li ions over many crystallographically distinct sites in LPSCl causes chemical exchange meaning only the average chemical shift to be resolvable. Despite these limitations, some important insights are still available from ^{7}Li NMR such as being able to track the formation of LiCl. The ^{7}Li spectra (Figure 3.14) of pristine LPSCl is a very narrow peak centered around 1.52 ppm, in agreement with previous reports.[42]

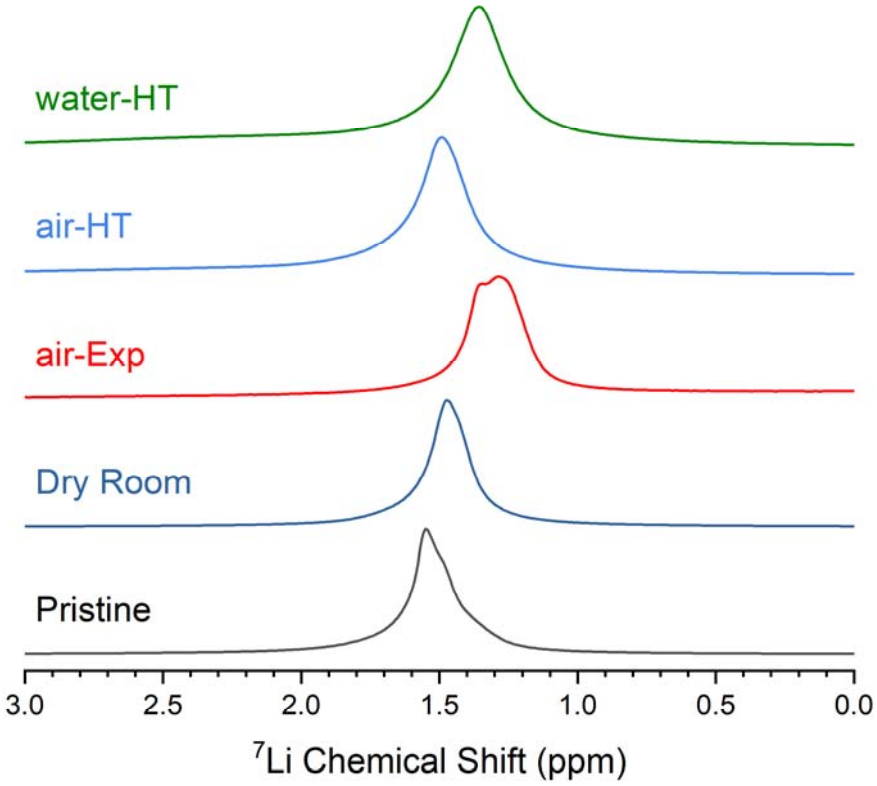

Figure 3.14. ^{7}Li spectra focused on the chemical shift range around LPSCl. The water exposed sample is omitted because it lacks a LPSCl signal and its breadth is beyond the axis scale.

Because of the rapid Li ion motion, the Li ion experiences many chemical environments within the NMR experimental timeframe thus only one or two peaks are observable. However, the location of the narrowed peaks still provides insight to the local Li chemical environments. After air exposure the peak shifts to ~1.3 ppm and another peak arises at 1.24 ppm indicating there are two separate regions of rapid Li conduction. After heat treatment of the air exposed sample the narrow peak shifts back to 1.49 ppm, very close to the pristine LPSCl peak. The slightly lower frequency indicates the Li ions are moving through sites with slightly less sulfur. This can also explain the more dramatic lower frequency shift (peak at 1.36 ppm) in the heat-treated water exposed sample that has higher sulfur loss. Beyond the subtle changes in the fast Li ion

conducting peaks, the formation of decomposition products like LiCl and Li_2S are more obvious (Figure 3.15).

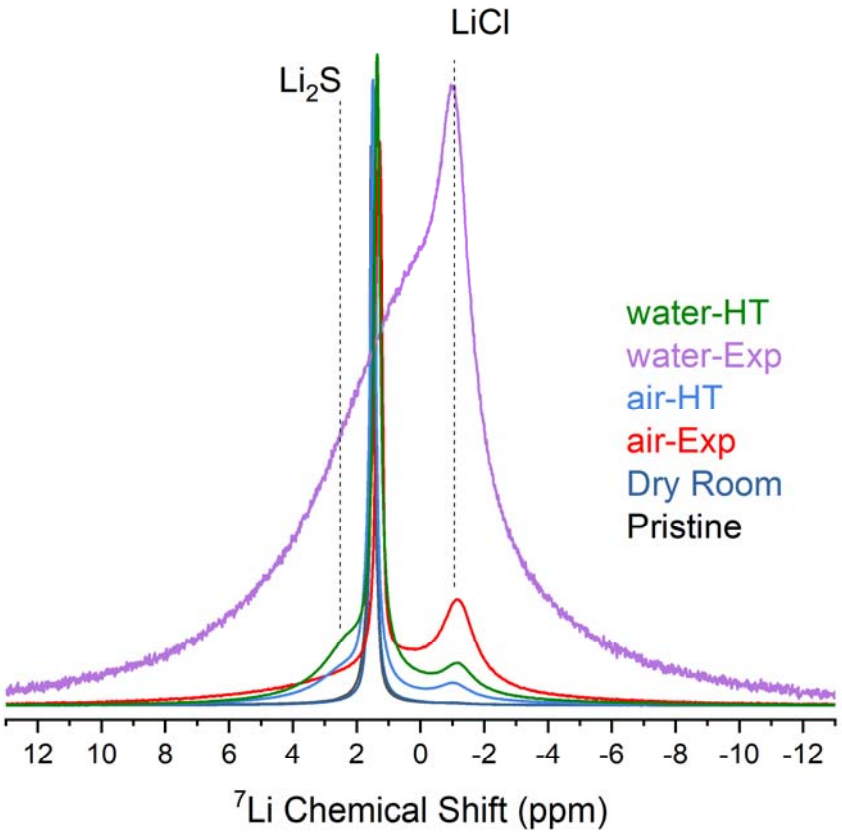

Figure 3.15. An overlay plot of all ^{7}Li spectra to show the progressive increase of LiCl and Li_2S after exposure and heat-treatment.

After exposure, a broad peak at −1.1 ppm corresponding to LiCl becomes prominent. As evident from ^{31}P NMR, water exposure eliminates the sharp peak LiPSCl signal leaving the LiCl peak and a very broad peak at 0.68 ppm that is likely immobile Li within the hydrated oxysulfide phosphorous phases. ^{7}Li within phosphorous oxide environments have chemical shifts between 1 to 0.14 ppm, so a slight shielding indicates the presence of more oxygen in the Li coordination sphere.[45, 46] After heat treatment, along with the reformation of LPSCl, the LiCl peak remains along with a prominent shoulder at 2 ppm that is assigned to Li_2S.[48] The signal for Li_3PO_4 is not

resolvable but is likely contributing to the additional broadening of the peaks between 1 – 0 ppm. ^{7}Li spin-lattice relaxation times were measured on all the samples and found largely similar results as obtained by ^{31}P SLR measurements (Table 3.2). The ^{7}Li T_1 of LPSCl is on the order of 100-200 ms while oxysulfide and Li_2S phases have T_1 values around 9 s and LiCl has a T_1 of ~26 s.

As both IR and NMR spectroscopy indicate that LPSCl becomes hydrated, it is worth investigating the dehydration process during the heat treatment. Therefore, a combination of TGA, DSC, and MS were conducted to monitor the decomposition processes and gas evolution of H_2O, H_2S, and CO_2 during heating. Figure 3.16 presents the TGA / DSC – MS of a pristine LPSCl sample. Little to no mass loss, endothermic, or exothermic reactions were observed in TG and DSC curves, indicating that the material is stable throughout the whole temperature range of the experiment. Nevertheless, the minor gas evolution observed can be explained by the short exposure to air during sample transfer to the instrument. As such, the pristine sample is used as the baseline when comparing the results of the air exposed samples.

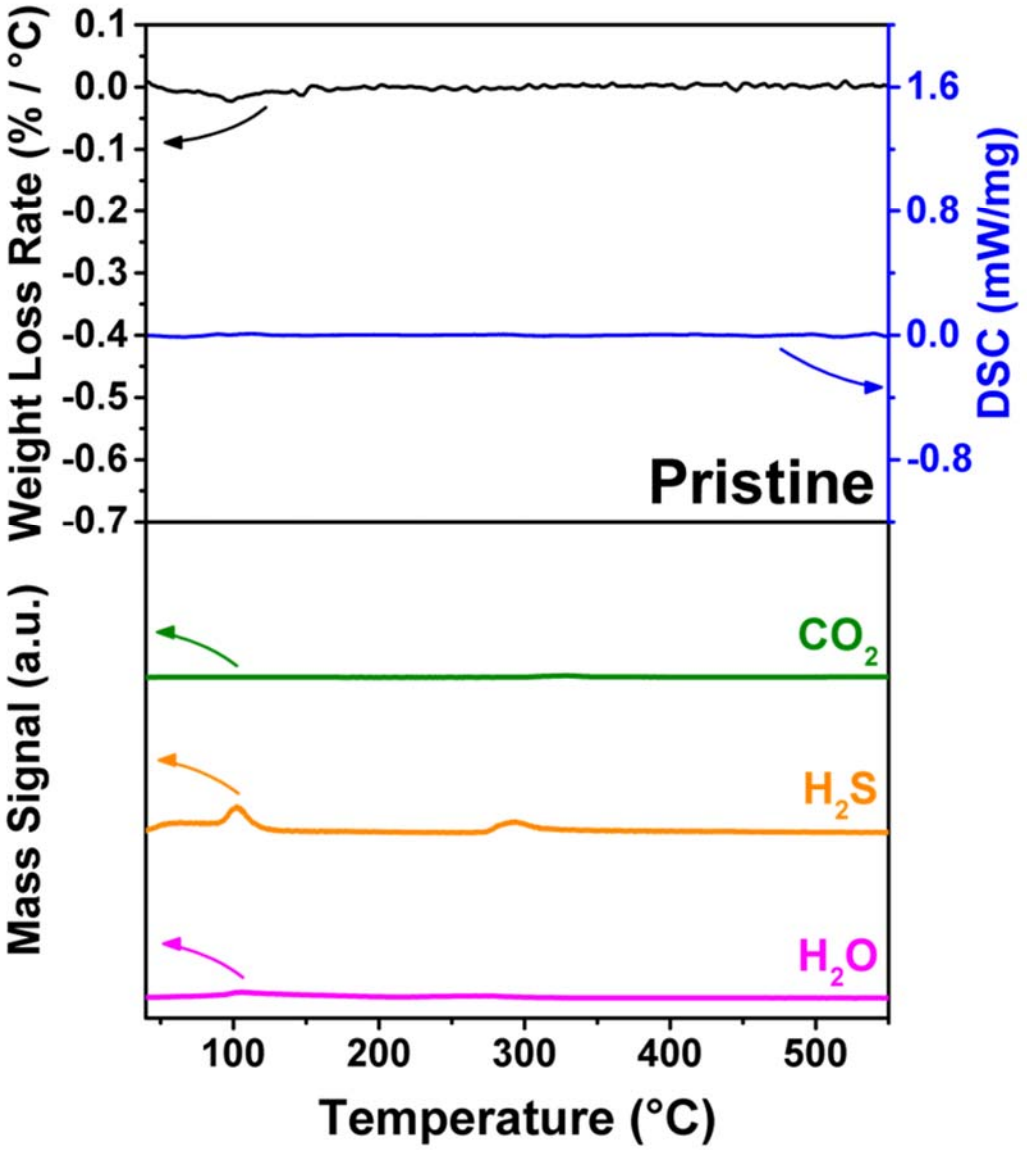

Figure 3.16. The TGA / DSC – MS of pristine LPSCl. No obvious mass loss and DSC signal were observed. Due to short exposure to air during the sample preparation, there are slight H_2S and H_2O evolution.

After the exposure, both the air (Figure 3.17a) and water exposed (Figure 3.18) samples exhibited significant mass loss in the TG curves and each of these mass losses is accompanied by gas evolution and endothermic or exothermic reactions. On the DSC curve, the reactions for both samples were located near 140, 300, and 430°C, with the main mass loss and gas evolution

occurring at around 140°C. Both H_2O and H_2S evolution were observed and thus both dehydration and hydrolysis (reaction between LPSCl and hydrated water at elevated temperature, generating H_2S) reactions take place at this temperature. As the DSC curve indicates an overall endothermic result, the dehydration process is dominating over the hydrolysis (dehydration reactions are endothermic, while hydrolysis reactions are exothermic). The shapes of the curves are different for the air and water exposed samples, consistent with the different major hydrated species detected in the two samples, as shown in the ^{31}P NMR results. At 296°C, both samples exhibit an exothermic peak accompanied with H_2O and H_2S evolution. This indicates that the hydrolysis reaction dominates at this temperature. There is an extra exothermic reaction at 332°C (accompanied with CO_2 evolution) in the air exposed sample, suggesting that a carbonate species decomposes at this temperature. This reaction was not observed in the water exposed sample, as no carbonates formed under these conditions. This is consistent with the FTIR results presented in Figure 3.9a. For both samples, no gas evolution was detected after 350°C, suggesting the complete removal of H_2O and CO_2. One endothermic reaction occurs around 430°C. As there is no mass loss and gas evolution associated with this reaction, this is purely a phase transformation reaction and it requires further characterization.

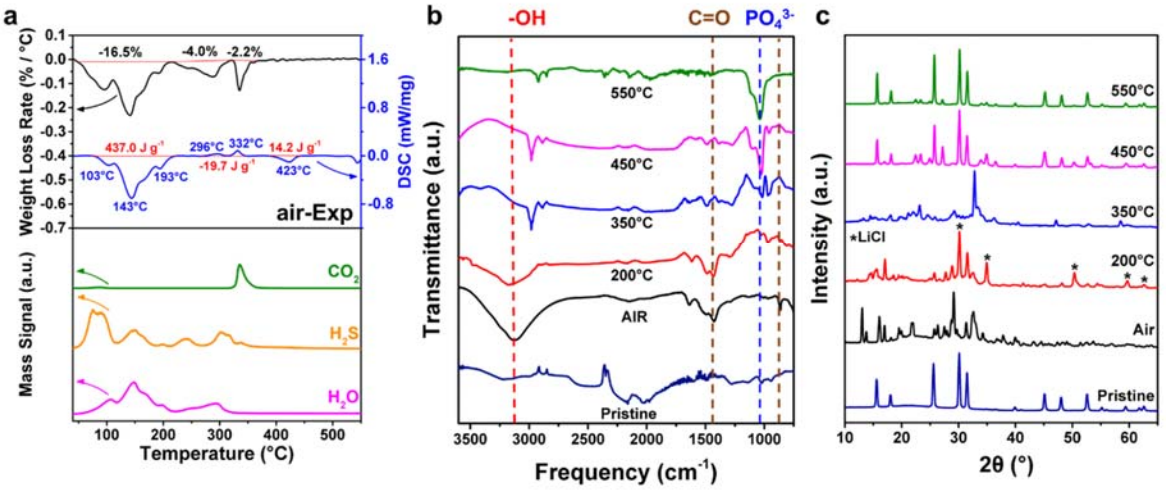

Figure 3.17. a) Coupled TGA / DSC and mass spectrometry measurements of the air exposed sample (air-Exp). b) FTIR spectra and c) XRD pattern of the air-Exp sample heat treated at different temperatures.

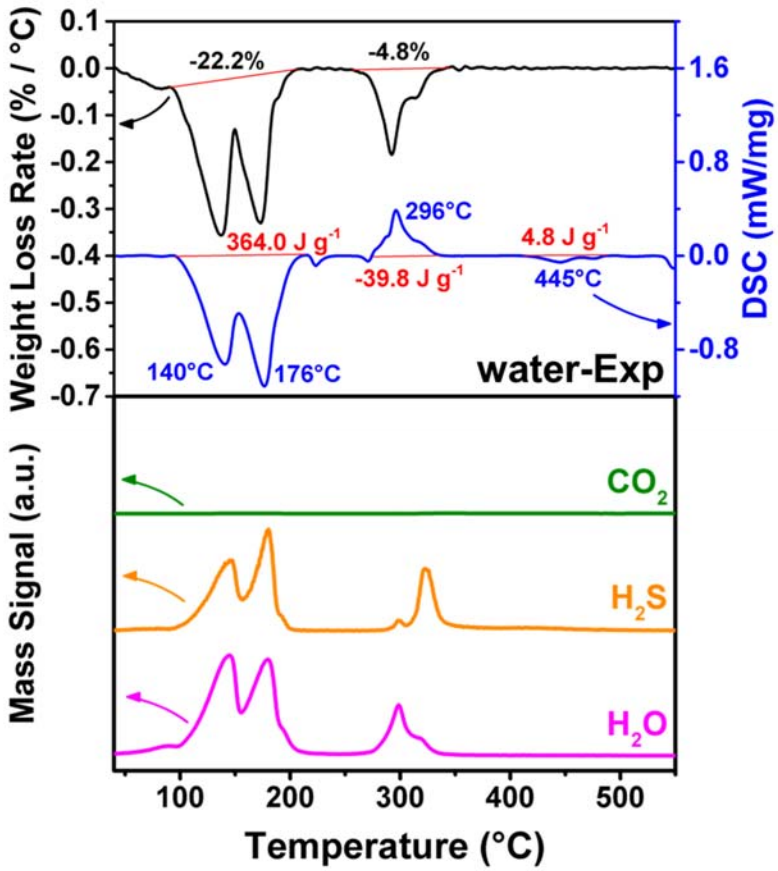

Figure 3.18. The TGA / DSC – MS of water-exposed LPSCl (water-Exp).

To confirm the reactions during the heating process, the air exposed sample was heat treated at selected temperatures: 200, 350, and 450°C, chosen according to the TGA / DSC results (Figure 3.19a). FTIR (Figure 3.17b), XRD (Figure 3.17c), and EIS (Figure 3.19b-d, Table 3.4-3.5) were conducted after heat treatment. When heated to 200 °C, OH stretching and CO_3^{2-} vibrations still appear on the FTIR spectra, but these signals disappear after heating above 350 °C. After heating to 450 °C, the PO_4^{3-} stretching signal was observed, indicating the formation of Li_3PO_4 at this temperature. Moreover, the XRD data also indicates the reformation of LPSCl at this temperature, as the diffraction pattern is similar to that of the air exposed sample heated to 550°C (air-HT). The EIS measurements also show that the ionic conductivity increased by 3 orders of magnitude after the heat treatment at 450°C. Both results imply that the reformation of LPSCl occurs at approximately 430°C.

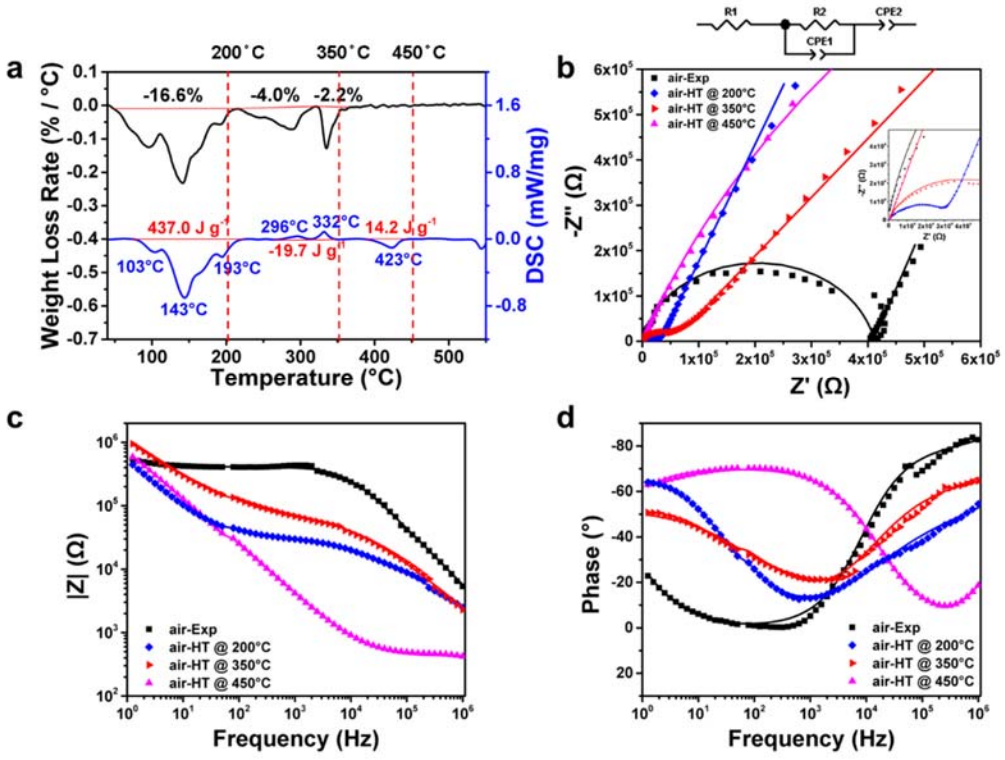

Figure 3.19. According to a) TGA / DSC – Mass result, AIR was heat treated at lower temperatures: 200, 350 and 450°C for 8 hours and the b) Cole-Cole plot, c) magnitude and d) phase of Bode plots of air-Exp sample heat treated at all temperature were measured.

Table 3.4. The EIS fitting results of air-EXP and air-HT samples heat treated at 200, 350 and 450°C.

Sample	$R_1 + R_2$	CPE_1-T	CPE_1-P	CPE_2-T	CPE_2-P
air-Exp	7.10×10^{4}	1.46×10^{-9}	8.05×10^{-1}	1.59×10^{-6}	6.01×10^{-1}
air-HT @ 200°C	3.23×10^{4}	4.70×10^{-8}	5.68×10^{-1}	4.03×10^{-7}	7.65×10^{-1}
air-HT @ 350°C	5.52×10^{4}	5.76×10^{-9}	7.17×10^{-1}	2.95×10^{-7}	5.82×10^{-1}
air-HT @ 450°C	4.39×10^{2}	5.76×10^{-11}	7.28×10^{-1}	2.51×10^{-7}	7.87×10^{-1}

Table 3.5. A summary of ionic conductivity of air-HT heat-treated at 200, 350 and 450°C.

Ionic Conductivity (S cm^{-1})	
Pristine	2.90×10^{-3}
air-Exp	1.72×10^{-7}
200°C	2.17×10^{-6}
350°C	1.26×10^{-6}
450°C	1.59×10^{-4}

The wide array of characterization results show that LPSCl is most significantly affected by moisture exposure. As such, LPSCl may show improved stability if the humidity of the atmosphere is controlled. To prove this hypothesis, LPSCl was exposed to air in a dry room with a dew point of −45°C for 1, 2, 3, and 24 hours. Figure 3.20a shows the ionic conductivity as a function of the exposure time, the corresponding Nyquist plots and fit values are presented in Figure 3.21a and Table 3.6. The electrolyte conductivity decreased linearly during the first 3 hours of exposure, but maintained a value of 2.33×10^{-3} S cm^{-1} after 24 hours of exposure, which is 3 orders of magnitude higher than air-Exp sample. The ionic conductivity of dry room exposed LPSCl can be partially recovered to 2.77×10^{-7} S cm^{-1} after a heat treatment at 550°C for 8 hours. As shown in Figure 3.21b, the electronic conductivity of LPSCl did not increase after dry room exposure.

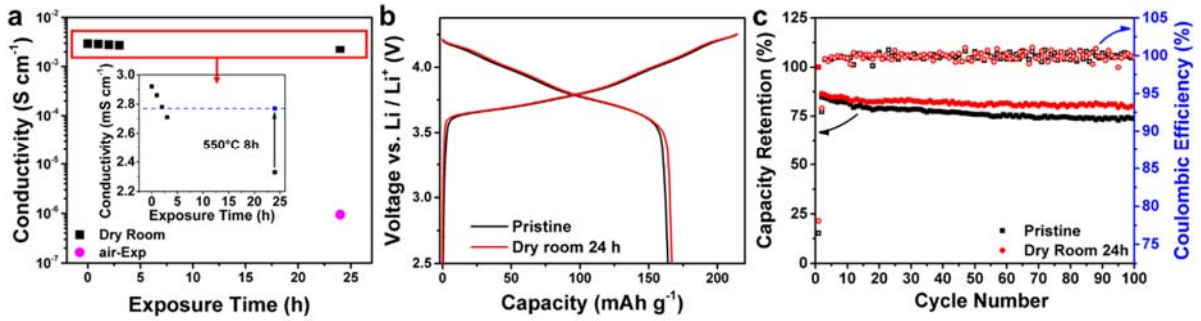

Figure 3.20. a) Ionic conductivity of pristine LPSCl, LPSCl samples exposed in a dry room for 1, 2, 3, 24 hours, a heat-treated sample following 24 hours of dry room exposure, and air-exposed LPSCl. b) 1st cycle voltage profiles, c) capacity retention and Coulombic efficiency of NCM811 | LPSCl | LiIn cells assembled using pristine or 24h dry room exposed LPSCl electrolytes.

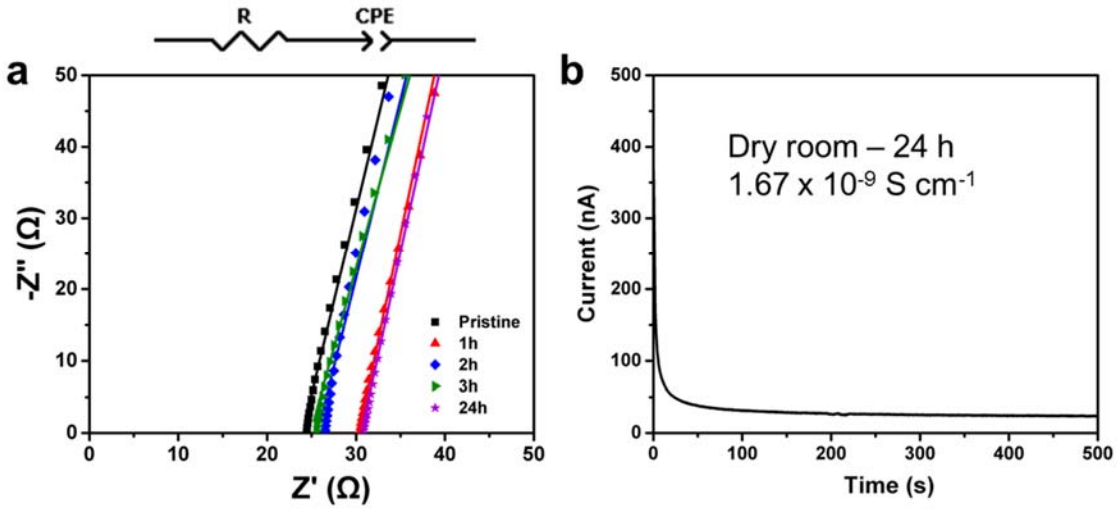

Figure 3.21. a) The Nyquist plots of LPSCl exposed in a dry room for 1, 2, 3 and 24 hours. b) the DC polarization of LPSCl exposed in a dry room for 24 hours. No significant increase in electronic conductivity was observed.

Table 3.6. The EIS fitting results of LPSCl samples exposed in a dry room for 1, 2, 3 and 24 hours.

Sample	R	CPE-T	CPE-P
Pristine	2.86×10^{1}	6.85×10^{-8}	9.16×10^{-1}
1 hour	3.03×10^{1}	2.01×10^{-6}	8.93×10^{-1}
2 hours	2.57×10^{1}	2.00×10^{-6}	8.74×10^{-1}
3 hours	2.49×10^{1}	3.20×10^{-6}	8.60×10^{-1}
24 hours	3.06×10^{1}	2.20×10^{-6}	8.90×10^{-1}

XRD (Figure 3.22), Raman (Figure 3.23), ^{31}P NMR (Figure 3.10a) and ^{7}Li NMR (Figure 3.14) show no large-scale decomposition happened to the material during exposure in the dry room environment even after 24 hours, as these data are very similar to those of the pristine LPSCl sample.

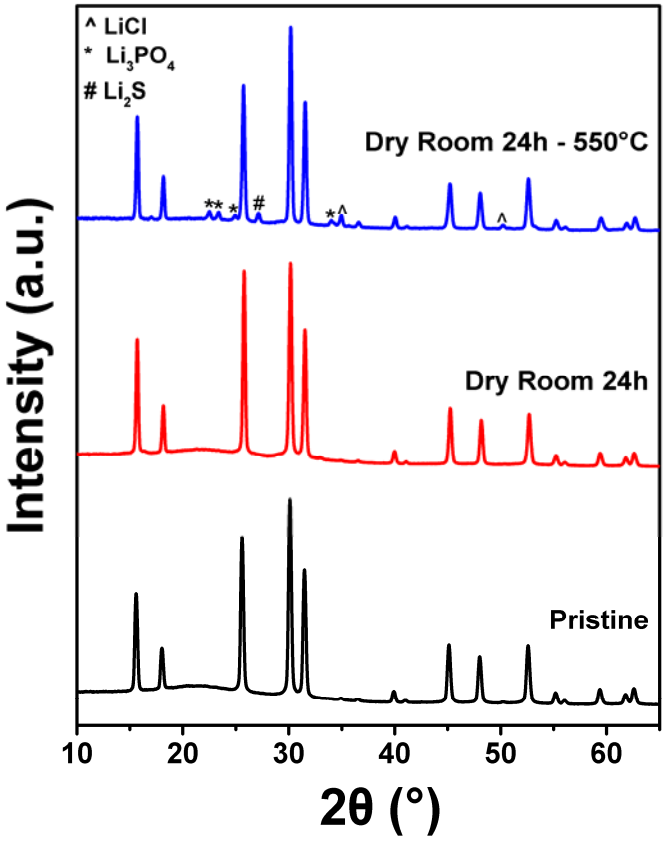

Figure 3.22. The XRD patterns of pristine LPSCl, LPSCl exposed in a dry room for 24 hours, and followed by a heat treatment at 550°C.

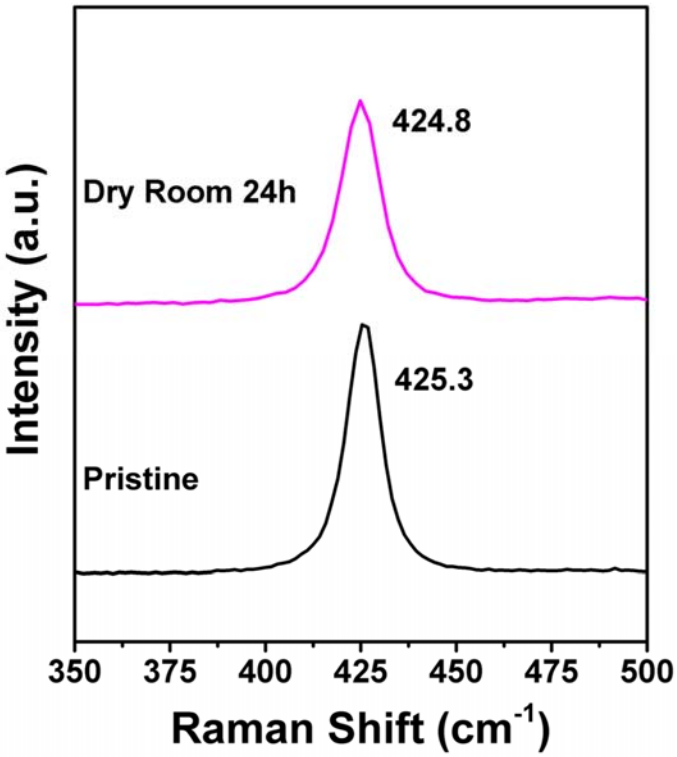

Figure 3.23. The Raman spectra of pristine LPSCl and after exposing in a dry room for 24 hours.

Nevertheless, FTIR (Figure 3.24) shows an increasing CO_3^{2-} signal with increasing exposure time, indicating the formation of carbonate species. Attempts at measuring ^{13}C-^{1}H cross-polarization NMR to further characterize the carbonate species were unsuccessful, thus indicating the quantity of carbonates is extremely low or the carbonates are not spatially close to protons.

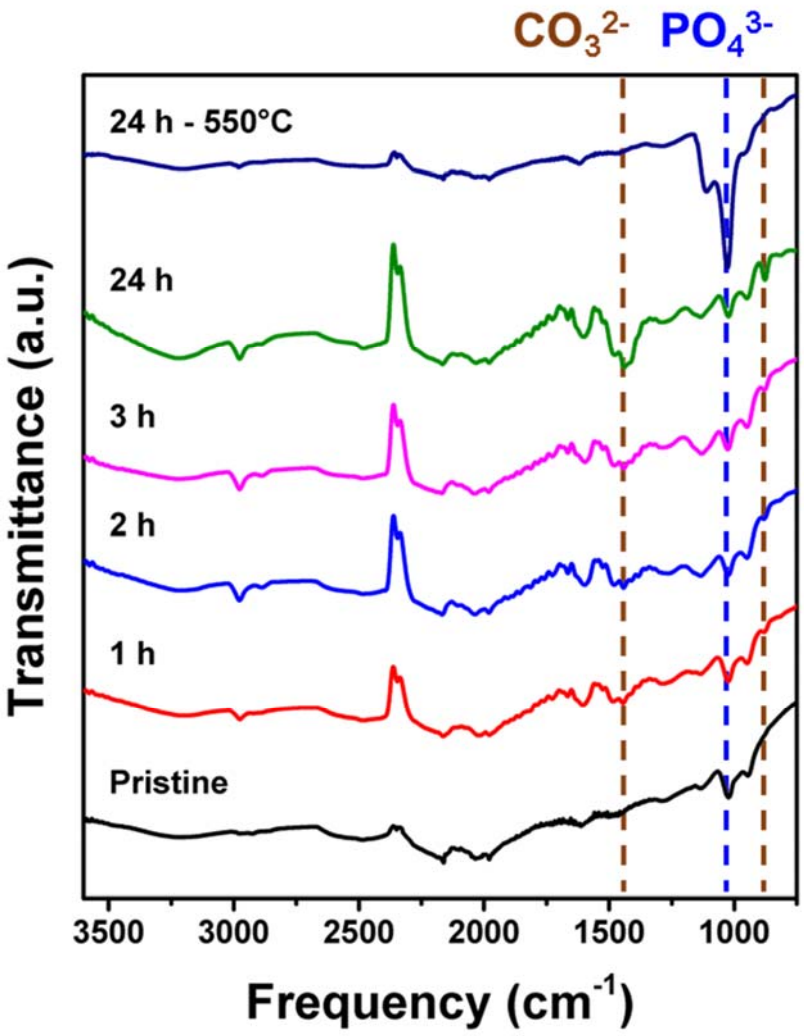

Figure 3.24. The FTIR spectra of pristine LPSCl and LPSCl exposed in a dry room for 1, 2, 3, 24 hours and followed by a heat treatment at 550°C.

The CO_2 evolution peak observed near 330°C in the TGA/DSC – MS measurements (Figure 3.25) also confirm the existence of carbonates. Therefore, carbonate formation may explain the ionic conductivity drop. After removing carbonates with a heat treatment at 550°C for 8 hours, as suggested by the TGA results, the CO_3^{2-} signal no longer appears in the FTIR spectrum and the ionic conductivity is also mostly recovered. However, there is evidence of LPSCl decomposition in the FTIR spectrum (PO_4^{3-} signal at 1030 cm^{-1}) and the XRD pattern (LiCl, Li_2S,

and Li_3PO_4 peaks are identified), which may explain why the ionic conductivity is not fully recovered.

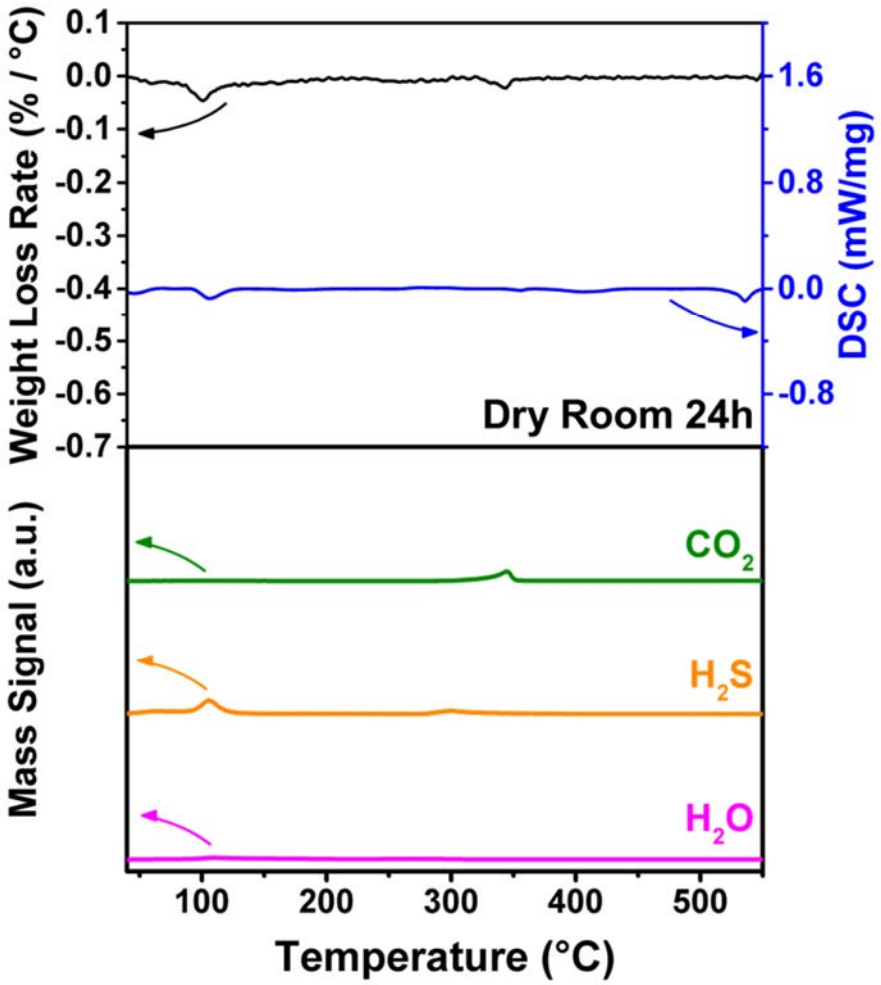

Figure 3.25. The TGA / DSC – MS of LPSCl exposed in a dry room for 24 hours.

Lastly, the dry room adaptability of LPSCl was examined by comparing the performance of two $LiNi_{0.8}Co_{0.1}Mn_{0.1}O_2$ (NCM811) | LPSCl | LiIn all-solid-state cells, fabricated with either the pristine or the dry room exposed (24 hours) LPSCl. Both cells exhibit similar 1st cycle charge capacity of around 214 mAh g^{-1} and 1st cycle Coulombic efficiency (CE) of 78.1% (Figure 3.20b). Moreover, the cell performance (Figure 3.20c) in further cycles (CE and capacity retention) are also similar, proving that this particular sulfide SSE is dry room compatible.

3.4 Conclusion

This study elucidates the degradation mechanism of a sulfide electrolyte, LPSCl, during exposure to air and moisture. The effects of post-heat treatment at 550°C on the exposed LPSCl were also studied. As evidenced by our results, both hydration and hydrolysis reactions occur during the exposure. To investigate the mechanism in detail, XRD, XPS, Raman, FTIR, and NMR characterizations were conducted at various exposure and heat treatment states. When exposed to ambient air and water, LPSCl not only partially hydrolyzes to generate H_2S, resulting in permanent sulfur loss, but also forms two different hydrated species and carbonates (depending on the amount of water). Heat-treatment at 350°C can fully dehydrate LPSCl and completely decompose the carbonates. Nevertheless, the hydrolysis reaction can still occur during the heat treatment. LPSCl can be partially recovered when heated to 450°C, during which LiCl, Li_2S and Li_3PO_4 are also formed, accompanying the sulfur loss due to the hydrolysis reaction. When exposed to a dry room atmosphere, where the level of moisture is strictly controlled (around 100 ppm), LPSCl does not undergo significant decomposition and retains most of its ionic conductivity even after 24 hours of exposure. Nevertheless, minor carbonate formation still occurs, explaining the slight reduction in conductivity. These carbonate species can also be removed via heat treatment at 550°C. Finally, the dry room exposed LPSCl was used to fabricate a NCM811 | LPSCl | LiIn all solid-state cell and compared with the pristine electrolyte. Both cells showed similar electrochemical performance and capacity retention, indicating that this argyrodite electrolyte is dry room compatible. Our work thus provides a foundation for the academic field to move forward and focus on developing scalable ASSBs.

Chapter 3, in full, is a reprint of the material “Investigating dry room compatibility of sulfide solid-state electrolytes for scalable manufacturing.” as it appears in Journal of Materials Chemistry A. Chen, Y.-T.; Marple, M. A.; Tan, D. H. S.; Ham, S. Y.; Sayahpour, B.; Li, W. K.; Yang, H.; Lee, J. B.; Hah, H. J.; Wu, E. A.; Doux, J.-M.; Jang, J.; Ridley, P.; Cronk, A.; Deysher, G.; Chen, Z.;

Meng, Y. S. 2022, *10*, 7155−7164. The dissertation author was the first author of this paper, all authors contributed to this work.

References

1. T. Chen, Y. Jin, H. Lv, A. Yang, M. Liu, B. Chen, Y. Xie and Q. Chen, *Trans. Tianjin Univ.*, 2020, **26**, 208-217.

2. Y. Horowitz, C. Schmidt, D.-h. Yoon, L. M. Riegger, L. Katzenmeier, G. M. Bosch, M. Noked, Y. Ein-Eli, J. Janek and W. G. Zeier, *Energy Technology*, 2020, **8**, 2000580.

3. Y. S. Jung, D. Y. Oh, Y. J. Nam and K. H. Park, *Isr. J. Chem.*, 2015, **55**, 472-485.

4. K. Kerman, A. Luntz, V. Viswanathan, Y.-M. Chiang and Z. Chen, *J. Electrochem. Soc.*, 2017, **164**, A1731.

5. H. Lee, P. Oh, J. Kim, H. Cha, S. Chae, S. Lee and J. Cho, *Adv. Mater.*, 2019, **31**, 1900376.

6. K. J. Kim, M. Balaish, M. Wadaguchi, L. Kong and J. L. Rupp, *Adv. Energy Mater.*, 2021, **11**, 2002689.

7. Y. Seino, T. Ota, K. Takada, A. Hayashi and M. Tatsumisago, *Energy Environ. Sci.*, 2014, **7**, 627-631.

8. N. Kamaya, K. Homma, Y. Yamakawa, M. Hirayama, R. Kanno, M. Yonemura, T. Kamiyama, Y. Kato, S. Hama and K. Kawamoto, *Nat. Mater.*, 2011, **10**, 682.

9. J. Janek and W. G. Zeier, *Nat. Energy*, 2016, **1**, 1-4.

10. K. Takada, M. Osada, N. Ohta, T. Inada, A. Kajiyama, H. Sasaki, S. Kondo, M. Watanabe and T. Sasaki, *Solid State Ionics*, 2005, **176**, 2355-2359.

11. W. D. Jung, M. Jeon, S. S. Shin, J.-S. Kim, H.-G. Jung, B.-K. Kim, J.-H. Lee, Y.-C. Chung and H. Kim, *ACS omega*, 2020, **5**, 26015-26022.

12. T. Ohtomo, A. Hayashi, M. Tatsumisago and K. Kawamoto, *J. Non-Cryst. Solids*, 2013, **364**, 57-61.

13. T. Kimura, A. Kato, C. Hotehama, A. Sakuda, A. Hayashi and M. Tatsumisago, *Solid State Ionics*, 2019, **333**, 45-49.

14. Z. Zhang, J. Zhang, Y. Sun, H. Jia, L. Peng, Y. Zhang and J. Xie, *Journal of Energy Chemistry*, 2020, **41**, 171-176.

15. X. Li, J. Liang, K. R. Adair, J. Li, W. Li, F. Zhao, Y. Hu, T.-K. Sham, L. Zhang and S. Zhao, *Nano Lett.*, 2020, **20**, 4384-4392.

16. S. Ahmed, P. A. Nelson and D. W. Dees, *J. Power Sources*, 2016, **326**, 490-497.

17. D. Li, L. Cao, C. Liu, G. Cao, J. Hu, J. Chen and G. Shao, *Appl. Surf. Sci.*, 2019, **493**, 1326-1333.

18. C. Yu, S. Ganapathy, J. Hageman, L. van Eijck, E. R. van Eck, L. Zhang, T. Schwietert, S. Basak, E. M. Kelder and M. Wagemaker, *ACS applied materials & interfaces*, 2018, **10**, 33296-33306.

19. C. Yu, L. van Eijck, S. Ganapathy and M. Wagemaker, *Electrochim. Acta*, 2016, **215**, 93-99.

20. S. Wang, Y. Zhang, X. Zhang, T. Liu, Y.-H. Lin, Y. Shen, L. Li and C.-W. Nan, *ACS applied materials & interfaces*, 2018, **10**, 42279-42285.

21. X. Randrema, C. Barcha, M. Chakir, V. Viallet and M. Morcrette, *Solid State Sciences*, 2021, 106681.

22. W. Arnold, D. A. Buchberger, Y. Li, M. Sunkara, T. Druffel and H. Wang, *J. Power Sources*, 2020, **464**, 228158.

23. J. Auvergniot, A. Cassel, D. Foix, V. Viallet, V. Seznec and R. Dedryvère, *Solid State Ionics*, 2017, **300**, 78-85.

24. A.-K. Hatz, R. Calaminus, J. Feijoo, F. Treber, J. Blahusch, T. Lenz, M. Reichel, K. Karaghiosoff, N. M. Vargas-Barbosa and B. V. Lotsch, *ACS Appl. Energy Mater.*, 2021, **4**, 9932-9943.

25. F. Friedrich, B. Strehle, A. T. Freiberg, K. Kleiner, S. J. Day, C. Erk, M. Piana and H. A. Gasteiger, *J. Electrochem. Soc.*, 2019, **166**, A3760.

26. J. P. Yesinowski and H. Eckert, *J. Am. Chem. Soc.*, 1987, **109**, 6274-6282.

27. D. Massiot, F. Fayon, M. Capron, I. King, S. Le Calvé, B. Alonso, J. O. Durand, B. Bujoli, Z. Gan and G. Hoatson, *Magn. Reson. Chem.*, 2002, **40**, 70-76.

28. M. A. Kraft, S. P. Culver, M. Calderon, F. Böcher, T. Krauskopf, A. Senyshyn, C. Dietrich, A. Zevalkink, J. r. Janek and W. G. Zeier, *J. Am. Chem. Soc.*, 2017, **139**, 10909-10918.

29. A. Ievină, M. Straumanis and K. Karlsons, *Z. Phys. Chem.*, 1938, **40**, 146-150.

30. W. Buehrer, F. Altorfer, J. Mesot, H. Bill, P. Carron and H. Smith, *J. Phys.: Condens. Matter*, 1991, **3**, 1055.

31. N. I. Ayu, E. Kartini, L. D. Prayogi and M. Faisal, *Ionics*, 2016, **22**, 1051-1057.

32. H. Peisert, T. Chassé, P. Streubel, A. Meisel and R. Szargan, *J. Electron. Spectrosc. Relat. Phenom.*, 1994, **68**, 321-328.

33. A. Vizintin, M. Lozinšek, R. K. Chellappan, D. Foix, A. Krajnc, G. Mali, G. Drazic, B. Genorio, R. m. Dedryvère and R. Dominko, *Chem. Mater.*, 2015, **27**, 7070-7081.

34. Z. Tai, W. Zhu, M. Shi, Y. Xin, S. Guo, Y. Wu, Y. Chen and Y. Liu, *J. Colloid Interface Sci.*, 2020, **576**, 468-475.

35. S. Yin, Y. Zeng, C. Li, X. Chen and Z. Ye, *ACS applied materials & interfaces*, 2013, **5**, 12876-12886.

36. H. Chung, Z. Lebens-Higgins, B. Sayahpour, C. Mejia, A. Grenier, G. E. Kamm, Y. Li, R. Huang, L. F. Piper and K. W. Chapman, *J. Mater. Chem. A*, 2021, **9**, 1720-1732.

37. N. V. Faenza, L. Bruce, Z. W. Lebens-Higgins, I. Plitz, N. Pereira, L. F. Piper and G. G. Amatucci, *J. Electrochem. Soc.*, 2017, **164**, A3727.

38. S. M. Benoy, S. Singh, M. Pandey and B. Manoj, *Materials Research Express*, 2020, **6**, 125624.

39. D. H. Tan, A. Banerjee, Z. Deng, E. A. Wu, H. Nguyen, J.-M. Doux, X. Wang, J.-h. Cheng, S. P. Ong and Y. S. Meng, *ACS Appl. Energy Mater.*, 2019, **2**, 6542-6550.

40. I. Hanghofer, B. Gadermaier and H. M. R. Wilkening, *Chem. Mater.*, 2019, **31**, 4591-4597.

41. H. J. Deiseroth, S. T. Kong, H. Eckert, J. Vannahme, C. Reiner, T. Zaiß and M. Schlosser, *Angew. Chem.*, 2008, **120**, 767-770.

42. D. H. Tan, E. A. Wu, H. Nguyen, Z. Chen, M. A. Marple, J.-M. Doux, X. Wang, H. Yang, A. Banerjee and Y. S. Meng, *ACS Energy Letters*, 2019, **4**, 2418-2427.

43. I. Hanghofer, M. Brinek, S. Eisbacher, B. Bitschnau, M. Volck, V. Hennige, I. Hanzu, D. Rettenwander and H. Wilkening, *PCCP*, 2019, **21**, 8489-8507.

44. A. Hayashi, H. Muramatsu, T. Ohtomo, S. Hama and M. Tatsumisago, *J. Alloys Compd.*, 2014, **591**, 247-250.

45. G. O. Hartley, L. Jin, B. J. Bergner, D. S. Jolly, G. J. Rees, S. Zekoll, Z. Ning, A. T. Pateman, C. Holc and P. Adamson, *Chem. Mater.*, 2019, **31**, 9993-10001.

46. M. A. Marple, T. A. Wynn, D. Cheng, R. Shimizu, H. E. Mason and Y. S. Meng, *Angew. Chem. Int. Ed.*, 2020, **59**, 22185-22193.

47. M. Murakami, K. Shimoda, S. Shiotani, A. Mitsui, K. Ohara, Y. Onodera, H. Arai, Y. Uchimoto and Z. Ogumi, *The Journal of Physical Chemistry C*, 2015, **119**, 24248-24254.

48. M. U. Patel, I. Arcon, G. Aquilanti, L. Stievano, G. Mali and R. Dominko, *ChemPhysChem*, 2014, **15**, 894-904.

Chapter 4. Investigating Dry Room Compatibility of Chloride Solid-State Electrolytes for Scalable Manufacturing

4.1 Introduction

Nowadays, Li-ion batteries (LIBs) have become part of daily life with billions used in electronic devices and electric vehicles. As conventional LIBs utilize flammable liquid electrolytes, increasing efforts are being invested to develop all-solid-state batteries (ASSBs) employing less or non-flammable solid-state electrolytes (SSEs).[1-4] Moreover, SSEs can also enable anode materials with higher capacity like Si and Li.[5-8] Unlike conventional LIBs, whose manufacturing process has been very well developed, there are still plenty of challenges when fabricating all-solid-state Li batteries (ASSLBs) on a commercial scale. The use of dry rooms is already well established for LIBs so it would be ideal if ASSLBs could also be made in the same facilities. Therefore, it is important to validate whether SSEs are stable in dry room conditions, however, the dry room stability of many SSEs has yet to be properly evaluated.

Most inorganic SSEs for ASSLBs can be grouped into three categories: oxides, sulfides, and halides.[9] Although oxide SSEs possess superior chemical and electrochemical stability, their high synthesis temperature and high Young's modulus limit their use in many applications.[9-12] Sulfide SSEs are frequently utilized in ASSLBs due to their high ionic conductivity, ease of synthesis, and high elemental abundance. However, sulfide electrolytes exhibit a narrow electrochemical stability window, leading to limited applications with cathode materials requiring a high cut-off voltage ($LiNi_{0.5}Mn_{1.5}O_2$) or large surface area ($LiFePO_4$) due to excessive sulfide oxidation and cathode electrolyte interphase (CEI) formation. Chlorides SSEs possess a higher oxidation stability so they can be employed when a high cut-off voltage is required at the cathode side.[13-14]

Several chlorides with the general formula Li_3MCl_6 (M = Tb^{3+}, Lu^{3+}, Y^{3+}, and Sc^{3+}) have been reported in the 1990s.[15-16] Depending on the size of the M^{3+} cation and the Li^+ distribution in the structure, these chlorides can crystallize in the trigonal ($P\bar{3}m1$), orthorhombic ($Pmna$), or monoclinic ($C2/m$) structures.[9, 15] Halide SSEs started receiving renewed attention after Asano et al. reported that Li_3YCl_6 (LYC) and Li_3YBr_6 synthesized by a mechanochemical method, exhibited ionic conductivities of 0.51 and 1.7 mS cm^{-1}, respectively, much higher than those previously reported.[17] As the Cl^- anion exhibits a higher oxidation stability than S^{2-}, chloride SSEs are more oxidatively stable than sulfide electrolytes. The oxidation electrochemical window can reach approximately 4.2 V for chlorides.[9, 16, 18-19] Unlike conventional synthesis methods using high-temperature solid-state reactions, various halide SSEs at metastable phases and different crystal structures can be prepared using a mechanochemical approach.[19] Moreover, such an approach can improve the ionic conductivity of halide SSEs by introducing disorders into the cation and anion sublattices.[9, 20-21] Tuning the crystal structures and the concentration of Li ions by partial substitution of the central metal cations is another effective method to boost ionic conductivity. $Li_{3-x}M_{1-x}N_xCl_6$ (M = Er^{3+}, Y^{3+}, and Yb^{3+}; N = Zr^{4+} and Hf^{4+}) electrolytes were reported to exhibit an enhanced ionic conductivity than the unsubstituted Li_3MCl_6 electrolytes due to the formation of new phases with a lower migration barrier for Li ions.[22-23] For example, Kwak et al. improved the ionic conductivity of Li_2ZrCl_6 (LZC) by Fe^{3+} substitution, resulting from the increased concentration of Li^+.[21]

Despite their superior oxidation stability over sulfide SSEs, the adaptability of chloride SSEs to scalable manufacturing conditions needs to be evaluated. A recent study on the dry room compatibility of Li_6PS_5Cl (LPSCl) has shown that LPSCl is prone to hydrolysis when exposed to moisture, but a maximum dew point of −40 °C is sufficient to minimize H_2S evolution to prevent ionic conductivity loss and to ensure workers' safety.[24-25] Likewise, chloride SSEs have been known to be sensitive towards hydrolysis upon moisture exposure. [9, 26-27] Li_3InCl_6 (LIC) has been

reported to form stable hydrate upon storage in air, but it can be recovered by heating above 200 °C.[28] On the other hand, some chloride SSEs have been found to undergo either decomposition or severe hydrolysis when exposed to air. Therefore, the dry room compatibility of chloride SSEs should be evaluated to identify the most promising chemistry and suitable processing conditions for mass production.

This study aims to investigate the dry room compatibility of chloride SSEs where the obtained results can be used as criterion for material selection for future upscaling processes. Three promising chloride SSEs possessing high ionic conductivities at ambient temperature, e.g., LZC, LYC, and LIC, were chosen for this study. Prior to testing the dry room stability, all materials were first exposed to ambient air (air-Exp), containing a higher humidity level than dry rooms, to speed up degradation for the ease of mechanistic study. Afterward, the exposed samples were recovered and underwent heat treatment (air-HT) to evaluate recoverability of the initial material. The obtained results show that LZC underwent severe hydrolysis, while LYC and LIC underwent hydration. Only LIC was recoverable after the heat treatment, rendering it the most stable chloride SSE among the three. Finally, the three chloride SSEs were exposed to a dry room environment, with reduced moisture level, for 3 h. The exposed electrolytes were used as catholytes in NCM811|LiIn half cells and exhibited higher cell impedance and lower discharge capacity. Compared to LPSCl,[25] the chloride SSEs studied here are more sensitive to moisture exposure.

4.2 Materials and Methods

4.2.1 Synthesis of Chloride SSEs

All chloride SSEs were synthesized via a mechanochemical approach using a Retsch PM200 planetary ball-mill. Precursors, including LiCl (Sigma Aldrich), $ZrCl_4$ (Sigma Aldrich), YCl_3 (Alfa Aesar), and $InCl_3$ (Alfa Aesar), were stoichiometrically mixed with a mortar and a pestle, and 1.5 g of precursor mixture were transferred to a 50 mL air-tight ZrO_2 jar with fifteen 10 mm ZrO_2

milling media in an Ar-filled glovebox. LZC and LIC were ball-milled at 550 rpm for 3 h, and LYC was at 500 rpm for 1 h.

4.2.2 Exposure and Heat Treatment of Chloride SSEs

Air-Exp samples were prepared by placing 0.5 g of chloride SSEs evenly in a 125 mL wide-mouth glass jar in an Ar-filled glovebox and then transferring them to the antechamber with a total volume of 250 L. The chamber door was opened for 1 min to fill the antechamber with ambient air having a relative humidity between 45 – 55 %. After 24 h of exposure, the antechamber was vacuumed and purged with Ar, and the air-Exp samples were collected. The Air-HT samples were obtained by heating the Air-Exp samples in quartz tubes under a dynamic vacuum at assigned temperatures (LZC: 350℃;[29] LYC: 550℃;[17] LIC: 260℃[30]). Dry room exposed samples were prepared by distributing multiple batches of 0.5 g SSEs on petri dishes in a dry room environment with a dew point of −60℃ for 3 h.

4.2.3 Electrochemical Characterization

To avoid air exposure, all cell fabrication and measurements were done in an Ar-filled glovebox. To obtain the ionic conductivity, 75 mg of chloride SSE was placed in a 10 mm PEEK die and pressed at 370 MPa using a pair of titanium plungers to obtain the pellet. The SSE thickness is estimated by measuring the length difference of the cell with and without the SSE pellet with a Vernier caliper. The cell was tightened to 75 MPa using a cell holder. Electrochemical impedance spectroscopy (EIS) measurements were performed from 1 MHz to 0.1 Hz, with an applied AC amplitude of 30 mV. The acquired Nyquist plots were analyzed with Z-View software. To obtain the electronic conductivity, a DC voltage of 0.5 V was applied to the SSE pellet and the residual current induced by the excitation pulse was recorded. To obtain the oxidation potential of the pristine and dry room exposed chloride SSEs, the powders were mixed with acetylene black (AB) at a weight ratio of 7:3 (SSE:AB) with mortar and pestle. LiIn anode was prepared by vortex

mixing Li and In powder (MSE Supplies) at a weight ratio of 1:33. LiIn alloy was used as both counter and reference electrode. Linear scan voltammetry (LSV) was conducted using SSE-C | LPSCl | LiIn cells at a scan rate of 0.1 mV s^{-1} from open circuit voltage (OCV) to 5 V vs. Li/Li^+. The measurements were conducted using a Solartron 1260 Impedance Analyzer at room temperature.

Half cells were employed to evaluate the electrochemical performance of chloride SSEs (LZC, LYC, and LIC) before and after exposure to the dry room environment. The half cells were constructed by pelletizing 15 mg of NCM811 cathode composites, 70 mg of LPSCl and 50 mg of LiIn alloy anode with PEEK dies. The cathode composites were fabricated by mixing $LiNi_{0.8}Co_{0.1}Mn_{0.1}O_2$ (NCM811, LG Energy Solution), chloride SSEs, and vapor grown carbon fiber (VGCF, Sigma-Aldrich) at a weight ratio of 66:31:3 with mortar and pestle. The half cells were tested using Neware Battery cyclers (A211-BTS-1U-ZWJ) with cut-off voltages of 2.5 V and 4.3 V *vs.* Li/Li^+ at room temperature. The cells underwent two formation cycles at C/10 (1 C = 200 mAh g^{-1}) and EIS were recorded in the second formation discharge at 50% state of charge. Afterward, the cells were cycled at C/3 with an additional constant voltage cut-off of C/10 at the end of charging for 50 cycles. Subsequently, the cells were again cycled at C/10 and the other EIS was recorded when discharged to a state-of-charge of 50%.

4.2.4 Characterization

X-ray diffraction (XRD) patterns of chloride SSEs were obtained using a Bruker APEX II. The powder was sealed in a 0.7 mm boron-rich glass capillary in an Ar-filled glovebox. Measurements were taken using Mo Kα radiation (λ = 0.70926 Å) over a 2θ range of 5° to 40°, with a step size of 0.01°. Le Bail refinement was done using FullProf software. Space group *P*-3*m*1 was selected to refine LZC and LYC, and *C*2/*m* was selected for LIC.[9, 29, 31-32] Energy dispersive X-ray spectroscopy (EDS) was obtained with a FEI Scios DualBeam Focused ion

beam/scanning electron microscope, and the samples were prepared in an Ar-filled glovebox and transferred with an air-tight loader to avoid any atmosphere exposure. A NETZSCH STA 449 F3 Jupiter Simultaneous Thermal Analyzer with Coupled QMS 403 D Aëolos Mass Spectrometer was used to obtain thermogravimetric analysis/differential scanning calorimetry coupled mass spectrum data (TGA/DSC–MS). To observe H_2O and HCl evolution, MS was set to monitor molecular weights at 18 and 36 $g \cdot mol^{-1}$. 15–20 mg of chloride SSE samples were placed in Al_2O_3 pans (6.8 mm in diameter / 85 µL). The samples were prepared within 2 mins to minimize air exposure. All measurements were conducted in an N_2 atmosphere, scanning from 30 to 450℃ at a scan rate of 5℃ min^{-1}

4.3 Results and Discussion

To understand the impact of moisture exposure and potential recoverability, pure phase LZC, LYC, and LIC (confirmed with Le Bail refinement in Figure 4.1) were exposed to ambient air followed by heat treatment. EIS at each stage was measured and is shown in Figure 4.2. Before the exposure, all three materials exhibited ionic conductivities in the range of 10^{-4} S cm^{-1}, comparable to previous literature.[17, 29-30] After the exposure, the ionic conductivities of the SSEs all dropped to 10^{-6} mS cm^{-1} or lower, indicating some reaction has taken place. Note that the conductivity values only reflected the ionic conductivity of the decomposed or the hydrated products, rather than the degree of reactions. After heat treatment, only LIC recovered close to its pristine ionic conductivity, while both LZC and LYC exhibited further decay.

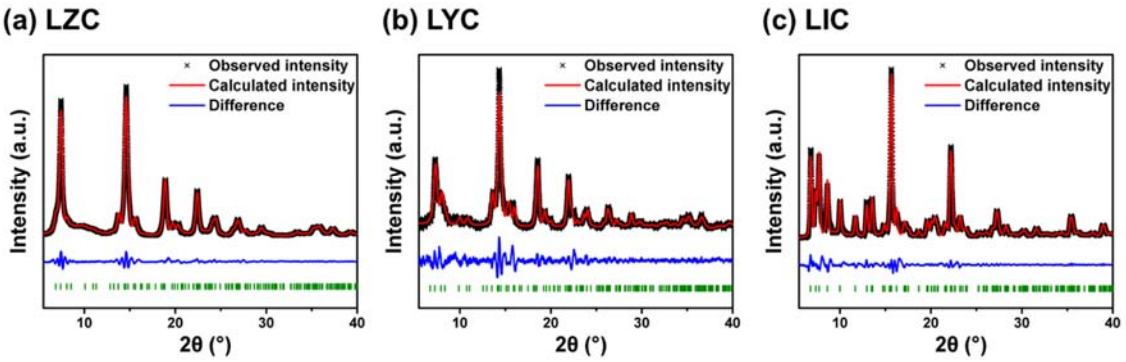

Figure 4.1. The Le Bail refinement of (a) LZC, (b) LYC, and (c) LIC. The three SSEs are confirmed to be a pure phase.

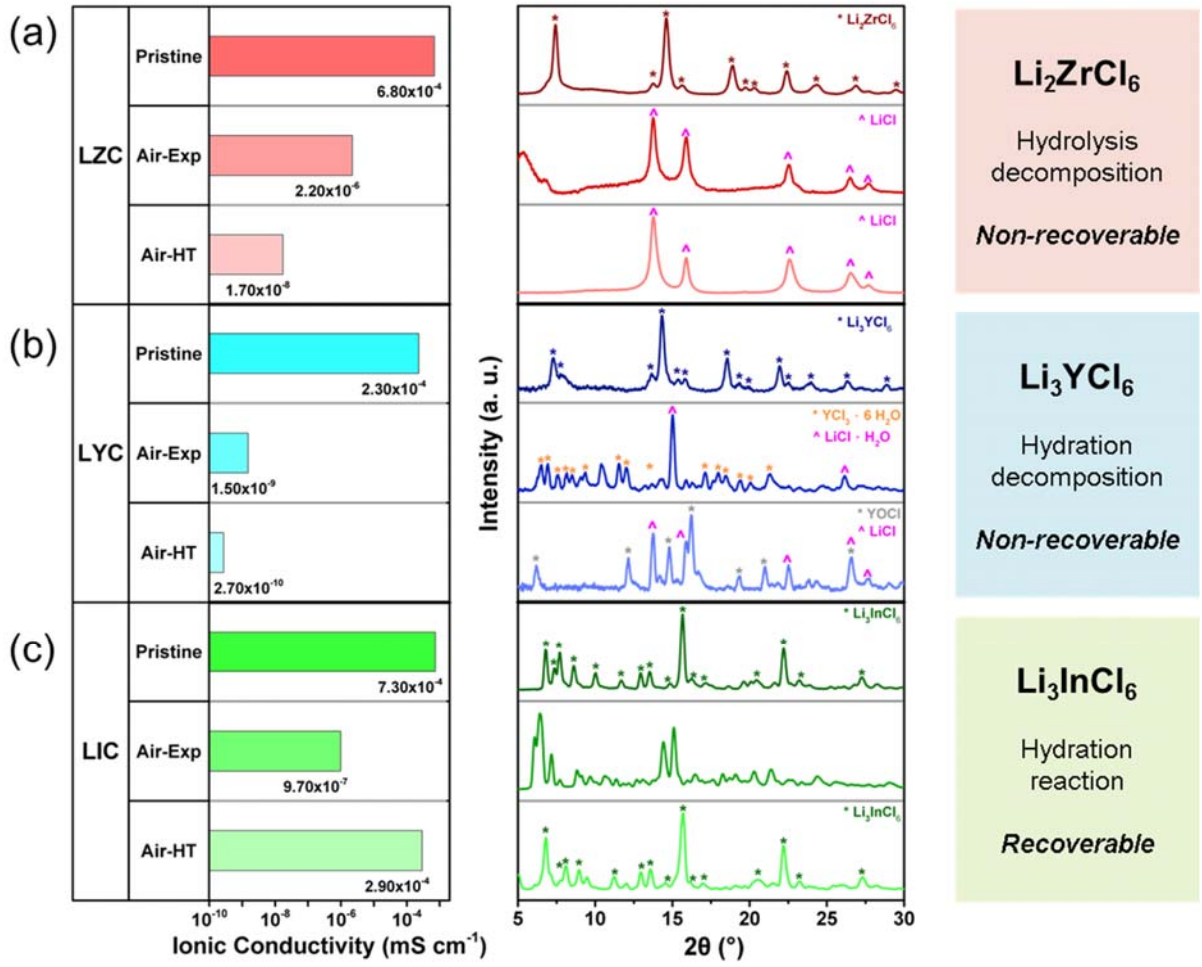

Figure 4.2. Ionic conductivities and XRD patterns of (a) LZC, (b) LYC, and (c) LIC before and after air exposure and after the heat treatment.

The pristine and Air-Exp chloride SSEs exhibited similar electronic conductivities in the range of 10^{-9} S cm^{-1} (Figure 4.3), implying an electronically conductive phase was not formed after air exposure.

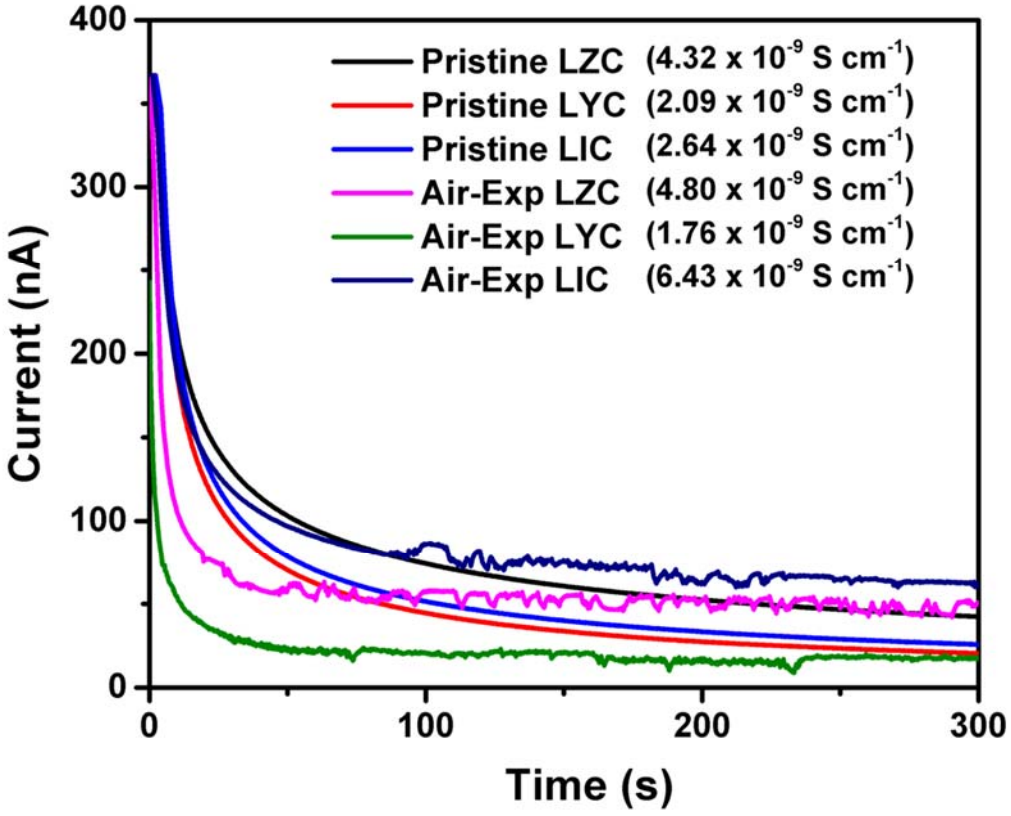

Figure 4.3. The DC polarization of pristine and Air-Exp chloride SSEs.

XRD patterns of all chloride SSE samples were investigated to understand the chemical reactions occurring during the moisture exposure and heat treatment. The XRD patterns showed that all three materials were fully or close to fully decomposed or hydrated, as the peaks of their pristine states were not observed. After exposing, the XRD pattern of LZC showed the formation of LiCl. The pattern remained similar after the heat treatment, suggesting that the Air-Exp LZC cannot be recovered. As $ZrCl_4$, one of its precursors, has high tendency to hydrolyze and form ZrO_2, it is likely to present in Air-Exp LZC.[33] Since ZrO_2 exhibited diffraction peaks with similar

diffraction angles to those of LiCl (Figure 4.4), EDS was employed to inspect the elemental ratio and the spectra are shown in Figure 4.5.[34-35]

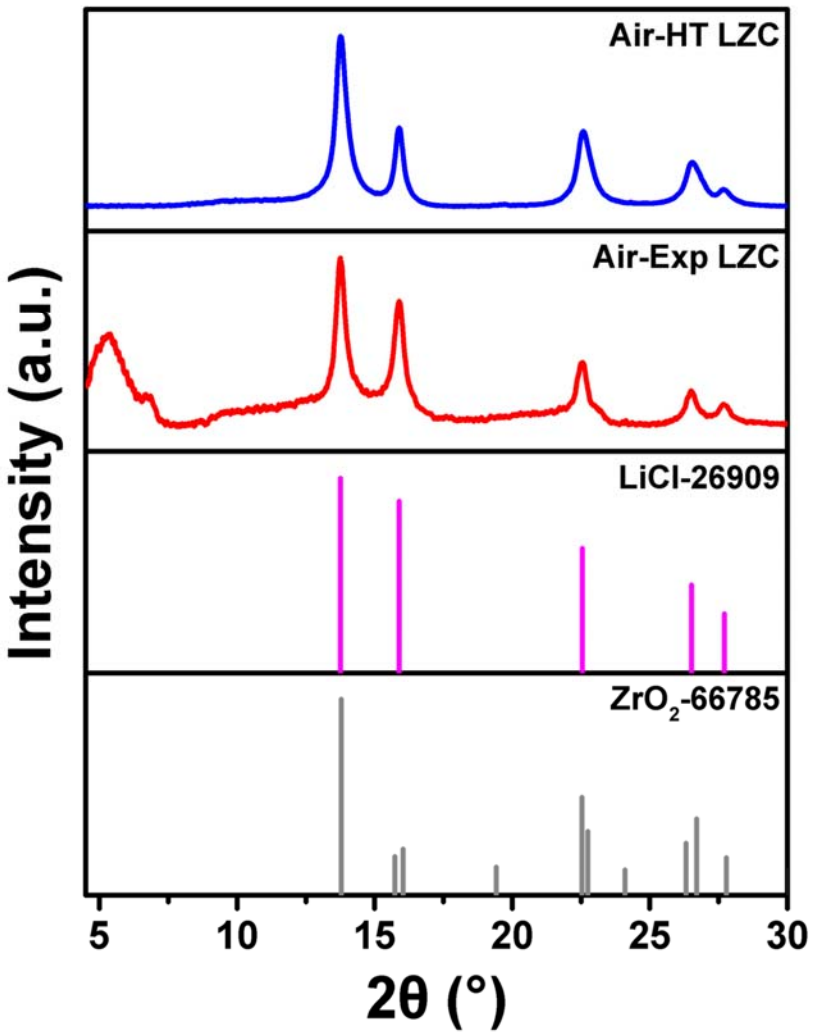

Figure 4.4. The XRD patterns of Air-Exp and Air-HT LZC in comparison to the theoretical pattern of LiCl (ICSD 26909) and ZrO_2 (ICSD 66785).[34-35] As ZrO_2 and LiCl exhibit diffraction peaks at similar 2θ, EDS was done to confirm the formation of both compounds.

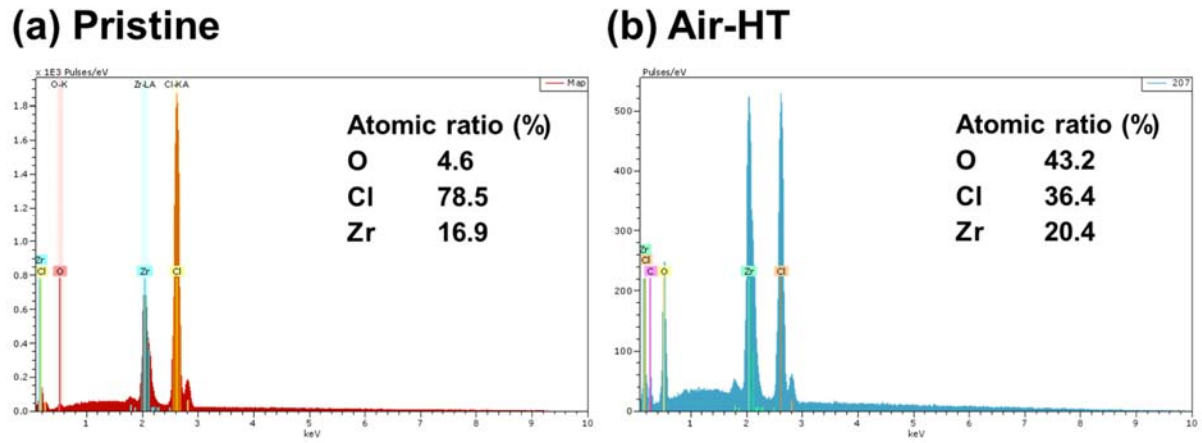

Figure 4.5. The EDS spectra of (a) pristine and (b) Air-HT LZC.

The oxygen atomic ratio increased significantly to 43.2% after the air exposure and heat treatment, indicating that LZC chemically reacted with air. As Air-HT LZC exhibited an approximate atomic ratio of Zr:Cl:O = 1:2:2, the net chemical reaction after the exposure can be deduced:

$$Li_2ZrCl_6 + 2\ H_2O \rightarrow 2\ LiCl + ZrO_2 + 4\ HCl \quad (1)$$

The XRD pattern of Air-Exp LYC can be deconvoluted into $YCl_3{\cdot}6H_2O$ and $LiCl{\cdot}H_2O$ (Figure 4.6), indicating that LYC decomposed into the hydrates of its precursors upon contact with air.[36-37] The chemical reaction can be written as:

$$Li_3YCl_6 + 9\ H_2O \rightarrow YCl_3{\cdot}6\ H_2O + 3\ LiCl{\cdot}H_2O \quad (2)$$

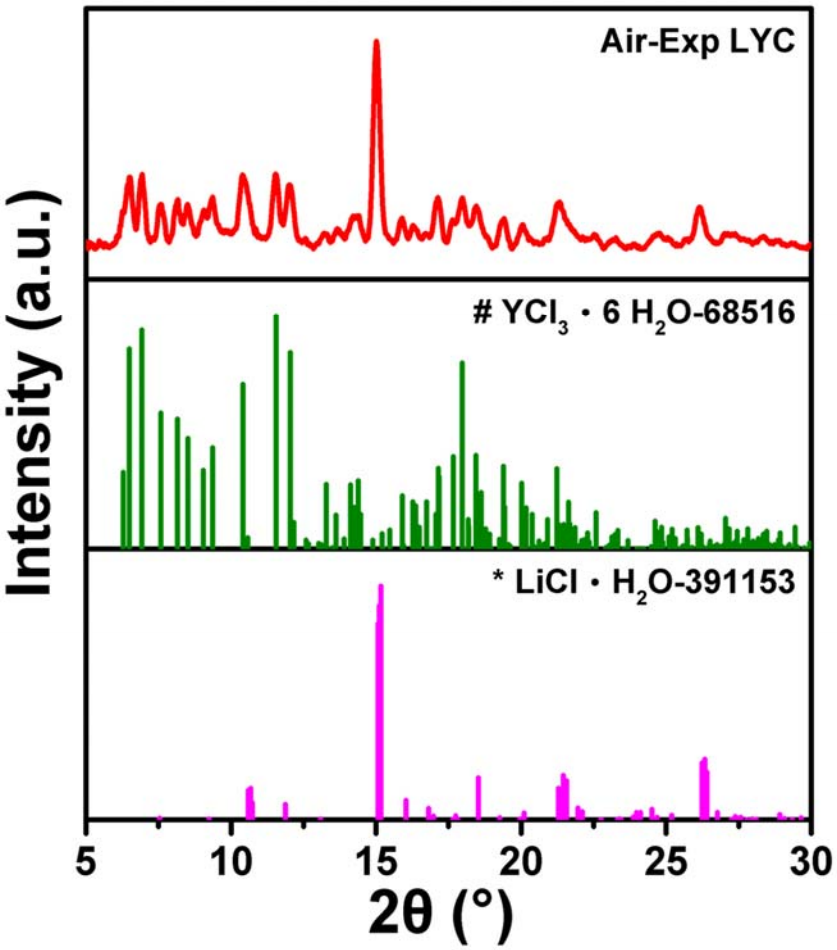

Figure 4.6. The XRD patterns of Air-Exp LYC in comparison to the theoretical pattern of $YCl_3 \cdot 6H_2O$ (ICSD 68516) and $LiCl \cdot H_2O$ (ICSD 391153).[36-37]

While anhydrous LiCl can easily be obtained by heating $LiCl \cdot H_2O$, $YCl_3 \cdot 6H_2O$ underwent a hydrolysis reaction to form YOCl.[27, 38-40] Consequently, LiCl and YOCl were observed in the XRD pattern (Figure 4.7) showing that LYC was not recoverable after heat treatment.[34, 40-41]

$$YCl_3 \cdot 6\ H_2O + 3\ LiCl \cdot H_2O \rightarrow YOCl + 3\ LiCl + 8\ H_2O + 2\ HCl \qquad (3)$$

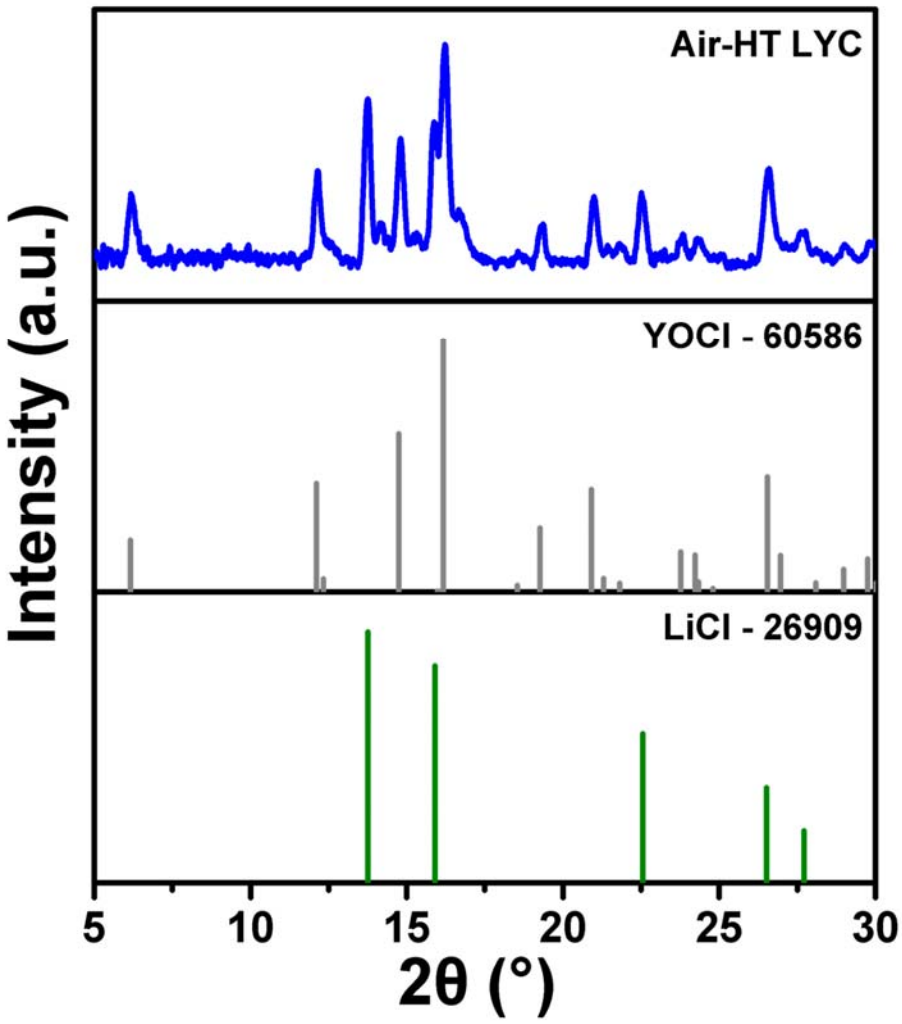

Figure 4.7. The XRD patterns of Air-HT LYC in comparison to the theoretical pattern of YOCl (ICSD 60586) and LiCl (ICSD 26909).[34, 41]

The crystal structures of chloride SSEs have no relationship with their behaviors towards moisture exposure. The crystal structure is more relevant to the ratio of ionic radii between cations and anions.[18]

To determine the moisture stability at room temperature, it is often effective to look at the Z^2 / r ratio and the Pauling electron negativity of the metal center (where Z is the oxidation number and R is the ionic radius). The higher the Z^2 / r and the electron negativity are (higher valence

number and smaller ionic radius), the more acidity, or tendency to hydrolyze the metal center is. This can be described by the formula.[42]

$$pK_a = 15.14 - 0.8816\left[\frac{Z^2}{r} + 9.60\left(\chi_{Pauling} - 1.50\right)\right]$$

The Z^2 / R ratio and electron negativity combined ranking in a decreasing order is Zr^{4+}, In^{3+} and Y^{3+}. Indeed, LZC hydrolyzes severely, and LYC does not hydrolyze at room temperature, which the theory explains well. However, rare earth metal halide salts (Sc, Y, and La-Lu)[40, 43] form oxihalides when their hydrates are heated. For example, LYC shows the least acidity at room temperature, it forms YOCl when heated to higher temperature, which the theory is no longer accurate.

To avoid confusion, a convenient way to predict the stability is to study the chemical properties of their chloride precursors, namely, $ZrCl_4$, YCl_3 and $InCl_3$, as they have identical metal centers and will behave similarly.

Unlike LZC and LYC, LIC can form stable hydrates without significant decomposition.[28, 30] It can be restored to its original phase after heating at 260°C, as shown in the XRD patterns in Figure 4.2c. Nevertheless, formation of minuscule In_2O_3, resulting from slight hydrolysis, was reported due to weak acidity of In^{3+} in aqueous solution, resembling the property of its $InCl_3$ precursor.[44]

Since HCl and H_2O evolution is a key indication of hydrolysis and dehydration reactions, it is important to detect them directly. However, HCl and H_2O are volatile and cannot be observed using XRD. TGA/DSC–MS was used to monitor both the weight change and gas evolution of the samples during the thermal treatment at high temperatures. The TGA/DSC–MS results of the three chloride SSEs at the pristine (Figure 4.8) and air-exposed (Figure 4.9) states were examined. At the pristine state, significant weight losses were only observed in pristine LZC above 350 °C,

due to the sublimation of $ZrCl_4$.[45] All the other minor weight losses and gas evolution were a result of short air exposure during the sample preparation. After 24 h of air exposure, all three exhibited endothermic signals due to the dehydration reaction or desorption of H_2O. Air-Exp LZC released HCl when heated to 80 °C, indicating that the hydrolysis reaction started close to room temperature. As LZC was fully hydrolyzed, $ZrCl_4$ sublimation signals were no longer observed above 350 °C. Different from LZC, Air-Exp LYC did not have HCl evolution before 150℃, indicating that Li_3YCl_3 hydrate was stable and started to hydrolyze and formed YOCl after 150 °C. No obvious HCl evolution was observed in Air-Exp LIC and H_2O evolution ends at approximately 230 °C, in consistent with the recovery of the LIC phase after heat treatment at 260 °C observed in the XRD result.

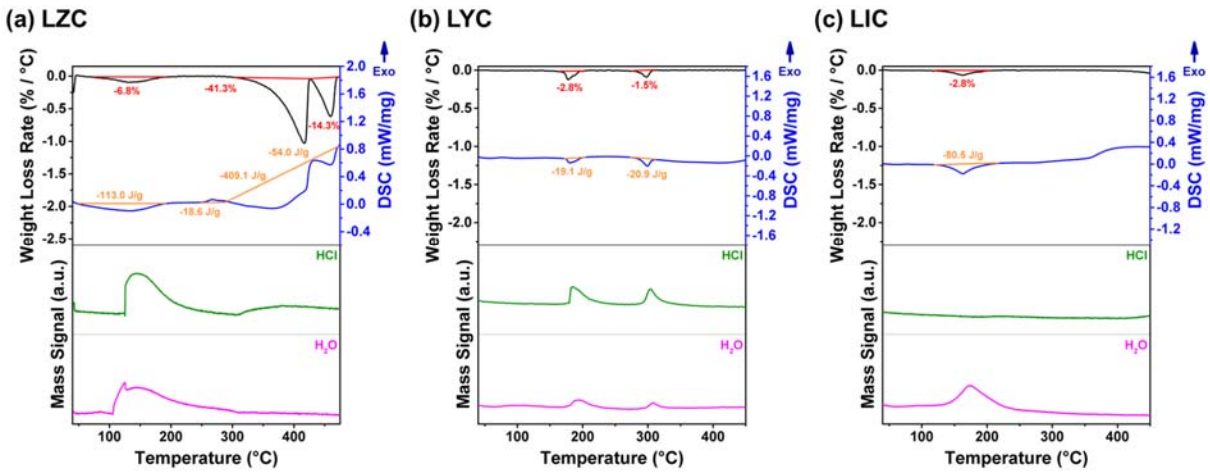

Figure 4.8. The TGA/DSC–MS of pristine (a) LZC, (b) LYC, and (c) LIC. The minor H_2O and HCl evolution are due to the short air exposure during sample preparation.

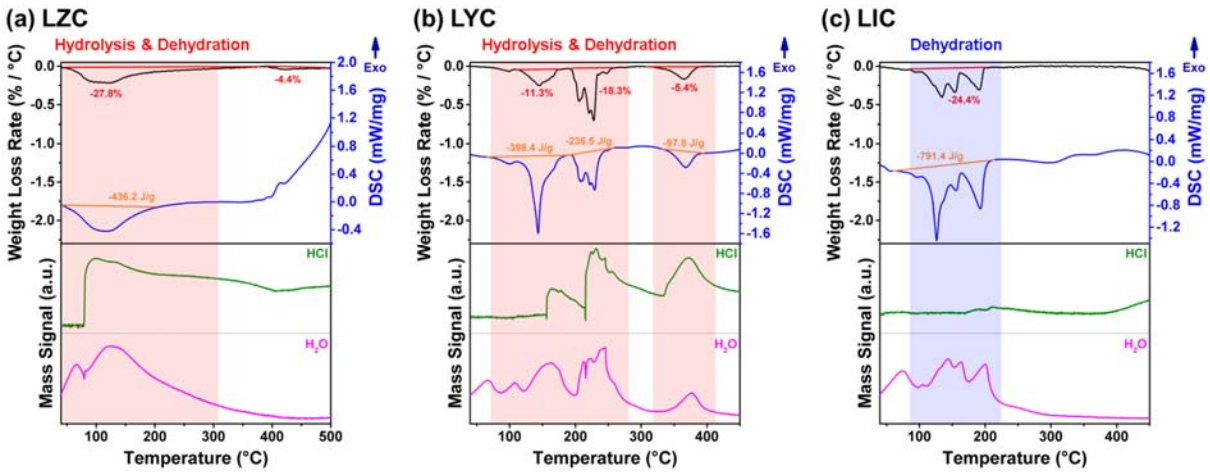

Figure 4.9. The TGA / DSC – MS of air-exposed (a) LZC, (b) LYC, and (c) LIC. HCl and H_2O were monitored, as they are the product of hydrolysis and dehydration reactions, respectively.

To verify the chemical reaction deduced from the XRD result, the weight changes after air exposure and TGA (heat treatment), and net weight change are summarized in Table 4.1. To calculate the theoretical weight change, the molar mass of pristine SSEs and solid products (i.e., ignoring HCl and H_2O) are calculated. The theoretical values of the three SSEs can be obtained following Table 4.2.

Table 4.1. The weight changes of LZC, LYC and LIC after air exposure and TGA.

Unit (%)	LZC	LYC	LIC
Air-Exp	−4.3	36.5	28.1
TGA	−32.2	−35.0	−24.4
Net change	−35.1	−11.3	−3.2

Table 4.2. The chemical formulas of pristine SSEs and their solid products. The theoretical weight changes can be calculated accordingly.

	LZC	LYC	LIC
Pristine SSE	Li_2ZrCl_6	Li_3YCl_6	Li_3InCl_6
Solid products	ZrO_2 + 2 LiCl	YOCl + 3 LiCl	Li_3InCl_6
Theoretical change (%)	−34.6	−17.0	0

LZC exhibited a negative weight change of −4.3% after the exposure, indicating that it started to hydrolyze and gave off HCl upon contacting moisture. A further weight change of −32.2% was observed during the TGA, because of HCl and H_2O removal. This led to a net weight loss of −35.1%, which is close to the theoretical value of −34.6%. LYC gained 36.5% weight during air exposure and lost 35.0% weight in TGA, leading to a net weight change of −11.3%. The difference between the experimental and theoretical value (−17.0%) could result from sample inhomogeneity during air exposure. LIC gained 28.1% after air exposure and lost 24.4% in TGA, resulting in a net change of −3.2%, close to the theoretical value of 0%. The weight analysis results are overall consistent with the XRD results. Based on the XRD and TGA/DSC–MS results, the chemical evolutions of the three chloride SSEs during air exposure and heat treatment can be summarized in Figure 4.10.

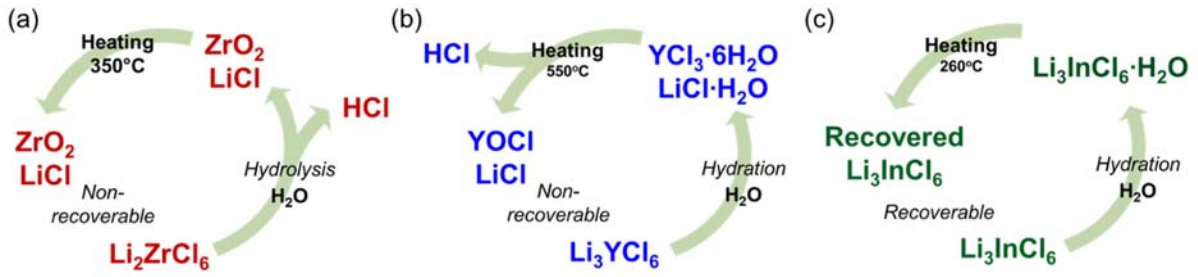

Figure 4.10. Summarized scheme of moisture stability and recovery process of (a) Li_2ZrCl_6, (b) Li_3YCl_6, and (c) Li_3InCl_6.

Lastly, all SSEs were exposed to a dry room environment with a dew point of −60 °C for 3 h. Figure 4.11 presents the ionic conductivity changes and XRD patterns of the SSEs before and after dry room exposure. The ionic conductivities of all the SSEs dropped to approximately a quarter of their original values despite little to no change observed in their XRD patterns.

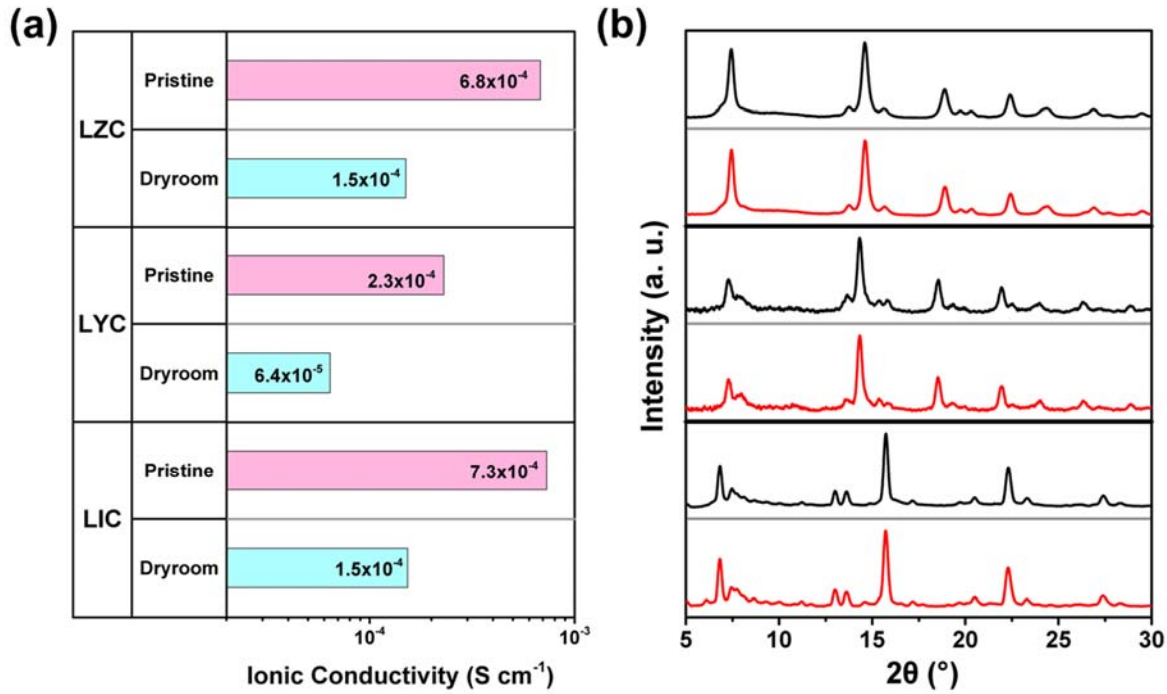

Figure 4.11. (a) Ionic conductivities and (b) XRD patterns of LZC, LYC and LIC after dry-room exposure.

The oxidation potential of the chloride SSEs after exposure to dry room was probed with LSV (Figure 4.12). The oxidation onset voltages were all approximately 4 V, which is close to the theoretical calculation.[19] The oxidation onsets remained almost the same after the dry room exposure, as only Cl^- is involved in the oxidation reaction ($2\ Cl^- \rightarrow Cl_2 + 2\ e^-$),[9] suggesting that the effect of hydration on the electrochemical window is minimal. To evaluate the electrochemical performance of the SSEs, they were paired with NCM811 cathode composites and assembled into NCM811-chloride SSE|LPSCl|LiIn half cells.

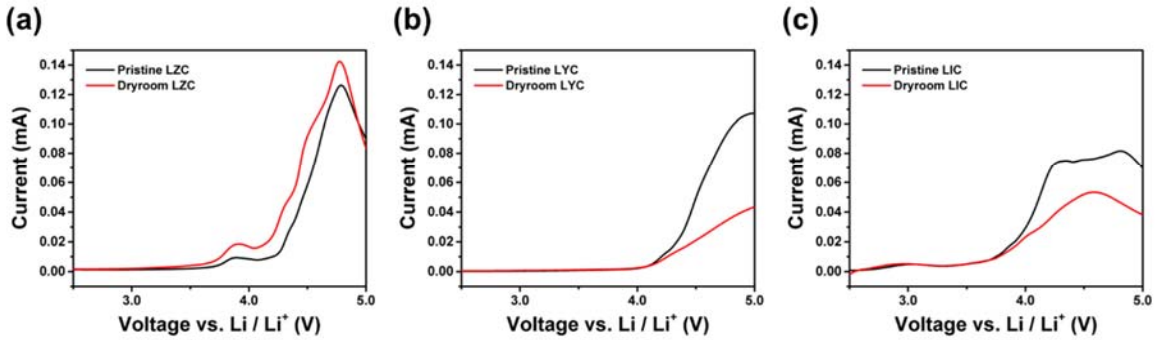

Figure 4.12. The LSV of pristine and Air-Exp chloride SSEs.

Figure 4.13 presents the cycling performance and impedance changes before and after 50 cycles (Detailed fitting results are shown in Figure 4.14). After dry room exposure, the impedance of the cells increased, especially the charge transfer impedance, indicating the decomposed products have negative impact to the electrochemical performance.

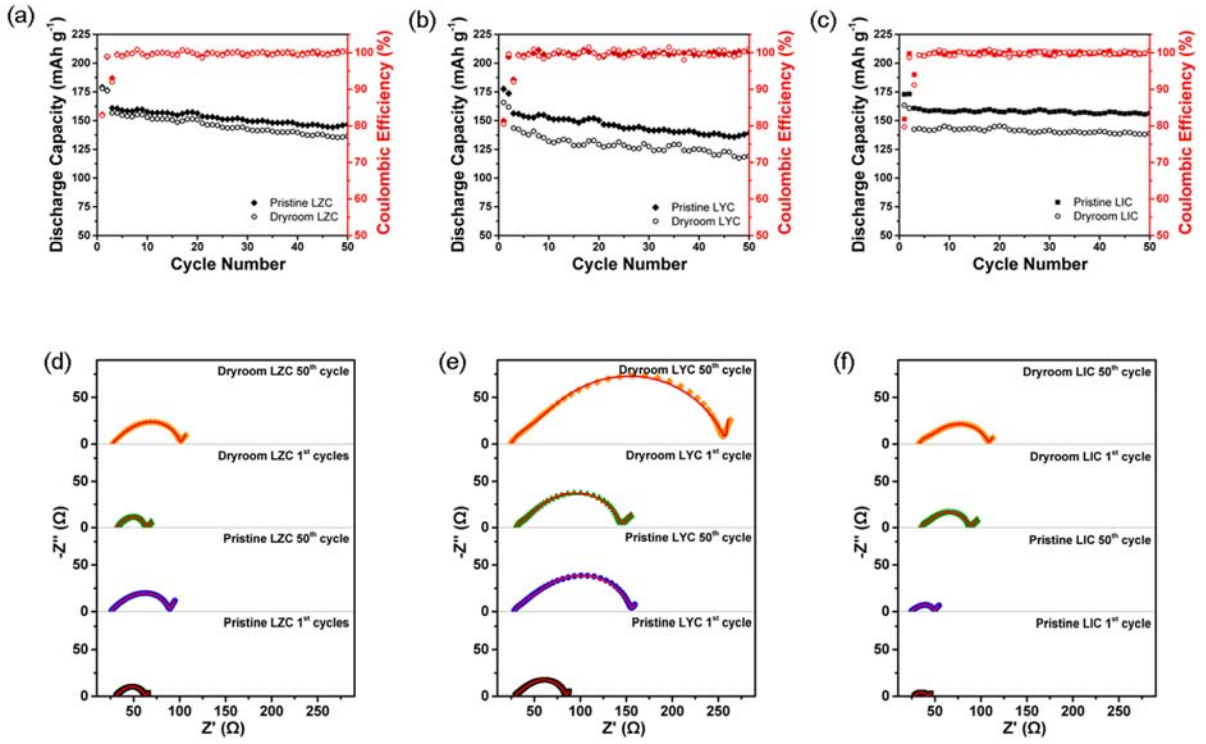

Figure 4.13. (a), (b), (c) Cycle performance and (d), (e), (f) corresponding impedance changes of NCM | Li-In half-cells whose cathode composites contain pristine and dry-room-exposed LZC, LYC, and LIC as catholytes.

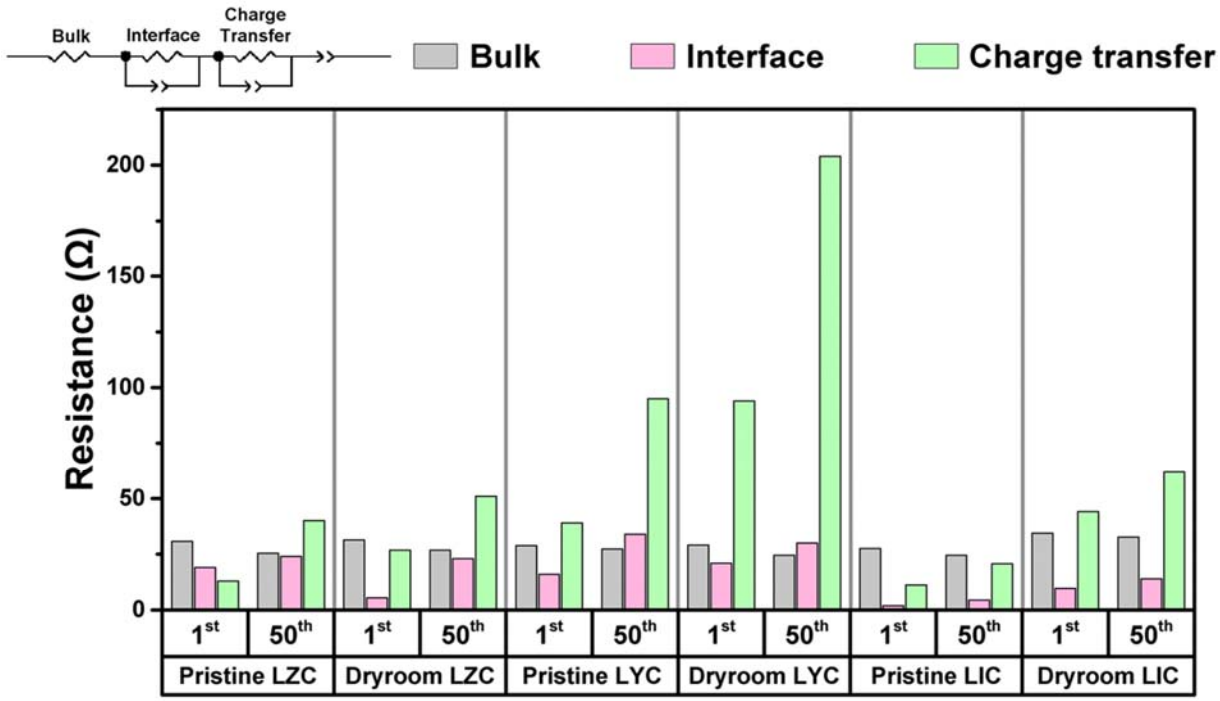

Figure 4.14. The fitted resistance values of the NCM811 | LiIn half cells using pristine and Air-Exp LZC, LYC and LIC as catholytes. The Nyquist plots in Figure 4.13(d), (e) and (f) are fitted with the top left circuit.

The larger cell impedance resulted in more polarization and longer constant voltage capacities at the end of charging (Figure 4.15). Consequently, NCM811 half cells using dry room exposed SSEs exhibited reduced capacities. The dry room exposed LZC cell exhibited the least capacity drop compared to its pristine form among the three SSEs, as the EIS had relatively minor degradation after the dry room exposure (Figure 4.13d). The LYC cell exhibited the worst capacity retention among the three SSEs, as the dry room exposed LYC also exhibited the lowest ionic conductivity of 6.4×10^{-5} S cm^{-1} (Figure 4.11a). A slight further capacity reduction can be observed in all cells, possibly because of contact loss or cathode electrolyte interphase formation, and it was reflected in the impedance increase shown in the Nyquist plots.[46-47]

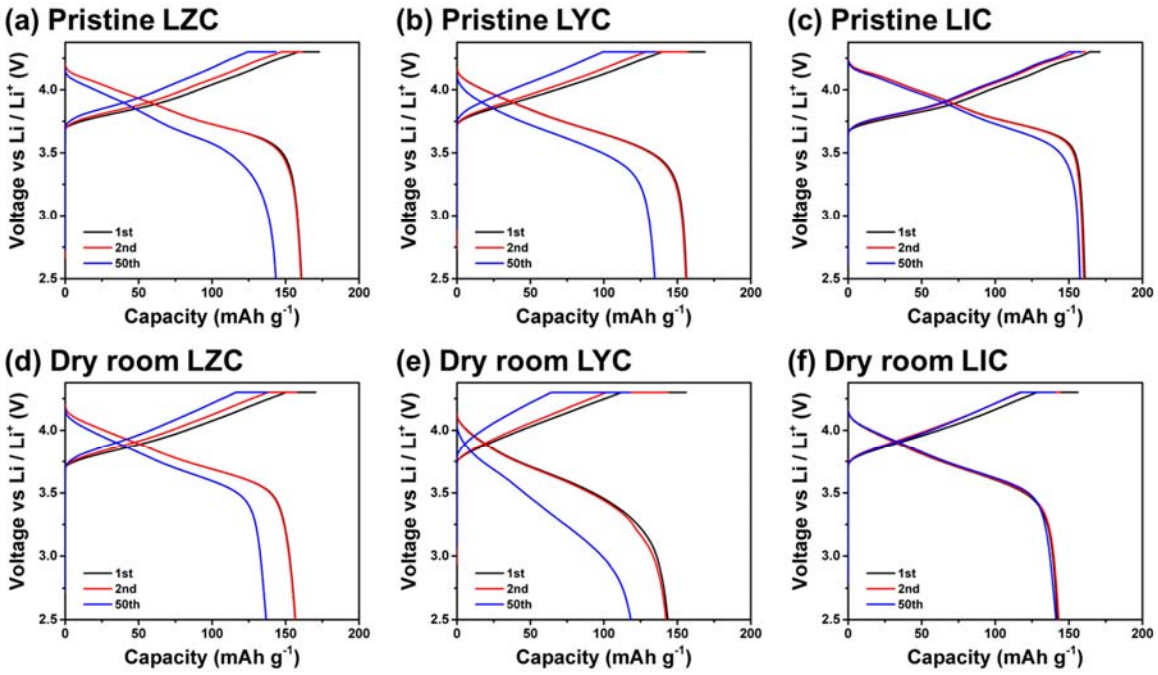

Figure 4.15. The voltage profiles of the NCM811 | LiIn half cells using (a) LZC, (b) LYC, (c) LIC, air-Exp (d) LZC, (e) LYC, and (f) LIC as catholyte.

4.4 Conclusion

In this study, three chloride SSEs, namely LZC, LYC, and LIC, were synthesized and their chemical evolution during air exposure and heat treatment was analyzed using EIS, XRD, and TGA/DSC–MS. The experimental analysis indicates that the chloride SSEs suffer from different decomposition in moisture atmosphere depending on its metal center. Firstly, LZC hydrolyzes into ZrO_2 and LiCl upon contacting moisture and is not recoverable after heat treatment. Secondly, LYC decomposes into $YCl_3 \cdot 6H_2O$ and $LiCl \cdot H_2O$ during the exposure and YCl_3 further hydrolyzes to form YOCl, making LYC unrecoverable. Lastly, LIC forms a stable hydrate and can be easily recovered when heated to 260 °C to remove hydrated water. Finally, all three materials were exposed to a dry room environment with a dew point of −60 °C for three hours. Subsequent electrochemical tests indicate that all SSEs suffer from ionic conductivity decay, which is reflected in the reduced discharge capacity of NCM811|LiIn half cells. The SSEs evaluated here are

sensitive to moisture even in dry room conditions. Nevertheless, surface modifications or doping can be explored to increase the moisture tolerance of chloride SSEs.

Chapter 4, in full, has been submitted for publication as “Investigating dry room compatibility of Chloride solid-state electrolytes for scalable manufacturing” as a research article in Journal of Electrochemical Society. Chen, Y.-T.; Tan, D. H. S.; Ham, S. Y.; Sayahpour, B.; Lee, J. B.; Kim, Y.; Song, M. S.; Nguyen, L. H. B.; Oh, J. A. S.; Ridley, P.; Cronk, A.; Deysher, G.; Jang, J.; Chen, Z.; Meng, Y. S. 2023, *170*, 080521. The dissertation author was the first author of this paper, all authors contributed to this work.

References

1. Horowitz, Y.; Schmidt, C.; Yoon, D.-h.; Riegger, L. M.; Katzenmeier, L.; Bosch, G. M.; Noked, M.; Ein-Eli, Y.; Janek, J.; Zeier, W. G., Between Liquid and All Solid: A Prospect on Electrolyte Future in Lithium-Ion Batteries for Electric Vehicles. *Energy Technology* **2020,** *8* (11), 2000580.

2. Jung, Y. S.; Oh, D. Y.; Nam, Y. J.; Park, K. H., Issues and challenges for bulk-type all-solid-state rechargeable lithium batteries using sulfide solid electrolytes. *Isr. J. Chem.* **2015,** *55* (5), 472-485.

3. Kerman, K.; Luntz, A.; Viswanathan, V.; Chiang, Y.-M.; Chen, Z., practical challenges hindering the development of solid state Li ion batteries. *J. Electrochem. Soc.* **2017,** *164* (7), A1731.

4. Lee, H.; Oh, P.; Kim, J.; Cha, H.; Chae, S.; Lee, S.; Cho, J., Advances and Prospects of Sulfide All-Solid-State Lithium Batteries via One-to-One Comparison with Conventional Liquid Lithium Ion Batteries. *Adv. Mater.* **2019,** *31* (29), 1900376.

5. Tan, D. H.; Chen, Y.-T.; Yang, H.; Bao, W.; Sreenarayanan, B.; Doux, J.-M.; Li, W.; Lu, B.; Ham, S.-Y.; Sayahpour, B., Carbon Free High Loading Silicon Anodes Enabled by Sulfide Solid Electrolytes for Robust All Solid-State Batteries. *arXiv preprint arXiv:2103.04230* **2021**.

6. Huo, H.; Janek, J. r., Silicon as Emerging Anode in Solid-State Batteries. *ACS Energy Letters* **2022,** *7* (11), 4005-4016.

7. Cangaz, S.; Hippauf, F.; Reuter, F. S.; Doerfler, S.; Abendroth, T.; Althues, H.; Kaskel, S., Enabling High-Energy Solid-State Batteries with Stable Anode Interphase by the Use of Columnar Silicon Anodes. *Adv. Energy Mater.* **2020,** *10* (34), 2001320.

8. Ham, S.-Y.; Yang, H.; Nunez-cuacuas, O.; Tan, D. H.; Chen, Y.-T.; Deysher, G.; Cronk, A.; Ridley, P.; Doux, J.-M.; Wu, E. A., Assessing the critical current density of all-solid-state Li metal symmetric and full cells. *Energy Storage Materials* **2023,** *55*, 455-462.

9. Kwak, H.; Wang, S.; Park, J.; Liu, Y.; Kim, K. T.; Choi, Y.; Mo, Y.; Jung, Y. S., Emerging Halide Superionic Conductors for All-Solid-State Batteries: Design, Synthesis, and Practical Applications. *ACS Energy Letters* **2022,** *7* (5), 1776-1805.

10. Park, K. H.; Bai, Q.; Kim, D. H.; Oh, D. Y.; Zhu, Y.; Mo, Y.; Jung, Y. S., Design Strategies, Practical Considerations, and New Solution Processes of Sulfide Solid Electrolytes for All-Solid-State Batteries. *Adv. Energy Mater.* **2018,** *8* (18), 1800035.

11. Kim, K. J.; Balaish, M.; Wadaguchi, M.; Kong, L.; Rupp, J. L., Solid-State Li–Metal Batteries: Challenges and Horizons of Oxide and Sulfide Solid Electrolytes and Their Interfaces. *Adv. Energy Mater.* **2021,** *11* (1), 2002689.

12. Kim, K. H.; Iriyama, Y.; Yamamoto, K.; Kumazaki, S.; Asaka, T.; Tanabe, K.; Fisher, C. A.; Hirayama, T.; Murugan, R.; Ogumi, Z., Characterization of the interface between LiCoO2 and Li7La3Zr2O12 in an all-solid-state rechargeable lithium battery. *J. Power Sources* **2011,** *196* (2), 764-767.

13. Jang, J.; Chen, Y.-T.; Deysher, G.; Cheng, D.; Ham, S.-Y.; Cronk, A.; Ridley, P.; Yang, H.; Sayahpour, B.; Han, B., Enabling a Co-Free, High-Voltage LiNi0. 5Mn1. 5O4 Cathode in All-Solid-State Batteries with a Halide Electrolyte. *ACS Energy Letters* **2022,** *7* (8), 2531-2539.

14. Cronk, A.; Chen, Y.-T.; Deysher, G.; Ham, S.-Y.; Yang, H.; Ridley, P.; Sayahpour, B.; Nguyen, L. H. B.; Oh, J. A. S.; Jang, J., Overcoming the Interfacial Challenges of LiFePO4 in Inorganic All-Solid-State Batteries. **2022**.

15. Bohnsack, A.; Stenzel, F.; Zajonc, A.; Balzer, G.; Wickleder, M. S.; Meyer, G., Ternäre Halogenide vom Typ A3MX6. VI [1]. Ternäre Chloride der Selten-Erd-Elemente mit Lithium, Li3MCl6 (M Tb Lu, Y, Sc): Synthese, Kristallstrukturen und Ionenbewegung. *Z. Anorg. Allg. Chem.* **1997,** *623* (7), 1067-1073.

16. Li, X.; Liang, J.; Yang, X.; Adair, K. R.; Wang, C.; Zhao, F.; Sun, X., Progress and perspectives on halide lithium conductors for all-solid-state lithium batteries. *Energy Environ. Sci.* **2020,** *13* (5), 1429-1461.

17. Asano, T.; Sakai, A.; Ouchi, S.; Sakaida, M.; Miyazaki, A.; Hasegawa, S., Solid Halide Electrolytes with High Lithium-Ion Conductivity for Application in 4 V Class Bulk-Type All-Solid-State Batteries. *Adv. Mater.* **2018,** *30* (44), 1803075.

18. Kim, K.; Park, D.; Jung, H.-G.; Chung, K. Y.; Shim, J. H.; Wood, B. C.; Yu, S., Material design strategy for halide solid electrolytes Li3MX6 (X= Cl, Br, and I) for all-solid-state high-voltage Li-ion batteries. *Chem. Mater.* **2021,** *33* (10), 3669-3677.

19. Wang, S.; Bai, Q.; Nolan, A. M.; Liu, Y.; Gong, S.; Sun, Q.; Mo, Y., Lithium Chlorides and Bromides as Promising Solid-State Chemistries for Fast Ion Conductors with Good Electrochemical Stability. *Angew. Chem. Int. Ed.* **2019,** *58* (24), 8039-8043.

20. Schlem, R.; Muy, S.; Prinz, N.; Banik, A.; Shao-Horn, Y.; Zobel, M.; Zeier, W. G., Mechanochemical synthesis: a tool to tune cation site disorder and ionic transport properties of Li3MCl6 (M= Y, Er) superionic conductors. *Adv. Energy Mater.* **2020,** *10* (6), 1903719.

21. Kwak, H.; Han, D.; Lyoo, J.; Park, J.; Jung, S. H.; Han, Y.; Kwon, G.; Kim, H.; Hong, S. T.; Nam, K. W., New Cost-Effective Halide Solid Electrolytes for All-Solid-State Batteries: Mechanochemically Prepared Fe3+-Substituted Li2ZrCl6. *Adv. Energy Mater.* **2021,** *11* (12), 2003190.

22. Park, J.; Han, D.; Kwak, H.; Han, Y.; Choi, Y. J.; Nam, K.-W.; Jung, Y. S., Heat treatment protocol for modulating ionic conductivity via structural evolution of Li3-xYb1-xMxCl6 (M= Hf4+, Zr4+) new halide superionic conductors for all-solid-state batteries. *Chem. Eng. J.* **2021,** *425*, 130630.

23. Park, K.-H.; Kaup, K.; Assoud, A.; Zhang, Q.; Wu, X.; Nazar, L. F., High-voltage superionic halide solid electrolytes for all-solid-state Li-ion batteries. *ACS Energy Letters* **2020,** *5* (2), 533-539.

24. Singer, C. l.; Töpper, H.-C.; Kutsch, T.; Schuster, R.; Koerver, R.; Daub, R. d., Hydrolysis of Argyrodite Sulfide-Based Separator Sheets for Industrial All-Solid-State Battery Production. *ACS Applied Materials & Interfaces* **2022**.

25. Chen, Y.-T.; Marple, M. A.; Tan, D. H.; Ham, S.-Y.; Sayahpour, B.; Li, W.-K.; Yang, H.; Lee, J. B.; Hah, H. J.; Wu, E. A., Investigating dry room compatibility of sulfide solid-state electrolytes for scalable manufacturing. *J. Mater. Chem. A* **2022,** *10* (13), 7155-7164.

26. Li, X.; Liang, J.; Adair, K. R.; Li, J.; Li, W.; Zhao, F.; Hu, Y.; Sham, T.-K.; Zhang, L.; Zhao, S., Origin of Superionic Li3Y1–x In x Cl6 Halide Solid Electrolytes with High Humidity Tolerance. *Nano Lett.* **2020,** *20* (6), 4384-4392.

27. Taylor, M. D., Preparation of Anhydrous Lanthanon Halides. *Chem. Rev.* **1962,** *62* (6), 503-511.

28. Li, W.; Liang, J.; Li, M.; Adair, K. R.; Li, X.; Hu, Y.; Xiao, Q.; Feng, R.; Li, R.; Zhang, L., Unraveling the origin of moisture stability of halide solid-state electrolytes by in situ and operando synchrotron X-ray analytical techniques. *Chem. Mater.* **2020,** *32* (16), 7019-7027.

29. Wang, K.; Ren, Q.; Gu, Z.; Duan, C.; Wang, J.; Zhu, F.; Fu, Y.; Hao, J.; Zhu, J.; He, L., A cost-effective and humidity-tolerant chloride solid electrolyte for lithium batteries. *Nature Communications* **2021,** *12* (1), 1-11.

30. Li, X.; Liang, J.; Luo, J.; Banis, M. N.; Wang, C.; Li, W.; Deng, S.; Yu, C.; Zhao, F.; Hu, Y., Air-stable Li 3 InCl 6 electrolyte with high voltage compatibility for all-solid-state batteries. *Energy Environ. Sci.* **2019,** *12* (9), 2665-2671.

31. Schmidt, M. O.; Wickleder, M. S.; Meyer, G., Zur Kristallstruktur von Li3InCl6. *Z. Anorg. Allg. Chem.* **1999,** *625* (4), 539-540.

32. Schlem, R.; Banik, A.; Ohno, S.; Suard, E.; Zeier, W. G., Insights into the lithium sub-structure of superionic conductors Li3YCl6 and Li3YBr6. *Chem. Mater.* **2021,** *33* (1), 327-337.

33. Fang, Z.; Dixon, D. A., Hydrolysis of ZrCl4 and HfCl4: The initial steps in the high-temperature oxidation of metal chlorides to produce ZrO2 and HfO2. *The Journal of Physical Chemistry C* **2013,** *117* (15), 7459-7474.

34. Ievină, A.; Straumanis, M.; Karlsons, K., Präzisionsbestimmung von Gitterkonstanten hygroskopischer Verbindungen (LiCl, NaBr). *Z. Phys. Chem.* **1938,** *40* (1), 146-150.

35. Bondars, B.; Heidemane, G.; Grabis, J.; Laschke, K.; Boysen, H.; Schneider, J.; Frey, F., Powder diffraction investigations of plasma sprayed zirconia. *Journal of Materials Science* **1995,** *30* (6), 1621-1625.

36. Bell, A.; Smith, A., Structure of hexaaquadichloroyttrium (III) chloride. *Acta Crystallogr. Sect. C: Cryst. Struct. Commun.* **1990,** *46* (6), 960-962.

37. Hönnerscheid, A.; Nuss, J.; Mühle, C.; Jansen, M., Die Kristallstrukturen der Monohydrate von Lithiumchlorid und Lithiumbromid. *Z. Anorg. Allg. Chem.* **2003,** *629* (2), 312-316.

38. Meyer, G.; Garcia, E.; Corbett, J. D., The ammonium chloride route to anhydrous rare earth chlorides—The example of YCl3. *Inorg. Synth.* **1989,** *25*, 146-150.

39. Wang, C.; Liang, J.; Luo, J.; Liu, J.; Li, X.; Zhao, F.; Li, R.; Huang, H.; Zhao, S.; Zhang, L., A universal wet-chemistry synthesis of solid-state halide electrolytes for all-solid-state lithium-metal batteries. *Science advances* **2021,** *7* (37), eabh1896.

40. Meyer, G.; Ax, P., An analysis of the ammonium chloride route to anhydrous rare-earth metal chlorides. *Mater. Res. Bull.* **1982,** *17* (11), 1447-1455.

41. Meyer, G.; Staffel, T., Die Tieftemperatur-Synthese von Oxidhalogeniden, YOX (X= Cl, Br, I), als Quelle der Verunreinigung von Yttriumtrihalogeniden, YX3, bei der Gewinnung nach der Ammoniumhalogenid-Methode. Die Analogie von YOCl und YSCl. *Z. Anorg. Allg. Chem.* **1986,** *532* (1), 31-36.

42. Wulfsberg, G., *Principles of descriptive inorganic chemistry*. University Science Books: 1991.

43. Meyer, G.; Dötsch, S.; Staffel, T., The ammonium-bromide route to anhydrous rare earth bromides MBr3. *Journal of the Less Common Metals* **1987,** *127*, 155-160.

44. Wang, S.; Xu, X.; Cui, C.; Zeng, C.; Liang, J.; Fu, J.; Zhang, R.; Zhai, T.; Li, H., Air sensitivity and degradation evolution of halide solid state electrolytes upon exposure. *Adv. Funct. Mater.* **2022,** *32* (7), 2108805.

45. Shin, J. H.; Choi, M. S.; Min, D. J.; Park, J. H., Isothermal and non-isothermal sublimation kinetics of zirconium tetrachloride (ZrCl4) for producing nuclear grade Zr. *Mater. Chem. Phys.* **2014,** *143* (3), 1075-1081.

46. Koerver, R.; Aygün, I.; Leichtweiß, T.; Dietrich, C.; Zhang, W.; Binder, J. O.; Hartmann, P.; Zeier, W. G.; Janek, J. r., Capacity fade in solid-state batteries: interphase formation and chemomechanical processes in nickel-rich layered oxide cathodes and lithium thiophosphate solid electrolytes. *Chem. Mater.* **2017,** *29* (13), 5574-5582.

47. Shi, T.; Zhang, Y.-Q.; Tu, Q.; Wang, Y.; Scott, M.; Ceder, G., Characterization of mechanical degradation in an all-solid-state battery cathode. *J. Mater. Chem. A* **2020,** *8* (34), 17399-17404.

Chapter 5. Enabling Uniform and Accurate Control of Cycling Pressure for All-Solid-State Batteries

5.1 Introduction

All-solid-state batteries (ASSBs) are hailed as one of the next generation storage technologies and tremendous efforts have been invested to their development. As solid-state electrolytes (SSEs) are employed to replace liquid electrolytes in conventional Li batteries, ASSBs exhibit reduced flammability and leakage issues.[1-4] Moreover, anodes with high energy density, such as pure Si,[5-6] have been reported to achieve long cycle life in ASSBs, but is challenging in liquid electrolytes as Si will suffer from pulverization during cycling resulting in continuous solid electrolyte interphase (SEI) formation.[7-11] Despite the advantages, there are many engineering challenges for ASSBs stemming from solid-solid contacts on interfaces.[12] The inability to flow and infiltrate into voids in electrode is a double-edged sword: it limits the SEI formation but volumetric changes in electrode can potentially cause detachment of electrode material – SSE interfaces.[13-14] As such, pressure becomes a crucial factor to maintain intimate interfacial contact and ensure the performance of ASSBs – not only in cell fabrication, but also during cell cycling.

Pellet type ASSBs are usually employed in research labs for electrochemical tests. A polymer die and a pair of metal plungers are employed to contain and apply fabrication pressure to pelletize the materials. During electrochemical tests, a cell holder consisting of bolts, nuts and plates is required to apply cycling pressure and the metal plungers serve as current collectors (Figure 5.1a). As most inorganic SSEs are brittle, SSE layers typically have a high thickness of approximately 500 μm to guarantee a sufficient strength to support the cells mechanically. This reduces the energy density of ASSBs, as SSE layers do not store energy.[15-18] Moreover, due to the friction at the die walls during uniaxial compaction, it is challenging to achieve a uniform density distribution throughout the whole pellet, and this may negatively affect their electrochemical performance. Having thinner layer thickness, larger electrode area, and do not

require polymer dies, pouch cells not only exhibit significantly higher energy density, but also achieve better density distribution after calendering (Figure 5.1b). As the wrapping materials of pouch cells are flexible, isostatic pressure can be applied to further improve the density uniformity, which has been well-demonstrated in the literature.[19-20]

Although multiple groups have claimed to demonstrate solid-state pouch cells in the literature, many adulterate excess amount of polymer binders, Li salts, and even solvents to boost the performance. These defeat the safety feature of ASSBs. Nevertheless, several all-solid-state pouch cells (ASSPC) with more than 3 mAh cm^{-2} employing only inorganic SSE (with low amount of binders) were reported (Table 5.1). Most pouch cells had areal capacities more than 3 mAh cm^{-2}, which is similar to or more than that in commercial Li batteries. Nevertheless, many cells were tested at C-rates lower than 0.1 C, and elevated temperature was required to realize higher C-rates and areal capacities. As SSEs do not flow and conform to the shape of electrode materials like liquid electrolytes, a pressure must be applied to ASSBs to ensure intimate interfacial contact, both in fabrication and during cycling.[12, 20-21] Most articles report only fabrication pressure, typically 300 to 500 MPa, without mentioning cycling pressure. However, cycling pressure is a more important metric for commercialization, as high cycling pressure will vastly increase the dead weight of the system and detriment the module energy density. Since a low cycling pressure usually reduces the interfacial contact, and thus results in worse electrochemical performance of ASSBs, it is critical to design cell holders that provide uniform cycling pressure.

Pouch cell holders consisting of bolts, nuts, and rigid plates are employed in most articles to apply uniaxial pressure to pouch cells (Figure 5.1c). Some may attach bearings between moving plates and bolts to ensure smooth movement and parallelism. However, several studies have observed that the cycling pressure of ASSBs changes during cell cycling due to the volume change of electrode materials.[22-23] For example, Si undergoes 300% of volume expansion and the thickness of Li metal anodes increases approximately 5 μm when each mAh cm^{-2} is plated.[24]

This may negatively affect their electrochemical performance, especially when pressure sensitive materials, such as Li metal, are used. To address this problem, Ham et al incorporate springs into the cell holders to accommodate cycling volume change. Such a design successfully reduced the cycling volume change of a $LiNi_{0.8}Co_{0.1}Mn_{0.1}O_2$ (NCM811) | Li cell from 2 MPa to less than 0.5 MPa, and thus doubled its critical current density.[23] Thus, an improved uniaxial pouch cell holder (UPCH) design containing springs and rubber gaskets was also proposed (Figure 5.1d).[16] Nevertheless, rubber and springs may be susceptible to material fatigue and the applied force would decrease over time. It is noteworthy that the cell pressure may also change if the ambient temperature fluctuates, since the thermal expansion coefficients of pouch cells and bolts are different. As such, pressure regulation systems are required to ensure the stability of cell cycling. Unfortunately, regulating the pressure accurately by turning the bolts is challenging, as the motors need to overcome large friction under high pressure load, and extra efforts are needed to synchronize the torque all bolts in one cell holder. To tackle this issue, fluids, including gases and liquids, can potentially be utilized as pressurizing media to apply isostatic cycling pressure. Gases can be used when light weight, low cost, or low X-ray absorption (e.g., in-situ cell characterization application) are addressed, and liquids can be employed when pressure load and heat dissipation are demanding. Instead of bolts and nuts, an isostatic pouch cell holder (IPCH) requires a chamber and gaskets to contain the pressurizing fluid and ASSPCs. A valve is installed to fill or evacuate the fluid, and a wire fit-through is implemented to electrically connect ASSPCs inside the chamber (Figure 5.1e). As fluids are significantly more compressible and conforming than solids, IPCHs can easily accommodate cell volume change during cycling. Moreover, the pressure regulating systems of pressurized fluids and gases are mature and widely available, and thus maintaining a constant cycling pressure in IPCHs for an extended period of time can be easily achieved, even in an environment with large temperature fluctuation. To verify our perspective, three cell holders were assembled.

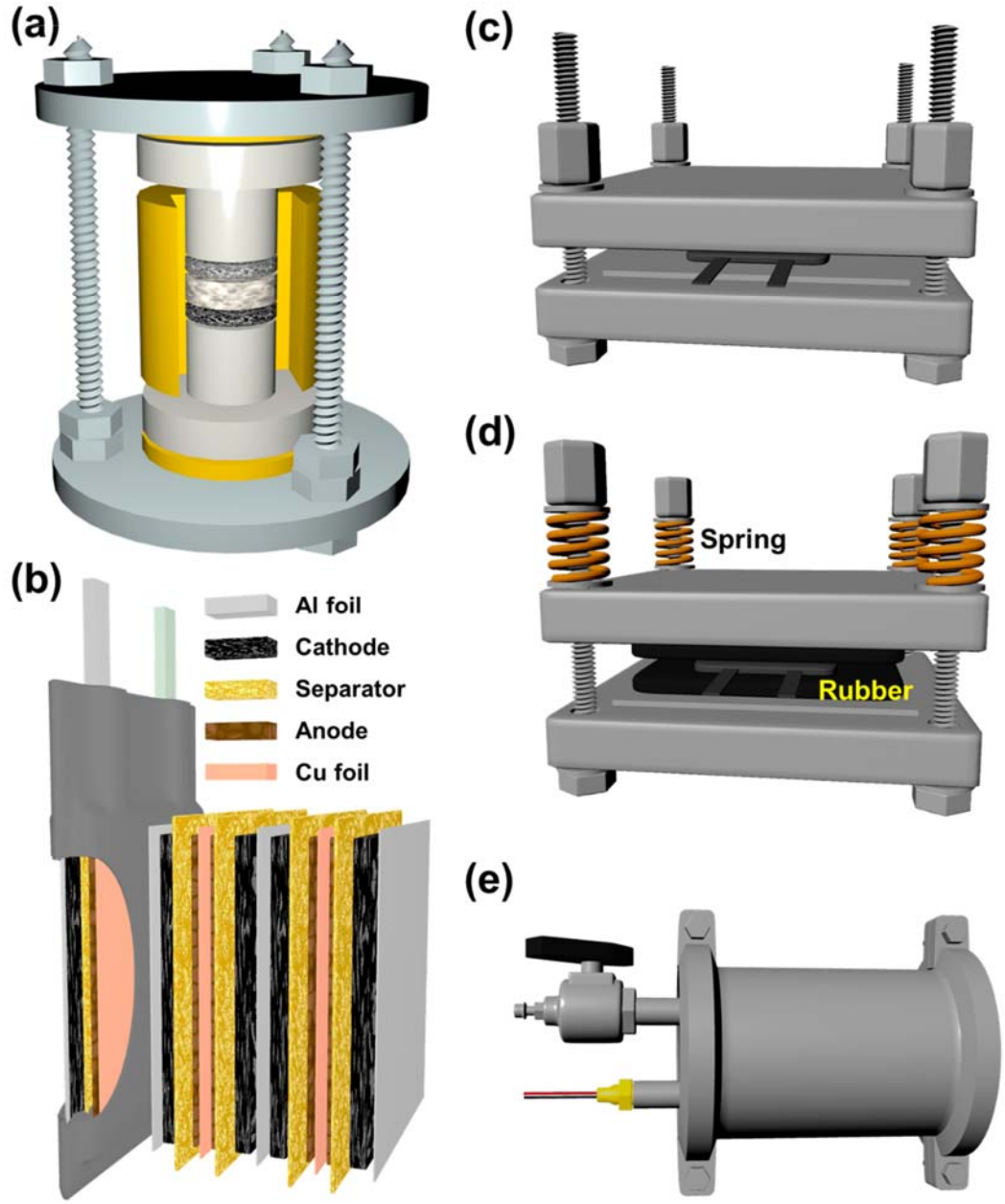

Figure 5.1. The structure of (a) a plunger cell clamped in a cell holder, and (b) a multilayer pouch cell. The schematic of (c) a bare UPCH with simple metal plates, (d) an improved UPCH with springs and rubber gaskets, and (e) an IPCH.

Table 5.1. The formats and the cycling conditions of ASSPC reported in the literature.

Ref	Cathode | SSE | Anode	Temperature (°C)	Fabrication pressure (MPa)	Cycling Pressure (MPa)	Cycle Number	Areal Capacity (mAh cm^{-2})	C rate	Dimension (cm^2)
[25]	$LiNi_{0.8}Co_{0.15}Al_{0.05}O_2$ | $Li_2SeP_2S_5$ | Graphite	25			100	4.2	0.1 C	8.8x5.3
[26]	$LiNi_{1/3}Co_{1/3}Mn_{1/3}O_2$ | 75 Li_2S·25 P_2S_5 | Graphite	30	330 MPa		10	1.536	C/24	2x2
[27]	$LiNi_{0.6}Co_{0.2}Mn_{0.2}O_2$ | Li_6PS_5Cl | Graphite	30	492 MPa			4.2	0.025 C	8x6
[19]	$LiNi_{0.8}Co_{0.1}Mn_{0.1}O_2$ | Li_6PS_5Cl | C-Ag	60	490 MPa	2	1000	6.8	0.5 C	11.2x6.7
[6]	$LiNi_{09}Co_{0.05}Mn_{0.05}O_2$ | Li_6PS_5Cl | PVD-Si	25	300 MPa	20	50	3	0.05 C	2.5x2.5
[28]	S | Li_6PS_5Cl | Li	30	300 MPa		10	3	0.01 C	3x3
[17]	$LiNi_{0.8}Co_{0.1}Mn_{0.1}O_2$ | Li_6PS_5Cl | LiIn	25			200		0.15 C	6x6
[29]	Sulfur | Solid electrolyte | LiIn	30	500 MPa		50	3.2	0.05 - 2 C	
[30]	$LiNi_{0.6}Co_{0.2}Mn_{0.2}O_2$ | Li_6PS_5Cl | LiIn				100	4	0.1 C	

5.2 Materials and Methods

5.2.1 Fabrication of Electrolytes and SSE Separators

Dry-processed $LiNi_{0.8}Co_{0.1}Mn_{0.1}O_2$ (NCM811, LG Energy Solution) cathode composite, dry-processed Li_6PS_5Cl (LPSCl, NEI Corporation) SSE separator and slurry-processed Si anode were employed in ASSPCs. To fabricate NCM811 cathode composite, NCM811, LPSCl, vapor grown carbon fiber (VGCF, Sigma-Aldrich) and polytetrafluoroethylene (PTFE) were mixed in a mortar and a pestle at a weight ratio of 66 : 31 : 3 : 0.1 until a dough formed. The dough was then transferred to a hot roller set at 60°C(TMAXCN) to fabricate films following the protocol described in the previous article.[31] Shear force was applied during mixing and rolling to fibrillate PTFE and strengthen the films.[31-34] A similar procedure was applied to fabricate LPSCl SSE separator, with a weight ratio of LPSCl : PTFE = 99.9 : 0.1. To prepare μ-Si electrodes, 99.9 wt% μ-Si

(Thermofisher) powder and 0.1 wt% PVDF binder was dispersed in N-Methyl-2-Pyrrolidone (NMP) solvent using a Thinky mixer to create a slurry. The slurry is casted on a piece of 10 μm copper foil current collector using a doctor blade on an automatic film coater. The electrode was vacuum dried at 80^{o}C overnight to remove the solvent. The dried electrode is then punched into suitable shapes to be used for ASSPC fabrication.

5.2.2 Fabrication of ASSPCs

Two pouch cell formats were used in this study: two-electrode, three-electrode electrochemical characterization cells, and bilayer cells. Cathode composite films with a dimension of 15 mm x 35 mm x 160 μm (resulted in an areal loading of 4 mAh cm^{-2}), SSE separators with a dimension of 20 mm x 50 x mm 300 μm, and Si anode with NP ratio of 1.2 and a dimension of 18 mm x 40 mm were selected for two-electrode electrochemical characterization cells. The area of cathode composite films was the smallest, as it was selected as capacity limiting component, and SSE separators were the largest to electronically separate cathodes and anodes. To assemble an electrochemical characterization cell, Cu, Si, LPSCl, NCM811 cathode composite and Al were stacked from button to top and secured with Kapton tape. An Al tab was welded to the Al current collector as the positive terminal, and a Ni tab to the Cu current collector as the negative terminal (both terminals are 4 mm in width). The whole stack was then vacuum sealed in the Al laminated film and calendered using a cold isostatic press (MTI Corporation). To understand the effect of calender pressure on the electrochemical performance, ASSPCs calendered at 150, 350 and 500 MPa with three-minute hold time were cycled and characterized (Figure 5.2 and 5.3). All cells successfully accomplished 100 cycles (Figure 5.2a-c). The ASSPCs used in fabrication study were cycled at ambient temperature, resulting in fluctuated Coulombic efficiency and capacity retention. Higher capacity retention was obtained as the fabrication pressure increased, as it increases interfacial contacts. The P-FIB / SEM cross-sectional images (Figure 5.3) of cathode composite calendered at different fabrication pressures were segmented

to identify the porosity (Figure 5.2d-f), and the porosity decreased as the fabrication increased. The EIS at the first and the thirtieth cycle also exhibited decreased cell impedance at higher fabrication pressure, explaining the capacity retention results.

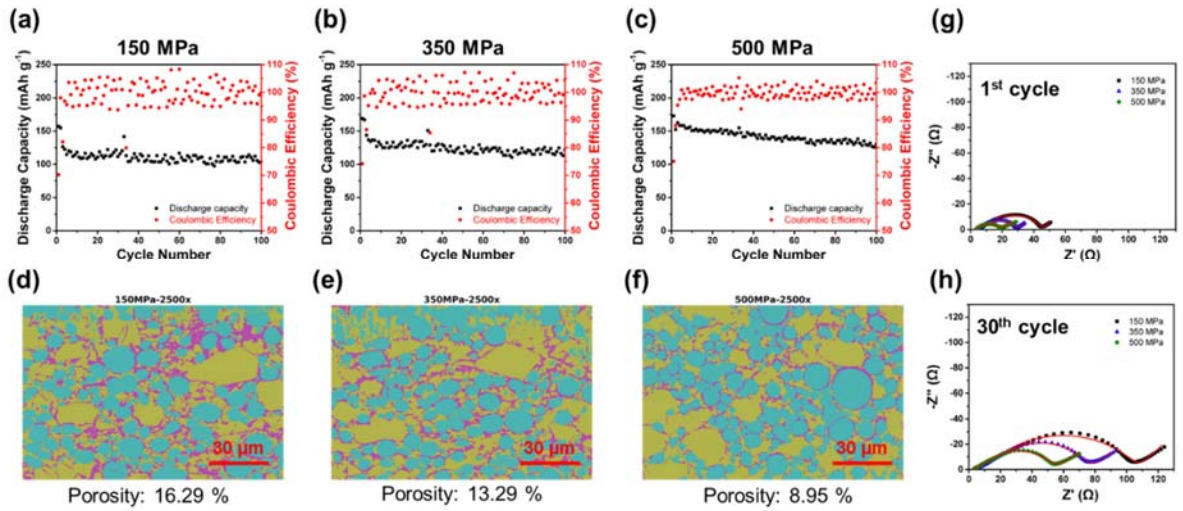

Figure 5.2. The capacity retention and Coulombic efficiency of pouch cells fabricated using (a) 150 MPa, (b) 350 MPa and (c) 500 MPa. The segmented FIB cross section images and porosities are shown in (d) to (f). The EIS of their (g) 1st cycle and (h) 30th cycle were measured.

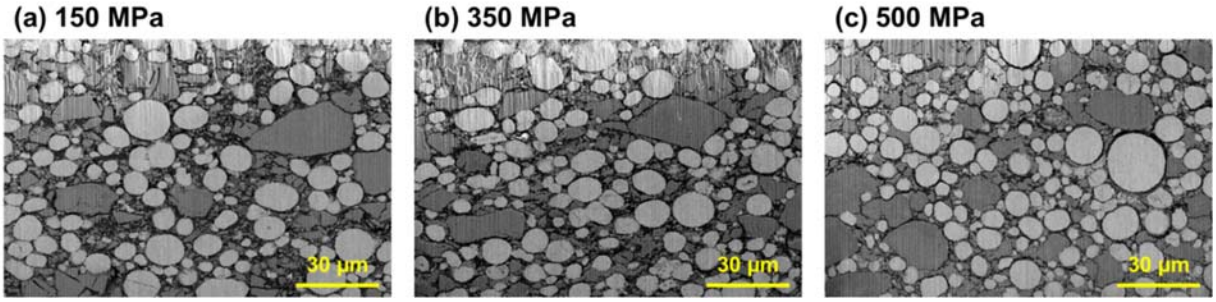

Figure 5.3. The P-FIB cross section of NCM811 cathode composite calendered at (a) 150 MPa, (b) 350 MPa and (c) 500 MPa.

500 MPa was selected to calendar the ASSPCs to study the effect of cycling pressure, as it was the largest pressure that the equipment could provide and yielded the best electrochemical performance. After calendering, cycling pressures were applied to ASSPCs using UPCHs and IPCHs. A torque wrench was used to control the cycling pressure of UPCHs, and a high-pressure air compressor was used to apply cycling pressure for IPCHs. To fabricate three-electrode

electrochemical characterization cells, the horizontal dimensions of cathodes and anodes were reduced to 10 mm × 35 mm and 12 mm × 40 mm. Two pieces of Li metal (20 μm thick) were placed next to the cathode and anode, and on both sides of the SSE separator (Figure 5.4a).[35] The cells were calendered at 150 MPa with minimal hold time to prevent excessive Li-creeping. The rest of the fabrication steps were identical to those of two-electrode electrochemical characterization cells. Cathode composite films with a dimension of 30 mm x 35 mm x 200 μm (resulted in an areal loading of 5 mAh cm^{-2}), SSE separators with a thickness of 35 mm x 40 mm 300 μm, and Si anode with NP ratio of 1.2 and a dimension of 35 mm x 37 mm were selected for bilayer cells. They were stacked in a sequence of Cu, Si, LPSCl, NCM811 cathode composite, Al, NCM811 cathode composite, LPSCl, Si, and Cu. The rest of the fabrication steps were identical to those of electrochemical characterization cells.

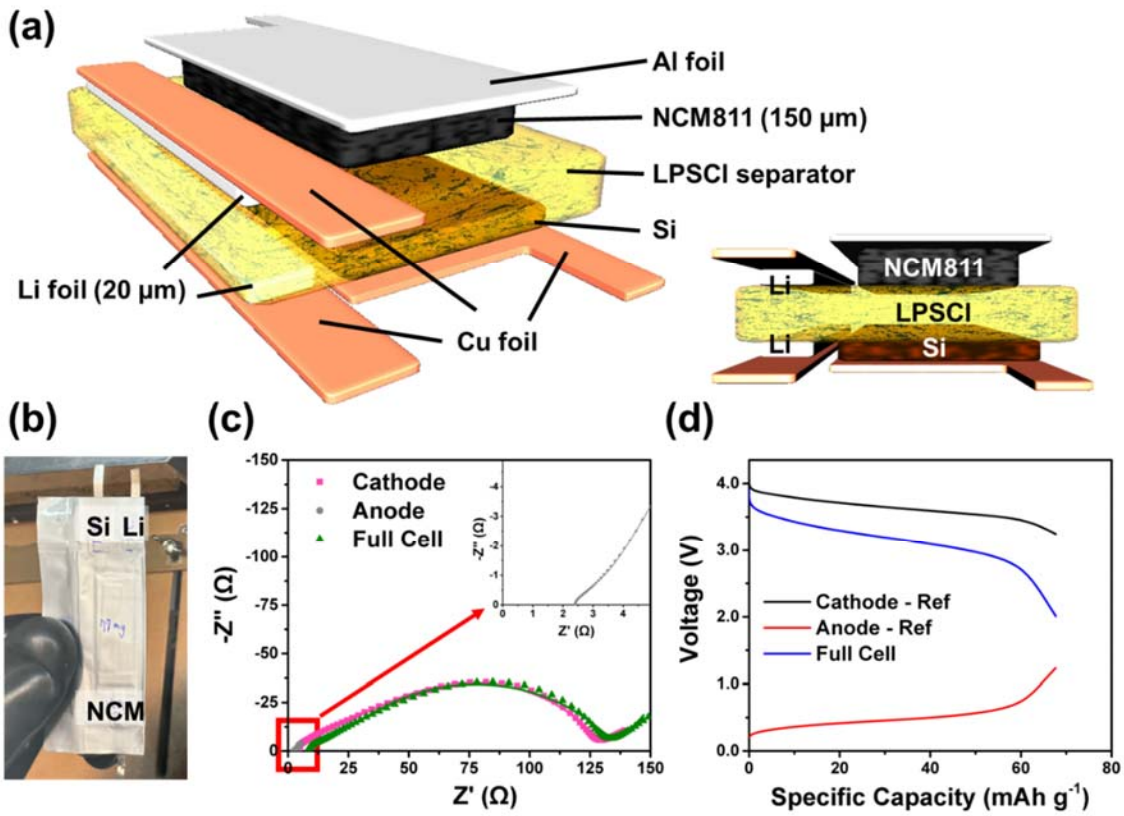

Figure 5.4. (a) The schematic of the structure and (b) a digital image of a three-electrode ASSPC. (c) The Nyquist plots of cathode – Li, anode – Li and full cell (anode – cathode) EIS at 50% state of charge in 11th discharge. (d) The voltage profiles of cathode – Li, anode – Li and full cell in 12th discharge.

5.2.3 Galvanostatic Cycling and Electrochemical Impedance Spectroscopy (EIS) of ASSPCs

Neware A211-BTS-4S-1U-100mA-124 battery cyclers and a Biologic VSP-300 were employed for galvanostatic cycling and EIS measurements. A voltage cutoff of 2 to 4.3 V was selected for NCM811 | Si system.[5] As Li diffusivity in pure Si can be improved only after lithiation[5], an activation cycle was introduced in all testing protocols. In the activation cycle, ASSPCs were cycled at 0.05 C for 5 hours, and then completed the whole cycle at 0.1 C. 5 MPa was applied in the activation cycle and reduced to target pressures afterwards. To obtain accurate cycling data, all ASSPCs were cycled in an oven set at 30°C to study the effect of cycling pressure. The rate capability test was conducted by running the ASSPCs at 0.1, 0.2, 0.3, 0.4, 0.5, 0.7, 1 and 0.1 C

and each C-rate for 3 cycles under 5 to 1 MPa. In the long-term cycling test, ASSPCs were cycled at 0.2 C and a constant voltage step till 0.05 C was applied at the end of charging. The ASSPCs were run till 100 cycles and EIS was obtained in the first and one hundredth cycle at state of charge of 50% during discharging. Z-View software was used to analyze EIS results. The three-electrode ASSPC was cycled at 30°C using a Neware A211-BTS-4S-1U-100mA-124 battery cycler for 10 cycles and its EIS was obtained at the ambient temperature in the 11^{th} cycle at state of charge of 50% during discharging using Biologic VSP-300. NCM811 cathode, Si anode and Li metal electrode were connected to working, counter and reference electrodes. Afterwards, the three-electrode ASSPC was cycled using Biologic VSP-300 at ambient temperature to record the voltage profiles of cathode – Li, anode – Li and full cell. The bilayer ASSPC was cycled at 0.1 C and a constant voltage step till 0.05 C was applied at the end of charging.

5.2.4 Characterization and Image Processing

A Helios G4 PFIB UXe DualBeam plasma focused ion beam / scanning electron microscope (P-FIB / SEM) with a xenon source was used to obtain the cross section of ASSPCs. After the ASSPCs were calendered, they were disassembled, and their cathode composites were attached to SEM stubs and sealed in an Ar-filled glovebox. The stubs were then transferred to P-FIB / SEM within 30 seconds of air exposure. Sample milling was conducted at 30 kV with a 2.5 μA current. Afterwards, a lower current (500 and 60 nA) was used to polish the cross-section. Electron imaging was conducted at 5 kV and 4 nA beam conditions. To segment the P-FIB / SEM images, they were imported into the Trainable Weka Segmentation Fiji module[36] to identify NMC811, LPSCl and pores. The segmentation relies on machine-learning algorithms that are manually trained by the user with the input images. The phase ratios were then computed in MATLAB. The images of pressure paper were also processed. Based on pictures of the pressure papers, the results were re-scaled in MATLAB using the ratio between the red color and the green and blue colors for each pixel in the jpg files.

5.2 Results and Discussion

The digital images of the bare UPCH and improved UPCH with springs and rubber gaskets are presented in Figure 5.5. To observe the pressure distribution, a pressure paper was placed in each cell holder. Upon receiving a pressure higher than its threshold, the pressure paper would turn red, and their digital images were taken (Figure 5.6a,b). To better visualize the pressure distribution, the digital images were converted to color gradient charts. When torquing the bare UPCH, a torque wrench was used to torque all four nuts sequentially and the torque value was gradually increased in each rotation to the target value to ensure parallelism of the metal plates. Nevertheless, an inhomogeneous pressure distribution was observed for the uniaxial set-up (Figure 5.7a). When a rigid surface (such as bare metal) is used to apply a uniaxial pressure, areas that are out of contact (e.g. the edges of ASSPCs or imperfect surface flatness of the metal plates forming concave regions) will receive a lower or no pressure. The pressure will concentrate on the rest of the area, resulting in over-pressurization (Figure 5.7b). These problems were mitigated with the improved UPCH, as rubber gaskets were able to conform to the shape of the metal plates and the ASSPC. Nevertheless, a uniform pressure distribution was still not observed (Figure 5.7c), as degree of deformation of the rubber gaskets was lower at the areas with larger gaps, resulting in lower pressure (Figure 5.7d).

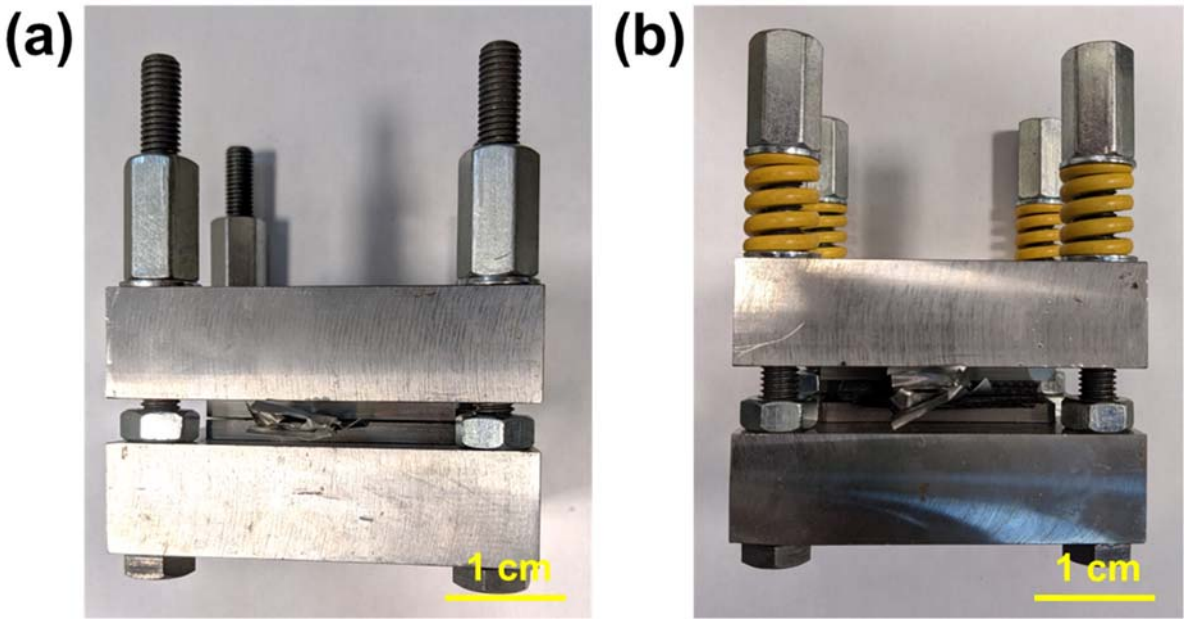

Figure 5.5. The digital images of (a) a bare UPCH with only bolts and nuts, and (b) an improved UPCH with springs and rubber gaskets.

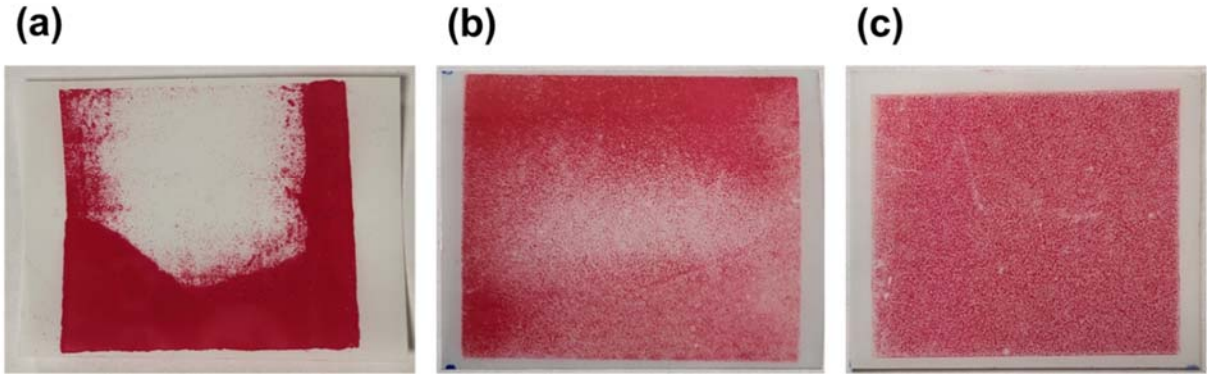

Figure 5.6. The digital image of pressure paper reflecting the pressure distribution of (a) a bare UPCH with metal surface, (b) an improved UPCH with rubber gaskets and springs, and (c) an IPCH.

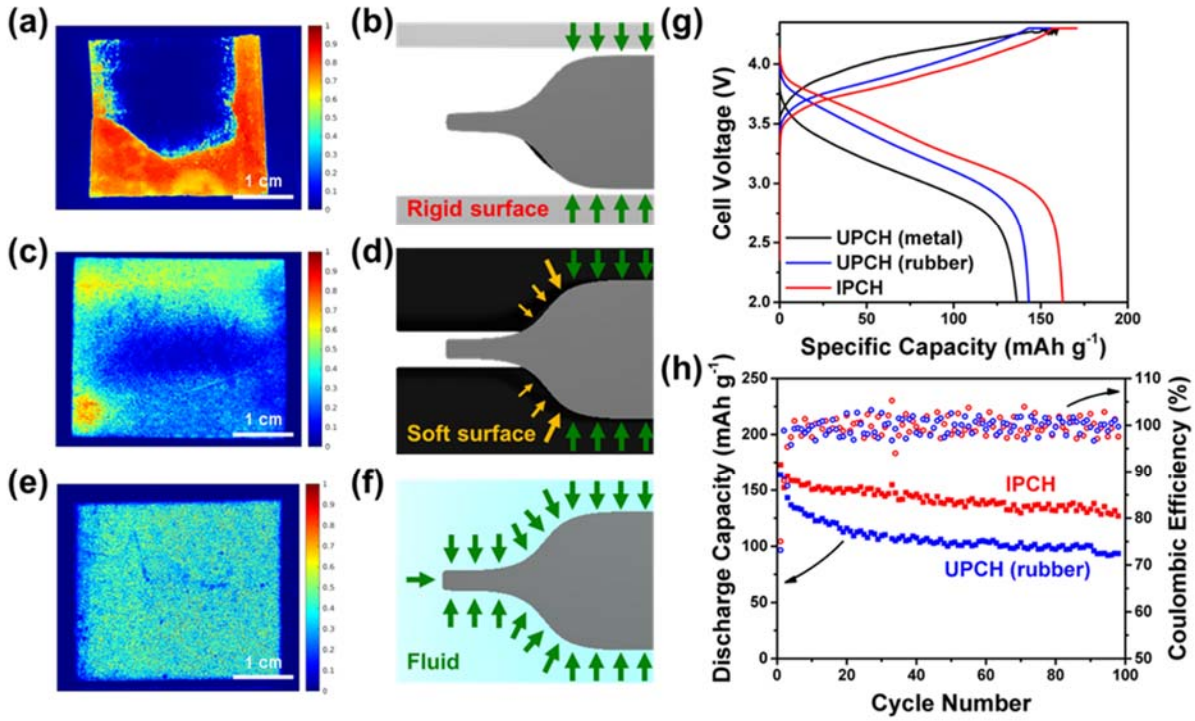

Figure 5.7. The experimental pressure paper observation and the schematics of the force distribution on the sealing edges of ASSPCs when (a,b) uniaxial pressure is applied by rigid metal surfaces with a bare UPCH, (c,d) uniaxial pressure is applied by soft rubber gaskets with an improved UPCH, and (e,f) isostatic pressure is applied by fluids with an IPCH, respectively. (g) The voltage profiles of 2nd cycle and (h) the reversible discharge capacity of ASSPCs when uniaxial and isostatic pressures were applied.

To further improve the uniformity of cycling pressure, IPCHs were designed, and their digital image and the schematic figure are presented in Figure 5.8. The structure of an IPCH consists of a sealed chamber to confine the pressurized fluid and accommodate the ASSPC, a pressure gauge to monitor the chamber pressure, a wire fit-through to enable cycling of the ASSPC sealed in its chamber, and a ball valve able to connect to an air compressor to pressurize, or depressurize the compressed air. Air was selected as pressurizing medium in this study because of availability and low cost. Pressure paper was vacuum sealed into a pouch bag, pressurized with an IPCH and the pressure distribution is presented in Figure 5.7e (the original image is shown in Figure 5.6c). A uniform pressure distribution was observed (Figure 5.7f). This can be explained by Pascal's principle, which states that a change in pressure applied at any point in the confined fluid at rest is transmitted undiminished throughout the fluid in all directions.

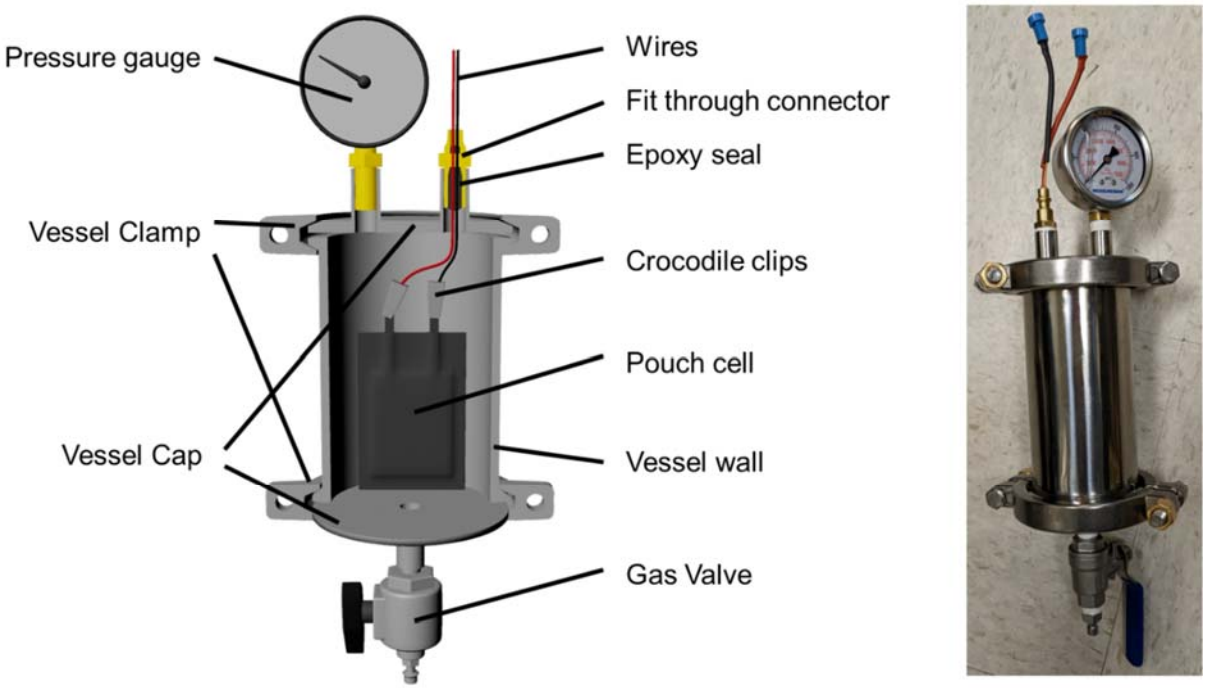

Figure 5.8. The schematic of the cross-sectional view and the digital image of an IPCH.

To understand how pressure uniformity affect electrochemical performance, three NCM811 | Li_6PS_5Cl (LPSCl) | Si ASSPCs with a cathode size of 3.5 x 1.5 cm^2 and an areal capacity of 4 mAh cm^{-2} were assembled, calendered at 500 MPa (this cell format was used for the rest of the article), pressurized with the three pouch cell holders, and cycled under 5 MPa at ambient temperature. The cycling pressure of the UPCH was estimated by the torque values of bolts and nuts, and that of IPCH was by observing the pressure gauge. Figure 5.7g shows voltage profiles of their first cycle. The cell became soft short during charging if uniaxial pressure was applied with rigid metal surfaces (bare IPCH), possibly due to the worst pressure uniformity causing inhomogeneous lithium flux in the system. The ASSPCs cycled with improved UPCH and IPCH successfully reached 100 cycles. As IPCH provides better pressure uniformity and less susceptible to structural fatigue (which might lead to cycling pressure drop over time), it exhibited

higher discharge capacity throughout 100 cycles and less capacity loss compared to those of improved UPCH.

Other than superior electrochemical performance, IPCHs can possibly provide higher energy density than UPCH in the module level due to the reduced demand of the structural components. There are two physical limitations that IPCHs can avoid: limited number of cells in a cell stack (Figure 5.9a), and flex of the pressurizing plates. When a UPCH is used (Figure 5.9b), pressure is transmitted through other ASSPCs. As such, all ASSPCs, including all layers inside pouches, must be perfectly aligned, which becomes more challenging and costly as the number of cells in one stack increases. The plates must also be sufficiently thick to resist deformation, which may result in applying higher pressure to the edges and lower pressure to the centers of ASSPCs (Figure 5.9c). As fluid is employed as pressurizing media in an IPCH, pressure is identically applied to all points in all directions. Hence, deformation of the vessel wall and arrangement of ASSPCs will not affect the pressure uniformity. As a result, thinner walls can be used in IPCHs to reduce module weight. The estimated required weights of UPCHs and IPCHs using different metal alloys with a pressure rating from 1 to 10 MPa are presented in Figure 5.10. IPCHs are all hypothetically lighter than UPCHs. The IPCHs can be lighter if polymers and composite materials (which often exhibit high tensile strength but low Young's modulus) are employed. Implementing ASSPC formats with higher energy density, such as jerry roll and Z-stacking, gives IPCH further edges, as there is fewer shape limitations for isostatic press.

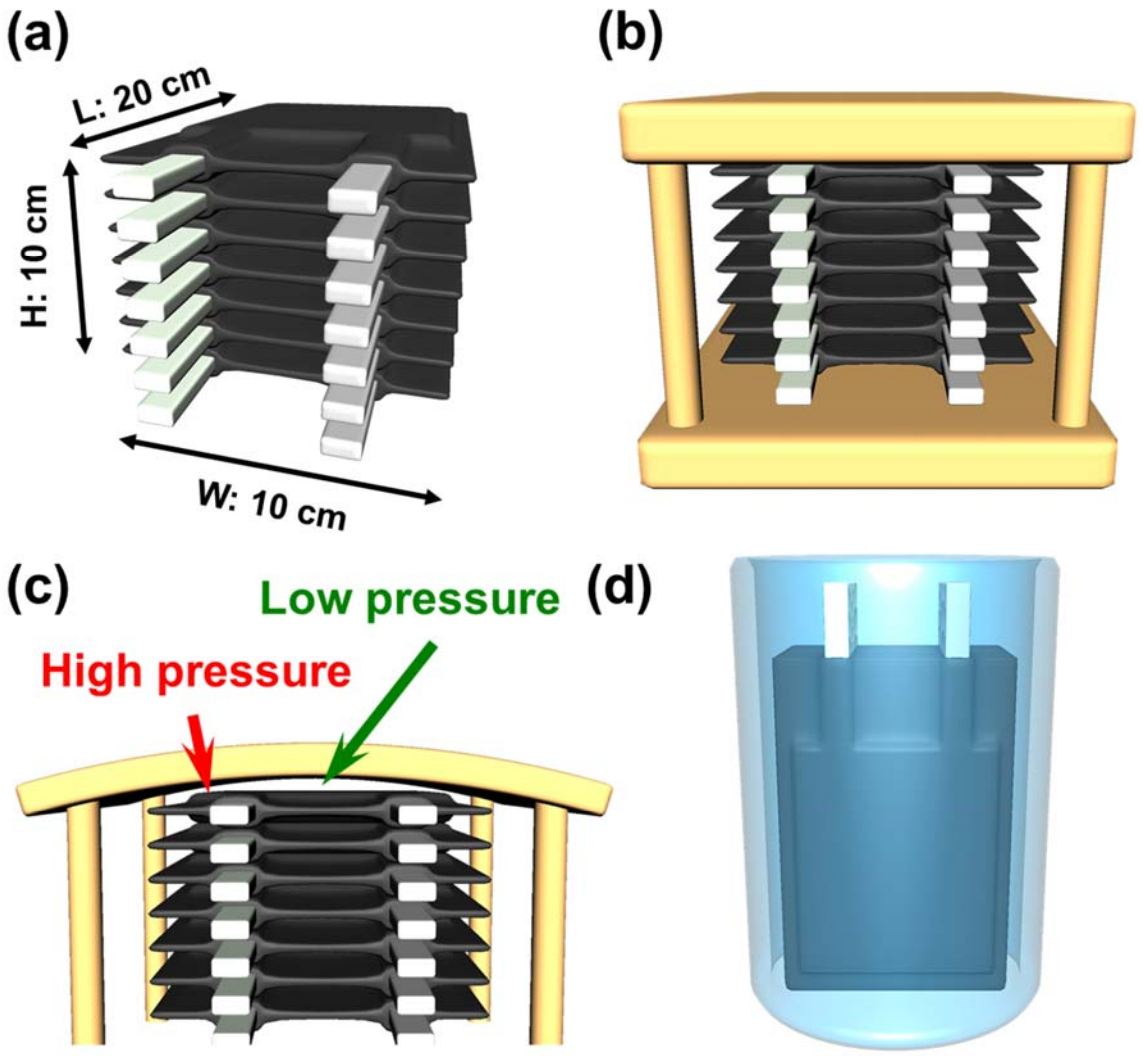

Figure 5.9. The schematic illustrating (a) a cell stack (the labelled dimension is used for energy density calculation in Figure 5.9), (b) a cell stack in a cylindrical UPCH, (c) bending of a UPCH plate when its thickness is insufficient, and (d) a cell stack in an IPCH. The dimension of the cell stack used to calculate the weight of pouch cell holders is 20 x 10 x 10 cm^3.

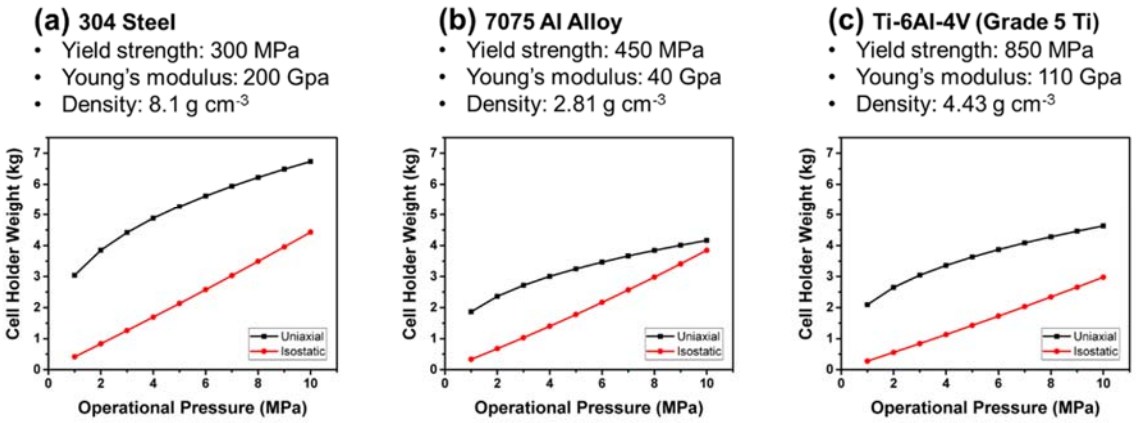

Figure 5.10. The weight – pressure rating plots of UPCHs and IPCHs. (a) 304 Steel, (b) 7075 Al alloy, and (c) Ti-6Al-4V Ti alloys are selected, as they have different density, yield strength and Young's modulus.

Taking advantage of accurate pressure control and uniform pressure distribution, the effect of cycling pressure of the IPCHs were further evaluated at 30°C to avoid the fluctuation of ambient temperature. It is worthy to note that the ASSPCs were activated at the first cycle at 5 MPa, and reduced to the target cycling pressures, from 5 MPa to 1 MPa (Figure 5.11a). At 0.1 C, cells cycled at all pressures except 1 MPa exhibited a similar discharge capacity of approximately 160 mAh g^{-1}, and the slight difference was due to batch variance of cathode composites. 2 MPa was the minimum required cycling pressure to keep a good interfacial contact in ASSPCs assembled in this study. The effect of cycling pressure became evident after the C-rate is above 0.3 C. At 1 C, the polarization of the cell grew so drastically that only 30 mAh g^{-1} could be obtained with a cycling pressure of 5 MPa. Nevertheless, ASSPCs cycled above 2 MPa regained most of their discharge capacities when the C-rate decreased back to 0.1 C. Three cycling pressures, 5, 3 and 2 MPa, were selected to conduct the long cycle test (Figure 5.11b-c), and they were tested at 0.2 C, since the current is moderate to distinguish the effect of cycling pressure to capacity retention while not vastly deteriorate the discharge capacities according to the rate capability test. As the cycling pressure decreased, it took more cycles for the Coulombic efficiency to reach close to 100%, and the initial discharge capacity decreased from 149.7 mAh g^{-1} at 5 MPa to 135.37 mAh g^{-1} at 2 MPa. The capacity retention after 100 cycles also deteriorated from 77.8% at 5 MPa

to 47.7% at 2 MPa, due to loss of interface contact. As electrode materials underwent repetitive volume change, it is crucial to apply pressure to maintain physical contact between SSE and electrode materials, and a higher pressure does better to support intimate interfacial contact.

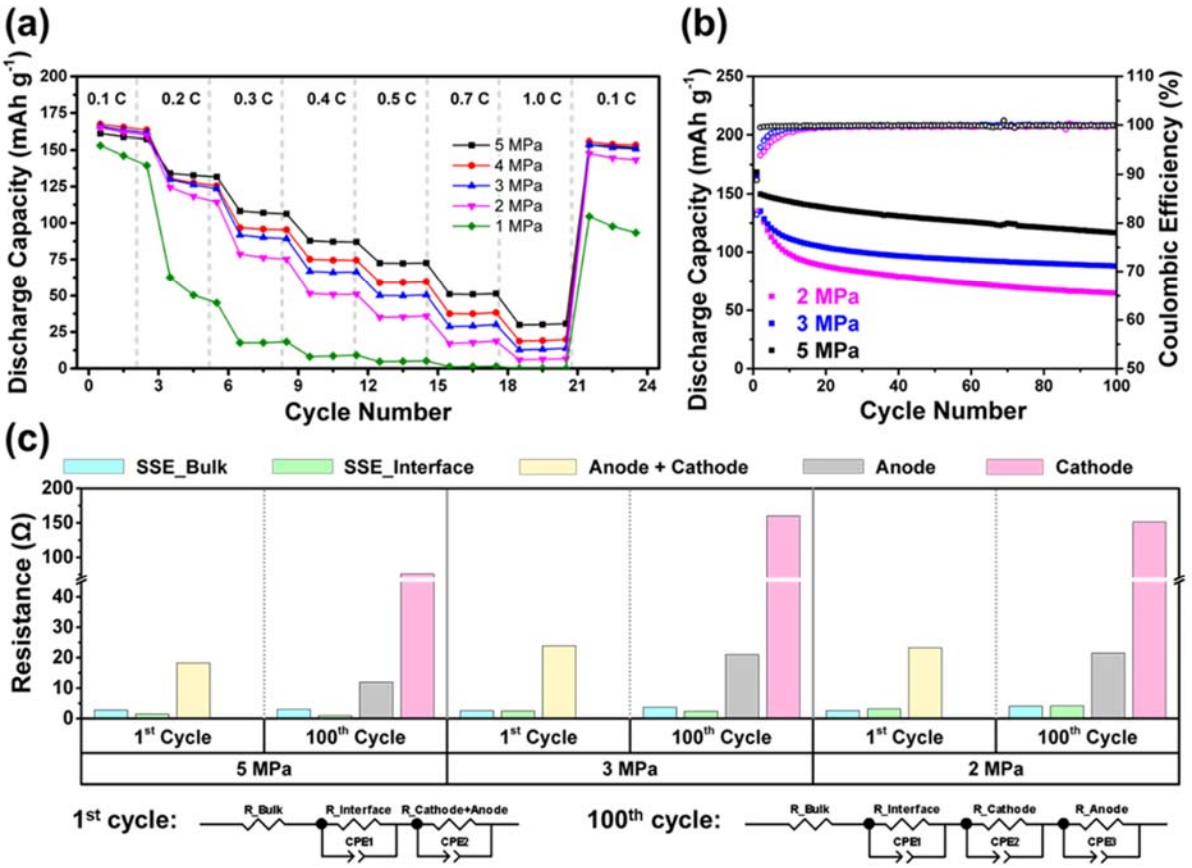

Figure 5.11. (a) Rate capability test of pouch cells with different operational pressure. (b) The capacity retention and Coulombic efficiency plots of pouch cells fabricated at 500 MPa and cycled at 5 MPa, 3 MPa and 2 MPa. (c) The EIS fitting results of the pouch cells measured after 1st and 100th cycle at 50% state of charge.

The electrochemical impedance spectroscopy (EIS) of first and one hundredth cycle of the three ASSPC (Figure 5.12, Table 5.2) were fitted (Figure 5.11c). Four components, the bulk, grain boundary interfaces of SSE, anode, and cathode, were used in the model.[37-39] The interfaces at cathode and anode were combined in the first cycle, as their time constants were either highly overlapped or were not able to be deconvoluted. All ASSPCs exhibited very similar SSE impedance values at different cycling pressures and cycle numbers, indicating that SSE separator

layers were stable during cycling and not sensitive to cycling pressure. After 100 cycles, an extra semicircle appeared. To determine the origin of the semicircle, a three-electrode ASSPC was tested.

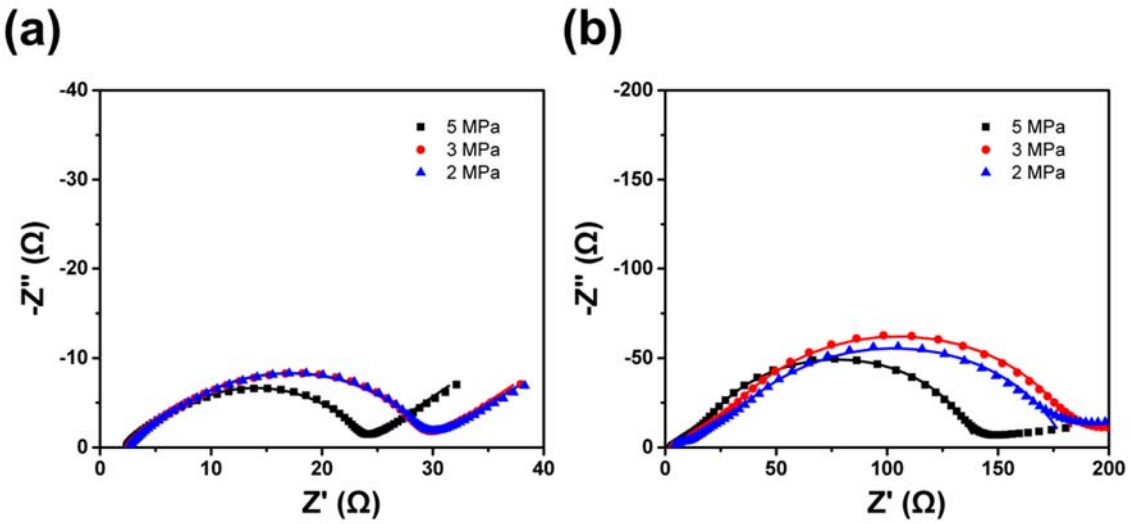

Figure 5.12. The Nyquist plots of pouch cells fabricated at 500 MPa and cycled at 5 MPa, 3 MPa and 2 MPa using IPCHs. The EIS of the pouch cells were measured in (a) the first and (b) the one hundredth cycle at the state of charge of 50%.

Table 5.2. The EIS fitted results of ASSPCs presented in Figure 5.12a.

Cycling Pressure	Cycle Number	Bulk	Interface	Cathode	Anode
5 MPa	1st	2.75	1.428	18.27	
	100th	3.022	0.97127	12.01	76.09
3 MPa	1st	2.609	2.462	23.92	
	100th	3.697	2.391	21.06	160.1
2 MPa	1st	2.575	3.182	23.25	
	100th	4.05	4.16	21.5	151.4

The schematic of the structure and the digital image of a three-electrode ASSPC are shown in Figure 5.4a and b. The working, counter and reference electrodes are NCM811 cathode, Si anode and Li metal (20 μm), respectively. After 10 cycles, the Nyquist plots (Figure 5.4c) indicated that cathode contributed much more than anode to the impedance. And thus, the smaller semicircle was assigned to anode. To further prove that the small anode impedance did not originate from short-circuiting between anode and reference electrodes, the discharge profiles of cathode, anode and full cell were recorded (Figure 5.4d). The anode voltage was over 250 mV throughout the whole discharge. The success of three-electrode ASSPC also highlighted the ability of IPCH to apply uniform pressure to uneven surfaces, as the thickness of Li, Si and NCM811 electrodes were not identical. When the cycling pressure decreased from 5 to 3 and 2 MPa, both cathode and anode impedance approximately doubled. Since the difference in the set-ups is operational pressure, this indicates that lower pressure IPCHs suffer from more loss in the physical contacts and such loss accumulate as it cycles. Consequently, it leads to increased polarization and more capacity fading.

In daily use, isostatic ASSPC modules may need to be depressurized during idling from time to time, and the effect of depressurizing to electrochemical performance needs to be evaluated. To probe the impedance evolution of ASSPCs under pressure change when it is not operational, an ASSPC experiencing 100 cycles was subjected to pressure decrease from 5 to 1 MPa, back to 5 MPa, and at last re-calendered at 500 MPa (the detailed procedure is described in Figure 5.13).

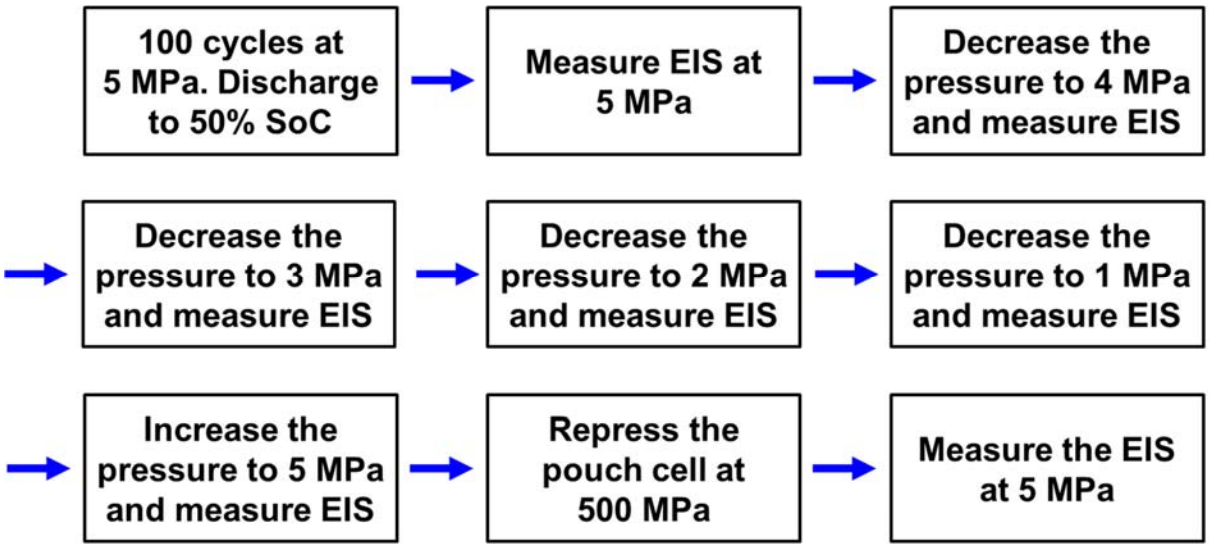

Figure 5.13. A schematic showing the pressurizing process of Figure 5.14a.

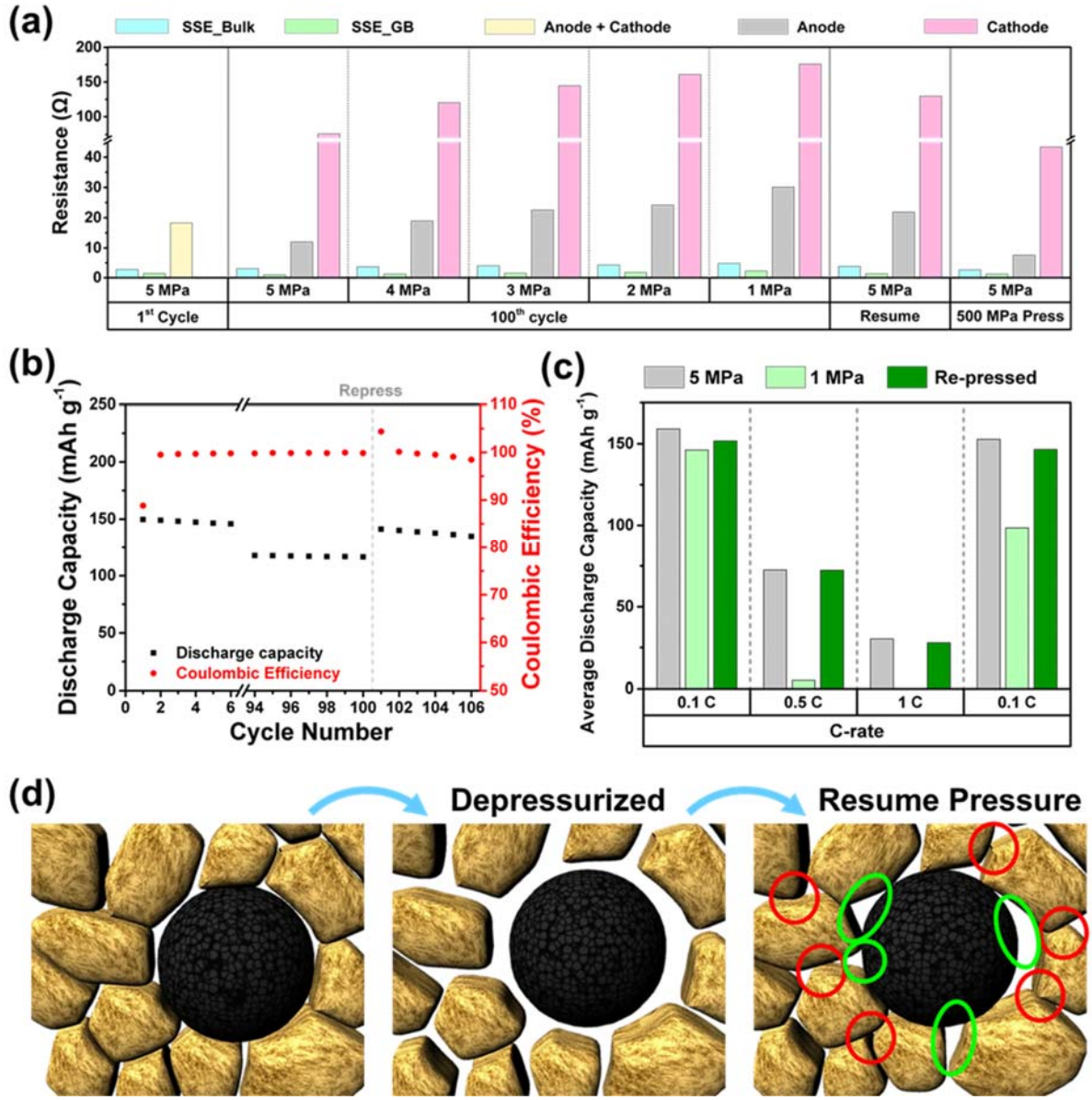

Figure 5.14. (a) The EIS results of the ASSPC cycled at 5 MPa after 100 cycles, decreased the pressure to 1 MPa, resume to 5 MPa, and then re-calendered at 500 MPa. (b) the capacity retention and CE of the pouch cell cycled at 5 MPa before and after re-calendering. (c) The average discharge capacity of the pouch cell having rate test at 1 MPa, re-calendering at 500 MPa, and having another rate test at 5 MPa. (d) Schematic of the evolution of the contact loss between SSE and cathode when insufficient pressure is applied and could not restore to their original state even the pressure is back to the initial value (red circles label the friction spots and green circles label the gaps). A much higher pressure must be applied to restore the contact between particles.

The EIS results are presented in Figure 5.14a, Figure 5.15 and Table 5.3.

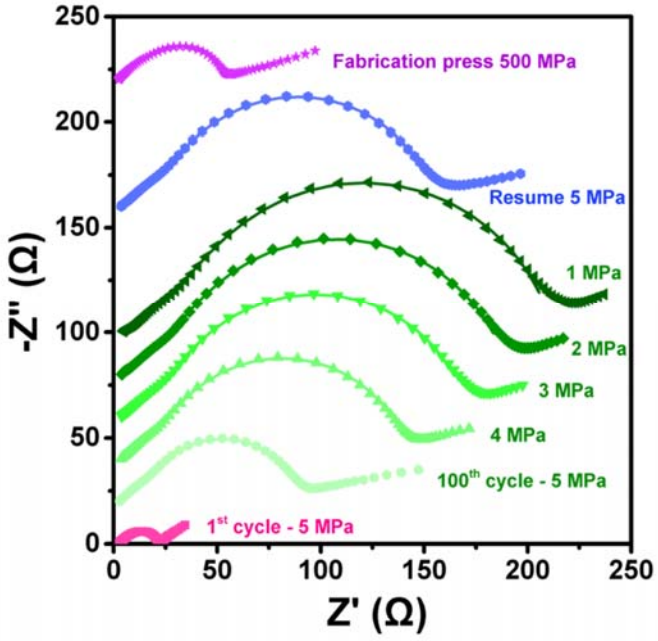

Figure 5.15. Decreasing the applied pressure from 5 to 1 MPa and then resume to 5 MPa of a pouch cell cycled at 5 MPa after 100 cycles. After the measurement, a fabrication pressure of 500 MPa was reapplied to the pouch cell and the EIS was measured at 5 MPa.

Table 5.3. The EIS fitted results of ASSPCs fabricated at 500 MPa and cycled at 5 MPa, 3 MPa and 2 MPa.

ASSPC States	Applied pressure	Bulk	Interface	Cathode	Anode
1st cycle	5 MPa	2.75	1.428	18.27	
100th cycle	5 MPa	3.022	0.97127	12.01	76.09
	4 MPa	3.574	1.21	18.93	120
	3 MPa	3.963	1.466	22.55	144.4
	2 MPa	4.199	1.755	24.2	160.8
	1 MPa	4.699	2.221	30.14	175.7
Resume	5 MPa	3.758	1.321	21.86	129.5
500 MPa press	5 MPa	2.545	1.214	7.662	43.39

As the pressure decreased, the impedance of the cell gradually increased. While the impedance of the SSE separator layer increased at a slower rate to 1.7 times, both the interfacial impedance at the anode and the cathode became approximately 2.5 times when the pressure decreased from 5 MPa to 1 MPa. The impedance of the ASSPC could not be restored even if the pressure resumed 5 MPa. The ASSPC cell impedance was significantly smaller than the initial state after 100 cycles but larger than in the first cycle after re-calendering. The re-calendered ASSPC was cycled again, its discharge capacity was also partially restored from 116.5 mAh g^{-1} in one hundredth cycle to 141.2 mAh g^{-1} in one hundred and first cycle (Figure 5.14b). To further understand the effect of re-calendering, the ASSPC undergoing rate capability test at 1 MPa was re-calendered and cycled again at 5 MPa, and the performance was also almost fully restored, similar to the ASSPC cycled at 5 MPa from the beginning (Figure 5.14c and Figure 5.16). Schematics using cathode composite as an example illustrating the impedance evolution are shown in Figure 5.14d. When the applied pressure decreases, both SSE and cathode particles could undergo elastic deformation and partially expand to their low-pressure state. This creates larger gaps, resulting in worse interfacial contact, and thus increases the cell impedance. As the friction between particles needs to be overcome to eliminate the gaps, it requires a larger pressure (re-calender) to reform the physical contact. It is worthy to note that the impedance could not be fully restored, as SEI and cathode electrolyte interface (CEI) had formed after a long cycle.[40]

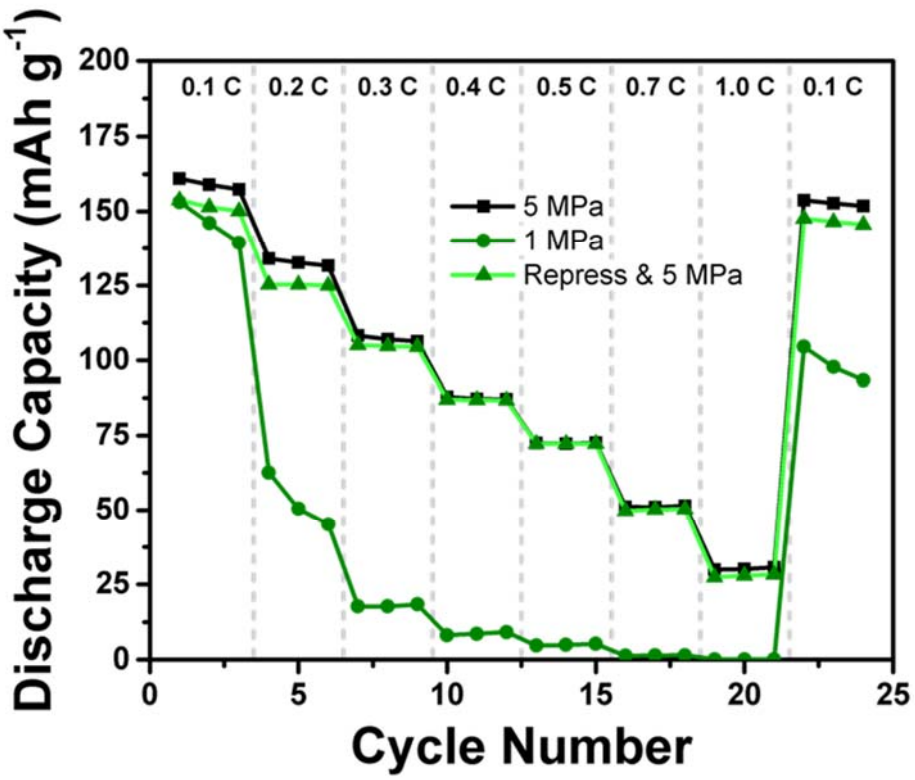

Figure 5.16. The rate capability test of an ASSPC cycled at 1 MPa, re-pressurized at 500 MPa and then tested again at 5 MPa. A similar rate capability as an ASSPC cycling at 5 MPa from the beginning was obtained.

To validate the feasibility of multi-layer pouch, a bilayer ASSPC (Cu | Si | SSE | NCM811 | Al | NCM811 | SSE | Si | Cu) with a total cathode area of 21 cm^2 and an areal theoretical capacity of approximately 5 mAh cm^{-2} (which led to a total theoretical capacity of over 100 mAh) was assembled, and cycled under 5 MPa at 30°C, 0.1 C. The FIB-SEM cross sectional images and the details of the cell format are shown in Figure 5.17a. The bilayer ASSPC exhibited an initial Coulombic efficiency of 76.9% and discharge capacity of 173.6 mAh g^{-1} (88.1 mAh) which is close to the single layer pouch cell indicating they have similar material utilization. After 100 cycles, a discharge capacity of 145 mAh g^{-1} was still retained (Figure 5.17b-c). To examine the power capability of the bilayer ASSPC, it was used to power an incandescent light with a rating of 2.5 V and 300 mA (Figure 5.17d), highlighting its ability to be operated at 3 C (Figure 5.17d). Although

the IPCH design might look bulky, its energy density can be further boosted by accommodating multiple ASSPCs in its chamber and improved module design.

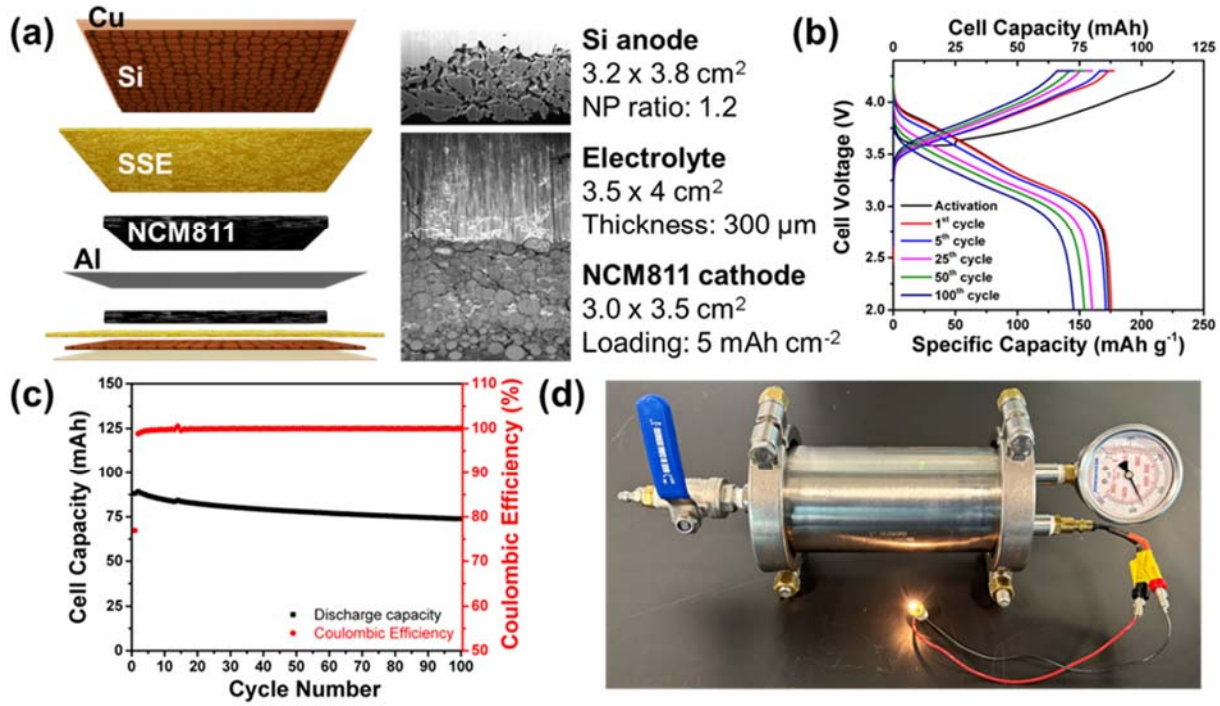

Figure 5.17. (a) The schematic and the P-FIB SEM cross section illustrating the bilayer pouch cell configuration. The (b) voltage profiles at different cycle numbers and (c) capacity retention of the 3 x 3.5 cm^2 bilayer ASSPC. (d) A bilayer ASSPC powering an incandescent light bulb with an input rating of 2.5 V – 300 mA at 5 MPa of cycling isostatic press.

5.3 Conclusion

As cycling pressure is required to maintain good interfacial contacts between different components in ASSBs, it is important to develop a pressurization system that enables uniform and accurate pressure to boost the electrochemical performance of ASSBs. In this study, we developed IPCHs that employed compressed air to apply a more homogenously distributed pressure than that of UPCHs with rigid metal surfaces or flexible rubber gaskets. As fluids do not suffer from material fatigue like many solid elastic materials, the IPCH showed a better capacity retention of an ASSPC than that of a UPCH was obtained over 100 cycles, crediting to a stable pressurization. The minimum required cycling pressure to cycle NCM811 | LPSCl | Si ASSPCs

was found to be as low as 2 MPa to deliver acceptable electrochemical performances, even at 1 C. However, a higher pressure is still preferred to maintain the intimate contact during long-term cycling. A bilayer ASSPC with a practical capacity of approximately 88.1 mAh was assembled, cycled in an IPCH at 0.1 C for 50 cycles. Moreover, the cell was capable of discharging at a rate of 3 C (300 mA) powering an incandescent light bulb. The concept of isostatic pressurization in this study not only provides a uniform and accurate pressurizing method to study the pressure effects on ASSPCs, but also endeavors on commercialization of ASSBs.

Chapter 5, in full, is a reprint of the material in preparation “Enabling uniform and accurate control of cycling pressure for all-solid-state batteries”. Chen, Y.-T.; Ham, S. Y.; Yang, J.; Lee, D. J.; Vicencio, M.; Lee, J. B.; Tan, D. H. S.; Chouchane, M.; Cronk, A.; Song, M. S.; Yin, Y. J.; Qian, J. T.; Oh, J. A. S.; Jang, J.; Chen, Z.; Meng, Y. S. The dissertation author was the first author of this papers, all authors contributed to this work.

References

1. Horowitz, Y.; Schmidt, C.; Yoon, D.-h.; Riegger, L. M.; Katzenmeier, L.; Bosch, G. M.; Noked, M.; Ein-Eli, Y.; Janek, J.; Zeier, W. G., Between Liquid and All Solid: A Prospect on Electrolyte Future in Lithium-Ion Batteries for Electric Vehicles. *Energy Technology* **2020,** *8* (11), 2000580.

2. Jung, Y. S.; Oh, D. Y.; Nam, Y. J.; Park, K. H., Issues and challenges for bulk-type all-solid-state rechargeable lithium batteries using sulfide solid electrolytes. *Isr. J. Chem.* **2015,** *55* (5), 472-485.

3. Kerman, K.; Luntz, A.; Viswanathan, V.; Chiang, Y.-M.; Chen, Z., practical challenges hindering the development of solid state Li ion batteries. *J. Electrochem. Soc.* **2017,** *164* (7), A1731.

4. Lee, H.; Oh, P.; Kim, J.; Cha, H.; Chae, S.; Lee, S.; Cho, J., Advances and Prospects of Sulfide All-Solid-State Lithium Batteries via One-to-One Comparison with Conventional Liquid Lithium Ion Batteries. *Adv. Mater.* **2019,** *31* (29), 1900376.

5. Tan, D. H.; Chen, Y.-T.; Yang, H.; Bao, W.; Sreenarayanan, B.; Doux, J.-M.; Li, W.; Lu, B.; Ham, S.-Y.; Sayahpour, B., Carbon Free High Loading Silicon Anodes Enabled by Sulfide Solid Electrolytes for Robust All Solid-State Batteries. *arXiv preprint arXiv:2103.04230* **2021**.

6. Cangaz, S.; Hippauf, F.; Reuter, F. S.; Doerfler, S.; Abendroth, T.; Althues, H.; Kaskel, S., Enabling High-Energy Solid-State Batteries with Stable Anode Interphase by the Use of Columnar Silicon Anodes. *Adv. Energy Mater.* **2020,** *10* (34), 2001320.

7. Chan, C. K.; Peng, H.; Liu, G.; McIlwrath, K.; Zhang, X. F.; Huggins, R. A.; Cui, Y., High-performance lithium battery anodes using silicon nanowires. *Nat. Nanotechnol.* **2008,** *3* (1), 31-35.

8. Wu, H.; Chan, G.; Choi, J. W.; Ryu, I.; Yao, Y.; McDowell, M. T.; Lee, S. W.; Jackson, A.; Yang, Y.; Hu, L., Stable cycling of double-walled silicon nanotube battery anodes through solid–electrolyte interphase control. *Nat. Nanotechnol.* **2012,** *7* (5), 310-315.

9. Liu, N.; Lu, Z.; Zhao, J.; McDowell, M. T.; Lee, H.-W.; Zhao, W.; Cui, Y., A pomegranate-inspired nanoscale design for large-volume-change lithium battery anodes. *Nat. Nanotechnol.* **2014,** *9* (3), 187-192.

10. Cui, L.-F.; Ruffo, R.; Chan, C. K.; Peng, H.; Cui, Y., Crystalline-amorphous core− shell silicon nanowires for high capacity and high current battery electrodes. *Nano Lett.* **2009,** *9* (1), 491-495.

11. Su, X.; Wu, Q.; Li, J.; Xiao, X.; Lott, A.; Lu, W.; Sheldon, B. W.; Wu, J., Silicon-based nanomaterials for lithium-ion batteries: a review. *Adv. Energy Mater.* **2014,** *4* (1), 1300882.

12. Banerjee, A.; Wang, X.; Fang, C.; Wu, E. A.; Meng, Y. S., Interfaces and interphases in All-Solid-State batteries with inorganic solid electrolytes. *Chem. Rev.* **2020,** *120* (14), 6878-6933.

13. Koerver, R.; Aygün, I.; Leichtweiß, T.; Dietrich, C.; Zhang, W.; Binder, J. O.; Hartmann, P.; Zeier, W. G.; Janek, J. r., Capacity fade in solid-state batteries: interphase formation and chemomechanical processes in nickel-rich layered oxide cathodes and lithium thiophosphate solid electrolytes. *Chem. Mater.* **2017,** *29* (13), 5574-5582.

14. Shi, T.; Zhang, Y.-Q.; Tu, Q.; Wang, Y.; Scott, M.; Ceder, G., Characterization of mechanical degradation in an all-solid-state battery cathode. *J. Mater. Chem. A* **2020,** *8* (34), 17399-17404.

15. Chen, Y.-T.; Duquesnoy, M.; Tan, D. H.; Doux, J.-M.; Yang, H.; Deysher, G.; Ridley, P.; Franco, A. A.; Meng, Y. S.; Chen, Z., Fabrication of high-quality thin solid-state electrolyte films assisted by machine learning. *ACS Energy Letters* **2021,** *6* (4), 1639-1648.

16. Tan, D. H.; Meng, Y. S.; Jang, J., Scaling up high-energy-density sulfidic solid-state batteries: A lab-to-pilot perspective. *Joule* **2022,** *6* (8), 1755-1769.

17. Liu, S.; Zhou, L.; Han, J.; Wen, K.; Guan, S.; Xue, C.; Zhang, Z.; Xu, B.; Lin, Y.; Shen, Y., Super Long-Cycling All-Solid-State Battery with Thin Li6PS5Cl-Based Electrolyte. *Adv. Energy Mater.* **2022,** *12* (25), 2200660.

18. Wang, C.; Kim, J. T.; Wang, C.; Sun, X., Progress and Prospects of Inorganic Solid-State Electrolyte-Based All-Solid-State Pouch Cells. *Adv. Mater.* **2023,** *35* (19), 2209074.

19. Lee, Y.-G.; Fujiki, S.; Jung, C.; Suzuki, N.; Yashiro, N.; Omoda, R.; Ko, D.-S.; Shiratsuchi, T.; Sugimoto, T.; Ryu, S., High-energy long-cycling all-solid-state lithium metal batteries enabled by silver–carbon composite anodes. *Nat. Energy* **2020,** *5* (4), 299-308.

20. Dixit, M.; Beamer, C.; Amin, R.; Shipley, J.; Eklund, R.; Muralidharan, N.; Lindqvist, L.; Fritz, A.; Essehli, R.; Balasubramanian, M., The Role of Isostatic Pressing in Large-Scale Production of Solid-State Batteries. *ACS Energy Letters* **2022,** *7* (11), 3936-3946.

21. Zhang, F.; Guo, Y.; Zhang, L.; Jia, P.; Liu, X.; Qiu, P.; Zhang, H.; Huang, J., A review of the effect of external pressure on all-solid-state batteries. *Etransportation* **2022**, 100220.

22. Koerver, R.; Zhang, W.; de Biasi, L.; Schweidler, S.; Kondrakov, A. O.; Kolling, S.; Brezesinski, T.; Hartmann, P.; Zeier, W. G.; Janek, J., Chemo-mechanical expansion of lithium electrode materials–on the route to mechanically optimized all-solid-state batteries. *Energy Environ. Sci.* **2018,** *11* (8), 2142-2158.

23. Ham, S.-Y.; Yang, H.; Nunez-cuacuas, O.; Tan, D. H.; Chen, Y.-T.; Deysher, G.; Cronk, A.; Ridley, P.; Doux, J.-M.; Wu, E. A., Assessing the critical current density of all-solid-state Li metal symmetric and full cells. *Energy Storage Materials* **2023,** *55*, 455-462.

24. Lin, D.; Liu, Y.; Cui, Y., Reviving the lithium metal anode for high-energy batteries. *Nat Nanotechnol* **2017,** *12* (3), 194-206.

25. Ito, S.; Fujiki, S.; Yamada, T.; Aihara, Y.; Park, Y.; Kim, T. Y.; Baek, S.-W.; Lee, J.-M.; Doo, S.; Machida, N., A rocking chair type all-solid-state lithium ion battery adopting Li2O–ZrO2 coated LiNi0. 8Co0. 15Al0. 05O2 and a sulfide based electrolyte. *J. Power Sources* **2014,** *248*, 943-950.

26. Sakuda, A.; Kuratani, K.; Yamamoto, M.; Takahashi, M.; Takeuchi, T.; Kobayashi, H., All-solid-state battery electrode sheets prepared by a slurry coating process. *J. Electrochem. Soc.* **2017,** *164* (12), A2474.

27. Nam, Y. J.; Oh, D. Y.; Jung, S. H.; Jung, Y. S., Toward practical all-solid-state lithium-ion batteries with high energy density and safety: comparative study for electrodes fabricated by dry-and slurry-mixing processes. *J. Power Sources* **2018,** *375*, 93-101.

28. Yuan, H.; Nan, H. X.; Zhao, C. Z.; Zhu, G. L.; Lu, Y.; Cheng, X. B.; Liu, Q. B.; He, C. X.; Huang, J. Q.; Zhang, Q., Slurry-coated sulfur/sulfide cathode with Li metal anode for all-solid-state lithium-sulfur pouch cells. *Batteries & Supercaps* **2020,** *3* (7), 596-603.

29. Fiedler, M.; Cangaz, S.; Hippauf, F.; Dörfler, S.; Abendroth, T.; Althues, H.; Kaskel, S., Mechanistic Insights into the Cycling Behavior of Sulfur Dry-Film Cathodes. *Advanced Sustainable Systems* **2023**, 2200439.

30. Li, J.; Li, Y.; Zhang, S.; Liu, T.; Li, D.; Ci, L., Long cycle life all-solid-state batteries enabled by solvent-free approach for sulfide solid electrolyte and cathode films. *Chem. Eng. J.* **2023,** *455*, 140605.

31. Lee, D. J.; Jang, J.; Lee, J. P.; Wu, J.; Chen, Y. T.; Holoubek, J.; Yu, K.; Ham, S. Y.; Jeon, Y.; Kim, T. H., Physio-Electrochemically Durable Dry-Processed Solid-State Electrolyte Films for All-Solid-State Batteries. *Adv. Funct. Mater.* **2023**, 2301341.

32. Wang, C.; Yu, R.; Duan, H.; Lu, Q.; Li, Q.; Adair, K. R.; Bao, D.; Liu, Y.; Yang, R.; Wang, J., Solvent-free approach for interweaving freestanding and ultrathin inorganic solid electrolyte membranes. *ACS Energy Letters* **2021,** *7* (1), 410-416.

33. Li, Y.; Wu, Y.; Wang, Z.; Xu, J.; Ma, T.; Chen, L.; Li, H.; Wu, F., Progress in solvent-free dry-film technology for batteries and supercapacitors. *Mater. Today* **2022,** *55*, 92-109.

34. Hippauf, F.; Schumm, B.; Doerfler, S.; Althues, H.; Fujiki, S.; Shiratsuchi, T.; Tsujimura, T.; Aihara, Y.; Kaskel, S., Overcoming binder limitations of sheet-type solid-state cathodes using a solvent-free dry-film approach. *Energy Storage Materials* **2019,** *21*, 390-398.

35. An, S. J.; Li, J.; Daniel, C.; Kalnaus, S.; Wood, D. L., Design and demonstration of three-electrode pouch cells for lithium-ion batteries. *J. Electrochem. Soc.* **2017,** *164* (7), A1755.

36. Arganda-Carreras, I.; Kaynig, V.; Rueden, C.; Eliceiri, K. W.; Schindelin, J.; Cardona, A.; Sebastian Seung, H., Trainable Weka Segmentation: a machine learning tool for microscopy pixel classification. *Bioinformatics* **2017,** *33* (15), 2424-2426.

37. Zhang, Z.; Chen, S.; Yang, J.; Wang, J.; Yao, L.; Yao, X.; Cui, P.; Xu, X., Interface re-engineering of Li10GeP2S12 electrolyte and lithium anode for all-solid-state lithium batteries with ultralong cycle life. *ACS applied materials & interfaces* **2018,** *10* (3), 2556-2565.

38. Hori, S.; Kanno, R.; Sun, X.; Song, S.; Hirayama, M.; Hauck, B.; Dippon, M.; Dierickx, S.; Ivers-Tiffée, E., Understanding the impedance spectra of all-solid-state lithium battery cells with sulfide superionic conductors. *J. Power Sources* **2023,** *556*, 232450.

39. Cao, D.; Sun, X.; Li, Y.; Anderson, A.; Lu, W.; Zhu, H., Long-Cycling Sulfide-Based All-Solid-State Batteries Enabled by Electrochemo-Mechanically Stable Electrodes. *Adv. Mater.* **2022,** *34* (24), 2200401.

40. Tan, D. H.; Wu, E. A.; Nguyen, H.; Chen, Z.; Marple, M. A.; Doux, J.-M.; Wang, X.; Yang, H.; Banerjee, A.; Meng, Y. S., Elucidating Reversible Electrochemical Redox of Li6PS5Cl Solid Electrolyte. *ACS Energy Letters* **2019,** *4* (10), 2418-2427.

Chapter 6. Summary and Perspectives

In this thesis, we have covered material selection and cell engineering for scalable manufacturing of ASSBs. To obtain high quality slurry-processed films, slurries with suitable rheological is requisite. Three of the manufacturing parameters, liquid to solid ratio, binder ratio and cosolvent ratio, that affect the rheological properties were selected for the study and machine learning was employed to analyze the collected dataset. On top of ionic conductivity, film uniformity was found to be another crucial factor to determine the film quality. Guided by machine learning, a film selected from the group with both good ionic conductivity and uniformity was assembled into a film cell and survived 100 cycles, while the other film with good ionic conductivity but low uniformity became short circuit very soon. Other than manufacturing techniques, material selection addressing dry room adaptability is another essential factor for scalable manufacturing. As LPSCl and chloride SSEs exhibit desirable ionic conductivity, synthesis cost and mechanical properties for ASSB fabrication, they were selected to evaluate their chemical stability in the dry room environment. Both types of SSEs undergo hydrolysis and hydration reactions when exposed to moisture. The hydrolysis of LPSCl forms H_2S, which results in sulfur loss, and decomposes into LiCl, Li_3PO_4 and Li_2S, while Hydrated LPSCl can be partially recovered with formation of little oxysulfide species. Depending on the metal center, chloride SSEs undergo different degrees of hydration and hydrolysis. LZC fully hydrolyzes and form ZrO2 and LiCl upon exposure; LYC forms hydrate during exposure but fully hydrolyzes to form YOCl and LiCl when heated; LIC forms hydrate but is fully recoverable after heating. When exposed to dry room environment, LPSCl preserved ionic conductivity at least two times better than chloride SSEs and fully maintain its electrochemical performance in NCM811 | LiIn test, while chloride SSEs show significantly decreased capacity retention. Hence, LPSCl is more dry room adaptable, and surface protective measures may be required for chloride SSEs. Lastly, all techniques and experiences were integrated into pouch cell fabrication. IPCHs with the ability to provide stable and uniform pressure

are designed. It is also easy to control the pressure accurately and achieve higher energy module energy density with such design. ASSPCs were tested and compared using IPCHs and UPCHs and IPCHs exhibited superior capacity utilization and retention. To demonstrate the potential of IPCHs in ASSB research, ASSPCs were cycled at pressures ranging from 1 to 5 MPa. The rate capability and capacity retention were found to increase with cycling pressure due to better interfacial contact at higher cycling pressure. A bilayer ASSPC with a total capacity of 100 mAh was assembled and achieved 100 cycles at a C rate of 0.1 C under 30°C. It also lit up an incandescent light bulb rated 2.5 V and 300 mA.

Despite all the achievements, there are several essential issues that need to be addressed on the way of commercialization of ASSBs:

1. Increasing the active material loading and initial Coulombic efficiency of cathode composites. All cathode composites shown in this thesis exhibited mediocre initial Coulombic efficiency of less than 80%, and a low active material ratio of 66%. These influence the practical energy density of ASSBs. There are few feasible ways to optimize the cathode composite: optimizing the particle size of SSEs, utilizing SSEs with better oxidation stability and ionic conductivity, such as newly developed oxychloride SSEs[1-2]; employing single crystal cathode material to mitigate ionic transport bottle neck.

2. Developing binders that are mechanically strong and stable against anodes. The slurry processed SSE separators exhibited weak mechanical strength and are not suitable for forming free standing films. Although the issue of being mechanically weak can be addressed by adapting dry process, PTFE used in dry process exhibits inferior reduction stability and will form electrochemical conductive side products that result in short circuit of the cell. As such, an extremely low PTFE ratio of less than 0.2% needs to be used, but once again results

in low mechanical strength. As the stacking process of pouch cells needs films with sufficient mechanical strength, it is urgent to develop new binders that meet the requirements.

3. Investigating pressure distribution inside multilayer ASSPCs and pouch cell format facilitating pressure uniformity. To increase energy density, pouch wrapping materials should be minimized and multilayer stacking should be employed. When the thickness of ASSPCs increases, the pressure distribution on each layer may vary, especially layers locating in the middle. Uneven pressure distribution may deteriorate electrochemical performance. Hence, the limitations on maximum number of layers and cell formats that improve pressure uniformity needs to be investigated.

References

1. Hu, L.; Wang, J.; Wang, K.; Gu, Z.; Xi, Z.; Li, H.; Chen, F.; Wang, Y.; Li, Z.; Ma, C., A cost-effective, ionically conductive and compressible oxychloride solid-state electrolyte for stable all-solid-state lithium-based batteries. *Nature Communications* **2023,** *14* (1), 3807.

2. Zhang, S.; Zhao, F.; Chen, J.; Fu, J.; Luo, J.; Alahakoon, S. H.; Chang, L.-Y.; Feng, R.; Shakouri, M.; Liang, J., A family of oxychloride amorphous solid electrolytes for long-cycling all-solid-state lithium batteries. *Nature Communications* **2023,** *14* (1), 3780.